



**INSTITUTO POTOSINO DE INVESTIGACIÓN  
CIENTÍFICA Y TECNOLÓGICA, A.C.**

**POSGRADO EN CIENCIAS AMBIENTALES**

**Synthesis and Adsorption Performance of a  
Biochar Improved with Carbon Nanostructures  
for Fast Gasoline Emissions Removal**

Tesis que presenta

**Joel de Jesús Gutiérrez Martínez**

Para obtener el grado de

**Doctor en Ciencias Ambientales**

**Director de la Tesis:**

**Dr. José René Rangel Méndez**

San Luis Potosí, S.L.P., 30 de mayo de 2022



## Constancia de aprobación de la tesis

La tesis “**Synthesis and Adsorption Performance of Biochar Improved with Carbon Nanostructures for a Fast Gasoline Emissions Removal**” presentada para obtener el Grado de Doctor(a) en Ciencias Ambientales fue elaborada por **Joel de Jesús Gutiérrez Martínez** y aprobada el **día 30 de mayo de 2022** por los suscritos, designados por el Colegio de Profesores de la División de Ciencias Ambientales del Instituto Potosino de Investigación Científica y Tecnológica, A.C.

---

**Dr. José René Rangel Méndez**  
Director de la tesis

---

**Dr. Elena V. Basiuk**  
Miembro del Comité Tutorial

---

**Dr. César Nieto Delgado**  
Miembro del Comité Tutorial

---

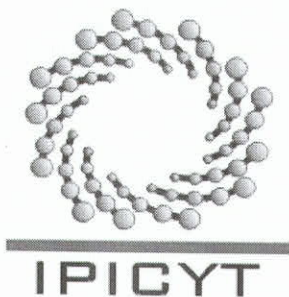
**Dr. Miguel Ávalos Borja**  
Miembro del Comité Tutorial



## **Institutional acknowledgement**

The present thesis was developed in the Adsorption and Ionic Exchange Laboratory, Instrumental Analysis Laboratory and Environmental Biotechnology Laboratory of the Environmental Sciences Division of the Instituto Potosino de Investigación Científica y Tecnológica, A.C (IPICyT); under the direction of PhD. José René Rangel Méndez.

During the accomplishment of this work, the author received an academic grant from the National Council of Science and Technology (CVU No. 634215) and financial support from IPICyT.



# Instituto Potosino de Investigación Científica y Tecnológica, A.C.

## Acta de Examen de Grado

La Secretaría Académica del Instituto Potosino de Investigación Científica y Tecnológica, A.C., certifica que en el Acta 031 del Libro Primero de Actas de Exámenes de Grado del Programa de Doctorado en Ciencias Ambientales está asentado lo siguiente:

En la ciudad de San Luis Potosí a los 30 días del mes de mayo del año 2022, se reunió a las 16:00 horas en las instalaciones del Instituto Potosino de Investigación Científica y Tecnológica, A.C., el Jurado integrado por:

<b>Dr. Miguel Avalos Borja</b>	<b>Presidente</b>	<b>IPICYT</b>
<b>Dra. Elena Golovataya Dzhymbeeva</b>	<b>Secretaria</b>	<b>UNAM</b>
<b>Dr. César Nieto Delgado</b>	<b>Sinodal</b>	<b>IPICYT</b>
<b>Dr. José René Rangel Méndez</b>	<b>Sinodal</b>	<b>IPICYT</b>

a fin de efectuar el examen, que para obtener el Grado de:

**DOCTOR EN CIENCIAS AMBIENTALES**

sustentó el C.

**Joel de Jesús Gutiérrez Martínez**

sobre la Tesis intitulada:

*Synthesis and Adsorption Performance of a Biochar Improved with Carbon Nanostructures for Fast Gasoline Emissions Removal*

que se desarrolló bajo la dirección de

**Dr. José René Rangel Méndez**

El Jurado, después de deliberar, determinó

**APROBARLO**

Dándose por terminado el acto a las 18:40 horas, procediendo a la firma del Acta los integrantes del Jurado. Dando fe la Secretaría Académica del Instituto.

A petición del interesado y para los fines que al mismo convengan, se extiende el presente documento en la ciudad de San Luis Potosí, S.L.P., México, a los 30 días del mes de mayo de 2022.

  
**Mtra. Ivonne Lizette Cuevas Vélez**  
Jefa del Departamento del Posgrado

  
**Dra. Lina Raquel Riego Ruiz**  
Secretaría Académica





# Dedicatória

## Acknowledgements

I wish to express my sincere thanks to my thesis directors, PhD. José René Rangel Méndez for her constant support, commitment, and feedback in this research. To PhD. Cesar Nieto Delgado for your broad scientist criteria, commitment, and the most objective feedback in this research.

My sincere thanks are expressed to the committee members, PhD. Miguel Avalos Borja and Elena Golovataya Dzhymbeeva for their invaluable comments and attentions.

My gratitude to Laboratorio Nacional de Investigaciones de Nanociencias y Nanotecnología (LINAN). I am especially thankful to MC. Beatriz Adriana Rivera Escoto, MC. Ana Iris Peña Maldonado, and PhD. Hector Gabriel Silva Pereyra for your technical support and advice for XRD, Raman spectroscopy, SEM and TEM.

My gratitude is also expressed to academic technicians from Environmental Sciences Division of IPICYT, MC. Juan Pablo Rodas Ortiz, and MC. Guillermo Vidriales Escobar and Ing. Ma. Del Carmen Rocha Medina. A special gratitude is expressed to PhD. Elizabeth Diane Isaacs Paez for your invaluable technical support and friendship.

Also, thank you to PhD. Carlos Enrique Flores Chaparro for your important support and experience in the mathematic model analysis developed in this research. Also, thank you to PhD. Esmeralda Nguyen López for your time and dedication to express this work into an outreach scientific paper.

My gratitude to all the funding: National CONACYT scholarship CVU No. 634215

To my laboratory co-workers for their time, knowledge, experience, and friendship.

Thank you to Itzel, Toño, Charly, Gerry, Emilia, Edgardo, Rodolfo, Erika, Nohemi, Efren, Pancho, Chuy, Tibu, David, Chino, and Pao for your invaluable support and friendship during eight years in IPICYT.

Finally, to my friends Benja, Luis, German, Victor, Manuel, Jade, Noe and Oscar for always being in the good times but more so in the bad.

# Content

---

Constancia de aprobación de la tesis	ii
Institutional acknowledges	iii
Acta de examen	iv
Dedicatorias	v
Acknowledgement	vi
Content	vii
List of tables	xi
List de figures	xiii
Resumen	xviii
Abstract	xx

---

## CHAPTER 1: Introduction

1.1. Overview about air pollution caused by volatile organic compounds	2
1.1.1. Emission inventory of VOCs	3
1.1.2. Effect of VOC on human health and environment	4
1.1.3. Processes for VOCs removal	5
1.2. Vehicular emissions	7
1.2.1. Evaporative emissions	8
1.2.2. Evaporative emission control system (EVAP)	9
1.3. Porous adsorbents for VOCs adsorption	11
1.3.1. Activated carbon	11
1.3.2. Biochar	12
1.3.3. Carbon nanostructure	15
1.3.3.1. Carbon nanotubes	16
1.3.3.2. Carbon nanofibers	18
1.3.3.3. Carbon nanospheres	20
1.3.3.4. Graphene and its derivatives	22
1.4. Surface modification for enhancing VOC adsorption	23
1.4.1. Conventional modification techniques	23
1.4.2. Chemical vapor deposition	25
1.5. Adsorption of VOCs on carbon-based materials	28

1.5.1.	Mechanisms of adsorbate-adsorbent interaction	29
1.5.2.	Gas adsorption set up	30
1.5.3.	VOCs adsorption performance	32
1.5.4.	Adsorbent regeneration.	34
1.6.	Key factors controlling VOCs adsorption	36
1.6.1.	Adsorbent properties	36
1.6.1.1.	Textural properties	36
1.6.1.2.	Chemical functional groups	38
1.6.2.	Adsorbate properties	39
1.7.	Motivation of this research	41
1.8.	Hypothesis	41
1.9.	General objective	42
1.9.1.	Specific objectives	42
<b>CHAPTER 2: Fast benzene vapor capture by natural macroporous biochar improved with carbon nanostructures</b>		
	Abstract	44
2.1.	Introduction	44
2.2.	Materials and methods	47
2.2.1.	Reagents and precursor	47
2.2.2.	Biochar production and catalyst impregnation	48
2.2.3.	Chemical vapor deposition setup	49
2.2.4.	Characterization techniques	49
2.2.5.	Adsorption experiments	50
2.3.	Results and discussion	51
2.3.1.	Substrate characterization and catalyst dispersion	51
2.3.2.	Carbon nanostructures morphology over carbonized fibers	56
2.3.3.	Structural characterization	62
2.3.4.	Surface area analysis	67
2.3.5.	Benzene adsorption analysis	70
2.4.	Conclusions	74

### **CHAPTER 3: Macroporous biochar enhanced with carbon nanostructures for fast adsorption of representative VOCs from gasoline**

Abstract	76
3.1. Introduction	77
3.2. Experimental procedure	79
3.2.1. Reagents	79
3.2.2. Biochar pre-treatments	79
3.2.3. Growth of carbon nanostructures on biochar	80
3.2.4. Analytical methods	81
3.2.4.1. Physical characterization	81
3.2.4.2. Chemical characterization	81
3.2.5. Adsorption experiments	82
3.3. Results and discussion	83
3.3.1. Pre-treated biochar performance	83
3.3.2. Materials characterization	85
3.3.2.1. Physical properties	85
3.3.2.2. Chemical properties	92
3.3.3. Adsorption behavior	100
3.3.3.1. Kinetics adsorption	100
3.3.3.2. Correlation adsorbate-adsorbent in VOCs adsorption	106
3.3.3.3. Adsorption mechanism	109
3.4. Conclusions	113

### **CHAPTER 4: Effective dynamic adsorption- desorption of representative gasoline emissions by a novel biochar/carbon nanostructures composite**

Abstract	116
4.1. Introduction	117
4.2. Methods	119
4.2.1. Materials	119
4.2.2. Chemical vapor deposition process	120
4.2.3. Analytical methods	121
4.2.4. Dynamic adsorption measurements	121
4.2.5. Regeneration experiments	125

4.3.	Results and Discussions	125
4.3.1.	Structural properties of the adsorbent	125
4.3.2.	Dynamic adsorption/desorption study	133
4.3.3.	Reusability of biochar/carbon nanostructures composite	150
4.4.	Conclusions	153
<b>CHAPTER 5: Multicomponent adsorption from real gasoline emissions onto a biochar/ carbon nanostructures composite</b>		
	Abstract	156
5.1.	Introduction	157
5.2.	Experimental section	158
5.2.1.	Materials	158
5.2.2.	Dynamic adsorption experiments	159
5.3.	Results and discussion	160
5.3.1.	Adsorption study of multicomponent mixtures of VOCs	160
5.3.2.	Gasoline breakthrough curves	172
5.4.	Conclusions	179
<b>CHAPTER 6: General discussion</b>		181
<b>CHAPTER 7: Final Conclusions</b>		
7.1.	Conclusions	191
7.2.	Perspectives and challenges	194
<b>References</b>		197
<b>Supplementary information</b>		223

## List of tables

---

<b>Table 1.1</b> - Technological characteristics of VOCs removal methods	6
<b>Table 1.2</b> - Composition of target VOCs in neat gasoline and gasoline vapor headspace at three diurnal temperatures [20].	8
<b>Table 1.3</b> - TEM images of different morphologies of carbon nanospheres synthesized by different methods.	21
<b>Table 1.4</b> - Summary of physiochemical properties and performance of different porous materials for VOCs adsorption.	33
<b>Table 1.5</b> - Desorption of VOCs from various carbon-based materials.	35
<b>Table 2.1</b> - Elemental analysis of the carbon substrate with and without catalyst.	60
<b>Table 2.2</b> - Textural properties of adsorbent materials tested in adsorption experiments.	69
<b>Table 2.3</b> - Kinetic constants for adsorption of benzene onto adsorbent materials.	73
<b>Table 3.1</b> - Surface area and pore volume of carbon adsorbents.	92
<b>Table 3.2</b> - Properties of VOCs under study and parameter measured on the serologic bottles headspace at 25°C and 1 atm of barometric pressure.	101
<b>Table 3.3</b> - Adsorption rates calculated for the first 12 h of kinetic study.	103
<b>Table 3.4</b> - Kinetic constants for adsorption of evaporative emissions onto adsorbent materials.	105
<b>Table 4.1</b> - Textural properties of powder adsorbent materials tested in dynamic adsorption experiments.	134
<b>Table 4.2</b> - Operating parameters on dynamic adsorption of VOCs in the fixed-bed column.	135
<b>Table 4.3</b> - VOC Desorption rates calculated at the highest weight loss, between minutes 4 and 12.	141
<b>Table 4.4</b> - Experimental parameters obtained from breakthrough curves for different adsorbents and adsorbates.	143
<b>Table 5.1</b> - Dynamic adsorption parameters and capacities of activated carbon and BCVD600-1pTT.	169



**Table 5.2** - Breakthrough curve parameters of Yoon-Nelson model for binary and multicomponent pollutants onto activated carbon and BCVD6000-11TT. 171

**Table SI4.** - Overall variables and parameters obtained at the evaluated experimental conditions of dynamic adsorption. 216

---

## List of figures

---

<b>Fig. 1.2</b> - VOCs emissions from different anthropogenic sources in 2015 [2], [7].	4
<b>Fig. 1.3</b> - The different types of emissions from vehicles. Image from <a href="http://www.eea.europa.eu/es">www.eea.europa.eu/es</a> .	7
<b>Fig. 1.4</b> - Schematic drawing of EVAP working system.	10
<b>Fig. 1.5</b> - Production of biochar from lignocellulosic waste material scheme	14
<b>Fig. 1.6</b> - Molecular models showing different carbon nanostructures categorized by their dimensionality. Image from Zhang et al. [42].	16
<b>Fig. 1.7</b> - (a) Schematic illustration of structures of armchair, zigzag, and chiral single-walled CNTs. (b) Scanning electron microscopy image of CNTs, and (c, d) transmission electron microscopy images of multiwalled CNTs [48], [49].	17
<b>Fig. 1.8</b> - Details of the nanostructure of different types of carbon nanofibers: (a) single-walled CNTs, (b) multiwalled CNTs, (c) bamboo-like CNTs, (d) platelet, (e) fishbone, ribbon, (g) stacked cup, (h) amorphous. (i) TEM images of CNTs showing graphitic sheets and nonhomogeneous morphology along the CNFs length [53].	19
<b>Fig 1.9</b> - a) Schematic representation of CVD process in a rotatory furnace reactor. Growth mechanism of CNTs by b) base growth model and c) tip-growth model. Image from [80].	27
<b>Fig. 1.10</b> - Traveling of the mass transfer zone (MTZ) through the packed bed and development of the breakthrough curve. Image from [88].	31
<b>Fig. 2.1</b> - (a) FTIR spectra of raw bagasse fibers and biochar, (b) Distribution of incremental pore volume of biochar. SEM secondary electrons images of (c) cross and (d) longitudinal section of biochar.	52
<b>Fig. 2.2</b> - EDS analysis on longitudinal surface of biochar.	53
<b>Fig. 2.3</b> - SEM a) secondary electrons and b) backscattered electrons images of catalyst impregnated biochar covered with CMC.	54
<b>Fig. 2.4</b> - (a-c) SEM backscattered electrons images of biochar impregnated with three iron concentrations treated at 700 °C: (a) 0.1, (b) 1 and (c) 10 g L <sup>-1</sup> , simulating the catalyst performance before CVD process. The insert in (a) and (b) shows the interaction of iron with calcium rods, and (c) shows the iron particles covered with condensed carbon.	55

**Fig. 2.5** - SEM secondary electrons images of carbon nanostructures grown on biochar by CVD during 300 s, using three iron concentration: (a,b,c) 0.1, (d,e,f) 1, (g, h, i) 10 g L<sup>-1</sup>. A comparison between samples obtained after CVD process at 700 °C and after thermal post-treatment at 800 °C is made. 57

**Fig. 2.6** - SEM secondary electrons images of carbon nanostructures grown on biochar by CVD process during 60 s, using thermal post-treatment at 800 °C with three iron concentrations: (a, b) 0.1, (c, d) 1, (e, f, i) 10 g L<sup>-1</sup>. The insets are the corresponding SEM images under high magnification. 59

**Fig. 2.7** - Representative TEM images of different carbon nanostructures: (a, b) CNTs, (c) onion-like carbon, and (d) carbon black, grown on biochar using an iron concentration of 1 g L<sup>-1</sup> by CVD during 60 s at 700 °C, and post-thermal treatment at 800 °C. 60

**Fig. 2.8** - X-ray diffraction patterns (from up to bottom) of the samples BC, BCZVI700-1, BCVD700-60-1 and BCVD-60-1 with a step size of 0.01° 2θ at 10 sec per step. All four diffraction patterns were collected on the same day. 63

**Fig. 2.9** - Raman spectra (from up to bottom) of biochar (BC), catalyst impregnate biochar thermally treated-only at 700 °C (BCZVI700-1), biochar processed to CVD (BCVD700-60-1), and biochar processed to CVD and thermally post-treated at 800 °C (BCVD-60-1). The modified samples were evaluated at the same iron concentration (1 g L<sup>-1</sup>). 65

**Fig. 2.10** - Surface area evolution of the synthesized materials after a) CVD and b) thermal post-treatment at 800 °C. The modified samples are identified by their CVD temperature / iron concentration (g Fe/ L), i.e. 300/0.1. 68

**Fig. 2.11** - N<sub>2</sub> adsorption isotherms and incremental pore volume of adsorbent materials tested in benzene adsorption experiments. 69

**Fig. 2.12** - Benzene adsorption kinetics in static mode at 25 °C and 0.06 atm of vapor pressure, using activated carbon, biochar, and BCVD-60-1 samples. 72

**Fig. 3.1** - (a,b) SEM backscattered electrons images of raw and acid-washed biochar. (c) XRD pattern and (d) Raman spectra of BC and BCA spectra. 84

**Fig. 3.2** - Adsorption kinetics of (a) benzene and (b) pentane on raw and acid-washed biochar at 25 °C and ~1 atm of barometric pressure. 85

**Fig. 3.3** - SEM secondary electrons detector images of the biochar modified with continuous and pulsed CVD processes. 87

<b>Fig. 3.4</b> - Representative TEM images of different carbon nanostructures growth by pulsed-injected (a, b, c), and CVD continuous methodology (d, e, f) at 600 °C.	89
<b>Fig. 3.5</b> - HRTEM micrographs of (a) onion-like carbon, (b) CNFs, and (c, d) CNTs. Arrow highlights the presence of turbostratic graphitic carbon.	90
<b>Fig. 3.6</b> - TGA performance of CVD process by injecting acetylene at 600° C (a) during 2 min or (b) two pulses of 1 min each, respectively.	93
<b>Fig. 3.7</b> - X-ray diffraction patterns of biochar/carbon nanostructures composites with a step size of 0.01° 2θ at 10 sec per step. All four patterns were collected on the same day.	94
<b>Fig. 3.8</b> - Fitted Raman spectra of the modified biochar by continuous and pulsed-injection CVD.	96
<b>Fig. 3.9</b> - Water contact angle of carbon adsorbents.	97
<b>Fig. 3.10</b> - Surface charge distribution of studied materials as a function of pH at 25 °C, using 0.1 mol L <sup>-1</sup> NaCl as the supporting electrolyte.	98
<b>Fig. 3.11</b> - pK <sub>a</sub> distribution of surface acidic functional groups on the surface of unmodified and modified carbon adsorbents.	99
<b>Fig 3.12</b> - Adsorption kinetics of a) pentane, b) hexane, c) benzene and d) toluene on studied adsorbent in static mode at 25 °C.	103
<b>Fig. 3.13</b> - Correlation between VOCs adsorption capacity and adsorbate (a-d) and adsorbent properties (e, f).	108
<b>Fig. 3.14</b> - Diffusional and adsorption mechanisms of toluene, benzene, hexane, and pentane on carbonaceous adsorbents by chemical and physical adsorption.	112
<b>Fig. 4.1</b> - Schematic diagram of dynamic VOCs adsorption/desorption experiments set-up.	126
<b>Fig. 4.2</b> - XRD patterns of carbon adsorbent by using a step size of 0.01° 2θ at 10 sec per step.	127
<b>Fig. 4.3</b> - Raman spectra of the different carbonaceous adsorbents.	129
<b>Fig. 4.4</b> - Adsorption breakthrough and desorption curves of representative VOCs from gasoline at 25 °C on activated carbon (AC), biochar (BC) and biochar processed with CVD (BCVD600-1pTT). t <sub>b</sub> is the breakthrough time at which the outlet concentration reached 10%	

of the inlet concentration. Open symbols and dotted lines represent the second adsorption and desorption cycles, respectively. 139

**Fig.4.5** - Linear relationship between VOCs vapor pressure and mass transfer zone rate (a), adsorbent BET surface area and mass transfer zone rate (b), and adsorbent BET surface area and adsorption capacity (c). 145

**Fig. 4.6** - Regeneration effect on surface charge distribution and  $pK_a$  distribution of carbonous adsorbents as a function of pH at 25 °C. The blue and red lines correspond to the pristine and after being used in adsorption of VOCs, respectively. 147

**Fig. 4.7** - Overall illustration depicted the favorable mass transfer on exposed surface area of BCVD600-1pTT versus the diffusional difficulties of microporous activated carbon during dynamic adsorption in packed-bed columns. 148

**Fig. 4.8** - Adsorption mechanism on BCVD600-1pTT(a) and activated carbon (b). The effect of both curvature on carbon nanostructure and a more defective carbon structure on adsorption of aliphatic and aromatic VOC were illustrated. 150

**Fig. 4.9** - Reusability of BCVD600-1pTT after four adsorption (a) and desorption (b) cycles of benzene under air stream at 150 °C. 153

**Fig. 5.1** - Breakthrough curves of binary VOCs mixtures evaluating the interaction between a) aromatics VOCs, b) aliphatic VOCs, and c) aliphatic-aromatics in dynamic adsorption at 25 °C.  $t_b$  is the breakthrough time ( $C C_0^{-1}$ ). 164

**Fig. 5.2** - Multicomponent adsorption breakthrough curves for BCVD600-1pTT and activated carbon at 25 °C. 166

**Fig. 5.3** - Adsorption rate values ( $K_Y$ , [ $min^{-1}$ ]) for the evaluated systems. a) Binary systems with activated carbon and, b) Binary systems with BCVD6000-1pTT. c) Multicomponent evaluations for both adsorbents with the pollutants under study. 172

**Fig. 5.4** - Linearized Yoon-Nelson equations for pentane-hexane (a,b), multicomponent (c,d) and gasoline (e,f) systems with activated carbon and BCVD600-1pTT adsorbents. 174

**Fig. 5.5** - a) Breakthrough curves of gasoline emission for activated carbon and BCVD600-1pTT. b) Adsorption behavior of gasoline multicomponent emission by separating gas-chromatography detection times. The areas under the curve of GC analysis at the inlet and outlet of the column were used to develop the plotted curves vs time. 178

**Fig. 5.6** - Schematic mechanism of multicomponent adsorption system on activated carbon and BCVD600-1pTT adsorbents. 181

## Resumen

Considerando la importancia ambiental y económica de la recuperación y reúso de las emisiones de gasolina, esta tesis exploró la adsorción de compuestos orgánicos volátiles (COVs) de un nuevo compuesto de biochar/nanoestructuras de carbono con la intención de mejorar la cinética de adsorción y regeneración de un carbón activado comercial (CA) principalmente microporoso. El biochar fue desarrollado por pirólisis a 600 °C a partir de bagazo de agave. El área específica del biochar incremento de 120 a 243 m<sup>2</sup> g<sup>-1</sup> después de 1 min de deposición química de vapor (DQV) a 700 °C por el crecimiento de nanotubos de carbono tipo bambú, nanocebollas y carbón black. Este nuevo compuesto adsorbió 1.5 veces más benceno y 1.8 veces más rápido que el carbón activado. El uso de la estrategia de inyección pulsada permitió mejorar el uso de la fuente de carbono durante la DQV a 600°C, con una dispersión más homogénea de nanotubos de carbono, nanofibras de carbono, nanocebolla y nanolistones de carbono con área específica alta (240 m<sup>2</sup> g<sup>-1</sup>). Esta síntesis permitió mejorar entre 1.3 y 1.8 veces la capacidad de adsorción del biochar para pentano, hexano, benceno y tolueno, y aumentó la adsorción de benceno y tolueno hasta un 260 % y un 98 % en comparación con el CA. Además, las nanoestructuras de carbono aumentan el pH<sub>PZC</sub> del biochar de 8.5 a 10 y, por lo tanto, su hidrofobicidad. También se propuso que la adsorción por fuerzas dispersivas y el complejo donador-aceptor de electrones ocurren simultáneamente. El escalamiento de la síntesis por DQV en un horno rotatorio aumentó el área específica del biochar en polvo de 1 a 300 m<sup>2</sup> g<sup>-1</sup>, desarrollando nanofibras de carbono y nanocebollas. La adsorción dinámica en lechos empacados demostró que las curvas de ruptura y de desorción del compuesto mostraron un comportamiento similar después de cuatro ciclos de adsorción/desorción de benceno, con solo una disminución del tiempo de ruptura de 16 min, mientras que la del CA disminuyó hasta 20 min en el segundo ciclo. Después del proceso regenerativo a 150 °C, el compuesto mostró una acidificación superficial insignificante. Finalmente, la adsorción simultánea de varios COVs de gasolina mostró que los tiempos de ruptura de los sistemas binarios y multicomponentes se comportaron de manera similar a los sistemas individuales. La característica más importante fue observada por el cambio en la pendiente de las curvas de ruptura del CA, asociado con el desplazamiento de los COVs por la adsorción competitiva por los sitios activos, mientras que las curvas en forma Sigmoidal del compuesto sugirieron un proceso de adsorción y de transferencia de masa más homogéneo. Los resultados presentados en esta tesis doctoral representan un gran paso adelante en el desarrollo de adsorbentes macroporosos con menor tortuosidad y alta área de específica



reactiva para eliminar más rápidamente los COVs de forma individual y multicomponente de las emisiones de gasolina, así como para mejorar su capacidad regenerativa del carbón activado comercial usado en cánister automotriz.

**Palabra claves:** deposición química de vapor, compuestos orgánicos volátiles, biochar, nanoestructuras de carbono.

## Abstract

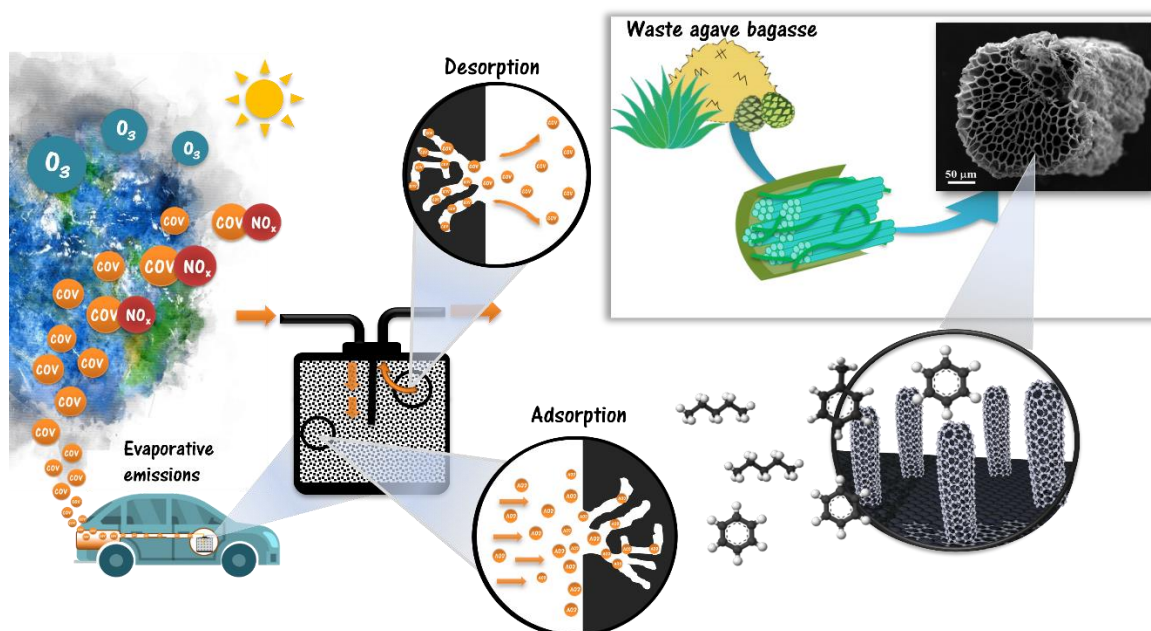
Considering the environmental and economic importance of recovery and reuse of gasoline emissions, this thesis explored the adsorption of volatile organic compounds (VOCs) from gasoline on a macroporous biochar/carbon nanostructures composite to improve the kinetic and regenerative performance of a commercial microporous activated carbon (AC). First, biochar was developed by pyrolysis at 600 °C from waste agave bagasse. The biochar surface area increased from 120 to 243 m<sup>2</sup> g<sup>-1</sup> after 1 min of chemical vapor deposition (CVD) at 700 °C by the growth of carbon nanostructures such as bamboo-like carbon nanotubes, onion-like carbon, and carbon black. Accordingly, this novel composite adsorbed 1.5 times more benzene and 1.8 times faster than AC. The use of pulsed-injection strategy allowed to improve the use of carbon source during CVD at 600°C, with a most homogeneous dispersion of carbon nanotubes, carbon nanofibers, onion-like carbon, and carbon nanoribbons with high surface area (240 m<sup>2</sup> g<sup>-1</sup>). This synthesis allowed to improve 1.3-1.8 times the biochar adsorption capacity for pentane, hexane, benzene, and toluene, and increased up to 260% and 98% the uptake of benzene and toluene compared to AC. In addition, carbon nanostructures increase the biochar p<sub>H<sub>PZC</sub></sub> from 8.5 to 10 and thus its hydrophobicity. It was also proposed that dispersive forces and electron donor-acceptor complex mechanisms can be carried out simultaneously. Then, scaled-up CVD synthesis in a rotary furnace increased the powder biochar surface area from 1 to 300 m<sup>2</sup> g<sup>-1</sup>, developing carbon nanofibers and onion-like carbons. Dynamic adsorption in packed-bed demonstrated that the breakthrough and desorption curves of this composite behaved similar after four cycles of adsorption/desorption of benzene, with only a decrease of breakthrough time of 16 min, while that of AC decrease up to 20 min in the second cycle. After the regeneration process at 150°C, biochar/carbon nanostructures composite showed negligible surface acidification. Finally, simultaneously adsorption of several VOCs from gasoline emissions showed that the breakthrough time of binary and multicomponent systems behaved similarly to those of single systems. The most important feature was observed by the change in the slope on the breakthrough curves of AC, associated with the displacement of VOCs by competitive adsorption for active sites, while the S-shape curves of biochar/carbon nanostructures composite suggested a more homogeneous adsorption and mass transfer process. The results presented in this doctoral thesis represent a major step forward in the development of macroporous adsorbents with less tortuosity and high reactive surface area to faster remove single and multicomponent VOCs from evaporative emissions, as well as

improve their regenerative capacity of a commercial activated carbon used in automotive canisters.

**Key words:** Chemical vapor deposition, volatile organic compounds, biochar, carbon nanostructures.

# CHAPTER 1

## Introduction



The evaporative emissions from gasoline are becoming a significant environmental problem of growing concern, especially for densely populated areas, and also results in a significant economic loss. In this sense, adsorption technologies with activated carbon have been used for evaporative emission for over 30 years and have proven to be very effective. However, activated carbon reusability in automotive canisters could be affected by narrow micropores. Thus, the development of novel adsorbent materials to improve the adsorption-desorption rate of evaporative emissions remains a challenge today. In the present thesis, it was studied the adsorption of volatile organic compounds (VOCs), representatives of evaporative emissions, and real gasoline vapors by biochar improved with carbon nanostructures at 25 °C, and compared with a commercial activated carbon (F-400). This chapter provides a brief description of the pollution issue by these components, as well as

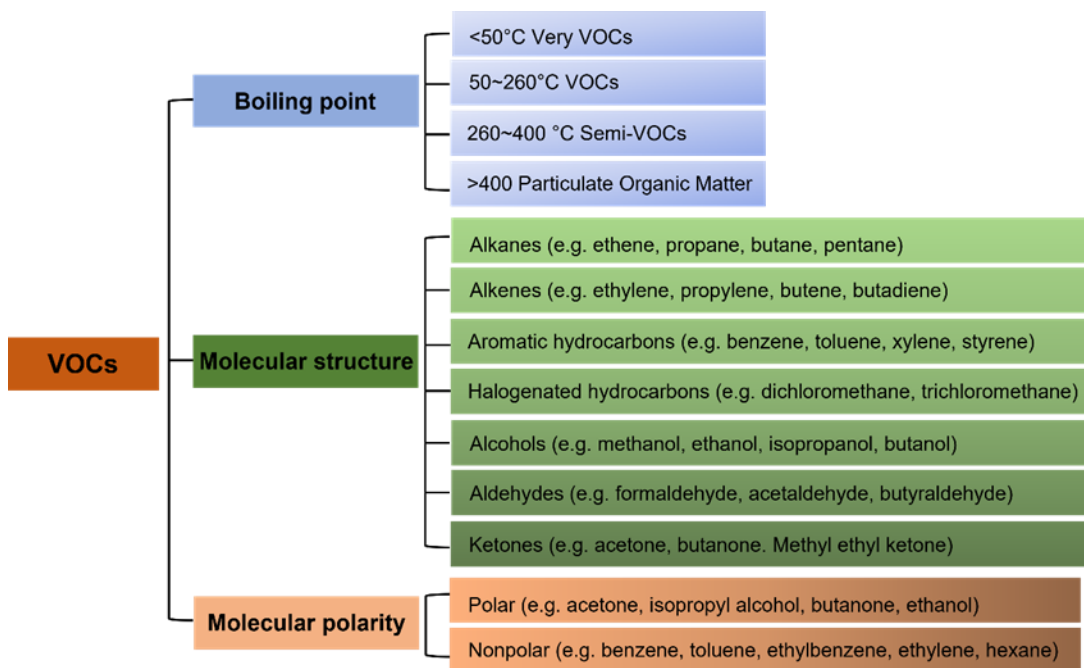


the most important aspects of gas adsorption behavior in carbon-based materials and all the scientific background.

### 1.1. Overview about air pollution caused by volatile organic compounds

People's lifestyle has changed dramatically over the past 50 years, particularly in the industrialized nations where increased urbanization, technological development and specialized industrial activities have led to the damage of several systems, especially in air [1]. To date, the increasing amount of polluting emissions has caused the deterioration of air quality. Air pollutants can be classified by the sources, chemicals, composition, size, and mode of release into indoor or outdoor environments [2]. In this sense, gaseous pollutants may be divided into volatile organic compounds, volatile inorganic compounds, and greenhouse gases as  $\text{CO}_2$ ,  $\text{CH}_4$ ,  $\text{N}_2\text{O}$ , HFC and others [3].

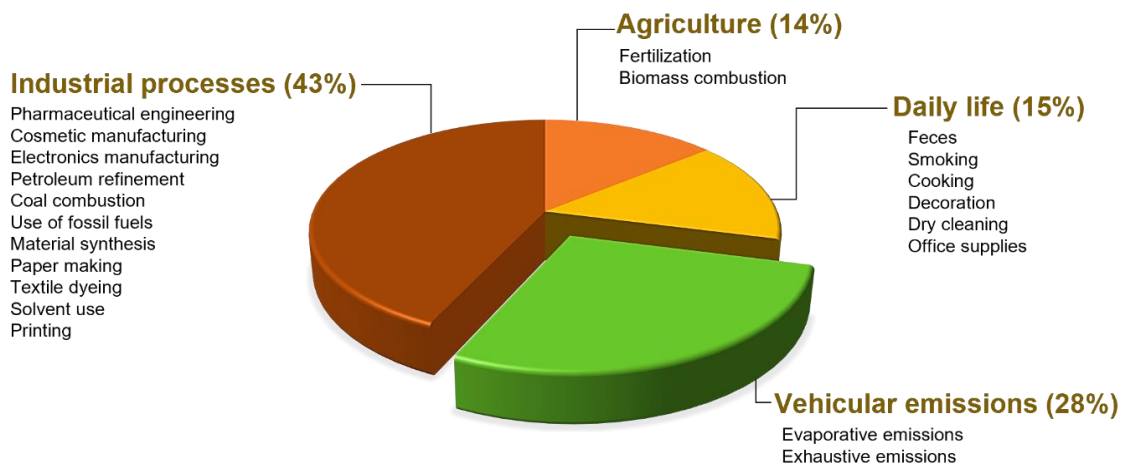
Between several gaseous pollutants that currently affect air quality, volatile organic compounds (VOCs) have attracted world-wide attention regarding their serious hazards on ecological environment and human health [4]. VOCs refers to a group of organic substances characterized by their low boiling point [5]. The various definitions of VOCs are conducted by main international organizations. This can be defined as any compound of carbon, excluding  $\text{CO}$ ,  $\text{CO}_2$ ,  $\text{H}_2\text{CO}_3$ ,  $(\text{NH}_4)_2\text{CO}_3$  and metallic carbides which participate in atmospheric photochemical reactions, according to the US Environmental Protection Agency (US EPA) [6]. The World Health Organization (WHO) describes VOCs as organic compounds with saturated vapor pressure over 133.3 Pa and boiling point ranging from 50 to 260 °C at atmospheric pressure. For volatile organic compounds, such low boiling points mean that they are easily evaporated from liquid or solid surfaces into indoor or ambient air. Probably several thousand chemicals, both synthetic and natural, can be called VOCs [7]. The common VOCs can be classified into several groups based on their different properties as shown in [Fig 1.1](#).



**Fig. 1.1** - The classification of different VOCs [7].

### 1.1.1. Emission inventory of VOCs

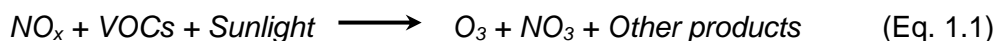
VOCs are a family of more than 300 carbon-based chemicals. VOCs come from anthropogenic and natural emissions. About 90% of atmospheric VOCs originate from biogenic sources, including wetlands, forest, oceans, and volcanoes with an estimated global emission rate of 1150 Tg C yr<sup>-1</sup> [2]. With the accelerated urbanization and industrialization, anthropogenic emissions are projected to increase annually (from 19.4 Tg C in 2005 to 61.2 Tg C in 2030) [7]. The portion of anthropogenic sources is getting larger, and their influence is getting worse because almost every human daily activity such as cooking, painting, smoking, building, would result in the emissions of VOCs to the atmosphere. Some examples of specific sources and processes that commonly emit high levels of VOCs include vent gas, water separation techniques, industrial wastewater, batch processes, petroleum refining, natural gas processing, petrochemical processes, and paints [3]. Fig. 1.2 lists the main sources of anthropogenic VOCs.



**Fig. 1.2** - VOCs emissions from different anthropogenic sources in 2015 [2], [7].

### 1.1.2. Effect of VOC on human health and environment

VOCs play a critical role in tropospheric chemistry and are associated with ozone production and secondary organic aerosols formation that pose serious harm to both the ecological environment and human health. Most VOCs are photo-chemically sensitive and when exposed to nitrogen and sunlight, would form ozone and other products as represented in Eq. 1.1:



This last reaction involves VOCs oxidation by  $\text{NO}_x$ . As the wide range of VOCs implies a broad range of reaction rates, VOCs are capable of being widely distributed and of accumulating in components of the environment [4]. VOCs are responsible for the greenhouse effect, especially methane, which is more than 20 times more potent than  $\text{CO}_2$ . Most VOCs, in particular aromatic compounds and polycyclic aromatic hydrocarbons, are malodorous, toxic, and carcinogenic even at low concentration (above  $0.2 \text{ mg m}^{-3}$ ). The main health affectations are related to respiratory deficiencies and damage to skin, and nervous





systems. Benzene is a well-known example, which is a carcinogen with a high potential to damage humans both specifically (e.g., the liver, kidneys, spleen, and stomach) and systematically (e.g., the nervous, circulatory, reproductive, immune, cardiovascular, and respiratory systems) [8]. For these reasons, the World Health Organization (WHO) recently reported that air pollution caused nearly seven million premature deaths in 2016, of which millions were related to VOCs [9].

### **1.1.3. Processes for VOCs removal**

Regarding the potential hazards of VOCs, several major environmental safety agencies, such as the National Institute of Occupational Safety and Health (NIOSH), Environmental Protection Agency (EPA) and European Agency for Safety and Health at Work (EU-OSHA), have established guidelines to limit the exposure of humans to VOCs in indoor and workplace air. Stringent regulations have been proposed to control VOCs by developed countries [10]. For instance, USA legislation calls for a 90% reduction in emissions of 189 pollutants over the next few years where VOCs occupy about 70% of those pollutants. In addition, the emissions reevaluation of the Goteborg protocol had stipulated that the reduction of VOCs emissions by 2020 should be half of the total amount released in 2002 [11]. Therefore, the development of effective VOCs removal techniques is urgent and of great significance. Many post-processing technologies have been developed for VOCs abatement, which can be categorized into destruction technology and recovery technology. The recovery methods mainly include adsorption, condensation, absorption, and membrane separation, while the destruction techniques include incineration, photocatalysis oxidation, ozone catalytic oxidation and biological degradation [12]. The destruction methods mainly convert VOCs into CO<sub>2</sub> and H<sub>2</sub>O, which consume large amounts of energy to generate high temperatures for the reaction, and they inevitably produce some toxic byproducts, secondary organic aerosols, etc. Recovery methods are more economic and



environmentally-friendly due to the mild reaction conditions and recovery of VOCs. The characteristics of VOCs removal techniques are summarized in [Table 1.1](#).

**Table 1.1** - Technological characteristics of VOCs removal methods.

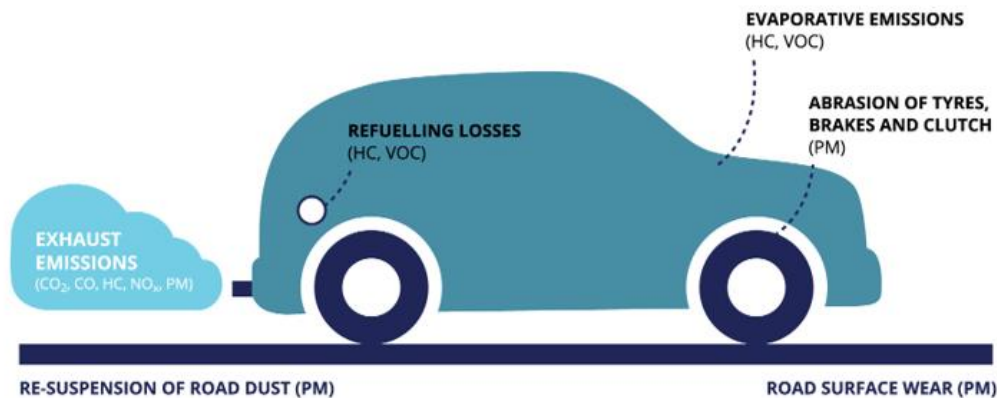
Methods	Efficiency	Reuse	Waste generation	Energy consumption	VOC concentration	Ref.
Incineration	>99% (40 min)	No	CO, Cox	Moderate	20%	[4]
Condensation	Moderate	Yes	---	High	>5000 ppm	[11]
Biological degradation	100% (7 months)	No	Acetaldehyde, propanol, etc.	Low	<5000 ppm	[12]
Adsorption	>90%	Yes	Spent adsorbent	Moderate	700 -10000 ppm	[13]
Photochemical oxidation	100% (5 min)	No	Strong oxidant OH radicals.	Moderate	---	[4], [14]
Membrane separation	90%	Yes	Clogged membranes	High	<25%	[15]

The adsorption technology is regarded as one of the most promising methods for enriching and separating VOCs in exhaust gases, and also because it is of low cost and high efficiency. It is necessary to point out that activated carbon, zeolites and organic polymers are considered as the most popular adsorbents for VOCs, according to the US EPA [7], [16]. In addition, the physical and chemical modification of the surface of a series of materials such as carbon-based materials, oxygen-containing materials, organic polymers, composites, and so on, have been investigated to improve the adsorption of VOCs.



## 1.2. Vehicular emissions

Fossil fuel-powered road transport represents the most important source of transport-related air pollution. Each vehicle releases pollutants from a number of sources. Vehicular emissions are one of the most important anthropogenic sources of VOCs in urban and suburban areas [8]. In this sense, it is reported that vehicular emissions contributed to more than 50% to the ambient VOCs at urban areas. Driving condition, class, age and mileage of engine, fossil fuel composition, and catalyst equipped in a pollutant removal system can significantly vary the chemical composition of vehicular emissions. Generally, air pollutants are emitted by vehicles in three ways: as tailpipe emission, related to engine combustion ( $\text{NO}_x$ ,  $\text{CO}_2$  and  $\text{CO}$ ) and unburned fuel vapors (VOCs); as evaporative emissions, which result from the escape of fuel vapors (VOCs) from vehicle while they are running or not running; and as the release of VOCs and particulate matter from vehicle equipment, including plastic panels, leather seats, and so on (Fig. 1.3) [17]. The amounts of VOCs emitted from vehicles were significant only for new cars and decreased with time. Tailpipe emissions have been well-controlled across the globe, while evaporative emissions have been largely neglected despite they constitute an increasing share of the VOC emissions inventory and impacts both air quality and energy [18]. Thus, evaporative emissions have been of increasing concern for the automotive industry and scientific community.



**Fig. 1.3** - The different types of emissions from vehicles. Image from [www.eea.europa.eu/es](http://www.eea.europa.eu/es).



### 1.2.1. Evaporative emissions

Evaporative emissions result from fuel-based VOCs evaporation in gasoline vehicles because the vapor pressure of gasoline is relatively high [19]. Automotive gasoline fuel is a mixture of over 100 VOCs with chains containing 4-12 carbons, and their vapors (evaporative emissions) mostly consist of light hydrocarbons (C4's-C7's). Nowadays, commercial gasoline contains mostly saturated hydrocarbons (55-77%), aromatics (9-36%) and some unsaturated hydrocarbons [20]. Information regarding VOCs composition of gasoline is scarce, only a few works have reported or analyzed the target composition and, even most important, the headspace composition as it is displayed in [Table 1.2](#). Gasoline vapors contain VOCs that were not measured such as butane, isobutene, pentane, and hexane, but they are present in high concentration [21].

**Table 1.2** - Composition of target VOCs in neat gasoline and gasoline vapor headspace at three diurnal temperatures [20].

VOC	Gasoline composition (mg L <sup>-1</sup> )	Headspace gasoline vapor (mg m <sup>3</sup> )		
		5 °C	20 °C	45 °C
Benzene	6140	3170	6940	13000
Toluene	15400	4280	9910	15900
Cyclohexane	9830	3120	6010	11800
n-heptane	12800	3020	6840	12800
n-octane	2800	106	275	491
Ethylbenzene	3080	58	148	283
m-Xylene	9120	182	466	624

Evaporative emissions from gasoline-fueled vehicles depend on four major factors: (a) gasoline volatility; (b) vehicle and fuel system design; (c) temperature variation; and (d) driving conditions [22]. In addition, evaporative emissions can be divided into three types:



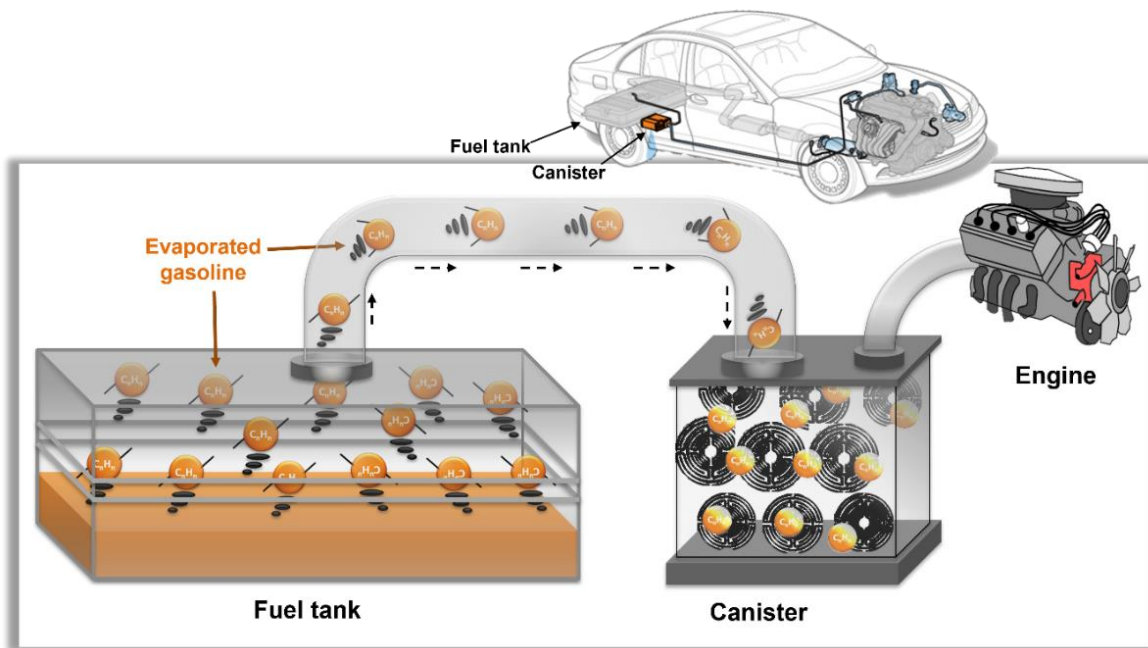
running losses, hot-soak losses, and diurnal breathing losses [18]. Running losses refers to evaporative emissions from the fuel tank and fuel-related parts that are caused by heat from the engine during vehicle operation. Hot soak losses are the emissions starting from when the car is stopped after being driven, with a warm engine and fuel system, and ending when they have cooled down to ambient temperature. Diurnal breathing losses is the daily emission while the car is parked, with increasing temperature in daytime and decreasing temperature at nighttime. Of these emissions, diurnal breathing losses are dominant [23]. The National Emission inventory reports that the quantity of VOCs produced by USA on-road vehicles in 2014 was equal to 2.38 million tons, that is 7.3 % of the total amount of pollutants from vehicles, after carbon monoxide (75%) and nitrogen oxide (15%) [24]. Currently, many countries have legislated to reduce pollutant emissions and developed corresponding reduction targets. Therefore, the recovery and reuse of evaporated gasoline from loading, unloading, and other handling process are of significant importance from both economic and environmental point of view.

### **1.2.2. Evaporative emission control system (EVAP)**

Evaporative emissions occur from the vehicle fuel tank owing to the expansion of evaporative gas caused by daily temperature differences. Accordingly, evaporated VOCs leak from the fuel system by permeating through the plastic material of the hoses, as well as flowing out of any opening in the fuel tank [25]. To control evaporative emissions from vehicles, international governments have agreed to various environmental treaties. For example, the US EPA restricts evaporative emissions to 1.2 g (two-day diurnal breathing loss test) and 0.95 g (three-day diurnal breathing loss test) for an hour of hot soak loss [19]. To deal with these regulations, almost all the gasoline-fueled vehicles are equipped with an evaporative emissions control system (EVAP). A standard EVAP system consists in a carbon canister filter filled with activated carbon that can adsorb and store gasoline vapors



coming from the fuel tank (Fig. 1.4). The gasoline vapors enter the canister through a top inlet and diffuse downwardly under its own pressure and gravity into the bed of carbon granules where these are adsorbed in temporary storage [26]. The adsorbed gasoline vapors are then periodically purged by opening a valve that allows for air flow through the canister into the engine for combustion.



**Fig. 1.4** - Schematic drawing of EVAP working system.

Once the canister loses the ability to store evaporative emissions because of a long parking duration and becomes fully saturated, the emissions are discharged directly to the atmosphere; this phenomenon is called canister breakthrough. Canister breakthrough is thought to be caused by fuel components that are not completely desorbed during the regeneration process [27]. Furthermore, serious diffusion restrictions imposed by micropores in activated carbon tend to encounter problems as pore blocking, hygroscopicity, and a lack of regenerative ability [28]. Adsorption performance decreases mainly due to micropores filling with high boiling VOCs, which can remain trapped even after the purging phase, and consequently reduce the effective volume of storage available in the pores.



Since this is a serious problem due to environmental pollution, through the years studies have been conducted to find better ecological and economical alternatives of adsorbents to improve the canisters performance [7], [29], [30].

### **1.3. Porous adsorbents for VOCs adsorption**

Among the recovery methods, adsorption technology has been considered one of the most favorable methods to treat VOCs, mainly because it is low cost and high efficiency. Characteristics of a suitable adsorbent material should include mainly a large surface area. Other features must consist of high mechanical strength, chemical and thermal stability, high porosity, and small pore diameter resulting into more exposed surface area and hence suitable surface chemistry giving rise to high adsorption capacity [31]. Adsorbents can be in the form of pellets, rods, moldings, or monoliths to fit the required application [32]. Some commonly used adsorbents include agricultural and industrial wastes, activated carbon, biopolymers, and nanomaterials [33]. Finding the optimal adsorbent is crucial for the commercial application.

#### **1.3.1. Activated carbon**

Activated carbon (AC) is the most widely applied adsorption material because of its good physical and chemical properties such as large specific surface area ( $600\text{-}1400\text{ m}^2\text{ g}^{-1}$ ), well-developed pore structure ( $0.5\text{-}1.4\text{ cm}^3\text{ g}^{-1}$ ), high VOCs adsorption capability ( $10\text{-}600\text{ mg g}^{-1}$ ), abundant functional groups, chemical and thermo-stability, high mechanical strength and acid and alkali resistance [34]. AC also has some disadvantages. During the adsorption of VOCs at high temperature, the activated carbon will spontaneously ignite or its porous structure collapses [7].

Industrial AC is commonly produced from carbon rich materials such as coal, wood, coconut shell, peat, and lignite, by the process of carbonization and activation. This can be





manufactured in form of pellets, granules, powder, or sphere [28]. Environmental applications of AC have been widely studied, for instance in wastewater treatment, solids remediation, and in air purification, especially for VOCs uptake. The adsorption mechanisms of pollutants onto AC have also been reviewed in previous studies [35]

AC has been widely used in adsorption to recovery most types of VOCs including alkane, alcohol, ethers, aldehydes, ketones, esters, aromatics, etc., [36]. The adsorption performance of AC on VOCs is influenced by adsorption conditions, physicochemical properties of the adsorbent, and the properties of VOCs such as molecular size and polarity. It seems that the large surface area and rich pore structure of AC shows a positive effect on the adsorption capacity for VOCs, while the presence of chemical functional groups is also a key factor for the removal of polar VOCs through chemical adsorption mechanisms [13].

There are challenges for further large-scale applications of AC at the industrial level that still exist. First, the characteristic micropore structure of AC would hinder the transport of VOCs molecules, especially those with larger molecular size, into the pores. Furthermore, the disordered pores of AC would prolong the adsorption equilibrium because of the increased resistance to diffusion in the irregular pore structures. It also implies that the incomplete desorption process affects the lifetime and regeneration cost of AC. This could be attributed to the irreversible adsorption including chemisorption, adsorbate coupling or decomposition. Moreover, the high transmission resistance, pore blocking and hygroscopicity of AC also restrict its widespread application in VOCs abatement [32].

### **1.3.2. Biochar**

Biochar is a representative member of the carbon family, of low cost, which is regarded as a potential alternative to commercial AC. Compared to AC, biochar is produced in a milder pyrolysis condition under an inert atmosphere [37]. The production temperature of



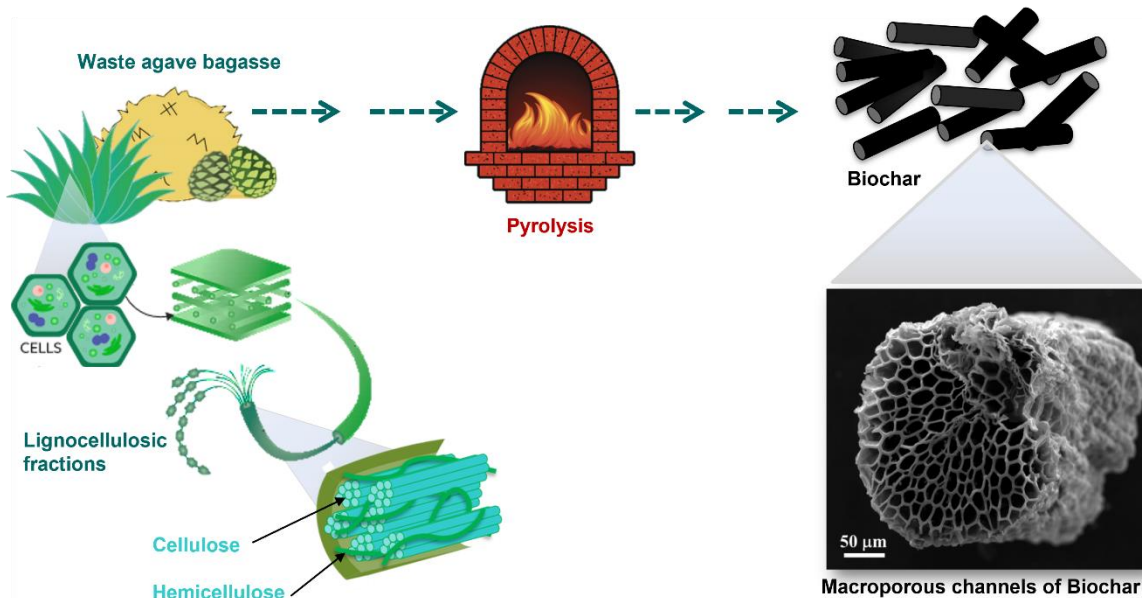
biochar is usually less than 700 °C, which is lower than that of AC. In addition, during the biochar production, the process of activation is unnecessary while it is crucial for AC production. Abundant carbon rich materials, such as wood materials, agricultural and forestry residues, fruits, byproducts, etc., can be used for biochar production. Its production cost of \$20 USD per ton is much cheaper than that of AC (\$1000 to \$1500 USD per ton) [38]. The features of biochar highly depend on the raw materials and production conditions. Generally, the raw material with high lignin and mineral content tend to produce high yield of biochar and the mineral content may decrease as the increasing pyrolysis temperature and time. The biochar produced by carbonization is a disordered graphitic structure with a rudimentary pore structure [39].

Biochar has been widely used in various fields, as soil fertility improvement, CO<sub>2</sub> uptake, catalytic conversion syngas into biodiesel, and pollution remediation. In fact, it has been indicated that the biochar applications are involved in almost every aspect of the pollution abatement, such as the treatment of liquids wastes, removal of toxic gases, as well as the treatment of solid wastes and soil remediation, however, limited reach has been done on VOC vapor adsorption onto biochar [40].

The Feedstock type of biochar determines its physicochemical properties that would further influence its adsorption performance. It has been reported that by using the same pyrolysis temperature of 600 °C, the surface area of woody plant biochar derived from pine wood, and hickory are 312 and 256 m<sup>2</sup> g<sup>-1</sup>, respectively, which are larger than that of herbaceous plant biochar. The biochar surface area from the herbaceous plants alfalfa, cotton, switchgrass corn straw, rice huck, and wheat straw at 600 °C are 0.2, 2.2, 15, 61, 168 and 182 m<sup>2</sup> g<sup>-1</sup>, respectively [41]. However, it is well known that most raw materials to produce biochar come from value-added agricultural sources, being a controversial discussion. Based on the latest, the use of raw lignocellulosic waste materials (agave



bagasse, rice straw, sugarcane bagasse, etc.) for the preparation of adsorbent materials (Fig. 1.5), has caught increased attention due to the large amount of raw material available and the potential reduction of the environmental pollution that cause their confinement [42].



**Fig. 1.5** - Production of biochar from lignocellulosic waste material scheme

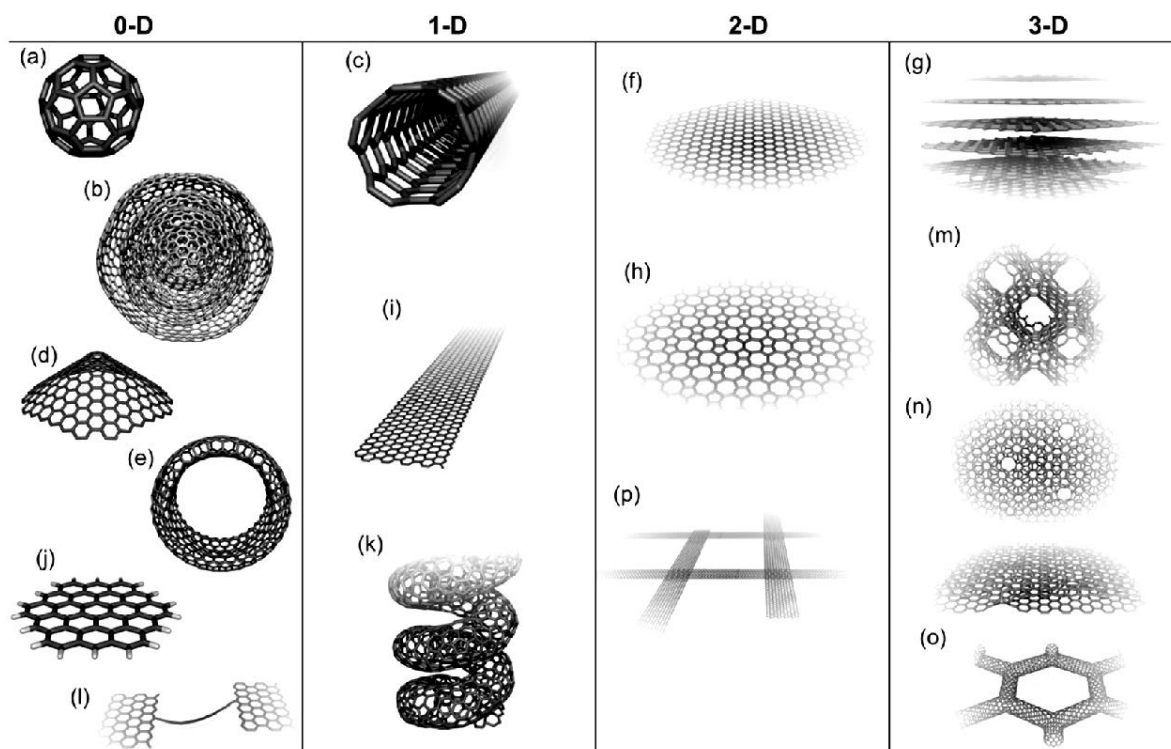
Pyrolysis conditions also affect the morphological structure and surface chemical functional groups of biochar and, hence, the performance of biochar on VOCs adsorption. In this sense, the surface area of biochar increases while its pore size would decrease with the pyrolysis temperature. Additionally, pyrolysis temperature influences the chemical functional groups of biochar. It has been widely reported that a high pyrolysis temperature facilitates the removal of oxygen-containing groups and increases the aromaticity of biochar, which would subsequently promote the adsorption of hydrophobic VOCs. For instance, the adsorption of trichloroethylene onto biochar produced at 700 °C has exhibited higher efficacy than biochar produced at 300 °C. A similar finding has been reported on the adsorption of naphthalene, nitrobenzene, and m-dinitrobenzene onto biochar produced at 100-700 °C. Moreover, the adsorption on acetone, cyclohexane, and toluene has been evaluated in 15



biochar from 5 common feedstocks. The surface area of these biochar ranged from 0.1 – 388 m<sup>2</sup> g<sup>-1</sup>, and the adsorption capacities were all of less than 90 mg g<sup>-1</sup> [11].

### 1.3.3. Carbon nanostructures

Among different adsorbent materials, microporous carbon materials such as activated carbon are one of the most used in the processes of capturing polluting gases, since require a simple synthesis process, are chemically and hydrothermally robust and have high surface areas. Nonetheless, some meso and macroporous carbon materials such as biochar have shown faster VOCs adsorption kinetics than microporous activated carbons [42]. The thermodynamic measurements indicate that VOCs are captured by a physisorption mechanism which involves direct access (through mesopores) to the micropores within the material. On the other hand, activated carbons generally have disordered and undefined pore structure, and as a result, both gas adsorption and regeneration processes are more complex [43]. This opens a new approach to design efficient adsorbents with a more exposed surface area which could compete with activated carbon adsorption capacities. One option that has attracted considerable attention is the synthesis of carbon nanostructures. Carbon nanostructures are new allotropes forms of carbon mostly sp<sup>2</sup> bonded with nanoscale dimensions (e.g., fullerenes, nanotubes, and graphene. See Fig. 1.6), exhibiting novel physicochemical properties, and having widespread potential applications [44]. For potential environmental applications, as superior adsorbents, carbon nanostructures have been studied for the removal of several organic pollutants due to their adequate organic affinity and high surface area [16]. The most important characteristic of some carbon nanostructures used to remove organic molecules are described below.



**Fig. 1.6** - Molecular models showing different carbon nanostructures categorized by their dimensionality. Image from Zhang et al. [42].

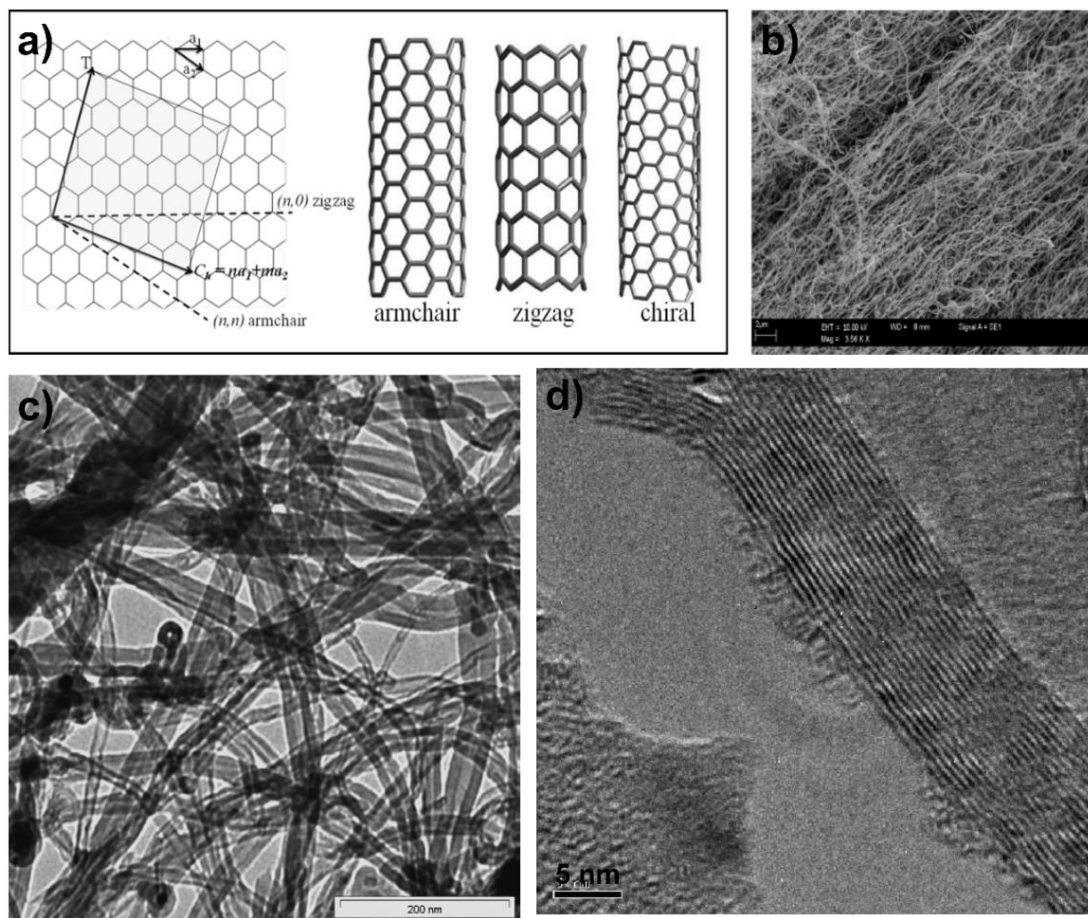
### 1.3.3.1. Carbon nanotubes

Carbon nanotubes (CNTs) are engineered carbon nanomaterials in form of rolling up graphene sheets in cylinders. CNTs are usually synthesized by arc discharge, laser ablation, and chemical vapor deposition [45]. According to the number of graphene sheets, CNTs can be divided into single-walled CNT, and multiwalled CNT (Fig. 1.7). Since the discovery of CNTs by Iijima [45] in 1991, they are widely used in many fields. CNTs have unique characteristics like electrical conductivity, optical activity, and mechanical strength. In addition, their large surface area, natural hydrophobicity, as well as strong thermal stability make CNTs superior to remove trace pollutants from liquid and gas phase [46]. The adsorption of CO<sub>2</sub>, NO<sub>x</sub>, H<sub>2</sub>, NH<sub>3</sub>, CH<sub>4</sub> and VOCs gas molecules on CNTs has been widely explored. In addition, CNTs have strong adsorption affiliation to organic compounds such as anthracene and its derivatives, *n*-nonane and CCl<sub>4</sub>, dioxin, thiophane and polyaromatic





hydrocarbons [47]. The adsorption capacities of organic compounds onto CNTs are usually higher than that onto AC and other carbon adsorbents.



**Fig. 1.7** - (a) Schematic illustration of structures of armchair, zigzag, and chiral single-walled CNTs. (b) Scanning electron microscopy image of CNTs, and (c, d) transmission electron microscopy images of multiwalled CNTs [48], [49].

The VOCs adsorption onto CNTs is primarily conducted by physical adsorption together with slight chemical reaction between surface functional groups of CNTs and VOC molecules. Because CNTs are composed of graphene sheets, they are highly hydrophobic, which facilitates the adsorption of VOCs by their aromatic rings. Generally, the adsorption of nonpolar VOCs onto CNTs is primarily controlled by physical processes, while the adsorption of polar VOCs onto CNTs has the participation of chemical interaction, which has been proven by the enthalpy changes and desorption activation energy. For example, the

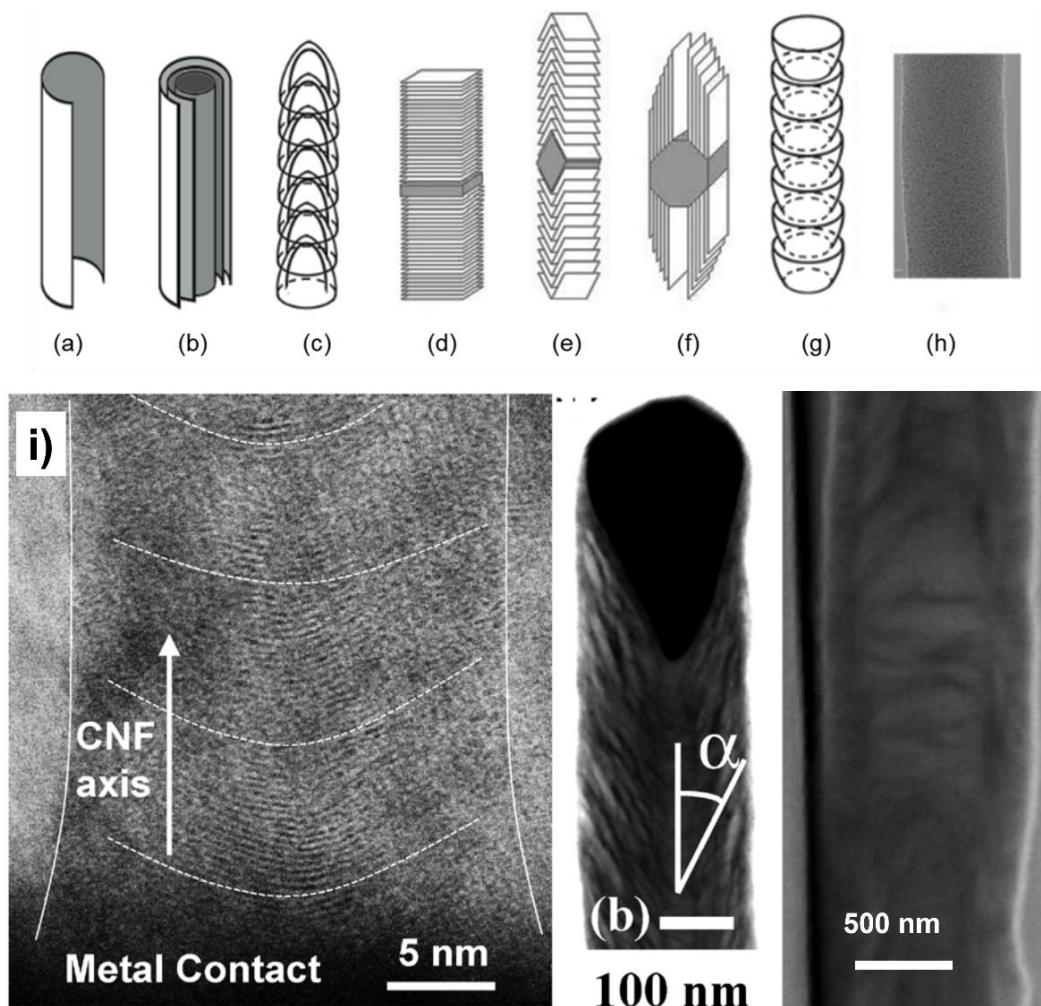


enthalpy changes of nonpolar VOCs adsorbed onto CNTs are relatively low, which is related to an exothermic processes and thus physical interaction. Otherwise, acetone has higher enthalpy changes and needs higher activation energy to desorb, indicating that the polar VOC acetone is adsorbed onto CNTs mainly through chemical interactions [50], [51].

Although CNTs are promising VOCs adsorbents, their aggregation is one of the most crucial drawbacks that limits their commercial applications. To overcome the CNTs aggregation, surface oxidation and coating with surfactants are effective solutions to disperse CNTs in liquid phase. On the other hand, supporting methods are more effective than oxidation and coating methods when CNTs are intended to be used in gas adsorption. This was previously demonstrated by the growth of multiwalled CNTs onto SiO<sub>2</sub> particles: it was found that the supported adsorbent has an excellent performance to adsorb gaseous chlorinated phenolic compounds [52].

### **1.3.3.2. Carbon nanofibers**

Carbon nanofibers (CNFs) can be defined as 1D carbon allotropes, which could include carbon nanotubes [53]. Their general morphology is characterized by a large aspect ratio between the diameter and the length of the fibers, the nano-classification is attributed to the nanoscale diameter of the fibers and the clearly defined structure at the nanoscale, with easily identifiable independent graphene planes [54]. Nevertheless, within this class, important differences are found between the most typical morphologies. CNTs are conceptualized as rolled-up graphene sheet, forming an empty shell cylindrical structure, and are usually classified regarding the number of graphene layers on their walls. CNFs are characterized by the absence of tubular nanostructure, consisting typically of a fishbone or platelet type arrangement, where graphene planes are stached forming the 1D fibrous morphology (Fig. 1.8). Certain synthesis methodologies can also produce carbon nanofibers with an amorphous crystalline structure, marked by the absence of graphitic sp<sup>2</sup> carbon [55].



**Fig. 1.8** - Details of the nanostructure of different types of carbon nanofibers: (a) single-walled CNTs, (b) multiwalled CNTs, (c) bamboo-like CNTs, (d) platelet, (e) fishbone, ribbon, (g) stacked cup, (h) amorphous. (i) TEM images of CNTs showing graphitic sheets and nonhomogeneous morphology along the CNFs length [53].

The 1D CNFs in their various morphologies share several properties that are relevant for their applications as adsorbent, namely those linked with the presence of the  $sp^2$  hybridized graphitic carbon planes in their structure. These are characterized by the presence of a high-density of delocalized  $\pi$ -electrons orbitals, which are responsible for the adsorptive properties of graphene and other allotropes of the same electronic configuration [16].

Gas adsorption, especially hydrogen adsorption capacities of CNFs, has been studied recently via theoretical calculations, experimental measurements, and molecular





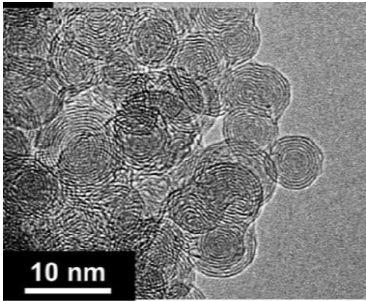
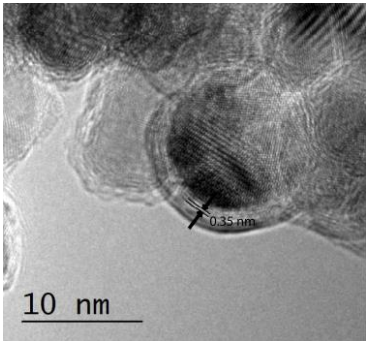
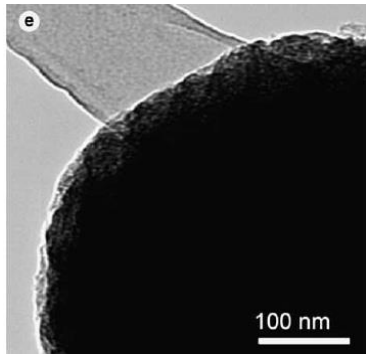
simulations. Several works deal with the adsorption of CO and CO<sub>2</sub>, Ar, O<sub>2</sub>, and CH<sub>4</sub> onto these kind of materials [56]. However, only a limited number of works have focused on adsorption of organic molecules onto CNFs. A few experimental studies have described adsorption isotherms for benzene, methanol, and methane, affinity for dioxins, adsorption kinetics for ethanol, isopropanol, cyclohexane, benzene, and hexane [56]. Additionally, there are also some other works that compare hydrogen adsorption by CNFs [57].

### 1.3.3.3. *Carbon nanospheres*

Carbon nanospheres (CNSs) are circular concentric graphic layers which are formed by pairing of pentagonal and heptagonal carbon rings. Their size ranges from about 50 nm to 1 μm, and their structure could have open dangling bonds, which make them promise for many applications [58]. They have been synthesized by using various methods such as chemical vapor deposition, hydrothermal synthesis, and solution combustion. Various carbon sources, such as hydrocarbons, glucose, sucrose, and biomass, have been utilized as well [59]. Generally, metal catalysts also play an important role in the formation of CNSs, although there are some syntheses of CNSs without the presence of catalyst. CNSs have been used in some applications such as adsorbent, anode in lithium-ion secondary batteries and sodium ion batteries, supercapacitors, and catalysts support [58]. Based on different synthesis conditions such as temperature, carbon source or precursors and presence of metal catalyst, it is possible to obtain different nanosphere-like structures as it is shown in [Table 1.3](#). Despite all these nanostructures have circular concentric graphic layers and display similar surface morphology, their internal structure is different, implying a variety in their chemical and physical properties [60].



**Table 1.3** - TEM images of different morphologies of carbon nanospheres synthesized by different methods.

Images	Name	Description	Ref.
	CNOs	Hollow spheres growth by graphitization of nanodiamonds at high temperatures (>1700 °C).	[61]
	CNOs	Encapsulated metal catalyst and growth by CVD process.	[62]
	Carbon black	Direct pyrolysis of a wide range of hydrocarbons in absence of catalyst.	[63]

Based on the above, CNSs produced with polyaromatic hydrocarbons and catalyst free could stimulate the growth of carbon black, where aromatic molecules condense like turbostratic carbon with a high density of  $sp^3$  hybridizations. On the other hand, the presence of catalyst promotes the growth of carbon nano-onions (CNOs) which are concentric graphitic shells resembling onion layers that were discovered from electron beam irradiation of carbon soot. Previously, CNOs were expensive to produce on a large scale, so their utility



was not considered [64]. However, different synthesis methods allowed to grow successfully high quality CNOs, which impulse to produce large quantities of CNOs. Therefore, CNOs may soon be able to replace other available carbon-based nanomaterials. Recent studies have shown major application of CNOs in electric storage, medicine, and most importantly, pollutants removal [65]. In some technological applications, such as in gas sensors, it is possible to use hollow carbon nanoparticles instead of carbon layer encapsulating nanoparticles. In other cases, these carbon nanoparticles are quasi-spheres and consist only of concentric graphene layers.

The CNSs have been referenced with potential features for adsorption applications, as well as being cost-effective for liquid and gas purification. To date, the use of CNSs in adsorption applications have mainly focused on removal of some pollutant from water, such as chromates, hexavalent chromium, and fluorescent dyes [66]. However, there is still a lack of information on VOCs removal using CNSs.

#### **1.3.3.4. Graphene and its derivatives**

Graphene with a two-dimensional structure consists of a sheet with hexagonally array carbon atoms that share  $sp^2$  hybridized orbitals of one carbon with three neighbors. Graphene oxide is one of the typical derivatives of graphene. Additionally, it is functionalized with oxygen-containing groups as carboxylic, hydroxyl, and epoxy groups. Regarding to its environmental application, graphene and its derivatives have demonstrated excellent performance on the treatments of wastewater containing heavy metals, dyes, and organic pollutants, and toxic gases such as  $NH_3$ ,  $H_2S$ , and VOCs [14], [67]. Graphene and its derivatives seem to be an attractive alternative for toxic gases adsorption; however, their aggregation restricts their commercial application as gas adsorbents.



Increasing the performance of benzene and toluene adsorption by graphene oxide has been reached by eliminating surface functional groups by chemical treatment or thermal annealing under  $N_2$  atmosphere. Accordingly, graphene oxide reduction increased the surface area from 237 to 293  $m^2 g^{-1}$ , as well as the adsorption capacities of benzene and toluene from 216 and 240  $mg g^{-1}$  to 276 and 304  $mg g^{-1}$ , respectively. It might be due to a more hydrophobic nature, lower oxygen content and more defect sites of the reduced graphene oxide [7]. It can be concluded that reduced graphene oxide exhibits strong hydrophobicity due to removal of plentiful oxygen groups, which favor adsorbing nonpolar or weak polar VOCs. However, the relative complicated synthesis and severe aggregation of graphene on composites remain a great challenge for its industrial application.

#### **1.4. Surface modification for enhancing VOC adsorption**

Carbon-based materials have been proven to be an effective adsorbent for the removal of a wide variety of organic and inorganic pollutant in liquid and gas phase. Nevertheless, the application of some carbon-based materials may be limited due to their sensibility to high temperature, lack of adsorption selectivity and hydrophilic nature [33]. To overcome these drawbacks, recent research has emphasized on modifying the physical and chemical attributes of carbon-based materials to enhance their affinities toward different organic molecules present in gas environment.

##### **1.4.1. Conventional modification techniques**

Surface modification implies tailoring the surface of a material to alter a wide range of material surface features such as surface energy, surface charge, roughness, surface area, hydrophobicity, reactivity, and functional groups [68]. This improvement of the material surface occurs by incorporation, elimination, or freezing some selected elements or functional groups to produce the desired changes or developments in the properties of the



interface [69]. Consequently, the adsorbent surface can be modified through several methods. The most implemented modification techniques can be classified as physical and chemical modification. Physical modification is commonly carried out under oxidizing gases such as CO<sub>2</sub>, steam, air, etc., at high temperature (700 -1000 °C). Chemical modification on the other hand involves carbonization and activation in a single step, where the raw material impregnated with a chemical agent is heated up under an inert atmosphere at lower temperature (<700 °C). Physical activation without using corrosive or harmful chemical agents is more environmentally friendly than chemical modification. Chemical modification requires a shorter production cycle, lower energy consumption and is flexible [70].

Regarding the improvement of carbon-based materials for the removal of evaporative emissions, physical and chemical activations exhibit some disadvantages. First, physical activation has a positive effect on the textural properties and surface chemistry of adsorbents. The well-developed pore structure and low content of oxygen groups caused by physical activation are beneficial for nonpolar VOCs adsorption. However, excessive activation would lead to the overexpansion of micropores and reduce the number of available pores, which is detrimental to VOCs adsorption [71]. Similarly, chemical activation with acid or alkali reagents develops a highly microporous structure which could imply diffusional restriction of VOCs, in addition to the plentiful introduction of oxygen-containing groups, which restrict the interaction between the acid adsorbent and polar VOCs [72]. Furthermore, the adsorbents modification by incorporating molecules or metals clusters onto the carbon surface is suitable for the selective uptake of specific VOCs with low concentration due to the limited reaction sites, while the deposition of metal nanoparticles leads to the reduction of available surface area due to pore blockage [7].

Taking into account that activated carbon is the most widely used adsorbent for VOCs removal in automotive canister, these last modification techniques could develop more



porosity and a more polar surface. Previous works are mainly focused on activated carbon modifications to increase the adsorption capacity of VOCs, while VOCs kinetics performance are inadequate for evaporative emissions adsorption. The latter is because during VOCs adsorption, these experience diffusion limitations in the narrow microporous structure of the activated carbon, and particularly during the regeneration for the saturated material [73]. Non-polar carbon materials with exposed surface area are a promising alternative to overcome the VOCs diffusion restriction during the canister operation [42]. In this sense, an adsorbent such as biochar with undeveloped porosity has been used as a potential adsorbent for evaporative emissions. However, the low surface area of biochar that could result in a low adsorption capacity, limits its use as adsorbent. Therefore, an alternative to implement biochar in the removal of VOCs from automotive gasoline, is to increase the exposed surface area without enlarging and open the incipient porous structure, as well as to increase the nonpolar active surface for VOCs adsorption.

A recent alternative to improve VOCs adsorption, is the nitrogen doping by ammonia treatment and coating with an organic polymer [7]. Both modification strategies allow to improve the performance of carbon-based materials because of the removal of polar functional groups, generating a mostly hydrophobic surface. However, to further improve the adsorption capacity of VOCs, it is necessary to increase the exposed surface area of nonporous carbon-based materials. Considering the high affinity of carbon nanostructures for organic molecules, this thesis proposes to grow carbon nanostructures by chemical vapor deposition onto biochar in order to generate a composite material with competitive VOCs kinetics and adsorption capacity.

#### **1.4.2. Chemical vapor deposition**

There are various methods to synthesize carbon nanostructures such as arc discharge, chemical vapor deposition (CVD), laser ablation, flame synthesis, high pressure carbon



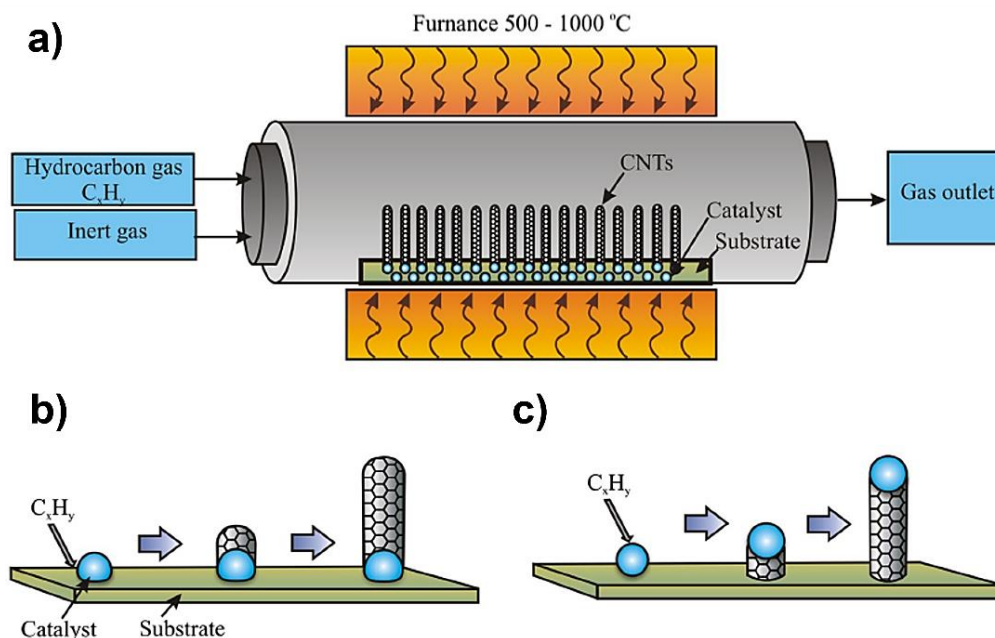
monoxide, electrolysis, pyrolysis, etc. [74]. The common characteristic of these techniques is to provide energy to a carbon source which will facilitate the carbon atoms to generate carbon nanostructures [75]. Currently, the common method widely accepted in the synthesis of carbon nanostructures is the CVD method due to its simplicity and low cost. This method was originally developed in the 1960s and 1970s and has been successfully used in the production of carbon nanofibers, graphene, and carbon nano-onions [63]. Nowadays, CVD has emerged as a potential method for large scale production and synthesis mainly of CNTs [76].

CVD synthesis is essentially a thermal dehydration reaction whereby a transition metal catalyst e.g., iron, nickel, or cobalt is used to lower the temperature required in order to crack a gaseous hydrocarbon feed into carbon and hydrogen [77]. This method is also known as thermal or catalyst CVD. Compared with arc-discharge and laser methods, CVD is a simple and economic technique for synthesizing CNTs at low temperature and ambient pressure. The CVD is a versatile process suitable for the manufacturing of coating, powders, fibers, and monolithic components, or even as a desired architecture of nanostructures at predefined sites on a patterned substrate [45].

CVD process involves passing a hydrocarbon vapor (typically for 15-60 min) through a tube furnace in which a catalyst material is present at sufficiently high temperature (600-1200 °C) to decompose the hydrocarbon [78]. CNTs grow over the catalyst and are collected upon cooling the systems to room temperature. In the case of a liquid hydrocarbon (benzene, alcohol, etc.), the liquid is heated in a flask and an inert gas is purged through it to carry the vapor into the reaction furnace [45]. The catalyst material may be also solid, liquid, or gas and can be placed inside the furnace. The catalytically decomposed carbon species of the hydrocarbon are assumed to dissolve in the metal nanoparticles and, after reaching supersaturation, precipitate out in the form of a fullerene dome extending in a



carbon cylinder with no dangling bonds and, hence, minimum energy [75]. When the substrate-catalyst interaction is strong, CNTs grows up with the catalyst particle rooted at its base (known as the “base growth model”). When the substrate-catalyst interaction is weak, the catalyst particle is lifted up by the growing CNTs and continues to promote CNT growth at its tip (the “tip growth model”) [79] (Fig. 1.9).



**Fig 1.9** - a) Schematic representation of CVD process in a rotatory furnace reactor. Growth mechanism of CNTs by b) base growth model and c) tip-growth model. Image from [80].

The three main parameters to control CVD synthesis are the hydrocarbon, catalyst, and growth temperature. It is known that low CVD temperature (600-900 °C) yields multiwalled CNTs. Whereas at higher CVD temperature (900 -1200 °C) reaction favors single-walled CNTs growth, indicating that this last one has a higher energy of formation [80]. On the other hand, transitional metals (Fe, Co, Ni) are the most commonly used catalyst since the phase diagram of carbon and these metals suggest finite solubility of carbon in these transition metals at high temperatures [81]. The essential role of these metal particles was thought to be their ability to provide a platform on which carbon atoms can form hemispherical cap,





and then a carbon nanotube can grow in self-assembled. In addition, catalyst particles size has been found to dictate the tube diameter. In addition, the material, morphology, and textural properties of the substrate greatly affect the yield and quality of the resulting CNTs. Carbon nanostructures has been synthesized on various substrates, such as metals, quartz, and silicon, or by template growth inside porous alumina. Conversely, CVD synthesis has been applied onto others carbon-based materials such as graphene oxide, biochar, and carbon fibers [82]. It has been mainly undertaken to improve their surface area in order to be applied as high-performance capacitors and field emitting electron sources [83]. Thus, carbon nanostructures-based composites have triggered a great interest in the materials science community, although the information related to their adsorption performance is very limited.

### **1.5. Adsorption of VOCs on carbon-based materials**

Adsorption is a surface occurrence that involves the accumulation of atoms, molecules or ions at the surface of a solid phase. It is mass transfer that leads to the sorption of gases or solutes by solid or liquid surfaces. The substance adsorbed is an adsorbate, and the solid on which the material accumulates is the adsorbent. Adsorption occurs due to surface energy created by an unbalanced force of attraction of the adsorbent. The process of adsorption can be physical or chemical [32]. Overall, physical adsorption occurs when van der Waals and electrostatic forces are the causes of attraction between adsorbent and adsorbate molecules. Physical adsorption is exothermic in nature and reversible. On the other hand, chemical adsorption results from chemical bonding between the adsorbent surface and adsorbate molecules. It is endothermic and irreversible [31]. Adsorption, being a simple, no toxic and economical technique has continued to maintain its polarity among the researchers towards environmental sustainability [33]. Over the last years, adsorption process has been very successful in treating air contaminated by organic pollutants.



### **1.5.1. Mechanisms of adsorbate-adsorbent interaction**

From the macroscopic point of view, the physical adsorption process of porous materials is determined by specific surface area, pore structure, surface properties, and adsorbate properties. From the microscopic view, it is mainly determined by dispersive forces micropore filling and capillary condensation. The large surface area and well-developed pore structure, especially in micropores, have positive effect on physical adsorption. However, physical adsorption is a complicated process, which is controlled by multi-factors instead of just one single factor [7]. Hence, it is important to consider both adsorbent and adsorbate characteristics while attempting to improve physical adsorption capacity.

Chemical adsorptions present more selectivity than physical adsorption because the chemical reaction only occurs between special groups and certain VOCs. Indeed, the adsorption capacity of polar VOCs compounds is affected by the amount of oxygen containing groups. It has been demonstrated that carboxyl and hydroxyl provide reactive sites for substitution reactions or acid-base neutralizations. Quinones are expected to join in the redox behavior to oxidize or reduce organic compounds, and then generate reactive oxygen species for further oxidation [84].

In general, the adsorption of organic compound onto carbonaceous adsorbent are mainly controlled by five potential interactions, i.e. hydrophobic effect,  $\pi$ - $\pi$  bonds, hydrogen bonds, Van der Waals interactions, and covalent and electrostatic interactions. The governing mechanism of VOCs adsorption onto biochar are mainly electrostatic attraction, interaction between polar VOCs and hydrophilic sites, interaction between nonpolar VOCs and hydrophobic sites, and partition in non-carbonized portion [41]. Furthermore, the adsorption of benzene and toluene on carbon adsorbents is mainly based on the formation of electronic complexes between acid functional groups (such as carboxyl) and benzene ring [16].



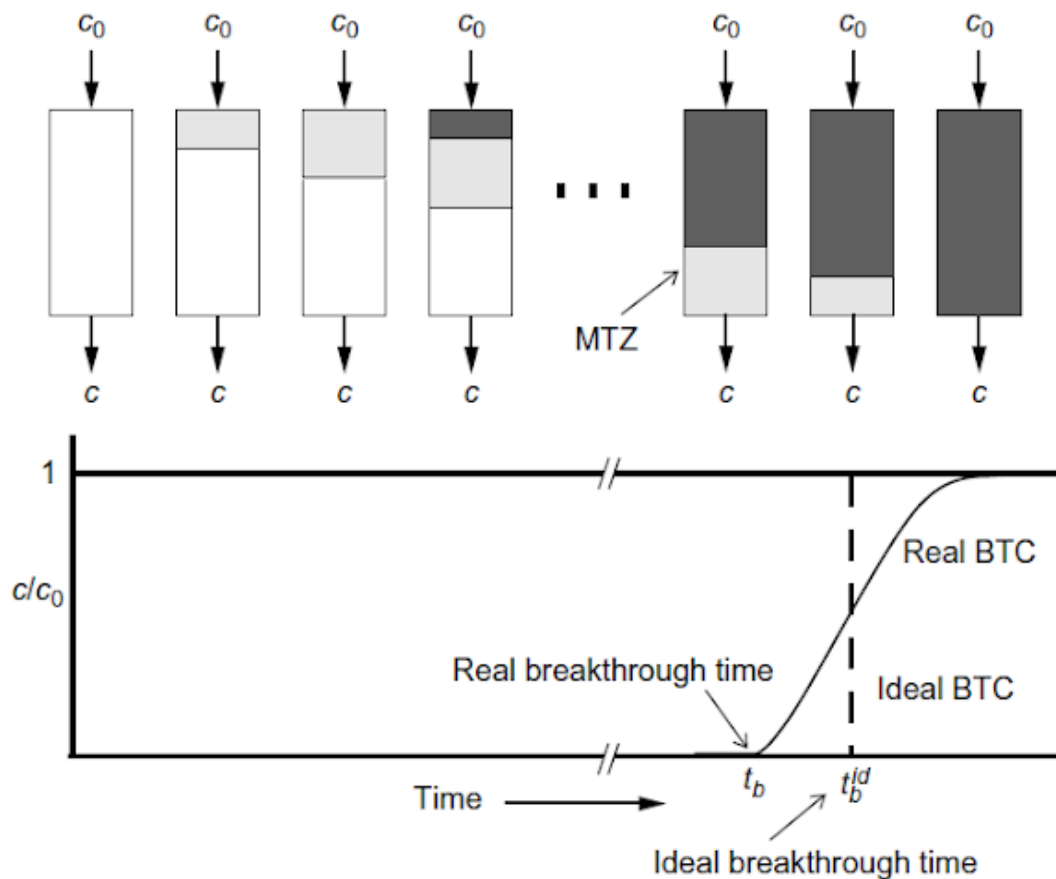
### 1.5.2. Gas adsorption set up

The removal of pollutants from gas phase depends experimentally on different parameters, of which the particle size of the carbon adsorbent is a key factor. Based on the high mobility of gas molecules at the reactor where adsorption process occurs, the smaller the particle, the greater the probability of adsorbent-adsorbate contact. In fact, the use of powder carbon adsorbent is preferred for gas pollutants, due to the convenience of its application, being completely opposite to water treatment. The study of adsorption of VOCs is performed under two configurations, static and dynamic adsorption. Static adsorption is carried out based on the mass change of the adsorbent before and after the adsorption procedure. Regarding the static adsorption of VOCs, the mass transfer is restricted by the natural diffusion of VOCs from the solution bulk to the adsorbent surface, where mainly the vapor pressure of each VOC controls its concentration and mobility.

The dynamic adsorption of hazardous compounds from gas phase by carbon-base materials is normally carried out in packed beds. In comparison to static adsorption, the dynamic adsorption in a packed bed is more complex. The VOCs are normally passed through the packed bed against gravity at some pressure, as the pressure of the system increases more molecules adsorb over the surface of the adsorbent [86]. Normally a release of the system pressure leads to the desorption of the adsorbed molecules, if only physical forces are involved during the process. The extent to which the contaminants are removed strongly depends on the gas vapor pressure, the concentration of the contaminant and the moisture content of the gas phase that might promote chemisorption reactions on the surface of the carbons [85]. Adsorption in a packed bed adsorber is a time and distance dependent process. During dynamic operation a zone is identified where the adsorption take place, known as mass transference zone (MTZ). The MTZ travels through the adsorber with a velocity and should be slower than the gas velocity. The stronger the adsorption of the



adsorbate, the greater the difference between the MTZ velocity and the gas velocity [88]. When the MTZ reaches the end of the column some pollutants are detected in the column outlet, this stage is identified as the breakthrough time. The dynamic adsorption performance is represented on a breakthrough curve (BTC) by the loss of concentration versus time. When the MTZ leaves the column, the outlet and inlet concentration of the objective pollutant is the same, indicating that the material is exhausted and needs to be replaced or regenerated (Fig. 1.10).



**Fig. 1.10** - Traveling of the mass transfer zone (MTZ) through the packed bed and development of the breakthrough curve. Image from [88].



### **1.5.3. VOCs adsorption performance**

As an alternative to commercial AC, a great range of carbon-based materials have been studied for the adsorption of different single VOCs, as well as mixtures of various polar and nonpolar VOCs, most of them have been summarized in several reviews [7], [11], [36].

There has been a recent increase in the studies related to the VOCs uptake by alternative carbon-based materials instead of activated carbon. On the other hand, it is difficult to make a direct comparison between the reported VOCs adsorption capacities, since most of the studies have different adsorption conditions of temperature, concentration, pressure, etc. However, selected works that are similar to the reported in this thesis are provided in [Table 1.4](#).



**Table 1.4** - Summary of physiochemical properties and performance of different porous materials for VOCs adsorption.

Adsorbent	$S_{BET}$ ( $m^2 g^{-1}$ )	$V_{total}$ ( $cm^3 g^{-1}$ )	Adsorbate	Adsorption set up	Operational conditions	Adsorption capacity ( $mg g^{-1}$ )	Ref.
AC coconut shell-base	868	0.500	Benzene	Dynamic	$N_2$ , 30°C, 400 mL $min^{-1}$	336	[87]
Biochar cotton stark	1256	0.880	Toluene	Dynamic	$N_2$ , 25 °C, 300 ppm, 30 ml $min^{-1}$	319	[85]
Graphite powder	293	-	Toluene	Dynamic	$N_2$ , 10 °C, 50 ppm, 40 ml $min^{-1}$	304	[88]
Zeolite/GO composite	1112	-	Toluene	Dynamic	Air, 30°C, 15 ml $min^{-1}$	116	[89]
Nitrogen doping porous carbon	2940	2.126	Acetone	Static	18kpa, 25°c	686	[90]
Porous hollow carbon	1082	1.110	Benzene	Dynamic	$N_2$ , 20 °C, 500 ppm, 50 ml $min^{-1}$	766	[91]
Urea-assisted biochar	3053	1.670	Toluene	Dynamic	$N_2$ , 25 °C, 600 ppm, 100 ml $min^{-1}$	724	[92]
Carbon-silica aerogel	758	0.530	Benzene	Dynamic	$N_2$ , 25 °C, 700 ppm, 100 ml $min^{-1}$	124	[93]
CNTs	609	0.952	Hexane	Static	$N_2$ , 25°c, 40-4000 ppm, $1 \times 10^{-4}$ $<p/p_0 < 0.95$	456	[94]



#### **1.5.4. Adsorbent regeneration.**

Adsorbent recyclability is also an important indicator because it determines the cost of the adsorption process. The desorption of VOCs requires elimination of the interaction between the VOCs molecule and the active site of the adsorbent. In addition, the adsorbent must maintain effective physical and chemical properties for effective reuse. Most of the VOC adsorbed onto the carbon materials can be recycled through desorption processes under various conditions (Table 1.5). The methods for regeneration of adsorbents commonly used are pressure swing, temperature swing, purge gas stripping, and microwave heating. Due to the simple equipment needed, low energy consumption and high desorption efficiency, temperature desorption is the most commonly used method for VOCs desorption in research and on an industrial scale.

During the VOCs desorption by temperature, the physical and chemical structure of the adsorbent inevitably change, which affect the sorption performance in the following cycles. The effect of the regeneration cycles on the adsorption capacity of different adsorption materials has been previously studied [36]. Overall, the VOCs adsorption capacity of several materials decrease with the number of regenerative cycles. The reusability of adsorbents vary since the heat resistance is different for each material. Carbon-based materials produced by carbonization and activation, or pretreated at high temperature have demonstrated good heat resistance. Despite commercial adsorbents such as activated carbon and zeolites have good reusability, their adsorption capacity decreases to 83 and 80%, respectively [95]. Thus, novel adsorbents with high reusability (>90%) are needed to be applied in automotive canister for VOCs removal from gasoline.



**Table 1.5** - Desorption of VOCs from various carbon-based materials.

Adsorbent	Adsorbate	Desorption strategies	Desorption conditions	Desorption efficiency	Cycles	Ref.
Biochar	Hexane	Thermal regeneration	Temperature (100 °C)	90%	4	[96]
Biochar	Toluene	Thermal regeneration	Temperature (350 °C)	95%	1	[98]
AC	Acetone	Thermal regeneration	Temperature (80°C)	95 %	8	[99]
AC	Toluene	Thermal regeneration	Temperature (180°C)	98.1%	5	[100]
AC fiber cloth	Toluene	Electrothermal desorption	1500 W kg <sup>-1</sup>	75%	5	[101]
Beaded AC	Mixture of various VOCs	Electrothermal desorption	400 °C	Not fully VOC desorbed in micropores	-	[102]
MOF/graphene oxide composite	Acetone	Vacuum desorption	25 °C, 0.04 mbar	91.3%	6	[103]
Microporous AC	Mixture of toluene, butyl acetate, and butanol	Temperature programmed desorption	150 °C	85 %	5	[104]





## 1.6. Key factors controlling VOCs adsorption

There are many factors controlling the adsorption of VOCs. The properties of adsorbent materials such as the content of surface functional groups, surface area, and pore structure are three crucial factors that directly affect the adsorption of VOCs. The properties of VOCs such as molecular weight, molecular diameter, boiling point, polarity, saturated vapor pressure, etc., also affect the adsorption process. The adsorption process is also affected by adsorption conditions such as temperature, humidity, and VOCs concentration. Therefore, for a comprehensive analysis of the adsorption behavior of VOC, it is necessary to consider the effect of various factors on adsorption rate and capacity.

### 1.6.1. Adsorbent properties

#### 1.6.1.1. Textural properties

It has been reported that for any adsorbent, a large surface area means superior adsorption performance because the surface area provides the sites for the adsorption process, which increases the probability of interaction between the adsorbent and VOCs [57]. Although, this is not always like this. The relationship between textural properties and adsorption capacity of different adsorbents has been studied. For instance, it has been reported that the adsorption capacity of toluene has good linear relationship with the surface area and pore volume of the adsorbent, indicating that the adsorption capacity of VOCs increases with the increase of the textural properties of the adsorbent [36].

The effect of surface area on toluene adsorption has been reported. It was found that toluene breakthrough time in AC of large surface area ( $1700\text{m}^2\text{g}^{-1}$ ) was four times of that of smaller surface area ( $1000\text{m}^2\text{g}^{-1}$ ) [104]. Similarly, the adsorption of acetone, benzene, trichloroethylene, and *n*-hexane has been compared between two kinds of CNTs, and higher VOCs adsorption capacities were observed on the CNTs with larger surface area [56].



However, AC with the highest surface area does not always mean the best adsorption capacity for organic compounds. An example is toluene adsorption onto AC, the tested AC with surface area of  $789 \text{ m}^2 \text{ g}^{-1}$  can adsorb  $656 \text{ mg g}^{-1}$  of toluene, much higher than that ( $346 \text{ mg g}^{-1}$ ) of another AC with higher surface area ( $2719 \text{ m}^2 \text{ g}^{-1}$ ) [105]. Similar phenomenon has been previously reported, indicating that adsorption is a complicated process controlled by many other factors in addition to surface area.

Because carbonaceous materials are porous adsorbents, the morphological structure, especially the distribution of pore size is responsible for their VOCs adsorption ability [106]. Their pores can be divided into micropores (pore diameter  $<2 \text{ nm}$ ), mesopores ( $2 \text{ nm} < \text{pore diameter} < 50 \text{ nm}$ ), and macropores (pore diameters  $>50 \text{ nm}$ ) [105]. VOCs adsorption onto carbon-based materials thus is affected by pore size in various ways. It has been pointed out that micropores dominate VOCs adsorption onto carbon materials. For instance, it was found that the adsorption capacity of chloromethanes and  $\text{CH}_3\text{I}$  on AC are close to the micropores volume. Similar observations have been reported on toluene and acetone adsorption by AC and biochar [107]. Theoretically, pores with pore diameter larger than the molecular diameter of VOCs can be effective adsorption sites. However, when the pore size is larger than the molecular diameter of VOCs, the adsorption force between the adsorbent and the VOCs molecules is too weak, and the pore can only play the role of channel. In general, micropores provide the main adsorption sites, while mesopores enhance the intraparticle diffusion and shorten the adsorption time.

Although the micropore volume is beneficial for VOCs adsorption onto carbon, the diffusion resistance may increase in the narrow pores, leading to low adsorption rates. The adsorption rates of VOCs in mesopore are faster than that in micropore due to the higher intraparticle diffusion rate. In this sense, it has been found that the diffusion rate constants of VOCs in ordered mesoporous carbon are almost twice of that in microporous AC [108].



Thus, the smaller the adsorbent pore size the smaller diffusion coefficient. Additionally, pore size of the adsorbent material determines the VOCs molecules than can be adsorbed. According to the size exclusion theory, only when the pore diameter is larger than the molecular diameter of the VOCs, the VOCs molecules can enter the pores of the adsorbent material [36]. This is in good agreement with the fact that micropores facilitate the adsorption of small size VOCs while large molecule of VOCs prefer mesopores. It should be noted that even when the VOC molecule is smaller than pore size, it not always guarantees that VOCs can enter the pores. Moreover, even though little VOCs would be adsorbed into the macropores or mesopores, these large pores would benefit for the VOCs adsorption because they would provide the necessary transport channels for VOCs especially for the ones with larger molecular sizes [73].

#### **1.6.1.2. Chemical functional groups**

The adsorption of VOCs onto carbonaceous adsorbents may be controlled by physical and chemical processes. Besides the morphology structure, surface chemical functional groups of carbon materials are directly responsible for VOCs adsorption performance [109]. The surface functional groups are associated with both the nature of the raw material and activation process, or with the modification methods previously discussed. The heteroatoms surface functional groups govern the adsorbents surface chemistry. The heteroatoms mainly include oxygen, nitrogen, halogens, hydrogen, etc., [71], among which the oxygen and nitrogen groups on the carbon-based material are recognized as the most important species for the adsorption of VOCs. In addition, the oxygen groups can be acidic, basic, or neutral.

Carbon surface acidity is mainly given because of oxygen functionalities, which contribute to the affinity of hydrophilic VOCs onto the carbon surface. The presence of oxygen functionalities could inhibit the specific interactions between hydrophobic VOCs and  $\pi$ -electron rich regions on carbonaceous adsorbents [37]. Therefore, hydrophobic VOCs prefer



to be adsorbed onto AC that does not have oxygen-containing groups. VOCs, such as *o*-xylene and benzene, have been poorly adsorbed by acidic modified ACs and acid-activated biochar compared with pristine ones, respectively [29].

To enhance the adsorption of hydrophobic VOCs onto carbonaceous adsorbents, suitable modifications should be done to eliminate the surface oxygen groups. It has been reported that surface functional groups would decompose at high temperature: carboxylic groups at 150–300 °C, acid anhydride and lactone at 300–500 °C, ethers, phenolic, hydroxyl, and carbonyl at 500–800 °C [110]. Thermal treatment of over 500 °C makes the surface of biochar be less polar and more hydrophobic due to the decomposition of O- and H-containing functional groups, which directly affect the VOC adsorption [41].

Some studies, however, have suggested that the chemical functional groups on the surface of adsorbents are not an important factor in VOCs adsorption [88]. Sometimes, correlation analyses fail to demonstrate the direct relationship between specific surface area, pore size, functional groups of carbon adsorbents and their VOC adsorption capacities. This is because the above-mentioned features never play the part on their own. Therefore, a balance between all the textural and chemical properties should be considered.

### **1.6.2. Adsorbate properties**

The properties of adsorbates, such as molecular structure, polarity, and boiling point, play an important role in VOC adsorption onto carbon materials. First, the molecular structure of VOCs determines their adsorption sites, while the larger VOCs cannot enter into the smaller pores. Moreover, large size VOC molecules such as naphthalene (kinetic diameter = 0.62 nm) are adsorbed in a small amount because these block the entrance of narrow micropores of AC. The adsorbate shape also influences VOCs adsorption. For instance, *o*-xylene, *m*-xylene, and *p*-xylene possess almost equal cross-sectional area of 0.375, 0.379 and 0.380



nm<sup>2</sup>, respectively, however, the adsorption of *p*-xylene on carbon materials is significantly higher than that of the others [108], [111].

The molecular polarity of VOCs is another property that directly impacts their adsorption onto carbonaceous adsorbents. Generally, polar VOCs prefer to be adsorbed onto adsorbents with polar groups, while nonpolar VOCs would like to be adsorbed onto the adsorbent without polar groups [112]. For example, nonpolar VOCs such as C<sub>6</sub>H<sub>6</sub> and CCl<sub>4</sub> exhibit higher adsorption capacity on biochar and non-oxidized AC than other polar VOCs, where the basic character of basal planes on these adsorbents displays a high affinity for VOCs with zero dipole moments.

Regarding the boiling point, it can be said that the physical adsorption process of adsorbate on porous adsorbents is similar to vapor-liquid phase transitions, where the adsorbate with higher boiling point would be preferentially adsorbed than those with lower boiling points because for the stronger intermolecular forces. Additionally, liquid-like condensation plays an important role in VOCs adsorption on AC, thus the boiling point of VOCs is a crucial factor to influence the adsorbent. It has been found that the adsorption capacity of low boiling molecules as dichloromethane (313.2 °C) and ethanethiol (308.2 °C) were 0.21 and 0.18 mol kg<sup>-1</sup>, respectively, which were less than the 1.23 mol kg<sup>-1</sup> of siloxane D4 (448.9 °C) [11]. Because of the strong affinity between the high boiling point of VOCs and adsorbents, the VOCs with lower boiling point will be easily replaced during the competitive adsorption process, whereas the desorption of VOCs with high boiling point from the adsorbent is more difficult due to their strong affinity with the adsorbent [28].



### **1.7. Motivation of this research**

Considering the hazardous effect of VOCs on the environment and human health, in recent years the control of these emissions has attracted much attention. Currently, many countries have focused their efforts to reduce polluting emissions and have developed legislation to meet their objective of minimum emissions to the environment. Therefore, the recovery and reuse of evaporated gasoline from loading, unloading, and other handling processes are of significant importance from both economic and environmental point of view.

Adsorption with activated carbon has been recognized as the preferred strategy for controlling VOCs emissions. However, serious diffusion restrictions by its narrow microporosity tend to cause problems as pore blocking, hygroscopicity, and difficulty to be regenerated. It was thought that by employing macroporous adsorbents, the problems associated with activated carbon could be overcome. Unfortunately, these materials possess a low surface area, resulting in a relatively reduced adsorption capacity. Therefore, the main motivation of this research was to grow carbon nanostructures on macroporous biochar, taking advantage of its high exposed surface area and high affinity for different VOCs of gasoline, to avoid diffusion restrictions of VOCs and obtain a high desorption performance.

### **1.8. Hypothesis**

The growth of carbon nanostructures by chemical vapor deposition on biochar from waste bagasse agave will increase its exposed surface area, and hence, the adsorption and desorption kinetics of different VOCs contained in commercial gasoline will be faster than those reported for commercial activated carbons used in automotive canisters.



## 1.9. General objective

The purpose of this research is to study the growth of carbon nanostructures onto macroporous biochar from waste agave bagasse by chemical vapor deposition to explore the adsorption and desorption performance of representative VOCs of gasoline in static and dynamic configurations.

### 1.9.1. Specific objectives

- To determine the synthesis conditions of CVD process in a thermogravimetric analyzer by growing carbon nanostructures through short synthesis times ( $< 5$  min) and low temperatures ( $\leq 700$ ).
- To characterize the novel composites by techniques such as  $N_2$  physisorption, FTIR, SEM, TEM, XRD, Raman spectroscopy, potentiometric titrations, and contact angle, and further understand the structure of these materials.
- To determine the static adsorption kinetics of different VOCs representative of evaporative emissions such as benzene, toluene, hexane, and pentane.
- To implement the TGA conditions used for carbon nanostructures by CVD in a furnace oven for larger-scale adsorbent production.
- To determine the dynamic adsorption of different VOCs from gasoline in packed bed columns, and the reusability of the biochar/carbon nanostructures composite.
- To determine the dynamic adsorption breakthrough of a commercial gasoline in a packed bed column.
- To compare static and dynamic performance of modified and non-modified biochar with a commercial porous carbon material often used for VOCs adsorption in automotive canisters.
- To propose the adsorption mechanisms involved in the VOC uptake, based on the VOCs and carbon-base materials properties.

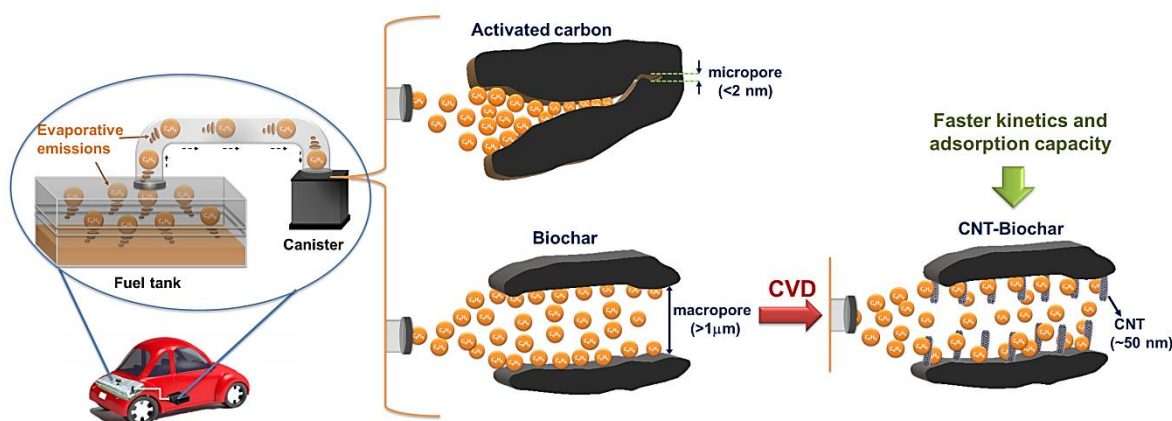
# CHAPTER 2

---

## Fast benzene vapor capture by natural macroporous biochar improved with carbon nanostructures

---

---



---

This chapter was adapted from: Fast benzene vapor capture by natural macroporous carbonized fibers improved with carbon nanostructures, *Separation and Purification Technology* 257 (2021) 117956.





### Abstract

We investigated the adsorption of benzene, as a model volatile organic compound from gasoline, in a novel macroporous carbon material, with the intention of improving the kinetics performance of porous materials in automotive canisters. In this research, we proposed agave bagasse fibers, that when pyrolyzed develop wide pores all along the fiber, that are helpful in vapor diffusion. To enhance the surface area of this biochar, we grew diverse carbon nanostructures onto biochar surface by chemical vapor deposition. The as-produced materials were characterized by  $N_2$  physisorption, FTIR, SEM, TEM, XRD and Raman spectroscopy. The carbon nanostructures formed, such as bamboo-like carbon nanotubes, onion-like carbon, and carbon black, increased the surface area of biochar from 120 to 185  $m^2 g^{-1}$ , while their thermal post-treatment at 800 °C doubled the surface area, up to 243  $m^2 g^{-1}$ , of the pristine biochar. The adsorption of benzene vapor showed that biochar containing carbon nanostructures have 1.8 times faster adsorption kinetics ( $0.0064 \text{ mmol min}^{-1}$ ) and 1.5 times higher adsorption capacity ( $55.53 \text{ mg g}^{-1}$ ) after 26 h of static adsorption than a commercial granular activated carbon, which is used nowadays in automotive canisters. The pseudo-second order model provided the best fit to the kinetic rates.

### 2.1. Introduction

The release of volatile organic compounds (VOCs) into the atmosphere has become a worldwide risk of growing concern [1], this because VOCs emissions are hazardous to human health, and contribute to serious environmental problems such as the destruction of the ozone layer, the formation of photochemical smog and global warming [3]. The emissions from gasoline in automotive fuel tanks are an important anthropogenic source of VOCs since these are leaked to the atmosphere for an average time of 24 h, even when the vehicle is not running. To avoid VOCs emissions, modern vehicles are equipped with evaporative loss control devices, also known as canisters, that adsorb the VOCs from



gasoline [107]. From the great variety of adsorbent materials, activated carbon is the most widely used for VOCs removal in automotive canisters, mainly because of its excellent adsorption capacity due to both, its non-polar surface chemistry, and its well-developed porosity [113], [114]. Nevertheless, the adsorption of VOCs in porous materials such as activated carbon has some limitations. During VOCs capture, they experience diffusion limitations in the narrow microporous structure of the activated carbon, and particularly during the regeneration of the saturated material [93], [115]. In this sense, the development of non-polar carbon materials with a considerable exposed surface area in wide-open pores is a promising alternative to overcome the VOCs diffusion restriction during their capture.

Because of the latest, biochar from agave bagasse is proposed as a potential adsorbent of VOCs. The open parallel channels, that go from tip to tip, formed after the carbonization of agave bagasse fibers can allow a fast adsorption-desorption rate during the canister operation process, while their surface chemistry, mostly non-polar, favors hydrophobic interactions with organic adsorbates [116]. The use of raw lignocellulosic waste materials as a renewable carbon source with high availability for the preparation of biochar as adsorbent materials, has caught increased attention due to the potential reduce of the environmental pollution that causes its confinement [117]. The carbonized agave bagasse fibers have relatively low surface area that could result in a low adsorption capacity, limiting its use as adsorbent [116]. Therefore, an alternative to implement this biochar in the removal of VOCs from automotive gasoline is the increase in their exposed surface area by the growth of carbon nanostructures within their channels.

Among all carbon-based materials, carbon nanostructures such as graphene, fullerenes, carbon nanotubes (CNTs), and carbon nanospheres (CNSs) have been considered promising adsorbents for the removal of organic molecules due to their adequate organic affinity and high surface area [118]–[120]. Researchers have reported a wide range of



surface area for CNTs ( $150 - 3000 \text{ m}^2 \text{ g}^{-1}$ ) and for a variety of CNSs like carbon black and carbon nano-onions ( $300 - 600 \text{ m}^2 \text{ g}^{-1}$ ), which is comparable to that of carbon-based adsorbents that are applied commercially [61], [121]. Unlike the porous carbon materials, these carbon nanostructures have a readily available surface area, making easy the pollutants diffusion during their adsorption [65]. CNTs adsorption isotherms have been evaluated in batch configuration for benzene, methanol, and methane [122], while CNTs adsorption kinetics have been tested for ethanol, isopropanol, cyclohexane, benzene, and hexane [118]. The use of CNSs in adsorption applications have mainly focused on the removal of some pollutants from water, such as fluorescent dyes [123], chromate [66], and hexavalent chromium [65]. On the other hand, nitrogen doped hollow carbon spheres have reported a remarkable dynamic benzene vapor adsorption capacity of  $766 \text{ mg g}^{-1}$  [91].

Carbon nanostructure materials are fine powders, and in order to implement them in a packed canister for the adsorption of gasoline emissions, they need to be immobilized or anchored on a solid matrix. Thus, carbon nanostructures-based composites have triggered a great interest in the materials science community, although the information related to their adsorption performance is very limited. For instance, the study of aligned growth of CNTs on other carbon substrates was mainly undertaken to improve their surface area in order to be applied as high-performance capacitors and field emitting electron sources [124], [125]. The exfoliation of graphene oxide sheets by the growth of CNSs embedded as pillars between layers increased the surface area of graphene oxide from  $219$  to  $476 \text{ m}^2 \text{ g}^{-1}$ , making a so-called sandwich composite [82]. As far as we know, there are no reports yet concerning the growth of carbon nanostructures directly on macroporous biochar obtained from the carbonization of agave bagasse, to create a novel material for VOCs adsorption. In addition, it is believed that carbon nanostructures could also further improve the mechanical, physical,



and chemical properties of biochar, providing an opportunity to apply this novel material as adsorbent of VOCs.

Hence, the purpose of this study is to develop a novel composite that combines the wide-open pores of biochar from agave bagasse with the highly non-polar surface area of non-oxidized carbon nanostructures. Characterization techniques such as  $N_2$  physisorption, FTIR, SEM, TEM, XRD and Raman spectroscopy are used to further understand the structure of this novel composite. The adsorption kinetics of benzene, as model VOC, is evaluated in static adsorption experiments, which resembles the operational conditions of automotive canisters, where no external gas flow carries the evaporated gasoline. Additionally, benzene adsorption kinetics and capacity of modified and non-modified biochar are compared to a commercial porous carbon material often used for VOCs adsorption in automotive canisters.

## 2.2. Materials and methods

### 2.2.1. Reagents and precursor

All the chemicals used in this research were reagent grade.  $FeSO_4 \cdot 7H_2O$  was purchased from Fermont Company.  $NaBH_4$ , sodium carboxymethylcellulose (CMC, M.W: 25,000) and benzene were obtained from Sigma Aldrich. Deionized water was used for the preparation of all solutions. The precursor (agave bagasse from *Agave salmiana* plant) was provided by a distillery located in San Luis Potosi, Mexico. Before the carbonization step, the bagasse fibers were washed with deionized water then dried at 90 °C for 24 h, and finally cut to the length of 0.5 cm.



### 2.2.2. Biochar production and catalyst impregnation

Biochar was obtained through carbonization of bagasse fibers in a tubular furnace under the following conditions: i) heating rate of  $5\text{ }^{\circ}\text{C min}^{-1}$  until reaching  $200\text{ }^{\circ}\text{C}$ ; after that automatically, ii) the heating rate was changed to  $10\text{ }^{\circ}\text{C min}^{-1}$  until  $600\text{ }^{\circ}\text{C}$ ; and iii) temperature was held at  $600\text{ }^{\circ}\text{C}$  for 80 min. All the process was carried out under a  $\text{N}_2$  atmosphere with a flow rate of  $1\text{ L min}^{-1}$ .

To promote the growth of CNTs on the biochar, zero-valent iron particles were used as catalyst. Herein zero-valent iron catalyst was prepared by using CMC to avoid particle agglomeration [126]. In brief, 250 mL of CMC  $4.96 \times 10^{-5}\text{ mol L}^{-1}$  solution was purged with  $\text{N}_2$  for 15 min to remove dissolved oxygen. In a typical preparation, 50 mL of  $\text{FeSO}_4 \cdot 7\text{H}_2\text{O}$  stock solution was added to CMC solution to yield a desired  $\text{Fe}^{2+}/\text{CMC}$  molar ratio. Keeping the CMC concentration constant, three iron concentrations ( $0.1$ ,  $1$  and  $10\text{ g L}^{-1}$ ) were explored to evaluate their effect on the CNTs growth. The zero-valent iron catalyst was prepared by the reduction of  $\text{Fe}^{2+}$  ions with 10 mL of  $\text{NaBH}_4$  solution as reducing agent, added drop by drop, at a  $\text{BH}_4^-/\text{Fe}^{2+}$  molar ratio of 2:1. The solution was stirred at  $230\text{ min}^{-1}$  under  $\text{N}_2$  atmosphere until  $\text{H}_2$  gas (formed by the reduction of  $\text{Fe}^{2+}$  to  $\text{Fe}^0$ ) evolution ceased after 15 min. Finally, the impregnation of the zero-valent iron catalyst onto the biochar surface was carried out by immersing 0.2 g of biochar in 20 mL of this iron nanoparticle suspension. The samples were stirred for 48 h at  $25\text{ }^{\circ}\text{C}$  under orbital stirring at  $125\text{ min}^{-1}$ . After the impregnation procedure, the samples were rinsed with deionized water to eliminate residual chemicals and dried at  $90^{\circ}\text{C}$  for 24 h.



### 2.2.3. Chemical vapor deposition setup

Carbon nanostructures were synthesized by means of chemical vapor deposition (CVD) at ambient pressure. The CVD system consisted of a thermogravimetric analyzer (Versa Therm) with a vertical quartz furnace as reactor. First, the impregnated biochar was placed in a mesh capsule while the tubular reactor was purged with  $N_2$  gas. Then, the samples were heated up at a rate of  $25\text{ }^\circ\text{C min}^{-1}$  until the temperature of CVD ( $700\text{ }^\circ\text{C}$ ) was reached. Then, the carbon source ( $C_2H_2$ ) was injected for 60 or 300 s. These conditions were tested for the three iron concentrations described above. Once the CVD process ended, the samples were cooled down to room temperature. After that, the sample was thermally post-treated at  $800\text{ }^\circ\text{C}$  for 10 min under  $N_2$  atmosphere to remove condensed soot and amorphous carbon.

### 2.2.4. Characterization techniques

Surface area and pore size distribution were estimated from the nitrogen physisorption isotherm, obtained in a Micromeritics ASAP 2020 instrument at 77 K. The surface area was calculated using the BET equation [127], and the pore size distribution was determined using the density functional theory (DFT), protocols established in the equipment. Functional groups were determined by attenuated total reflection Fourier transform infrared analysis (ATR-FTIR, Thermo-Nicolet, Nexus 470 FT-IR E.S.P). The spectra were obtained from  $550$  to  $4000\text{ cm}^{-1}$  with a resolution of  $6\text{ cm}^{-1}$ . X-ray diffraction (XRD) analysis of pristine and modified carbonized fibers was obtained in a SmartLab Rigaku diffractometer using a  $CuK_\alpha$  radiation. The XRD patterns were obtained with a step size of  $0.01^\circ$  with a step time of 10 sec. The peak positions of the crystal structures were identified from the ICDD-PDF-4 + 2015 database. Raman spectroscopy was performed by means of a confocal Raman spectrometer (inVia MICRORAMAN: RENISHAW) using a 514 nm laser and a 100x objective lens (spot size of  $0.3\text{ }\mu\text{m}$ ). Selected samples were observed by scanning electron



microscopy (ESEM FEI QUANTA 250 FEG); obtaining detailed information about the dispersion of catalysts on the biochar surface and synthesized carbon nanostructures under different CVD experimental conditions. The transmission electron microscope (TEM, Tecni FEI 300 operated at 300 kV) was used to observe with more detail the carbon nanostructures morphology. The sample was suspended in isopropanol and then sonicated for 5 min; finally, the sample was mounted onto copper TEM grid.

### 2.2.5. Adsorption experiments

The batch adsorption experiments were evaluated to explore the benzene adsorption kinetics of carbon materials. The experimental setup was as follows: we introduced 0.1 g of adsorbent material in a 1 mL glass syringe that has a metallic needle. The syringe packed with adsorbent was dried at 100 °C for 24 h to remove the physisorbed moisture and cooled down in a desiccator at room temperature. Besides, 5 mL of benzene were placed in a 50 mL serum bottle and sealed with black Teflon stoppers. The headspace of the bottle was replaced with N<sub>2</sub> atmosphere to avoid moisture effects. To stimulate the benzene gasification, the bottles were stirred in an orbital shaker for two days at 90 min<sup>-1</sup> at 25 °C. The syringe loaded with dry adsorbent material was weighed in a digital microbalance with a sensitivity of 0.01 mg. After that, the syringe needle was inserted in the serum bottle by crossing the septa to allow the benzene gas to diffuse through the needle cavity to the adsorbent material. The syringe was taken out from the bottle to monitoring its weight within the interval of 1- 26 h. The adsorption rate parameters were determined for selected models, including the pseudo-first and pseudo-second equations [128]. The *pseudo-first-order kinetic equation* is given by:

$$\ln(q_e - q_t) = \ln(q_e - k_1)t \quad (\text{Eq. 2.1})$$



where,  $q_t$  and  $q_e$  ( $\text{mg g}^{-1}$ ) are the adsorption capacities at time  $t$  (h) and equilibrium, respectively, and  $k_1$  ( $\text{h}^{-1}$ ) it the pseudo-first order rate constant.

The *pseudo-second order kinetic equation* can be represented by:

$$\frac{t}{q_t} = \frac{1}{k_2 q_e^2} + \frac{1}{q_e} t \quad (\text{Eq. 2.2})$$

where  $k_2$  ( $\text{mg (g}\cdot\text{h)}^{-1}$ ) is the pseudo-second order rate constant of sorption,  $q_e$  ( $\text{mg g}^{-1}$ ) is the amount of pollutant absorbed equilibrium, and  $q_t$  ( $\text{mg g}^{-1}$ ) is the amount of pollutant adsorbed at any time  $t$  (h).

## 2.3. Results and discussion

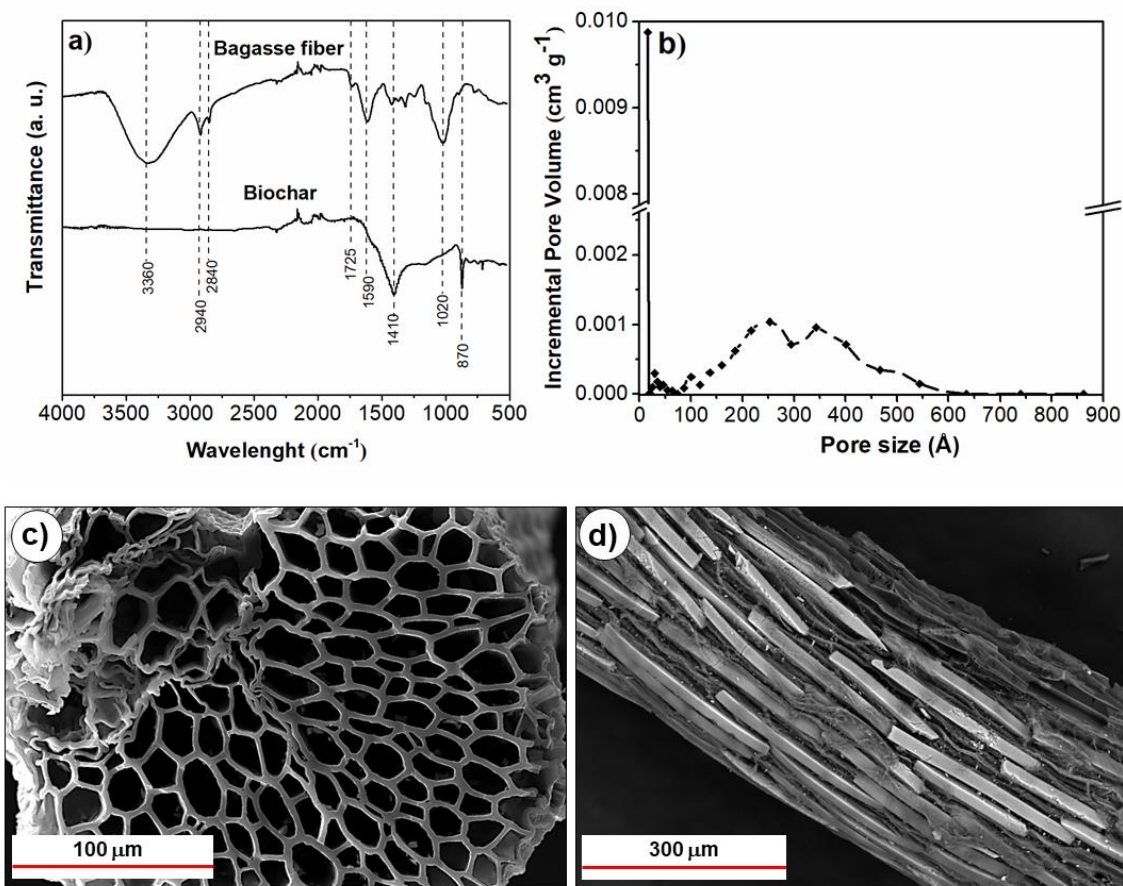
### 2.3.2. Substrate characterization and catalyst dispersion

It is accepted that the final properties of a carbon porous material depend essentially on the composition and morphology of the precursor. As stated above, agave bagasse is a lignocellulosic waste material from the tequila and mescal industry, and this does not have any commercial use [129]. The chemical composition of raw bagasse fibers and biochar is shown in the ATR-FTIR spectra (Fig. 2.1a). The characteristic absorption bands in the bagasse fiber sample indicated the presence of protonated carboxyl groups or ester groups around  $1725 \text{ cm}^{-1}$ , alkyl chains ( $-\text{CH}_2$  and  $-\text{CH}_3$ ) between  $2940 - 2840 \text{ cm}^{-1}$ , and  $-\text{OH}$  groups at  $3360 \text{ cm}^{-1}$ . Bands at  $1410$  and  $1020 \text{ cm}^{-1}$  correspond to vibrations of C-O and O-H, from acidic groups of aliphatic and phenolic structures, respectively, and also band at  $1590 \text{ cm}^{-1}$  correspond to vibration of C-C. These bands are related to the cyclic structures of cellulose or lignin molecules [117]. After carbonizing bagasse fibers, the absorption bands spectra show a loss in the signal intensity of most functional groups. The main difference is the removal of the wide absorption band at the range of  $3200\text{-}3600 \text{ cm}^{-1}$ , corresponding to the O-H stretching mode because of the removal of hydroxyl groups from cellulose and





hemicellulose structures. This result suggests the development of basal planes of graphitic-like layers by the graphitization of carbon condensed during the carbonization process.

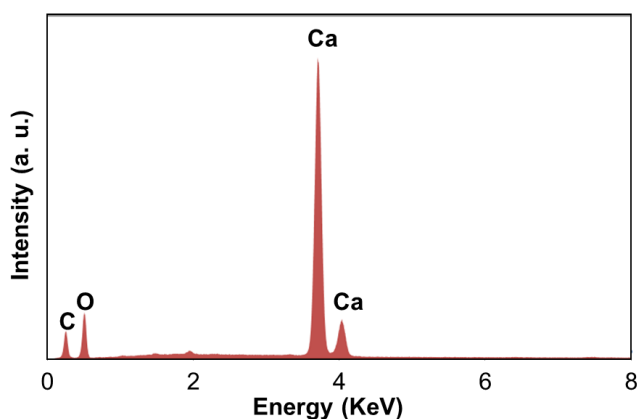


**Fig. 2.1** - (a) FTIR spectra of raw bagasse fibers and biochar, (b) Distribution of incremental pore volume of biochar. SEM secondary electrons images of (c) cross and (d) longitudinal section of biochar.

The raw bagasse fibers do not exhibit any particular porous structure. However, pyrolysis under inert atmosphere causes the thermal decomposition of the raw material by removing cellulose and hemicellulose structures that are thermally unstable above 600 °C [116], leading to a carbon skeleton with a wide pore structure inside the material (Fig. 2.1b). In contrast, other non-lignocellulosic raw precursors such as activated carbons and polymeric carbon fibers need a second thermal treatment to further develop porosity [34]. The pores

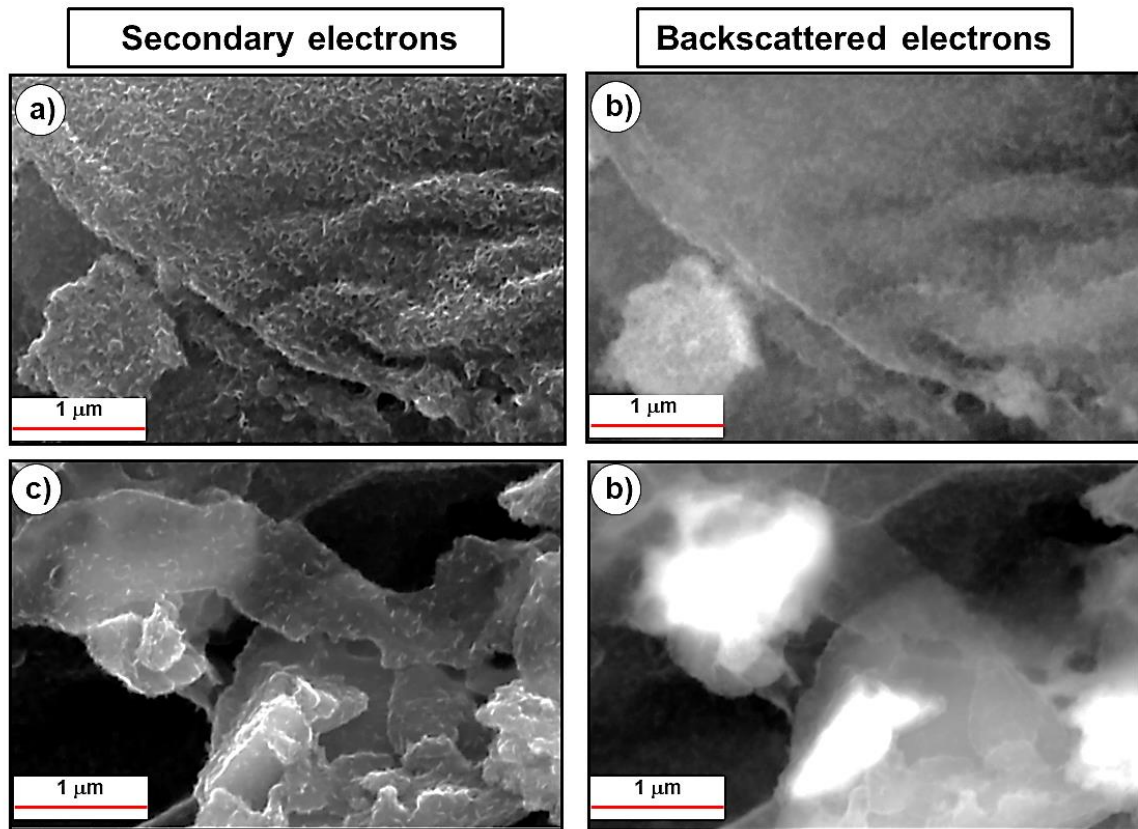


generated after the carbonization process form an arrangement of parallel channels along the fiber with diameters between 2 to 15  $\mu\text{m}$  (Fig. 2.1c). This porous structure is ideal for adsorption applications since the pore channels could enhance the mass transport of organic molecules in a gas stream [30]. Moreover, the periphery of the carbonized fibers was constituted of large rods with an average length of 250  $\mu\text{m}$  (Fig. 2.1d). EDS analysis shows that these rods are composed of calcium (Fig. 2.2). It is important to point out that these calcium rods come from calcium oxalates minerals, present in lignocellulosic materials that provide rigidity and hardness to the plant [130].



**Fig. 2.2** - EDS analysis on longitudinal surface of biochar.

In order to observe the distribution of catalyst particles by the effect of CMC, at different iron concentrations, the catalyst impregnated biochar was analyzed by scanning electron microscopy. SEM images show the samples after been thermally treated at 700  $^{\circ}\text{C}$  to simulate the arrangement of the catalyst just before the CVD process. Here, it is important to highlight that previous to the thermal treatment, the catalyst is covered by CMC (Fig. 2.3), although the catalyst particles were exposed during the thermal treatment.

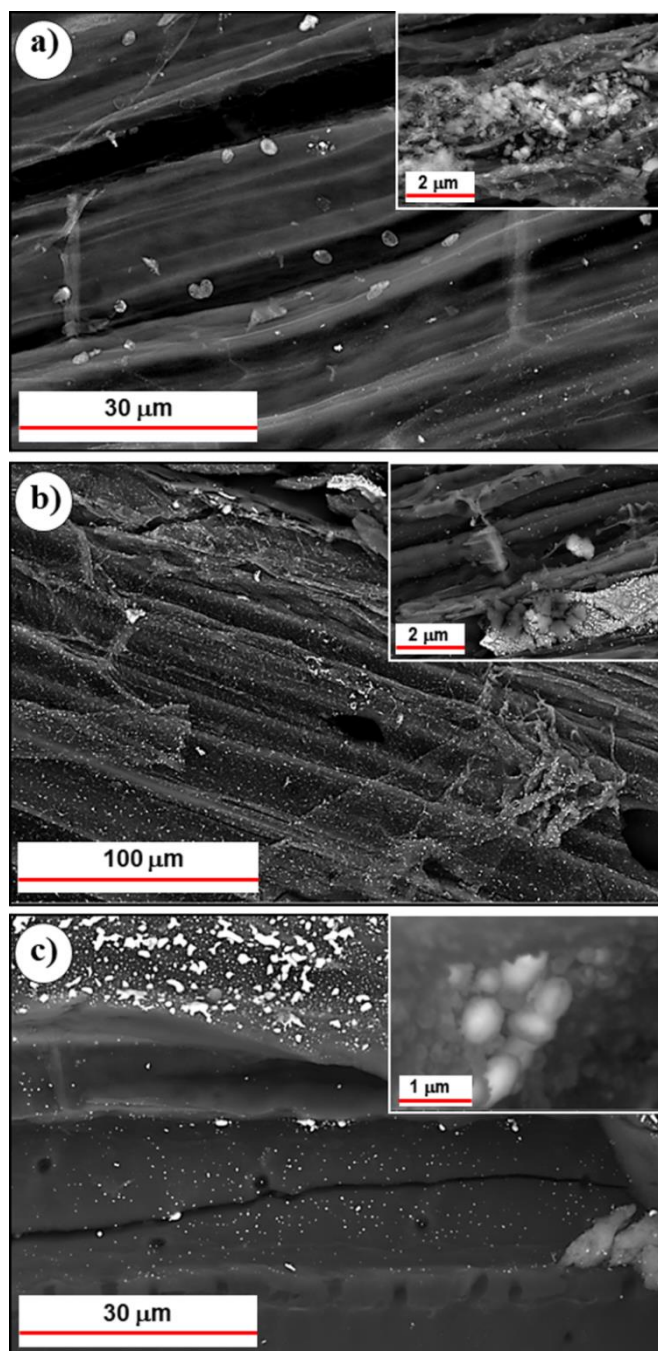


**Fig. 2.3** - SEM a) secondary electrons and b) backscattered electrons images of catalyst impregnated biochar covered with CMC.

The catalyst arrangement is important because its homogeneous distribution can control the dispersibility of carbon nanostructures, while at a smaller particle size of the catalyst its catalytic activity increases [79]. It was found that the iron concentrations of  $1 \text{ g Fe L}^{-1}$  allowed to obtain the most homogeneous catalyst dispersion on biochar, without agglomerates formation. The backscattered electrons images showed this homogeneous distribution of catalyst on biochar like white spots (Fig. 2.4). Furthermore, the catalyst presented strong affinity for the calcium rods, because of the interaction between hydroxyl groups of both calcium mineral and iron oxide that can form hydroxide ligand bridges. On the other hand, backscattered electron images showed brighter quasi-spheres shapes with higher atomic number, suggesting that these particles are principally composed of iron, while less bright



shapes with a lowest atomic number could be composed of carbon from biochar or CMC as can be observed in the inset of Fig. 2.4c.



**Fig. 2.4** - (a-c) SEM backscattered electrons images of biochar impregnated with three iron concentrations treated at 700 °C: (a) 0.1, (b) 1 and (c) 10 g L<sup>-1</sup>, simulating the catalyst performance before CVD process. The insert in (a) and (b) shows the interaction of iron with calcium rods, and (c) shows the iron particles covered with condensed carbon.



### 2.3.3. Carbon nanostructures morphology over carbonized fibers

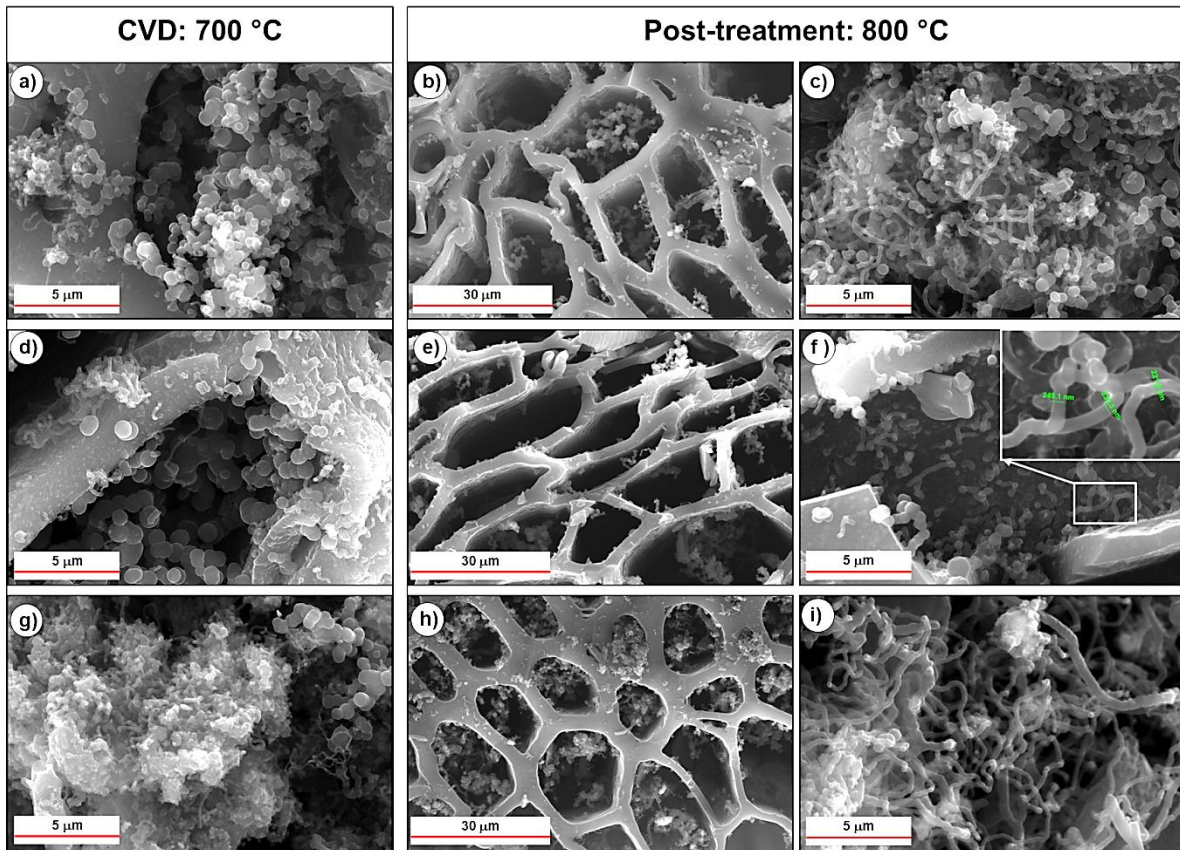
Morphological changes of biochar were analyzed by scanning electron microscopy (SEM) to corroborate the effect of CVD and thermal post-treatment on the structure and distribution of carbon nanostructures. The SEM observations after the CVD process during 300 s displays a high fraction of carbon nanostructures that cover the surface and inside channels of biochar (Fig. 2.5a, d, g). It is important to highlight that CVD induced the formation of CNSs, mainly, and CNTs onto biochar. These labels were assigned based on morphological similarity with other carbon nanostructures previously reported [61], [83], [119]. The CNSs reported herein, have a predominant arrangement of a bunch of grapes-like structures. This particular morphology has been previously reported as well in the study on hydrothermal decomposition of eucalyptus sawdust [131]. Indeed, it has been reported that during the production of the so-called hydrochar from lignocellulosic raw material, the growth of microspheres as a consequence of saccharides decomposition was preferentially promoted [132]. Additionally, it was found that carbon spheres with a diameter of 300 - 500 nm covered the surface of activated carbon during the thermal decomposing of a high concentration of glucose [133]. It was also described that saccharides macromolecules could decompose into various free radicals, including CHO, at elevated temperatures, which promote the formation of spherical amorphous carbon. All mentioned above finds are in a good concordance with the experimental results of the present work, where prior to C<sub>2</sub>H<sub>2</sub> supply, the CMC could be the precursor of the CNSs formation due to the decomposition/dehydration of the oligosaccharides or monosaccharides, as reported by Sevilla and Fuertes [132].

The thermal post-treatment at 800 °C certainly clear channel entrances of the CVD treated biochar. Two main features were distinguished herein. The most important is that the channels of biochar were apparently clean up to some extend by the removal of CNSs





(Fig 2.5b, e, h). The other feature is that the surface of the biochar was found to be more homogeneously covered with CNTs, with the higher covering density of CNTs in comparison to the samples processed by CVD-only (Fig 3c, f, i). Regardless of the iron concentration, the samples exhibit similar morphologies.

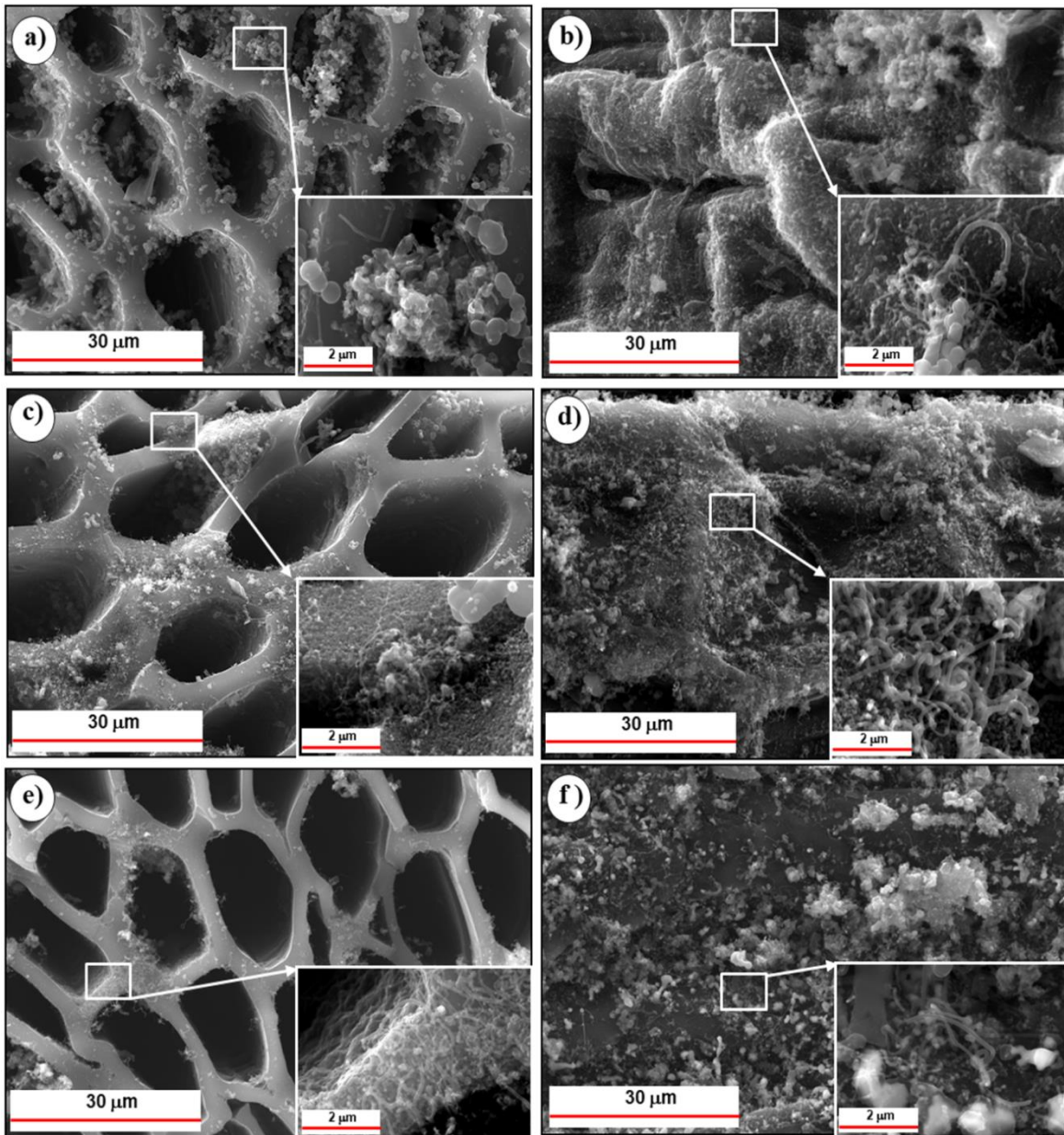


**Fig. 2.5** - SEM secondary electrons images of carbon nanostructures grown on biochar by CVD during 300 s, using three iron concentration: (a,b,c) 0.1, (d,e,f) 1, (g, h, i) 10 g L<sup>-1</sup>. A comparison between samples obtained after CVD process at 700 °C and after thermal post-treatment at 800 °C is made.

In order to obtain a better dispersion of carbon nanomaterials and avoid their agglomeration over the entire surface of biochar, the CVD time was reduced to 60 s. The surface morphologies did not show a significant change after thermal post-treatment in comparison with those of CVD-only. SEM secondary electrons analysis of these samples showed the growth of CNSs with analogous morphologies to those obtained by CVD for 300



s, although their length and diameter are shorter due to a lower carbon supply concentration, as seen in Fig. 2.6. SEM secondary electrons images of modified biochar taken crosswise (Fig. 2.6a, c, e) and longitudinally (Fig. 2.6b, d, f) revealed consistent and uniform growth of carbon nanostructures, being observable even at low magnification. At an iron concentration of  $0.1 \text{ g L}^{-1}$ , CNSs and a few carbon morphologies with irregular shapes are the predominant structures, with the presence of curved CNTs. The micrographs of this sample clarify that the carbon formed by CMC decomposition, condensed on biochar to promote the growth of CNSs due to low surface concentration of catalysts. Unlike, at higher iron concentrations ( $1$  and  $10 \text{ g L}^{-1}$ ) CNTs covered a major surface of biochar, stimulated by the well-dispersed catalyst onto the biochar surfaces (see Fig. 2.4). In addition, the growth of these CNTs on carbonized fibers is mainly curved. This behavior could be a consequence of diverse aromatic molecules such as 1,2,4-benzenetriol, and furfural-like compounds from the CMC decomposition [131]. The oxygen atoms presented in such aromatic compound during the CVD synthesis could bended the structure of CNTs [80]. Considering that the temperatures at which the biochar was treated overlap their thermal stability reported by TGA data [134], it was expected a substantial degradation and/or degasification of biochar. However, herein the porous structure and physical integrity of the biochar was preserved at  $800 \text{ }^\circ\text{C}$ , likely due to a carbon coating that could reinforce the biochar and improve their thermal stability (see inset in Fig. 2.6c).



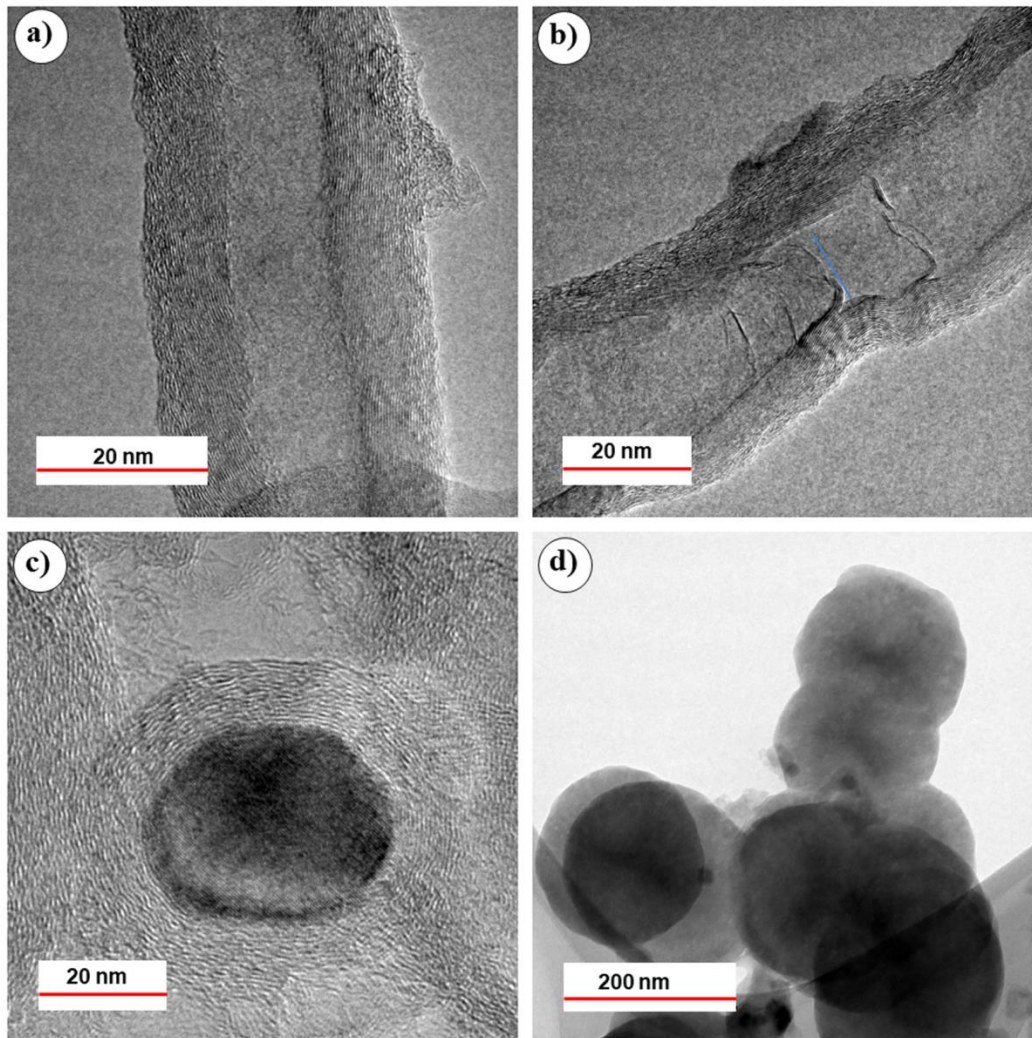
**Fig. 2.6** - SEM secondary electrons images of carbon nanostructures grown on biochar by CVD process during 60 s, using thermal post-treatment at 800 °C with three iron concentrations: (a, b) 0.1, (c, d) 1, (e, f, i) 10 g L<sup>-1</sup>. The insets are the corresponding SEM images under high magnification.

More detailed information about the morphology of the carbon nanostructures on biochar by CVD process, at 60 s, was obtained from transmission electron microscopy (TEM). After examining TEM images, it was found that the majority of CNSs was composed of carbon black (Fig. 2.7d), although a small proportion of these CNSs have a similar morphology to





the so-called onion-like carbons (Fig. 2.7c). In addition, the majority of CNTs displayed a bamboo-like morphology. The bamboo-like structure of CNTs exhibits thin compartment layers (Fig. 2.7b) [135]. The found outer diameter of CNTs is in a range of 30-100 nm, while the inner diameter and wall thickness are of about 12 nm and 10 nm, respectively.



**Fig. 2.7** - Representative TEM images of different carbon nanostructures: (a, b) CNTs, (c) onion-like carbon, and (d) carbon black, grown on biochar using an iron concentration of  $1 \text{ g L}^{-1}$  by CVD during 60 s at  $700 \text{ }^\circ\text{C}$ , and post-thermal treatment at  $800 \text{ }^\circ\text{C}$ .

To understand the effect of the heteroatoms such as nitrogen and oxygen on the morphologies of CNTs and CNSs obtained in this work, we analyzed the elemental composition of biochar with and without catalyst (Table 2.1). First, biochar analysis showed



the presence of nitrogen that is attributed to the precursor, bagasse agave, which contains nitrogen originated from inorganic (nitrate and/or ammonium ions) and organic (proteins). As it is well known, nitrogen atoms are incorporated into CNTs mainly in pyridine-like and graphite-like nitrogen ways in all cases [136]. Moreover, nitrogen doping in the pyridine-like nitrogen sites plays a key role in the interlinked compartments generated during the growth of bamboo-like CNTs [137], which agrees with the TEM images reported herein. In addition, the presence of oxygen in carbonized fibers come from the functionalities mainly presented in the periphery of basal planes, while the thermally treated impregnated biochar show the increased in the oxygen content since the thermal decomposition of CMC could induce the formation of turbostratic carbon with reactive oxygen functionalities. Based on the previous images shown in the inset of Fig. 2.4, it is proposed that once the oxygen associated with a carbon source from CMC condensed on catalyst during the heating process (previous to CVD), the formation of onion-like carbon takes place because temperatures below 700 °C are not enough to drive the growth of CNTs. These onion-like carbons have a closed quasi-spheres shape with a mean size of 30 nm and consist of several graphene-like shells enclosed one into another (Fig 2.7c). Nevertheless, the carbon condensed on biochar surface, catalyst free, stimulates the growth of carbon black (Fig. 2.7d), where the decomposition of CMC also produces oxidized aromatic molecules that condense like turbostratic carbon [132].

**Table 2.1** - Elemental analysis of the carbon substrate with and without catalyst.

ID Sample	%C	%N	%H	%O <sup>+</sup>	%Fe	%Ca
Biochar	54.9	9	7.9	23.2	0.03	0.5
BC-ZVI/CMC*	55.9	4	2.3	32.1	0.65	0.4

\*Biochar modified with zero-valent iron/CMC, and treated at 700 °C in N<sub>2</sub> atmosphere.

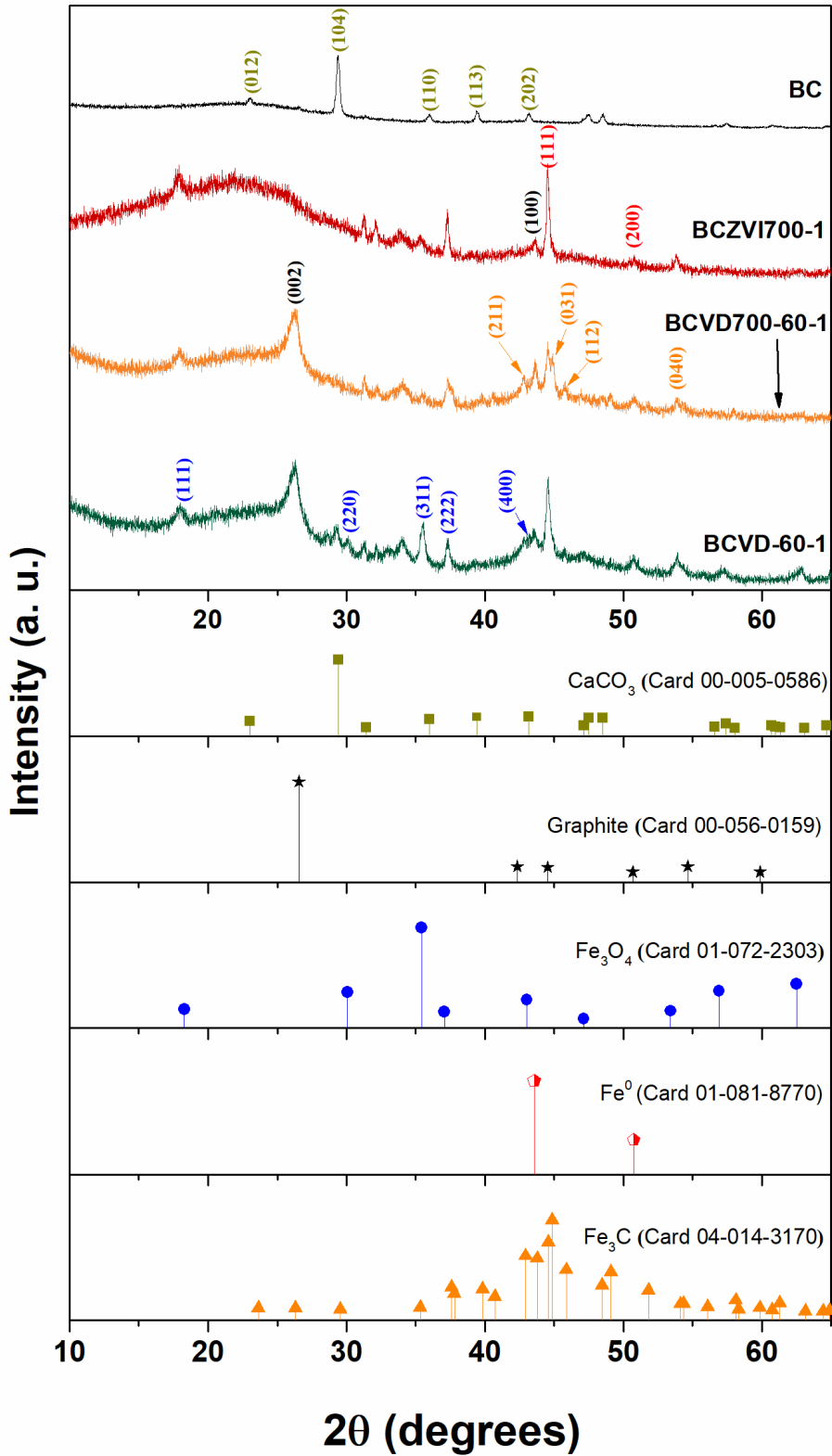
\*value obtained by difference.



#### 2.3.4. Structural characterization

The samples analyzed in the subsequent sections are labeled as follows: BC, biochar; BFZVI700-1, biochar with 1 g Fe L<sup>-1</sup> thermally treated to 700°C; BCVD700-60-1, biochar with 1 g Fe L<sup>-1</sup> induced to CVD at 700°C during 60 s; and BCVD-60-1, biochar with 1 g Fe L<sup>-1</sup> induced to CVD at 700°C during 60 s and thermally post-treated at 800 °C.

The X-ray diffraction (XRD) patterns of the synthesized materials are displayed in Fig. 2.8. The diffraction peaks of the sample BC are mainly assigned to calcium carbonate (ICDD-PDF Card 00-005-0586), matching with the calcium rods previously observed (see Fig. 2.1). The diffraction pattern of the sample BCZVI700-1 exhibits a characteristic wide band located at 2θ interval of 22-30°. The broadening of this peak suggests the low graphitization degree and the presence of amorphous carbon [63]. This last one behavior was also observed in both diffractograms BCVD700-60-1 and BCVD-60-1, in addition to the appearance of diffraction peaks at 2θ values of 26° and 43° (ICDD-PDF Card 00-056-0159), attributed to the (002) and (100) planes in crystalline graphitic structure, respectively. After CVD process, the sharp and highly intense peak at 26° indicates the formation of crystalline carbon from nanostructures on biochar. Additional diffraction peaks were observed for all the modified biochar at 2θ values of 43, 50 and 74° for iron (ICDD-PDF Card 01-081-8770); 37, 44, 45 and 46° for iron carbide (ICDD-PDF Card 01-074-3854); and 30, 35, 56 and 62° for magnetite (ICDD-PDF Card 01-072-2303). The iron species on biochar such as iron and magnetite reacted with the carbon atoms originated from the decomposition of C<sub>2</sub>H<sub>2</sub> and/or CMC, to form metastable iron carbides [80], which mainly allow the growth of CNTs and CNOs.



**Fig. 2.8** - X-ray diffraction patterns (from up to bottom) of the samples BC, BCZVI700-1, BCVD700-60-1 and BCVD-60-1 with a step size of 0.01° 2θ at 10 sec per step. All four diffraction patterns were collected on the same day.

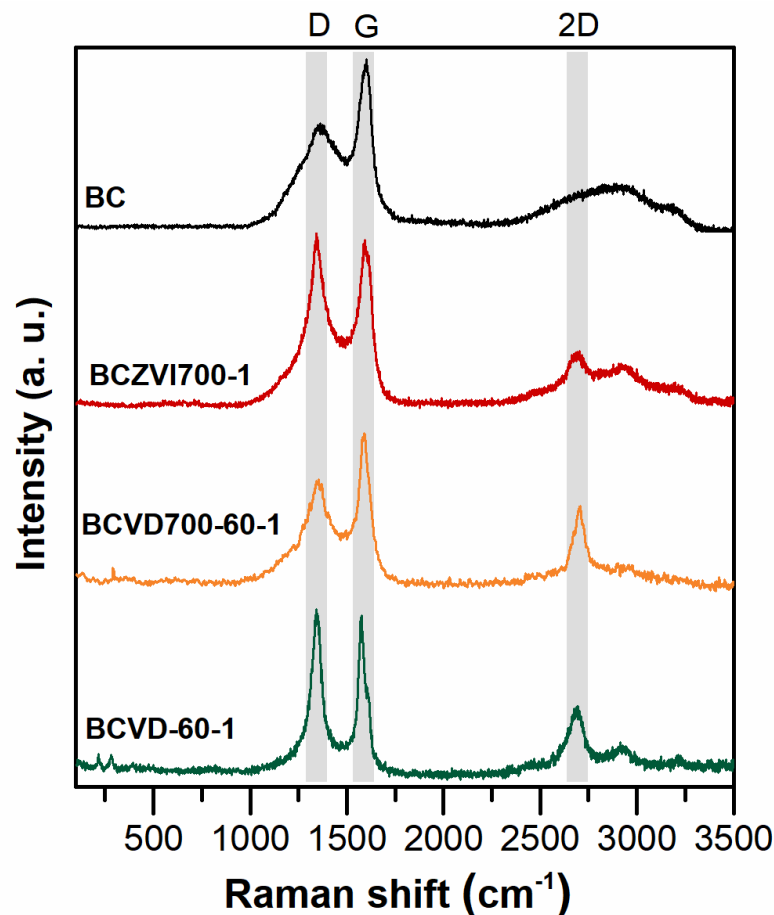


Further structural details were obtained by Raman spectroscopy. For the studied samples, the characteristic D, G and 2D bands in the region between 1000 and 3000  $\text{cm}^{-1}$  provide the most valuable information on the structural change of carbon materials (Fig. 2.9). The first two bands correspond to one-phonon process (the first-order Raman spectra): the G band at about 1580  $\text{cm}^{-1}$  come from the carbon atoms vibration in  $\text{sp}^2$ -hybridized carbon network resulting from defect-free graphitic domains (in-plane  $\text{E}_{2g}$  mode); and D band at about 1340  $\text{cm}^{-1}$  is associated to the breathing mode  $\text{A}_{1g}$  of the hexagonal carbon ring with defects such as vacancies, oxygenated groups,  $\text{sp}^3$ -hybridized carbons, foreign atoms and finite-size effects [138]. In curved carbon structures, like CNTs and CNSs, the D band is always present [139]. In the second-order Raman spectra, the 2D band at about 2700  $\text{cm}^{-1}$ , attributed to the overtone of the D band, is active for graphite crystals through the double resonance process involving phonons with opposite wave vectors, but unlike to D band, it is not activated by the proximate to defects [140].

In addition to SEM analysis, Raman spectroscopy allows analyzing the structural carbon transformation through the entire process to obtain a variety of carbon nanostructures. To clearly reveal the differences among the Raman spectra of the samples, the spectra were scaled up to have a similar intensity of the G peak. The spectra of the biochar (BC) showed broad peaks at the first-order spectra, indicating a rather low degree of ordering of the graphitic structures; similar features are reported for activated carbon and graphene oxide [141]. Several differences are clearly observed in the Raman spectra of the processed samples shown herein (BCZVI700-1, BCVD700-60-1, and BCVD-60-1). First, an evident increase in intensity of the D band for the sample BCZVI700-1 is observed. This band correspond to the presence of defects or disordered carbon formed by the decomposition of CMC into domains formed by  $\text{sp}^2$  hybridized carbon, and confined by  $\text{sp}^3$  hybridized bonds, with the dimensions comparable to polycyclic aromatic hydrocarbons [120]. The increase in



the G band after CVD (sample BCVD700-60-1) is well explained by the growth of carbon nanostructures mainly constituted of  $sp^2$  hybridized carbon atoms, although with the contribution of  $sp^3$ -hybridized carbon. The broad band presented between D and G bands could be a consequence of hidden additional peaks at 1180, 1500, and 1620  $cm^{-1}$ , which are related to impurities, amorphous carbon, and disordered carbon, respectively [142]. The presence of the five- and seven-membered carbon rings is expected in the region of high local curvature of carbon nanostructures, and also can explain the existence of these hidden peaks [138].



**Fig. 2.9** - Raman spectra (from up to bottom) of biochar (BC), catalyst impregnate biochar thermally treated-only at 700 °C (BCZVI700-1), biochar processed to CVD (BCVD700-60-1), and biochar processed to CVD and thermally post-treated at 800 °C (BCVD-60-1). The modified samples were evaluated at the same iron concentration ( $1 g L^{-1}$ ).



Furthermore, when the thermal post-treatment at 800 °C was applied to the carbon nanostructures (sample BCVD-60-1) an evident increase in the D band was observed. The relatively high intensity of the D band is the clear consequences of the curly morphology of formed CNTs. The obtained Raman spectra is similar to those reported for multi-walled CNTs with bamboo-like structure, caused by the defects and disorder induced by nitrogen doping [136]. The multi-walled CNTs also show a Raman pattern similar to char and carbon black [143]. In addition, it is observed a growth in the sharpness of the D and G bands, and a decrease of the hidden signals of amorphous carbon mentioned above. This last one is the most significant feature of the temperature-induced changes in the Raman spectra of CNSs, showing a strong reduction of the amorphous carbon [138], being consistent with our results of microscopy. The latter becomes more evident when the transitions of the 2D band are compared between samples. As seen on Fig. 2.9, the presence of broad D and G bands, in combination with the absence of 2D band for biochar, reveals their amorphous characteristics. The fact that the 2D band emerged from the processed samples spectra, can be taken as a clear indicator of a presence of a high content of graphitic structure due to the creation of few-layers graphene [120]. The 2D band in multilayer graphene has a strong dependence on the number of layers, where a sharper single 2D band is related to a lower number of layers [143]. In this sense, the presence of the single peak close to 2700  $\text{cm}^{-1}$ , shown for the biochar modified by CVD (sample BCVD700-60-1), is consistent with the morphologies of CNTs and onions-like carbon observed in TEM images. Moreover, after thermal post-treatment (sample BCVD-60-1), a new peak emerged at 2900  $\text{cm}^{-1}$  suggesting a phase transformation that could cause a volume expansion mainly of onion-like carbon. The increase in temperature removes oxygen surface functionalities, leading to the emergence of CO and CO<sub>2</sub> gases. Pyrolysis of functional groups causes the formation of dangling bonds on carbon atoms, which can be reconstructed and combined to form  $\pi$ -bonds, followed by the continuous graphitization from the outside to the inside of the





particles [61]. In addition, the carbon nanostructures expansion attributed to the higher lattice spacing of  $sp^2$  graphite-like carbon (0.35 nm), compared to  $sp^3$  defective shells (0.34 nm), leads to a decrease in particles density and a therefore an increase in surface area as is seen in the next section.

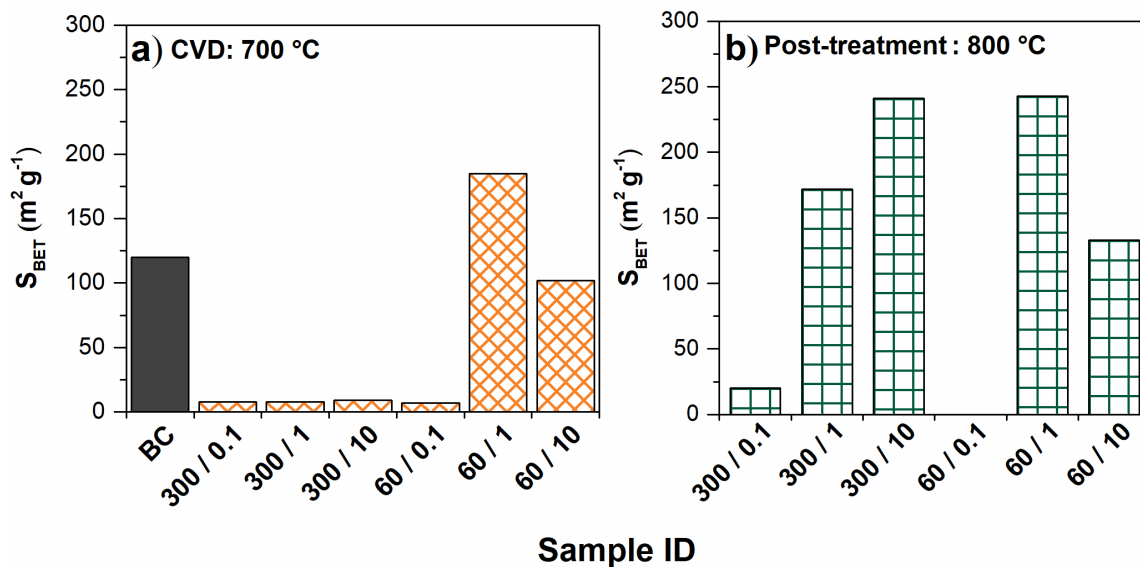
### 2.3.5. Surface area analysis

As stated above, biochar exhibits an arrangement of parallel channels developed after agave bagasse carbonization. This structure appears to be ideal for adsorption processes. The surface area of the carbonized fibers before and after the CVD process, as well as after the thermal post-treatment at 800°C, is reported in Fig. 2.10. Even though the surface area of the biochar is 120 m<sup>2</sup> g<sup>-1</sup>, it is necessary to increase the exposed surface area in order to obtain an adsorbent material that can be competitive with the adsorption capacity of commercial granular activated carbons that have a high surface area (250 – 900 m<sup>2</sup> g<sup>-1</sup>) [144]. Considering the importance of increasing the exposed surface area of biochar, it is relevant to establish the procedure conditions that will help to develop a higher surface area. In this sense, a thermal post-treatment was implemented to improve the surface area of modified biochar, since the CVD process compromises its surface area. It was found that the surface area of biochar was reduced when the CVD time was higher than 60 s. For instance, at a CVD time of 300 s the surface area of the biochar decreased from 120 to around 5 m<sup>2</sup> g<sup>-1</sup>. Nevertheless, the thermal post-treatment allows increasing the surface area, even doubling the initial value of biochar, as it is the case for the samples that undergo a CVD process under the following conditions: 300 s/10 g Fe L<sup>-1</sup> and 60 s/1 g Fe L<sup>-1</sup>. Due to the high temperatures of the thermal post-treatment (800 °C), the increase in surface area can be an effect of both the amorphous carbon removal and a carbon nanostructures rearrangement [145]. In addition, the surface area is not drastically modified by decreasing





the CVD time to 60 s at an iron concentration of 1 and 10 g L<sup>-1</sup>, and the post-treatment further improved the surface area values to 243 and 133 m<sup>2</sup> g<sup>-1</sup>, respectively.



**Fig. 2.10** - Surface area evolution of the synthesized materials after a) CVD and b) thermal post-treatment at 800 °C. The modified samples are identified by their CVD temperature / iron concentration (g Fe/L), i.e. 300/0.1.

The surface area readily available in these modified materials could be advantageous for VOCs removal in comparison with the higher surface area of a commercial activated carbon because the nanostructures provide an exposed reactive area in the channels of carbonized fibers in comparison to the poorly accessible micropores in the activated carbon. For this reason, the pore volume and surface area of modified biochar (BCVD-60-1 sample) were analyzed to understand the influence of nanostructures growth on the macroporous structure of biochar (Table 2.2). In addition, commercial activated carbon (bituminous F-400) was also analyzed by nitrogen physisorption to evaluate the effect of microporosity on benzene adsorption kinetic performance. Overall, biochar has a reduced pore volume, mainly in the mesopores range, and on the other hand, nanostructures improve the modified biochar surface area, presumably by the exposed surface area mainly granted by CNTs. In addition to these findings, CNTs also contribute to an increase in macropore volume, which

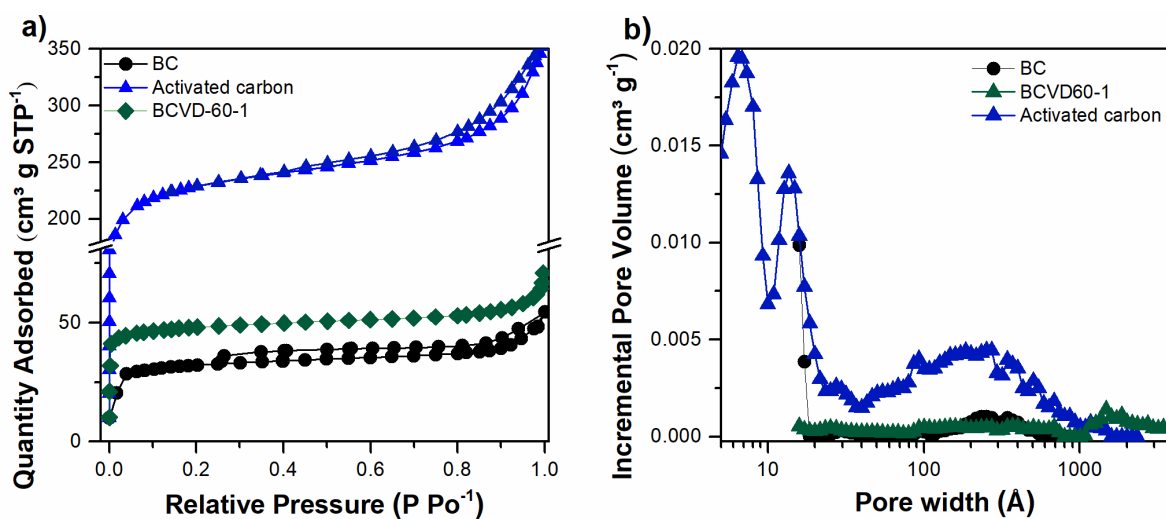


results in both higher benzene adsorption capacity and fast kinetics. In contrast, the high microporosity of activated carbon involves a restricted surface area, which makes it difficult for gas to diffusion in adsorption applications at atmospheric pressure. The corresponding  $N_2$  adsorption-desorption isotherms and incremental pore volume of these samples are displayed in Fig. 2.11.

**Table 2.2** - Textural properties of adsorbent materials tested in adsorption experiments.

Materials	$S_{BET}$ ( $m^2 g^{-1}$ )	$V_{total}$ ( $cm^3 g^{-1}$ )	$V_{micro}$ ( $cm^3 g^{-1}$ )	$V_{meso}$ ( $cm^3 g^{-1}$ )	$V_{macro}$ ( $cm^3 g^{-1}$ )
Activated carbon F-400	776	0.416	0.270	0.131	0.015
Biochar	120	0.056	0.041	0.015	N.D.
BCVD-60-1	243	0.088	0.059	0.016	0.013

N.D.: not detected



**Fig. 2.11** -  $N_2$  adsorption isotherms and incremental pore volume of adsorbent materials tested in benzene adsorption experiments.

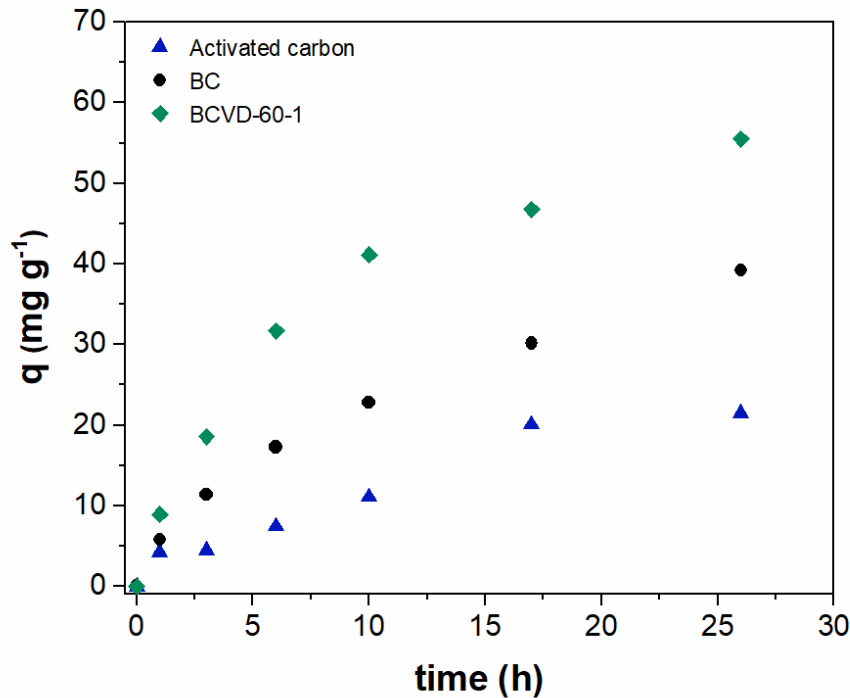


### 2.3.6. Benzene adsorption analysis

In order to implement these promising materials in automotive canisters, where more efficient and cost-effective adsorbent materials are needed, adsorption kinetics of a model VOC from gasoline emission was investigated. As is well known, fast adsorption rates are needed in regenerative adsorption/desorption processes that occurs in the evaporative emission control system of automotive canisters devices. A central point to evaluate in the adsorption kinetics studies was the time in which evaporative emissions from gasoline are emitted, about 24 h, known as diurnal losses. Additionally, the adsorption study of a model VOCs from gasoline emission was based on the static adsorption kinetics of benzene vapor at 25 °C and ~1 atm of barometric pressure. In the present work, the adsorption kinetics of a commercial bituminous activated carbon was compared with those of raw biochar and biochar containing carbon nanostructures (sample BCVD-60-1). The main reason to compare adsorption kinetics between activated carbon and these new adsorbents in diurnal conditions is to demonstrate that materials with a high exposed surface area and low tortuosity, such as biochar and sample BCVD-60-1, have a faster rate of adsorption than activated carbon, which is demanded in automotive canister. The adsorption study was based on the adsorbent mass change. In addition, it is important to highlight that adsorption experiment was carried out in triplicated, while standard deviations were not higher than 1.3. As shown in Fig. 2.12, sample BCVD-60-1 exhibits the fastest adsorption kinetics within the evaluated time interval of 0-26 h evaluated. At the lower times, 3-6 h, the result obtained is similar, which is relevant since in these time-lapse the so-called hot soak emissions also take place in automotive systems, which is the gasoline evaporated after turning off the vehicle. It was found that the benzene adsorption capacity of sample BCVD-60-1 during the first 3 h was 18.5 mg g<sup>-1</sup>, while the capacity of activated carbon and biochar was 4.5 and 11.4 mg g<sup>-1</sup>, respectively. As expected, the adsorption capacity of CVD treated biochar



increased after carbon nanostructures growth. For instance, the benzene uptake increased up to 90 % compared to biochar, and it is 1.5 times higher than that of activated carbon. In the first 6 h, the fastest adsorption rates of 0.0064, 0.0035 and 0.0013 mmol h<sup>-1</sup> were obtained for FCVD-60-1 sample, carbonized fibers, and granular activated carbon, respectively. As expected, these trends remained in the following 20 h, but the adsorption rates decreased. These values are consistent with the fact that the diffusion of benzene is only driven by its vapor pressure and its adsorption is carried out mainly on the most exposed area of the material during this short period of time. Therefore, although the surface area of activated carbon is higher (776 m<sup>2</sup> g<sup>-1</sup>), its adsorption kinetics at the time evaluated was lowest because its high microporosity limits the benzene diffusion. Besides, the abundant mesopores and macropores of the biochar and sample BCVD-60-1 have enhanced the benzene mass transport in short periods of time. In other words, benzene vapor can diffuse into pores easier, and the adsorption process is accomplished more quickly than in granular activated carbon, since the adsorbent tortuosity and pores size determine adsorption kinetics. Furthermore, it is considered that the sp<sup>2</sup> basal plane of carbon-based materials promotes a major affinity for benzene aromatic rings since these are mainly attached face-to-face by  $\pi$ - $\pi$  interactions [47, 119]. In addition, the higher adsorption capacity of the carbonized fibers containing carbon nanostructures could be attributed in part to the CNTs and onion-like carbon structures curvatures, which makes delocalized electrons of sp<sup>2</sup> hybridizations more reactive favoring benzene adsorption [47].



**Fig. 2.12** - Benzene adsorption kinetics in static mode at 25 °C and 0.06 atm of vapor pressure, using activated carbon, biochar, and BCVD-60-1 samples.

The experimental data of adsorption capacity of benzene as a function of time (Fig. 2.12) were fitted to the pseudo-first and pseudo-second order kinetic equations (Table 2.3). According to the calculated correlation coefficients ( $R^2 > 0.97$ ), the adsorption kinetics of biochar and BCVD-60-1 sample were better fitted by pseudo-second order reaction. Their rate constant of sorption ( $k_2$ ) was 0.001 and 0.002  $\text{mg}\cdot(\text{g}\cdot\text{min})^{-1}$ , respectively. While the pseudo-first and pseudo-second order reactions describe similarly the adsorption kinetics of activated carbon, with a  $R^2$  value close to 9.4 and a rate constant of sorption ( $k_2$ ) of 0.001  $\text{mg}\cdot(\text{g}\cdot\text{min})^{-1}$ . These results suggest that benzene vapor can diffuse and transport faster in BCVD-60-1 sample, and as a consequence the adsorption process is reached in a shorted period of time. This is because modified biochar exhibits high meso and macroporosity that enhance the mass transfers efficiency of benzene vapor [107].



**Table 2.3** - Kinetic constants for adsorption of benzene onto adsorbent materials.

Equation parameter	Activated carbon	Biochar	BCVD-60-1
<i>Pseudo first-order</i>			
$k_1$ ( $\text{min}^{-1}$ )	0.057	0.082	0.138
$q_e$ ( $\text{mg g}^{-1}$ )	28.87	42.71	54.91
$R^2$	0.948	0.976	0.989
SSE	15.28	18.30	16.98
<i>Pseudo second-order</i>			
$k_2$ ( $\text{g} \cdot (\text{mg} \cdot \text{min})^{-1}$ )	0.001	0.001	0.002
$q_e$ ( $\text{mg g}^{-1}$ )	44.96	59.11	70.80
$R^2$	0.946	0.984	0.994
SSE	15.86	11.93	8.725

$k_1$  = pseudo-first order rate constant.

$k_2$  = pseudo-second order rate constant.

$q_e$  = adsorption capacities at equilibrium.

$R^2$  = Determination coefficient.

SSE = Sum square errors.

Based on these results, short time adsorption kinetics showed the potential application of the modified biochar in automotive canisters, since these have higher adsorption capacity and kinetics than the commercial granular activated carbon. It is worth to note that many studies of static gas adsorption have evaluated only the maximum adsorption capacity, regardless of adsorption rates, because benzene adsorption kinetics in static method is considered slow for activated carbons; while the studies of adsorption kinetics have only been developed in dynamic mode, by passing a gas stream through a packed bed [108]. It is important to highlight that in a real operation the gasoline emissions are not driven by an external gas and time periods longer than 26 h are not needed because the adsorbent regeneration happens when the engine is started in this period of time.

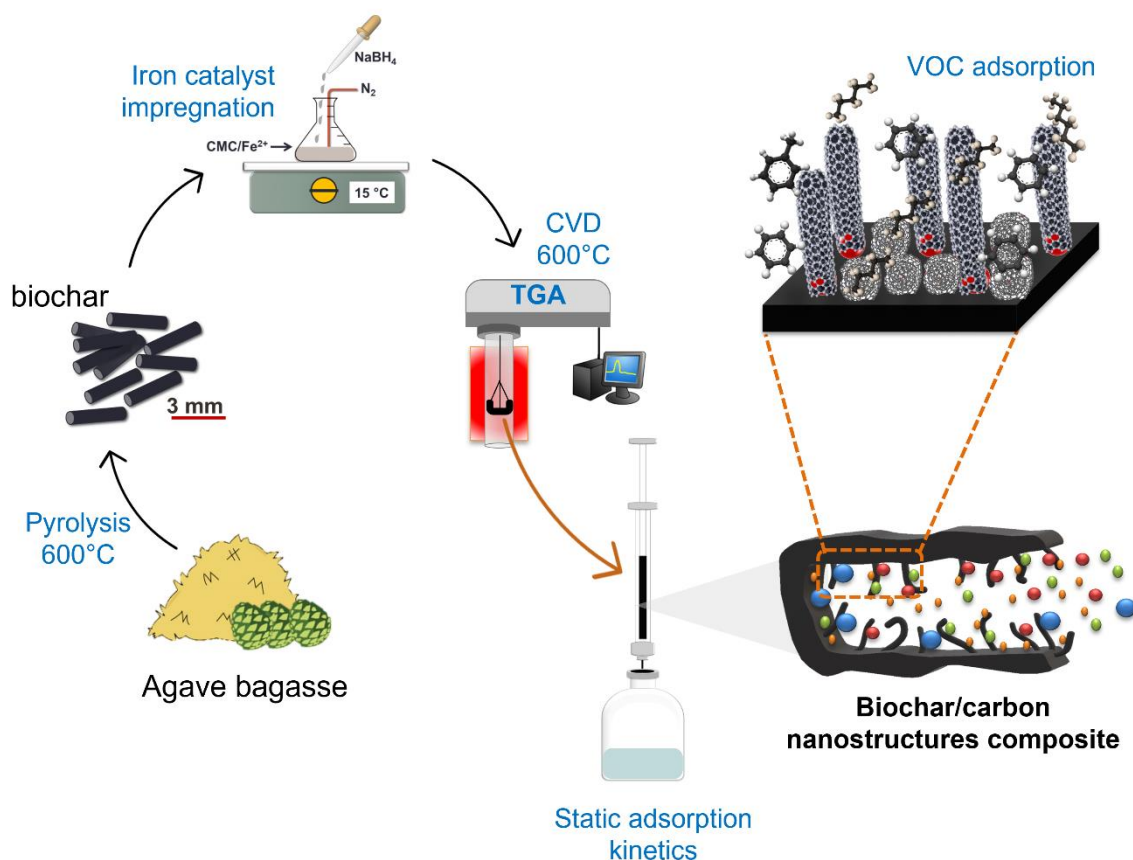


## 2.4. Conclusions

This work shows the growth of carbon nanostructures onto biochar, from waste agave bagasse, to be used as a potential porous adsorbent of VOCs. The CVD process in a thermogravimetric analyzer, as a furnace, successfully grows carbon nanomaterials, specifically CNTs, onions-like carbon and carbon black onto biochar. The nitrogen in biochar induces the formation of bamboo-like CNTs. In addition, the presence of CMC facilitates the effective control in size and dispersibility of catalysts on biochar, while its thermal decomposition yields turbostratic carbon with oxygen functionalities that promote the formation of onions-like carbon and carbon black. By using CVD during 60 s,  $1 \text{ g L}^{-1}$  of iron and  $700 \text{ }^{\circ}\text{C}$ , as optimum conditions, it is possible to obtain a high yield of homogeneously distributed carbon nanostructures onto biochar, which have the highest surface area ( $243 \text{ m}^2 \text{ g}^{-1}$ ) of the synthesized samples. However, when using CVD for more than 60 s the surface area of the biochar decreases to  $5 \text{ m}^2 \text{ g}^{-1}$ , but after thermal post-treatment at  $800 \text{ }^{\circ}\text{C}$  this increases to  $241 \text{ m}^2 \text{ g}^{-1}$ . The latter is mainly led by the removal of amorphous carbon. As indicated by adsorption kinetic, sample BCVD-60-1 shows the fastest benzene vapor removal with an adsorption rate of  $0.0064 \text{ mmol h}^{-1}$  in the first 6 h, overcoming 1.8 times that of a commercial activated carbon and removing 1.5 times more benzene with a maximum adsorption capacity of  $55.53 \text{ mg g}^{-1}$  at  $25 \text{ }^{\circ}\text{C}$  after 26 h, in a static adsorption system. Finally, this work shows the potential application of biochar containing carbon nanostructures for the removal of VOCs from gasoline emissions, which could replace commercial granular activated carbons used today in automotive canisters.

# CHAPTER 3

## Adsorption of aliphatic and aromatic VOCs by carbon nanostructures modified macroporous biochar in static conditions







### Abstract

The effectiveness of carbon canisters in removing volatile organic compounds from automotive gasoline emissions is highly dependent on the adsorbent available surface area as well as on its fast rate of adsorption. In this sense, aiming the production of a carbon adsorbent with faster VOCs adsorption kinetics than a commercial activated carbon, the exposed surface area on a macroporous biochar was enhanced by growing carbon nanostructures on its surface. The growth of carbon nanostructures was conducted by chemical vapor deposition, using a pulsed-injection system to improve the utility of carbon source throughout the overall process. All prepared adsorbents were characterized by TEM, SEM, XRD, Raman, contact angle, potentiometric titrations and  $N_2$  physisorption. Electron microscopy analysis displayed the growth of carbon nanotubes, carbon nanofibers, onion-like carbon, and carbon nanoribbons, with better dispersibility by using the CVD pulsed-injection mode. In addition, the growth of these carbon nanostructures improved textural properties by increasing the biochar surface area from 184 to 240  $m^2 g^{-1}$ , without developing micropores. Also, the increase in biochar basicity promoted the adsorption of nonpolar VOCs. The static adsorption behavior of pentane, hexane, benzene, and toluene was studied. The carbon composite (biochar/carbon nanostructures) exhibited higher adsorption capacity for all selected VOCs, 1.3-1.81 times more than biochar. Furthermore, this novel composite possessed a much higher benzene and toluene uptake (169 and 63  $mg g^{-1}$ , respectively), which increased up to 260% and 98%, respectively, compared with activated carbon, and also both adsorbents showed a similar removal capacity of aliphatic molecules. The positive linear correlation between surface area and adsorption capacities suggested a physical interaction as the most predominant adsorption mechanism. Considering these findings, the novel biochar/carbon nanostructures composite would be a potential alternative to activated carbon adsorbent for the recovery of gasoline vapors.



### 3.1. Introduction

Gasoline vapors emitted from a vehicle's fuel tank has long been recognized to be a serious source of atmospheric pollution, specifically in densely populated areas, and also results in significant economic losses [30]. This gasoline emissions, also known as evaporative emissions, mostly consists of volatile organic compounds (VOCs) [146]. Evaporative emissions occur as a consequence of the leakage of VOCs evaporated from gasoline by diurnal temperature differences [25]. Accordingly, US EPA demands that vehicles must be equipped with the evaporative emissions control system designed to store and dispose fuel vapors preventing them from escaping into the atmosphere [24].

Adsorption with activated carbon has been recognized as the preferred strategies for controlling evaporative emissions because it is highly effective and economical, especially for separating and recovering VOCs pollutants [107], [147]. However, serious diffusion restrictions by activated carbon micropores cause problems as pore blocking, hygroscopicity, and a low regeneration [13]. Therefore, non-microporous biochar adsorbents have been produced, especially from industrial wastes, to overcome VOCs mass transfer restrictions, in addition to reduce adsorbents production cost and to control the accumulation of waste materials in environment [7], [29]. Numerous research studies have shown that the adsorption performance of biochar can be significantly improved after physical or chemical modifications [39]. Recently, we synthesized a novel macroporous biochar from waste agave bagasse to improve the kinetics adsorption of benzene, a VOC representative of evaporative emissions [42]. Despite the moderate surface area of this biochar ( $120 \text{ m}^2 \text{ g}^{-1}$ ), the benzene uptake was 90% more than that of a bituminous activated carbon. In addition, the growth of carbon nanostructures onto the biochar surface allowed to improve 1.5 times the benzene uptake. This novel adsorbent has emerged as a potential alternative to commercial activated carbon due to its exposed adsorptive surface, and fast adsorption performance.



By using the chemical vapor deposition (CVD) process, it was possible to growth different carbon nanostructures such as carbon nanotubes (CNTs) and onion-like carbon (ONC) onto biochar, doubling the biochar surface area ( $243 \text{ m}^2 \text{ g}^{-1}$ ) [42]. Despite using short synthesis time ( $<5 \text{ min}$ ), one of the potential problems associated with CVD on heterogeneous substrates is the condensation of amorphous carbon, which is not beneficial for organic compounds removal. Indeed, amorphous carbon condensation is commonly observed in homogeneous catalyst-substrate surfaces by using high time CVD synthesis ( $>30 \text{ min}$ ) [83]. Thus, preventing the growth of amorphous carbon to a greater extent on biochar is of main concern when this adsorbent composite is intended to be used for evaporative emissions adsorption. In this sense, it is of significant advantage to control the carbon precursor condensation in such a way that provides mostly uniform deposition over large areas, good coverage, and selective deposition on catalyst [148]. Meanwhile, some works have tried to control the surface reaction of the carbon precursor with the substrate-catalyst surface by slowing down the flow rate of carbon source or by diluting it with an inert gas [83], other interesting attempts have also been made to explore the possibility of using pulsed-injection of the carbon source [149]. The CVD pulsed-injection technique has the possibility to produce and control the nanostructures composition, microstructures, and morphology, through a suitable choice of the substrate, precursor, and reactant, as well as deposition conditions. Purging of the reaction chamber between the pulses removes all excess byproducts and enhance catalyst-carbon source reaction [150]. To the best of our knowledge, there is currently few information available in the literature concerning to the CVD pulsed-injection synthesis by using heterogeneous carbon substrates. Therefore, an effort has been made to take advantage of the greatest amount of carbon sources during the CVD process by using this strategy, in addition to taking advantage of its physical and chemical properties for the removal of evaporative emissions.



Motivated by the above discussion, the present study reported the preparation of biochar/carbon nanostructures composite by evaluating the CVD pulsed-injection strategy, aiming, and creating carbon adsorbents with a larger exposed surface area for the adsorption of VOCs representatives of evaporative emissions. The adsorption performances of pentane, hexane, benzene, and toluene by unmodified and modified biochar were compared with a commercial activated carbon (F-400), including adsorption kinetics and adsorption mechanisms. The experimental kinetics data were correlated with pseudo-first and -second order models. Moreover, various analytical techniques were employed to study the morphology and surface properties of adsorbents, while the correlation between adsorbent properties and VOCs performance was evaluated.

### **3.2. Experimental procedure**

#### **3.2.1. Reagents**

All the chemicals used in this research (HCl, NaBH<sub>4</sub>, FeSO<sub>4</sub>·7H<sub>2</sub>O, C<sub>2</sub>H<sub>2</sub>, C<sub>5</sub>H<sub>12</sub>, C<sub>6</sub>H<sub>14</sub>, C<sub>6</sub>H<sub>6</sub>, C<sub>7</sub>H<sub>9</sub> and sodium carboxymethylcellulose (CMC)) were reagent grade. Deionized water (R ~ 18 MΩ·cm) was used for the preparation of solution. Biochar was previously obtained by the pyrolysis of agave bagasse fibers (from *Agave salmiana* plant) at 600 °C under N<sub>2</sub> atmosphere as it was reported by Gutiérrez-Martínez et al., [42]. The commercial bituminous based granular activated carbon Filtrasorb 400 from Calgon was selected as adsorbent for this study.

#### **3.2.2. Biochar pre-treatments**

Biochar was contacted with HCl 4M and stirred during 72 h at 25 °C at 125 rpm to remove the inorganics content. After acid washing, the samples were rinsed with deionized water until the pH approached neutrality, to eliminate residual chemicals, and then dried at 90 °C for 24 h.



Catalyst impregnation on Biochar was carried out as follows: 50 mL of  $\text{FeSO}_4 \cdot 7\text{H}_2\text{O}$  0.11 M was added to 250 mL of CMC  $4.96 \times 10^{-5}$  M solution, purged with  $\text{N}_2$  to remove dissolved oxygen. Subsequently, 10 mL of  $\text{NaBH}_4$  0.22 M was added drop by drop to the stirred solution of  $\text{Fe}^{2+}$ /CMC under  $\text{N}_2$  atmosphere [126]. Finally, 20 mL of  $\text{Fe}^0$ /CMC suspension was contacted with 0.2 mg of acid-washed biochar. The container was sealed and stirred for 48 h at 25 °C at 125 rpm to introduce zero-valent iron nanoparticles on the biochar surface. After impregnation, this was rinsed with double deionized water to eliminate residual chemical and dried at 90 °C for 24 h.

### 3.2.3. Growth of carbon nanostructures on biochar

The Chemical vapor deposition system was conducted in a thermogravimetric analyzer (Versa Therm) that has a vertical furnace as reactor. First, the impregnated biochar with iron catalyst was placed in a mesh capsule while the tubular reactor was purged with a  $\text{N}_2$  stream. Then, the sample was heated at rate of  $25 \text{ °C min}^{-1}$  up to 600 °C. Once the CVD temperature was reached, the carbon source ( $\text{C}_2\text{H}_2$ ) was injected at  $10 \text{ mL} \cdot \text{min}^{-1}$  (5 mm of TGA flowmeter) as follows: i) continuous CVD during 2 min, followed by 7 min without  $\text{C}_2\text{H}_2$  supply, and ii) CVD pulsed-injection during 1 min, followed by 5 min without  $\text{C}_2\text{H}_2$  supply, then  $\text{C}_2\text{H}_2$  was injected for 1 min again, followed by another 7 min without  $\text{C}_2\text{H}_2$  supply. After the CVD process, the samples were cooled down to room temperature. To increase the surface area and reduce the oxygen functionalities of these composites, the samples were thermally treated at 650 °C at a heating rate of  $15 \text{ °C min}^{-1}$  during 10 min under  $\text{N}_2$  atmosphere. It is important to highlight that the materials tested herein were labeled as follows: GAC, granular activated carbon; BC, biochar; BCA, acid-washed biochar; BCVD600-2, acid-washed biochar processed by continuous CVD; BCVD600-1p, acid-washed biochar processed by CVD pulsed-injection; BCVD600-2TT and BCVD600-1pTT, Biochar/nanostructures composites thermally treated.



### **3.2.4. Analytical methods**

#### **3.2.4.1. Physical characterization**

Nitrogen adsorption-desorption isotherms were measured by using a Micromeritics ASAP-2020 at 77 K. The surface area was calculated using the BET equation [127], and the pore size distribution was determined using the density functional theory (DFT), protocols established in the equipment. Morphological structures were examined by scanning electron microscopy (FEI - FIB Dual Beam Helios Nanolab 600). The transmission electron microscope (TEM, Tecni FEI 300 operated at 300 kV) was used to observe with more detail the carbon nanostructures morphology.

#### **3.2.4.2. Chemical characterization**

The points of zero charge ( $\text{pH}_{\text{PZC}}$ ) and surface charge distribution were calculated from a potentiometric titration curve obtained with an automatic titrator (Metler Toledo, PL 70), following the methodology previously reported by [151]). The titration curve (pH vs titran volume) was transformed to proton binding isotherm (Q, proton release vs pH) by using the proton balance equation as previously reported [152] . The pH at which the proton binding curve crosses the X-axis was considered as the  $\text{pH}_{\text{PZC}}$ . Finally, the  $\text{pK}_a$  distribution was obtained from the proton release curve by using the SAEIUS-pK-dist program © 1994, software [152], [153]. The surface hydrophobicity properties of the adsorbent materials were measured by the static contact angle of a demineralized water drop (approximately 20  $\mu\text{L}$ ) by using a goniometer Theta Lite (Theta Litoptical Tensiometer, Attension Theta Lite, Biolin Scientific, Phoenix, AZ, USA). The materials were fixed with double-sided tape and flattened on a glass slide before testing. X-ray diffraction (XRD) analysis of pristine and modified carbonized fibers was conducted in a SmartLab Rigaku diffractometer using a  $\text{CuK}\alpha$  radiation. The XRD patterns were obtained with a step size of  $0.01^\circ$  with a step time of 10



sec. The peak positions of the crystal structures were identified from the ICDD-PDF-4 + 2015 database. Raman spectroscopy was performed by means of a confocal Raman spectrometer (inVia MICRORAMAN: RENISHAW) using a 514 nm laser and a 100x objective lens (spot size of 0.3  $\mu\text{m}$ ).

### 3.2.5. Adsorption experiments

Adsorption experiments were conducted to evaluate the static adsorption kinetics of four VOCs on macroporous adsorbents. Here, benzene, toluene, hexane, and pentane were tested as representatives of evaporative emissions. Each VOC adsorption experiment was individually performed using the following procedure: 0.1 g of adsorbent sample, previously dried at 100 °C and cooled down in a desiccator, was introduced in a 1 mL glass syringe. Besides, 20 mL of individual VOC were placed in a 50 mL serum bottle and sealed with black Teflon stoppers. The headspace of the bottle was replaced with N<sub>2</sub> atmosphere to avoid moisture effects. The syringe loaded with dry adsorbent sample was weighed in a digital microbalance with a sensitivity of 0.01 mg, recording the initial weight. Subsequently, the syringe needle was inserted in the serum bottle by crossing the septa to allow the VOC gas to diffuse through the needle cavity to the adsorbent sample. The adsorption experiment was carried out in an incubator at 25 °C. Then, the syringe was taken out from the bottle to monitor its weight within the interval of 1- 48 h. Additionally, the headspace concentration of each VOC in serum bottles was analyzed by a gas chromatograph (Thermo Scientific Trace 1300) with flame ionization detector (GC-FID), and its manometric pressure was measured by a manometric devise (EXTECH). Finally, the adsorption rate parameters were determined by pseudo-first and pseudo-second order equations [128]. The *pseudo-first-order kinetic equation* is given by:

$$\ln(q_e - q_t) = \ln(q_e - k_1)t \quad (\text{Eq. 3.1})$$



where,  $q_t$  and  $q_e$  ( $\text{mg g}^{-1}$ ) are the adsorption capacities at time  $t$  (h) and equilibrium, respectively, and  $k_1$  ( $\text{h}^{-1}$ ) is the pseudo-first order rate constant.

The *pseudo-second order kinetic equation* can be represented by:

$$\frac{t}{q_t} = \frac{1}{k_2 q_e^2} + \frac{1}{q_e} t \quad (\text{Eq. 3.2})$$

where  $k_2$  ( $\text{mg (g}\cdot\text{h)}^{-1}$ ) is the pseudo-second order rate constant of sorption,  $q_e$  ( $\text{mg g}^{-1}$ ) is the amount of pollutant absorbed at equilibrium, and  $q_t$  ( $\text{mg g}^{-1}$ ) is the amount of pollutant adsorbed at any time  $t$  (h).

### 3.3. Results and discussion

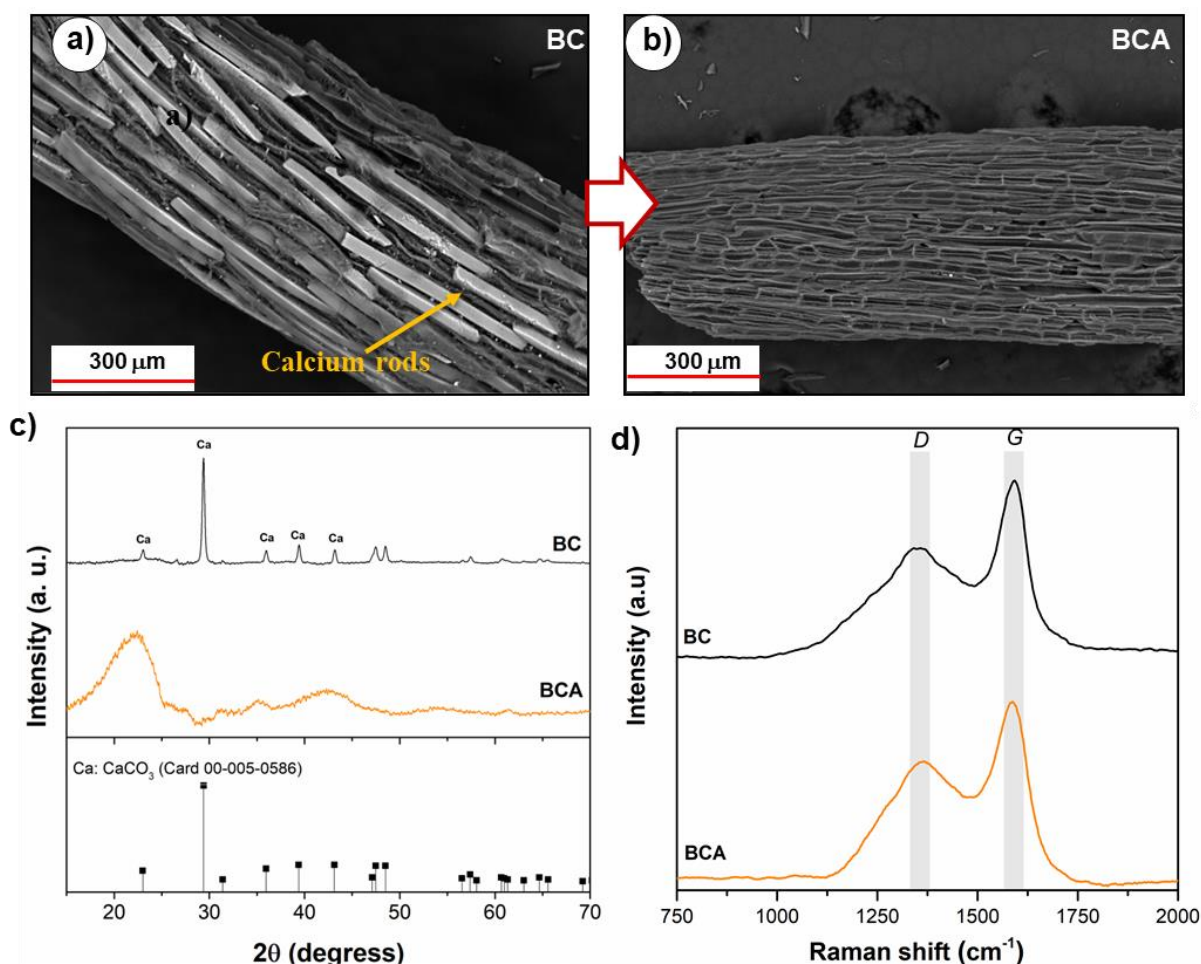
#### 3.3.1. Pre-treated biochar performance

The basic characteristic of biochar mainly varies with the feedstock type. The effect of the feedstock type on biochar properties have been attributed to the different composition and proportions of cellulose, hemicellulose, and lignin, although inorganic species are commonly present in lignocellulosic biomass [37]. Compared with cellulose and hemicellulose, lignin is more stable and resistant to the thermal decomposition of liquid and gaseous fractions, leading a skeleton with wide pore structure inside the material [129]. Moreover, the biochar periphery showed typical large calcium rods with an average of 250  $\mu\text{m}$  long (Fig. 3.1a). Regarding the applicability of biochar as substrate for the growth of carbon nanostructures by CVD process for adsorption purposes, a homogeneous dispersion of nanostructures on biochar is needed to increase the exposure of active sites to adsorb VOCs. In fact, this nanostructures arrangement is consequent of the well-dispersed impregnated catalyst prior to CVD process. However, the high accumulation of iron particles on calcium rods observed in Chapter 2 suggested the need to remove calcium to improve the catalyst dispersion onto biochar. Accordingly, biochar was contacted with non-oxidizing





acid solution to remove the inorganic content. Backscattered electron images showed the removal of rods particles on biochar after acid washing (Fig 3.1a, b), while the total inorganic content was reduced from 8.6 to 4.5 % w/w. XRD pattern allowed to corroborate the rods particles removal after acid washing since diffraction peaks assigned to calcium carbonate (ICDD-PDF Card 00–005-0586) were not identified in BCA sample (Fig. 3.1c). In contrast, Raman spectra did not show any structural carbon transformation, as it is corroborated by the similarity between the intensities of the G- and D-bands (Fig. 3.1d).

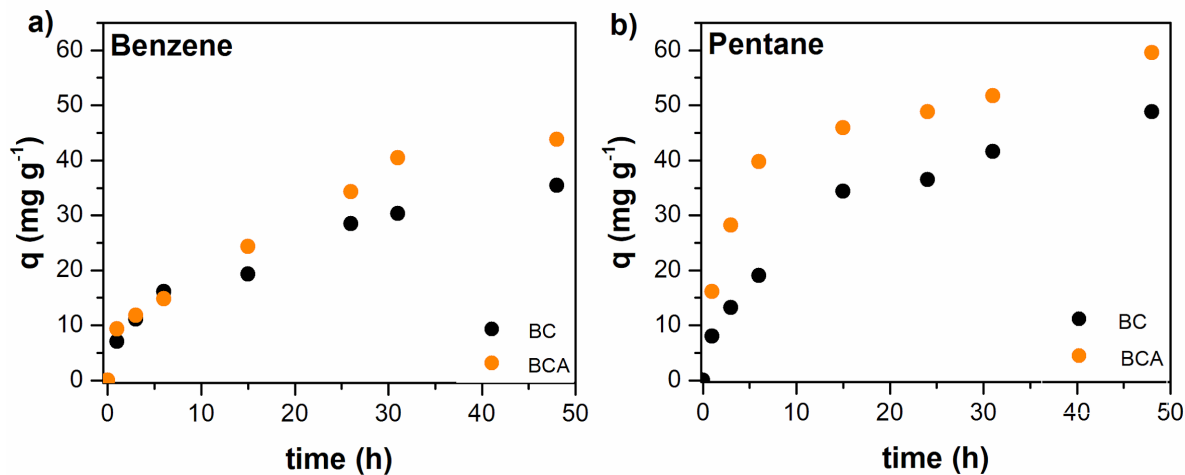


**Fig. 3.1** - (a,b) SEM backscattered electrons images of raw and acid-washed biochar. (c) XRD pattern and (d) Raman spectra of BC and BCA spectra.

Based on the null polarity of the VOCs of evaporative emissions, the removal of inorganics on biochar allowed to improve the adsorption capacity of pentene and benzene



in 20 and 22 %, respectively (Fig. 3.2). Taking into consideration that BCA surface could present more exposed  $sp^2$  basal planes, this should have more affinity for nonpolar VOCs since these are mainly attached by van der Waals interaction forces.



**Fig. 3.2** - Adsorption kinetics of (a) benzene and (b) pentane on raw and acid-washed biochar at 25 °C and  $\sim 1$  atm of barometric pressure.

Note: For practical purposes, the acid-washed biochar sample (BCA) will be referred as biochar in the following sections.

### 3.3.2. Materials characterization

#### 3.3.2.1. Physical properties

The surface morphology of biochar treated by the CVD processed is reported in Fig. 3.3. Scanning electron microscopy (SEM) images were taken at different point of the biochar samples, where it is observed a consistent and uniform growth of carbon nanostructures, even at low magnifications. Considering SEM images, it is difficult to distinguish if carbon nanostructures are carbon nanotubes (CNTs) or carbon nanofibers (CNFs). The comparison between SEM images (Fig 3.3a and b) showed a high agglomeration of carbon nanostructures onto the biochar after continuous CVD, with particles sizes of less than 100 nm, whereas observations on different micrographs suggested that CVD pulsed-injection



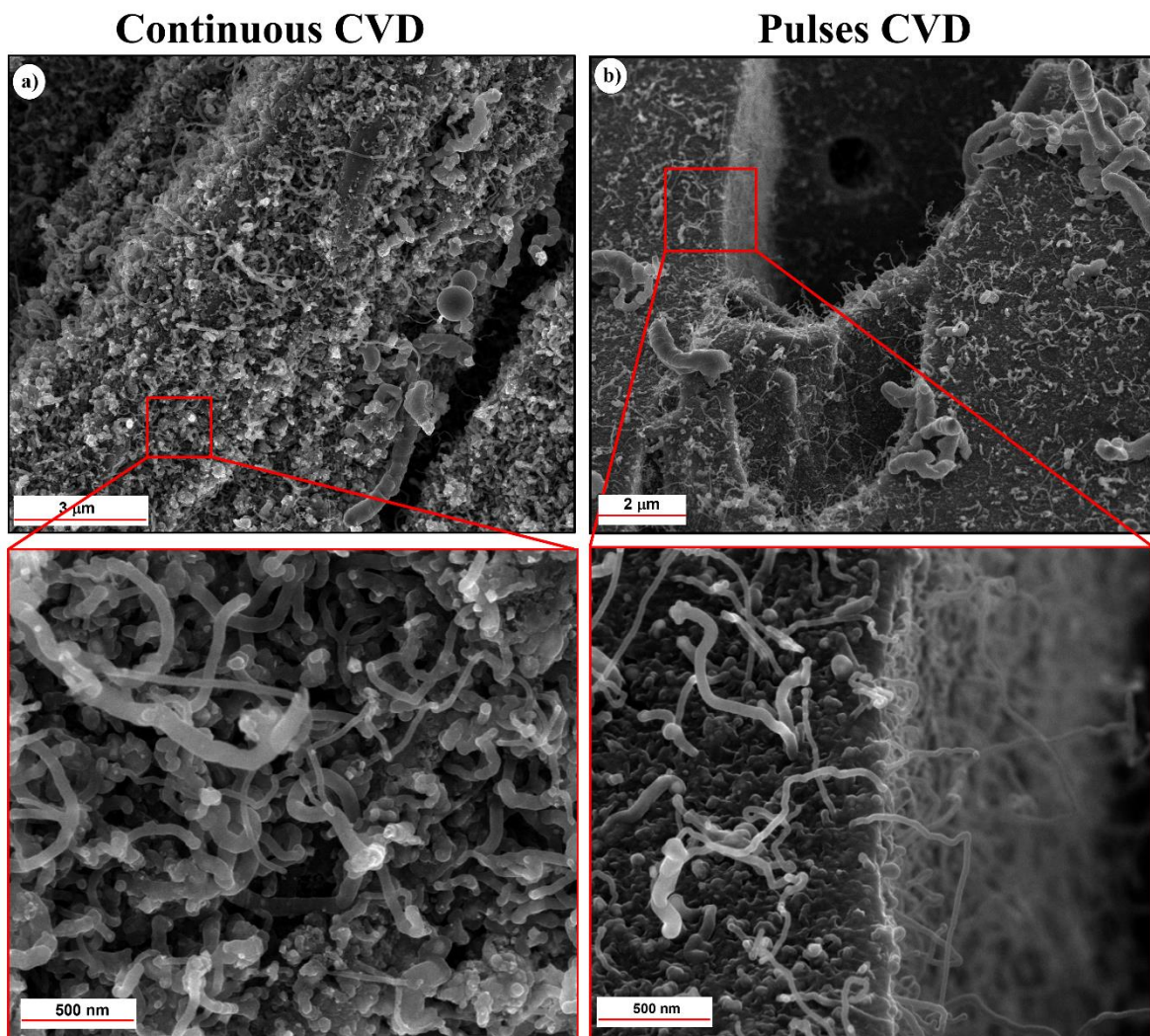
allowed the growth of thinner carbon nanostructures with diameters of less than 50 nm. Despite the lengths of the nanostructures on both treatments are diverse, SEM observation on the sample processed by CVD pulsed injection showed nanostructures larger than 1  $\mu\text{m}$ . The growth of some bigger carbon nanostructures could be a consequence of CMC decomposition through the CVD process [132]. Additionally, it has been previously reported that not every catalyst particle can nucleate carbon nanostructures [154].

When making a comparison with previous works [42], there are some advantages to highlight herein. First, micrographs clarify that the inorganics removal enhances the dispersion of carbon nanostructures that mostly covered the biochar surface, while calcium rods on non-pretreated biochar promote carbon nanostructures agglomeration. On the other hand, the effective growth of carbon nanostructures with morphological similarities to CNTs was possible at 600  $^{\circ}\text{C}$ . Based on theoretical and empirical knowledge [80], It has been reported that the growth of CNTs by CVD process is promoted at higher temperatures than 700  $^{\circ}\text{C}$ . In addition, it has been reported that the yield of carbon deposited on the catalyst is less than 23% at temperatures lower than 600  $^{\circ}\text{C}$ . As the reaction temperature increases, the yield of carbon deposited increases significantly [48]. In this work, the growth of carbon nanostructures could be possible because acetylene decomposition was thermodynamically favored at 600  $^{\circ}\text{C}$ , being possible the thermal decomposes of acetylene mainly in carbon atoms [80]. Taking advantage of the ability of grow carbon nanostructures at low temperatures ( $< 700$   $^{\circ}\text{C}$ ), the CVD process at 600  $^{\circ}\text{C}$  avoided unnecessarily subjecting the biochar to high temperatures, which could mainly induce a structural collapse of biochar macropores.

The formation of cap-like carbon structures was also observed on biochar after CVD pulsed-injection. These structures have been commonly developed in the early stages of CNT growth. This morphology was observed on biochar because during the well-known



fullerene-like cap step, the cap does not detach from the nanoparticle, encapsulating it and stopping the CNT growth [80]. Furthermore, the supply of a second pulsed-injection of acetylene could be able to increase the length of some CNT length, while more carbon condensed on catalyst during the first pulsed-injection could avoid the continuous growth in the following pulse. A further explanation will be provided by TEM analysis. Other important feature was that the surface of some carbon nanostructures was irregular with cavities, which could be a consequence of irregular carbon graphitic layers deposited during the second pulsed-injection. In continuous CVD this behavior was not observed.



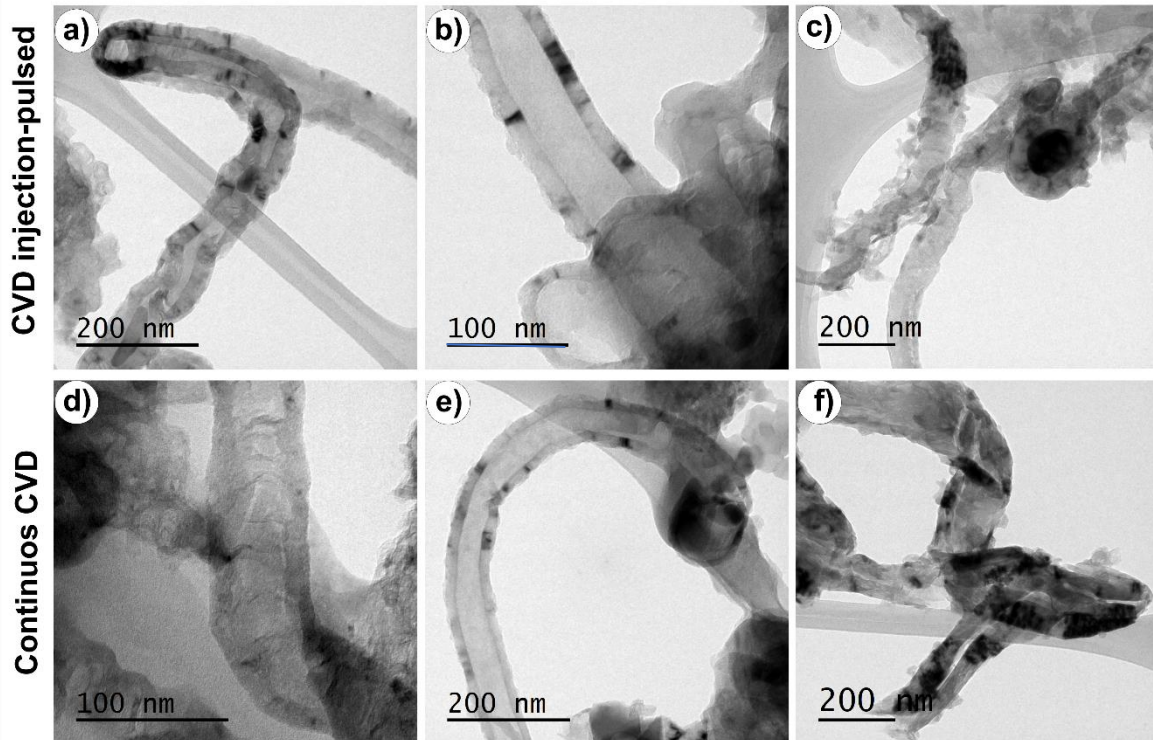
**Fig. 3.3** - SEM secondary electrons detector images of the biochar modified with continuous (a) and pulsed CVD (b) processes.



After SEM analysis, transmission electron microscopy (TEM) was carried out to observe the intern morphology of carbon nanostructures and the effect of each CVD approach in its inert structure (Fig 3.4). Due to substrate heterogeneity affects CVD process, it was possible to induce the growth of a variety of morphologies such as hollow-like CNTs, bamboo-like CNTs, and CNFs. TEM micrographs also showed carbon nanoribbons (Fig 3.4f) and quasi-spheres shape with iron core and carbon shells (Fig 3.4c). This last one morphology had diameters lower than 200 nm. These labels were assigned taking into account similarities to other TEM analysis previously reported [26]–[30]. The typical apparency of CNTs can be seen in Fig 3.4b and e, with smaller diameters than 80 nm. In addition, the majority of the bamboo-like structures of CNTs exhibits thin compartment layers, being frequently compared with the graphene structure arranged apparently as stacked cones of CNFs. Most of the CNTs and CNFs analyzed by TEM have a curved structure caused by kinks or defects, which is consistent with the SEM observations. It has been previously reported that these morphologies are mainly caused by heteroatoms such as oxygen and nitrogen, mainly from CMC and biochar [42], [131], [136]. These morphologies described above were observed on biochar processed with both CVD methodologies.

Considering the presence of graphitized carbon nanostructures observed in several TEM images and the absence of carbon black, it is suggested that the catalytic activity of iron never ceased during CVD pulsed-injection. In this sense, the catalyst allowed the growth of carbon walls of CNTs and/or plates of CNFs during the first deposition pulse, while the high surface diffusion of carbon on the active iron catalyst could allow the carbon deposition during the second pulse to continue the growth of the carbon nanostructures at 600 °C.



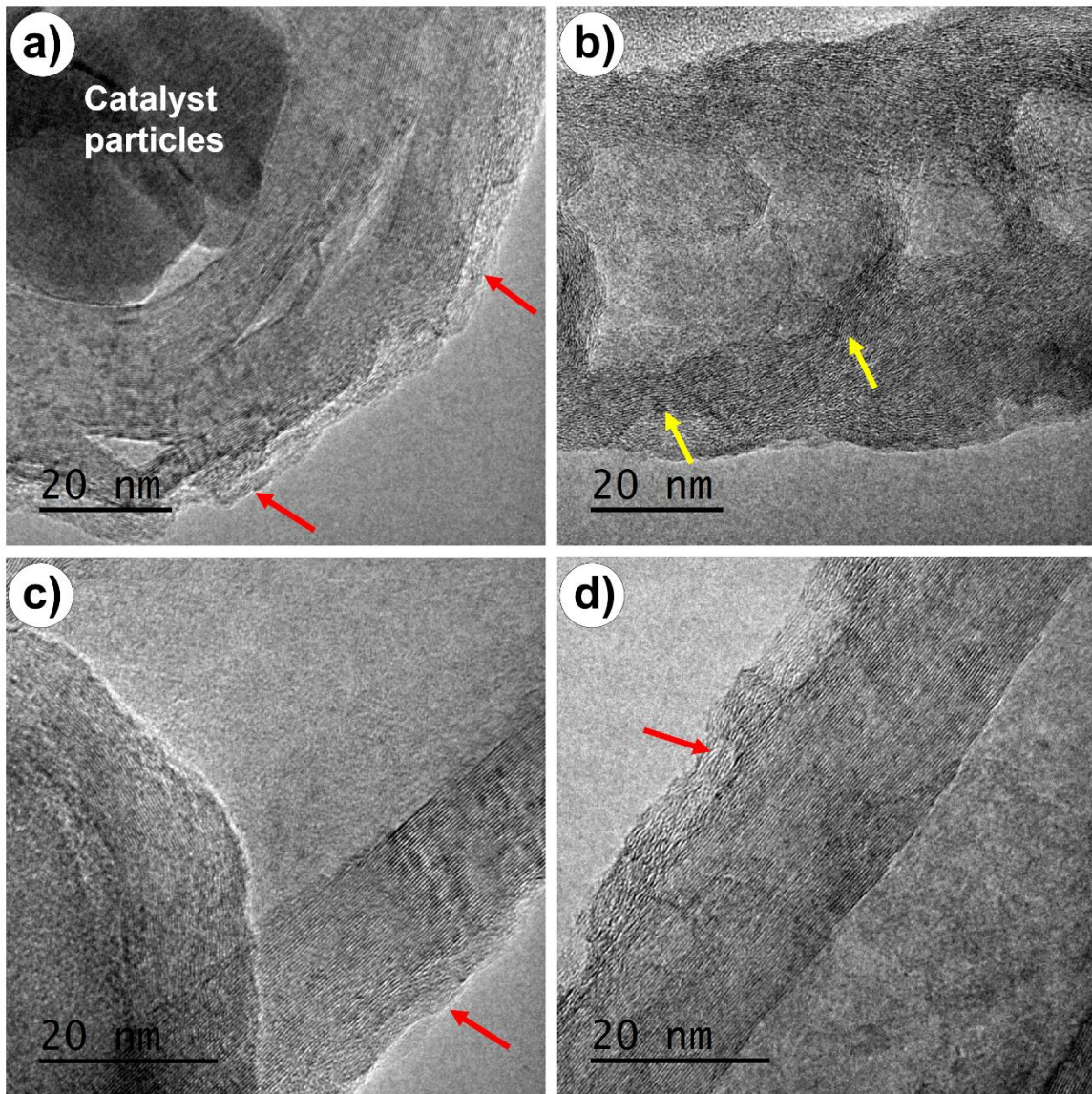


**Fig. 3.4** - Representative TEM images of different carbon nanostructures growth by pulsed-injected (a, b, c), and CVD continuous methodology (d, e, f) at 600 °C.

By using high resolution transmission microscopy (HRTEM), it was possible to observe a highly ordered crystalline structure of carbon nanostructures (Fig. 3.5). The HRTEM micrographs show that the carbon layers of the so-called quasi-spheres are surrounding the central iron nanoparticles, and it is observed a gap between catalyst core and the carbon shells (Fig 3.5a). Furthermore, TEM images showed the distinctive arrangement of CNFs where the layer of curved graphitic planes are in general not adjusted along the axis of the nanofiber and arranged as cups. While CNTs are mainly formed by cylindrical carbon structures with several graphene walls (Fig. 3.5c), CNFs consist of an arrangement of graphene structures organized as stacked caps (marked with yellow arrows) [53] [156]. On the other hand, TEM images display the well-graphitized carbon nanostructures and only a little carbonaceous material attached to the outer nanostructures surface. These carbonaceous materials could consist of few layers of turbostratic graphite. In this sense,



turbostratic carbon allowed to distinguish morphological differences on carbon nanostructures surfaces. Continuous CVD samples showed turbostratic graphitic layers on continuous graphitic wall of CNTs, while the CNTs surface of CVD pulsed-injection samples display interleaved patch of turbostratic graphitic and well-graphitized layers.



**Fig. 3.5** - HRTEM micrographs of (a) onion-like carbon, (b) CNFs, and (c, d) CNTs. Red arrows highlights the presence of turbostratic graphitic carbon and yellow arrows indicated the curved stacked caps.



The physical structural parameter of all the adsorbent determined from N<sub>2</sub> physisorption isotherms were quantitatively presented in Table 3.1. The pore volume and surface area of modified biochar were analyzed to understand the influence of biochar textural properties after inorganic removal, CVD processes and thermal treatment. In addition, a reference adsorbent such as bituminous activated carbon was also analyzed to evaluate the performance of a commercial microporous adsorbent with high surface area (776 m<sup>2</sup> g<sup>-1</sup>) on VOCs adsorption kinetics. On the other hand, it was found that the inorganic removal from biochar allow an increasement of 1.8 time the micropore volume, expanding the biochar surface area from 120 to 189 m<sup>2</sup> g<sup>-1</sup>. Since mesopore volume of biochar contribute to only 17 % of total volume pore and its micropore volumes was 3.2 times lower than of activated carbon, it is suggested that biochar microporosity is directly located on surface. After the CVD process, the biochar surface areas decreased by more than 90% since carbon deposition may block biochar pores, in addition to the carbon nanostructures having closed cups at the tip. Conversely, thermal treatment increased the surface area of biochar CVD-modified bichars from 19 to 96 m<sup>2</sup> g<sup>-1</sup> for BCVD600-2TT, and from 8 to 240 m<sup>2</sup> g<sup>-1</sup> for BCVD600-1pTT. An increment of 4.5 and 22 times in micropore volumes, respectively, explain the surface area enlargement, indicating the unblocking of biochar micropores by removal of possible amorphous carbon and the effect of carbon nanostructures interstices. In this sense, the higher micropores volume in BCVD600-1pTT than BCVD600-2TT may be relate to the best dispersion of carbon nanostructures observed by SEM analysis which promote pore volume between structures.





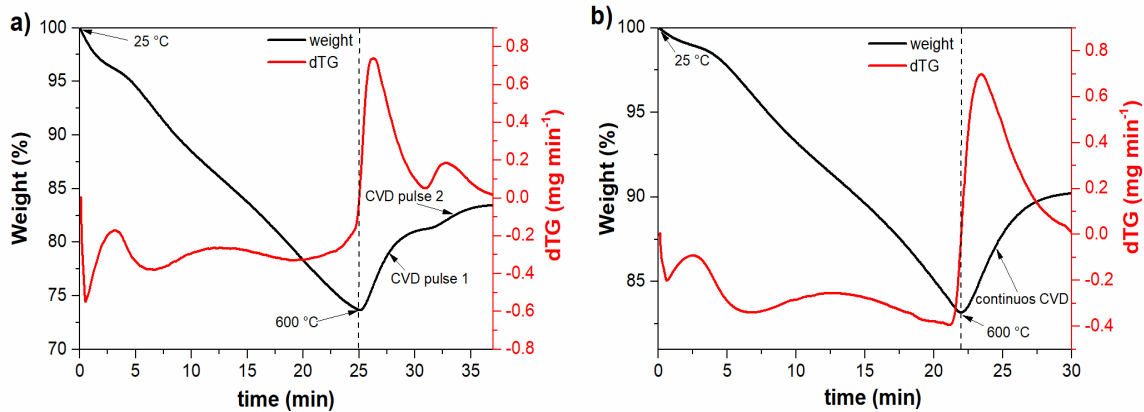
**Table 3.1** - Surface area and pore volume of carbon adsorbents.

ID sample	$S_{\text{BET}}$ ( $\text{m}^2 \text{g}^{-1}$ )	$V_{\text{total}}$ ( $\text{cm}^3 \text{g}^{-1}$ )	$V_{\text{micro}}$ ( $\text{cm}^3 \text{g}^{-1}$ )	$V_{\text{meso}}$ ( $\text{cm}^3 \text{g}^{-1}$ )	$V_{\text{macro}}$ ( $\text{cm}^3 \text{g}^{-1}$ )
GAC	776	0.416	0.270	0.130	0.016
BC	120	0.056	0.041	0.015	N.D.
BCA	184	0.093	0.075	0.017	0.001
BCVD600-2	19	0.016	0.007	0.007	0.002
BCVD600-2TT	96	0.051	0.032	0.010	0.009
BCVD600-1p	8	0.012	0.004	0.003	0.005
BCVD600-1pTT	240	0.110	0.088	0.020	0.001

GAC, granular activated carbon; BC, biochar; BCA, acid-washed biochar; BCVD600-2, acid-washed biochar processed by continuous CVD; BCVD600-1p, acid-washed biochar processed by CVD pulsed-injection; BCVD600-2TT and BCVD600-1pTT, Biochar/nanostructures composites thermally treated.

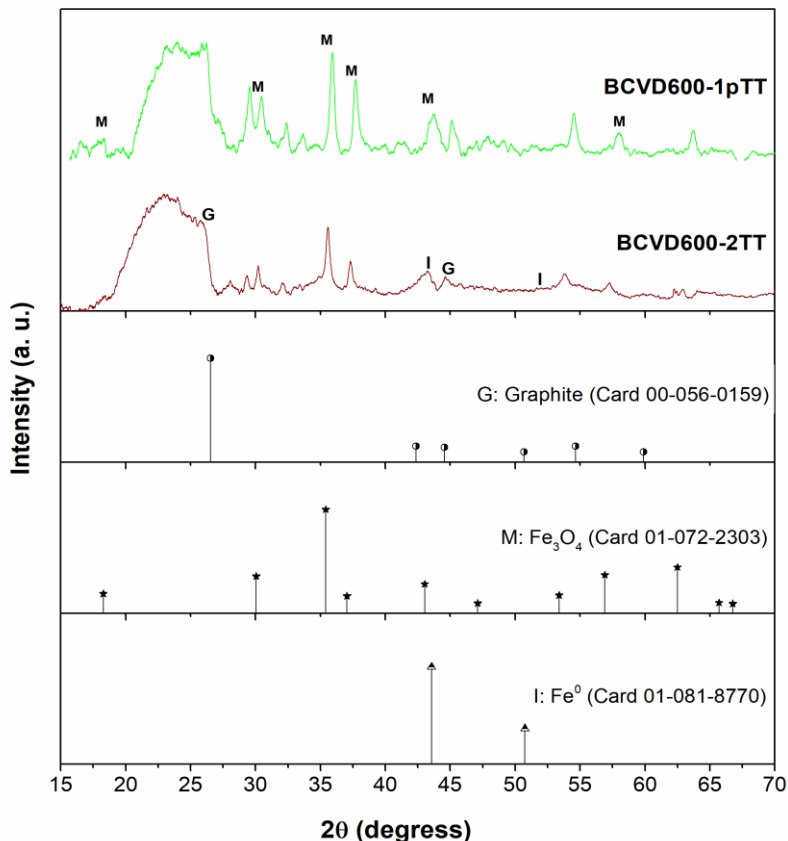
### 3.3.2.2. Chemical properties

Considering that the CVD process was developed in a TGA equipment, it was possible to evaluate the thermal stability of biochar throughout the process (Fig. 3.6). First, the average weight reduction of 21% during the heating process could be attributed to the decomposition of CMC since biochar showed a good thermal stability [40]. CVD temperature (600 °C) did not result in a substantial degradation of the biochar because it did not overlap its thermal stability, in comparison to the most reported CVD temperatures (~700 °C) [80],[84],[120],[157]. Through the CVD processes, an average weight increases of 9% was observed after continuous CVD process, while pulses CVD process displayed two weight increases of 7.5 and 2.1%, respectively. Despite both methodologies have a similar mass increase, the physical characterization points out that, by using CVD pulsed-injection, carbon nanostructures dispersed out in a better way and have better textural properties.



**Fig. 3.6** - TGA performance of CVD process by injecting acetylene at 600 °C (a) during 2 min or (b) two pulses of 1 min each, respectively.

Identification of the crystalline phases was carried out with X-ray diffraction (XRD) measurements (Fig. 3.7). The XRD pattern of biochar/carbon nanostructures composites showed a characteristic behavior of low graphitic carbon at  $2\theta$  interval of 22-30°, in which the line broadening cannot be explained for the presence of graphitic microcrystallites. However, crystalline graphitic structures with (0 0 2) and (1 0 0) planes were identified by diffraction peaks at  $2\theta$  values of 26° and 43° (ICDD-PDF Card 00-056-0159), respectively. Other peaks at  $2\theta$  43 and 51° match with the XRD pattern of iron (ICDD-PDF Card 01-081-8770), and 30, 35, 56 and 62° for magnetite. The presence of these iron species has been well-reported for the surface oxidation of iron catalyst that was previously synthesized by the chemical reduction of  $\text{FeSO}_4$  to zero-valent iron [126]. Catalyst particles could be composed of zero-valent iron core with magnetite phases on particle surface. On the other hand, it is observed that the XRD patterns of CVD pulsed-injection samples showed peaks with higher intensity than with continuous CVD, indicated a greater crystallinity of iron species and carbon nanostructures particles are very small to diffract.



**Fig. 3.7** - X-ray diffraction patterns of biochar/carbon nanostructures composites with a step size of  $0.01^\circ 2\theta$  at 10 sec per step. All four patterns were collected on the same day.

Another technique used for the characterization of biochar/carbon nanostructures composites was Raman spectroscopy (Fig. 3.8). Similar to the spectra of all  $\text{sp}^2$ -carbons, two noticeable peaks appeared at  $1350\text{ cm}^{-1}$  (D-band) and  $1590\text{ cm}^{-1}$  (G-band). In addition, the D-band overtone in the second order region between  $2600 - 2700\text{ cm}^{-1}$  (2D-band) was observed [143]. To characterize the quality and any change in the structural ordering of the carbon network, the ratio of maximum intensity of D-band to the maximum intensity of the G-band is commonly used. However, the variation of the area ratios of the deconvoluted D- and G-bands ( $A_D A_G^{-1}$ ) is a useful alternative to better describe the carbon structural information of the samples without very significant change in the band intensities [158]. Therefore, to obtain a good determination of the areas ratio, it is necessary to have an

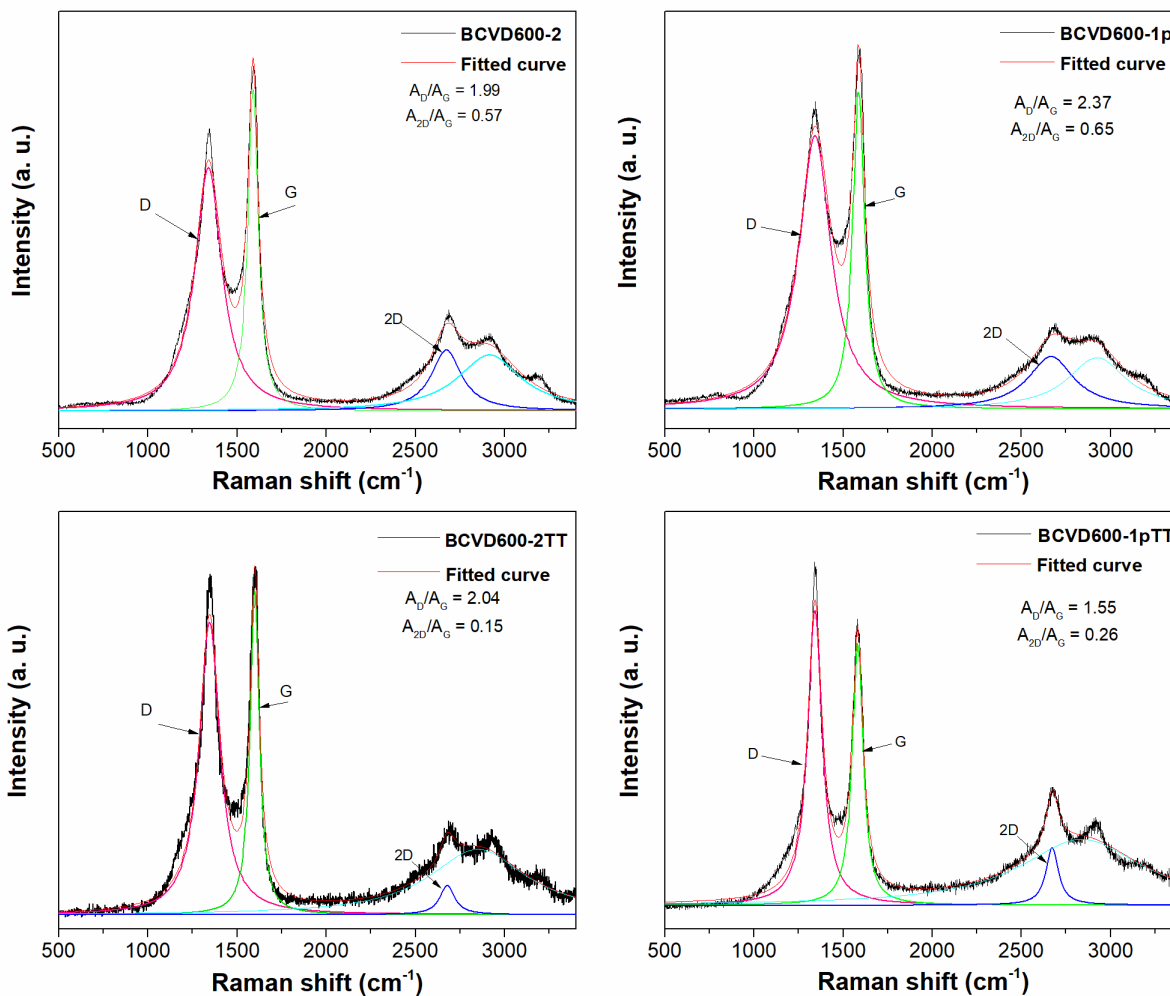


adequate deconvolution of the Raman spectra of these compounds [155]. For this reason, the Raman spectra were fitted by using Lorentzian curves. As it is seen in Fig. 3.8a and b, regardless the highly graphitic quality of CNTs and CNFs, the curly morphology of these carbon nanostructures showed a very intense D-band [139]. Furthermore, by comparing the  $A_D A_G^{-1}$  ratio of modified biochar by CVD pulsed-injected (ca. 2.37) with that of continuous CVD sample (ca. 1.9), the higher value of the sample BCVD600-1p is giving by a systematic broadening effect and higher valley lines between the D and G-bands after CVD pulsed-injection. In absence of amorphous carbon sighting by microscopy analysis, this behavior could be explained by the presence of the carbon cap morphology as described above, where its tip curvature contains five- and seven-membered carbon rings, characteristic of this Raman spectra. On the other hand, when thermal treatment was induced on the biochar/carbon nanostructures composite, the  $A_D A_G^{-1}$  ratio of the continuous CVD sample (BCVD600-2TT) showed a slight increase. An increase in this ratio has often been attributed to a high density of  $sp^2$  domains of small sizes due to the introduction of defects of varied nature (e.g., vacancies, functionalization, aromatic structures other than 6-membered units) [159]. Regardless the highest intensity of D-band on BCVD600-1pTT sample, the reduction on the  $A_D A_G^{-1}$  ratio from 2.37 to 1.55 after thermal treatment could also be accompanied by an increase in the  $sp^2$  domains. The latter is related to the removal of defective carbon and to the transformation of turbostratic carbon after the post-treatment at 800 °C, as it was inferred by HRTEM analysis. Since the reduction in the  $A_D A_G^{-1}$  ratio was accompanied by an increase in  $sp^2$  domains, we consider this evidence as a direct indicator of the presence of graphitic-like structures consisting in  $sp^2$  domains introduced by the graphitization of turbostratic carbon.

The ratio between the area of 2D and G peaks has been used as an indicative of the number of graphene layers, a value of around 2.0 is associated with a graphene monolayer,



whereas lower values correspond to more layers of graphene. It is clearly seen that when the thermal treatment was applied the  $A_{2D} A_G^{-1}$  ratio decreased due to the increasing number of stacked graphene layers [120]. Additionally, a lower  $A_{2D} A_G^{-1}$  ratio of the treated biochar by a continues CVD process agrees with the higher diameter of carbon nanostructures observed by microscopy analysis.

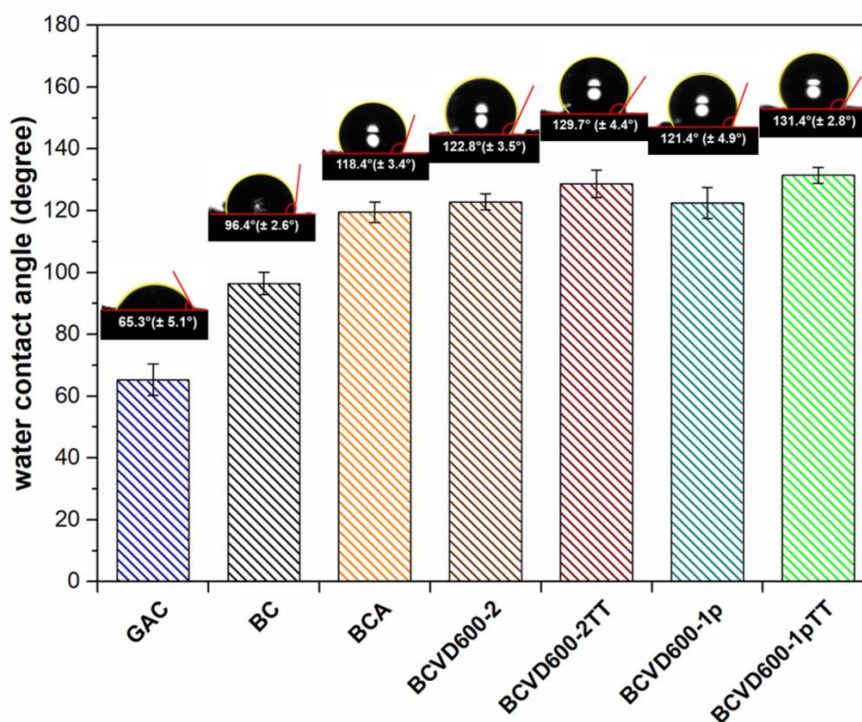


**Fig. 3.8** - Fitted Raman spectra of the modified biochar by continuous and pulsed-injection CVD.

To acquire information of the possible affinity of the carbon-based materials to VOCs, measurements of contact angle were carried out to evaluate the adsorbent hydrophobicity (Fig 3.9). If the water contact angle is greater than  $90^\circ$ , then the surface is classified as



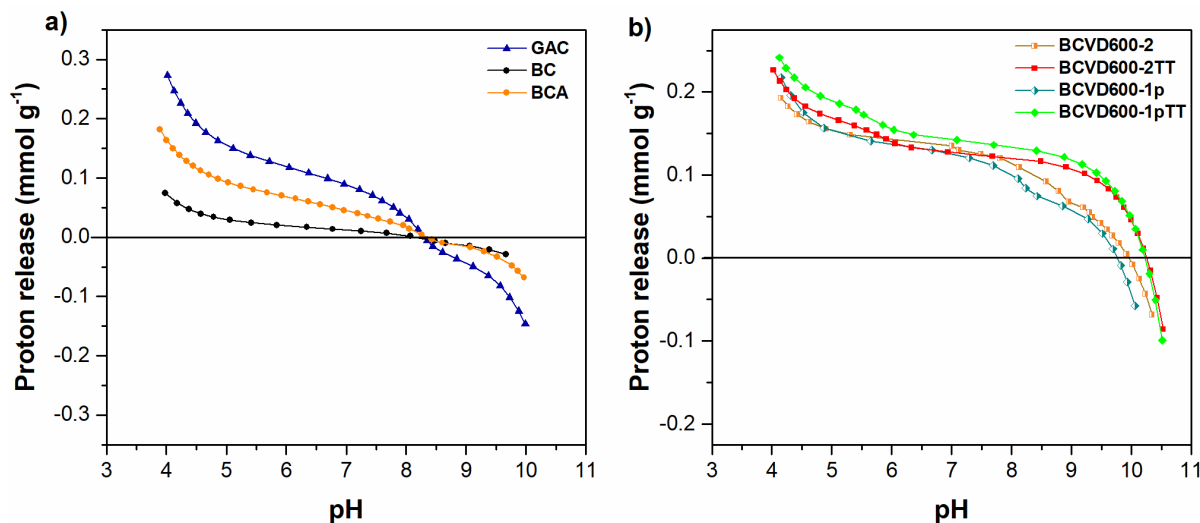
hydrophobic, and if it is less than  $90^\circ$ , then the surface is hydrophilic [96]. The water contact angles of activated carbon indicate a hydrophilic surface which might be related to the high inorganic content ( $> 8\%$  w/w) and oxygen functionalities (e.g., hydroxyl and carboxyl groups). After acid washed, the hydrophobicity of biochar slightly increased which is consistent with the increase in adsorption capacity shown in Fig. 3.2. On the other hand, the contact angle of biochar/carbon nanostructures composites was higher than  $121^\circ$ , thereby suggesting that  $sp^2$  basal planes developed after carbon deposition contribute to higher hydrophobicity to the biochar. In addition, thermal treatment also slightly increased the adsorbents hydrophobicity, possibly by acidic functionalities removal, being beneficial for VOCs adsorption purposes.



**Fig. 3.9**– Hydrophobic measurement of carbonaceous adsorbent by contact angle of a droplet water on the surface. BCVD600-2, acid-washed biochar processed by continuous CVD; BCVD600-1p, acid-washed biochar processed by CVD pulsed-injection; BCVD600-2TT and BCVD600-1pTT, biochar/nanostructures composites thermally treated.



The occurrence of changes in surface chemistry upon the growth of carbon nanostructures was analyzed by potentiometric titrations (Fig. 3.10). First, the  $\text{pH}_{\text{PZC}}$  value of BC and BCA confirmed that acid washing did not oxidize the biochar surface. Indeed, the high  $\text{pH}_{\text{PZC}}$  values of BCA and bituminous granular activated carbon (GAC) suggested a basic surface with a high extension of  $\text{sp}^2$  basal planes (Fig. 3.10a). It is worth noting that the absence of moisture onto carbonaceous materials during adsorption process denote not functionalities dissociation, and thus, the adsorption process could be influenced by its dipolar moment. In this sense,  $\text{pH}_{\text{PZC}}$  values and the surface functionalities of the adsorbent are critical to the adsorption of VOCs since the acidic functionalities increase the adsorbent polarity, which affect the adsorption of nonpolar VOCs [36]. This interpretation is consistent with the water contact analysis. On the other hand, the basic character of biochar/carbon nanostructures composites ( $\text{pH}_{\text{PZC}} > 10$ ) is granted by the increase in  $\text{sp}^2$  hybridized carbon after the carbon deposition process. Moreover, the further  $\text{pH}_{\text{PZC}}$  increase after the thermal treatment (Fig. 3.10b) agrees with defects removal and the increase in  $\text{sp}^2$  domains identified by Raman analysis.

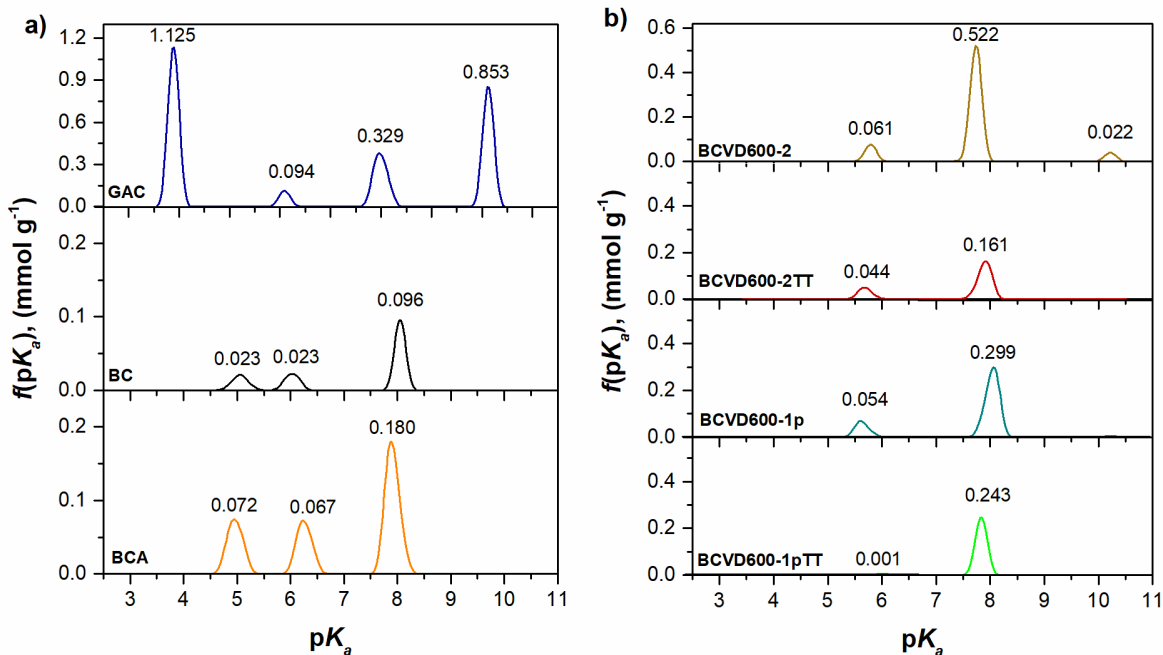


**Fig. 3.10** - Surface charge distribution of studied materials as a function of pH at 25 °C, using 0.1 mol L<sup>-1</sup> NaCl as the supporting electrolyte.

The acid surface groups were evaluated through the deconvolution of the proton release curves, obtaining the amount and characteristic  $\text{pK}_a$  of acid functionalities by means of the SAIEUS software [160]. Based on Bronsted acid-based nature of functionalities, from values 3 to 7, the peaks may correspond to carboxylic and carboxylic anhydride groups; from 7 to



10, the peaks could be attributed to lactone groups; and beyond 10, the peaks may correspond to phenolic groups [71]. As seen, the most intense peak in each  $pK_a$  domain was observed in activated carbon, particularly for carboxylic and phenolic groups [161]. The distribution of acidic groups on biochar showed two peaks with  $pK_a$  close to 5.5 and 8 that could correspond to dissociation of carboxylic and phenolic groups remaining from lignin fraction or by a slight oxidation of biochar caused during rinsing with water. The number of functionalities related to the low peak at 5.5  $pK_a$  is considerably lower after the biochar was processed by CVD. The slight shift in the  $pK_a$  values could be related to a different chemical environment in the different carbon nanostructures. Considering the development of aromatic functionalities with  $sp^2$  hybridized carbon after CVD process, the  $pK_a$  range of this basic group is not detected because it is between 16 and 23. However, the  $pK_a$  signal of 7.5-8.5 may be attributed to the proton release from aromatic basic groups measured during the limited pH window of the potentiometric titrations (3 – 11).



**Fig. 3.11** -  $pK_a$  distribution of surface acidic functional groups on the surface of unmodified and modified carbon adsorbents.





When comparing the biochar/carbon nanostructures composites previous and after thermal treatment, the functionalities related to a  $pK_a$  value of 8 were considerably reduced, however, the processed biochar by continuous CVD showed a higher number of functionalities. This result also showed that the acidic groups were removed by thermal treatment under inert conditions. In addition, the high carbon coverage of magnetite prevents to determine its dissociation constants at 4.5 and 9 [162].




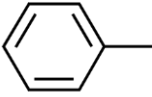
### **3.3.3. Adsorption behavior**

#### **3.3.3.1. Kinetics adsorption**

Regarding to the applicability of these novel composites in adsorption of evaporative emissions, it is needed to study the adsorption rate of different VOCs representatives of gasoline. First, to further analyze the adsorption kinetics results, a detailed look at the properties of the analytes is needed. [Table 3.2](#) compiles the characteristics that could affect not only the affinity for the adsorbent, but also the actual concentration of each VOC and, therefore, the degree of adsorption on each carbon-based material. Benzene, toluene, hexane, and pentane were chosen as VOCs representatives of evaporative emissions to evaluate the adsorption behavior of aliphatic and aromatic VOCs commonly found in the headspace of fuel tanks [20]. Based on their physical properties, the larger the molecular weight of the VOC, the higher the boiling point and therefore the lower the vapor pressure. Accordingly, at lower molecular weight the concentration and manometric pressure of the VOC will be higher, as it is observed in [Table 3.2](#). Furthermore, these compounds have distinct kinetic diameter ranging from 4.3 to 6 Å which must be considered in adsorption studies. Kinetic diameter allows to express the likelihood that a molecule of VOC collide with another molecule, indicating the molecule size as a target. Regardless of the fact that the kinetic diameters of benzene and toluene are similar (5.85 and 6 Å, respectively), their different dipole moment value also influences their uptake.



**Table 3.2** - Properties of VOCs under study and parameter measured on the serologic bottles headspace at 25°C and 1 atm of barometric pressure.

		Pentane	Hexane	Benzene	Toluene
Molecular structure					
Molecular weight	g mol <sup>-1</sup>	70.13	86.18	78.11	92.11
Boiling point	°C	36	69	80	111
Vapor pressure	atm	0.657	0.133	0.126	0.038
Kinetic diameter	Å	4.30	4.30	5.85	6.0
Dipole moment	D	0.00	0.00	0.00	0.36
Manometric pressure*	atm	0.225	0.126	0.151	0.041
Concentration*	mg L <sup>-1</sup>	2231	804	417	155

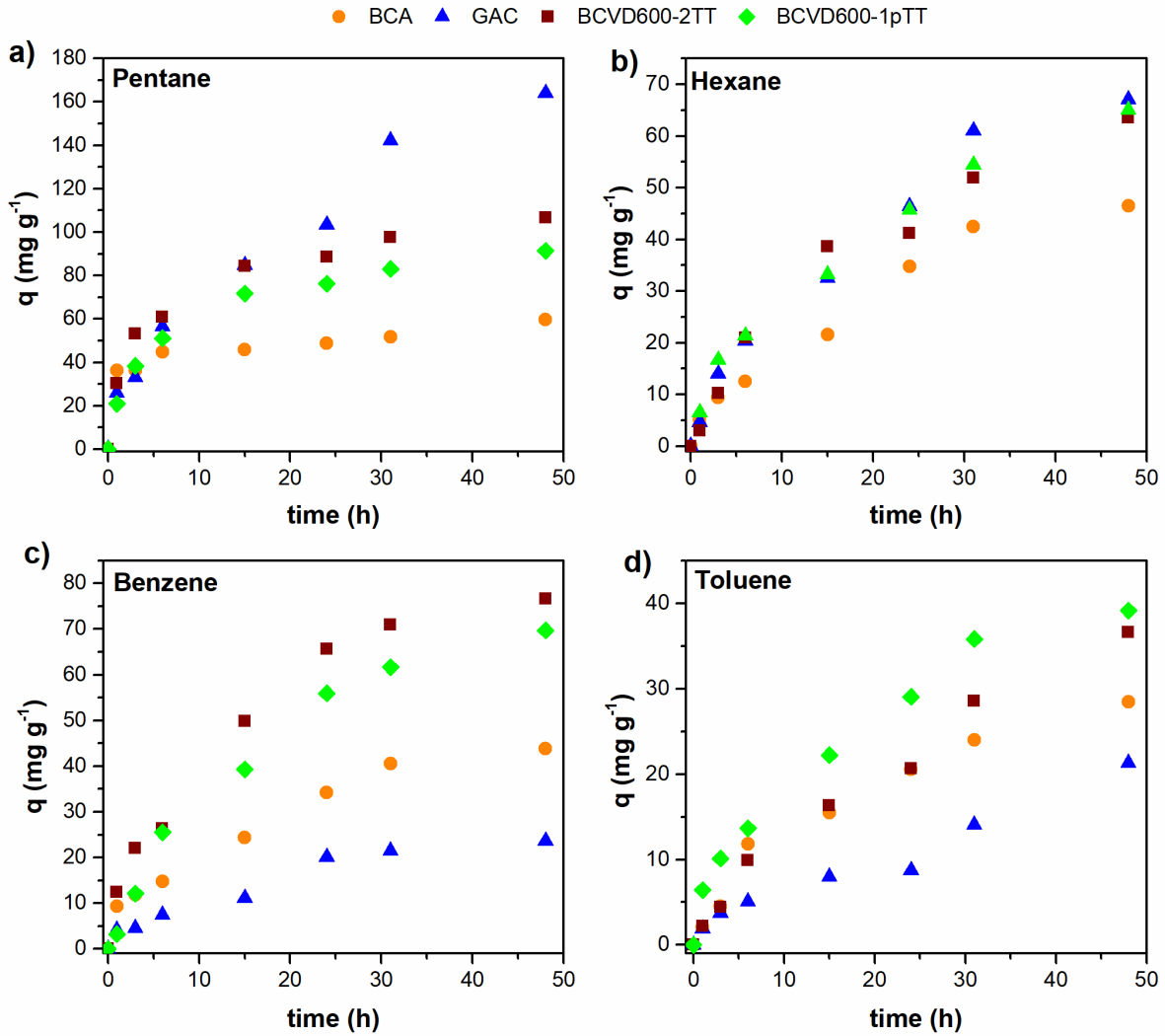
\* Measured before adsorption experiments.

To explore the kinetic behavior that could provide a carbon adsorbent with more exposed surface area and low tortuosity, the adsorption kinetics of pentane, hexane, benzene, and toluene on biochar and biochar/carbon nanostructures composites were evaluated in diurnal conditions. In addition, kinetics performance was compared with that of a commercial activated carbon. Overall, when comparing the removal of aliphatic molecules (pentane and hexane), activated carbon exhibited the highest adsorption capacity (169 and 63 mg g<sup>-1</sup>, respectively), whereas the aromatic molecules (benzene and toluene) uptake was higher by samples BCVD600-1pTT (73 and 38 mg g<sup>-1</sup>, respectively) and BCVD600-2TT (77 and 35 mg g<sup>-1</sup>, respectively). Nevertheless, it is important to highlight that activated carbon displayed a poor adsorption capacity for aromatic molecules (< 25 mg g<sup>-1</sup>), while samples



BCVD600-1pTT and BCVD600-2TT showed a very competitive aliphatic removal capacity compared to that of activated carbon. As it was expected, the VOCs adsorption capacity of biochar increased after the CVD process. In fact, adsorption removal of pentane, hexane and benzene increased 1.81, 1.44 and 1.67 times, respectively, compared with biochar. These results agree with a previous work where benzene uptake was improved after the growth of carbon nanostructures [42]. The lower volatility and concentration of toluene caused that the adsorption capacity of biochar only increased by 34% regardless of the growth of carbon nanostructures. A similar trend was observed when the adsorbents performance was analyzed from 6 h to the end of the kinetic measurement.

Taking in to account the well-known steps involved in particles diffusion in porous materials, intraparticle diffusion is currently the limiting factor during kinetics studies [164]. For instance, the narrow microporosity of activated carbon implied low adsorption rates since the high tortuosity provided by its pore morphology limits the intraparticle diffusion of VOCs [32]. Based on kinetics results, the novel adsorbent developed in this work counteracts this mass transfer disadvantage due to the more exposed surface area displayed by carbon nanostructures. The latest was proved by comparing the adsorption rates in the first 12 h (Table 3.3). Here is evident the restrictive diffusion of toluene ( $0.0005 \text{ mmol h}^{-1}$ ) in activated carbon. It is noteworthy that the biochar/carbon nanostructures composite showed faster adsorption rates of toluene ( $>0.0012 \text{ mmol h}^{-1}$ ) as a consequence of its negligible micropore volume ( $0.032 \text{ cm}^3 \text{ g}^{-1}$ ).



**Fig 3.12** - Adsorption kinetics of a) pentane, b) hexane, c) benzene and d) toluene on studied adsorbent in static mode at 25 °C.

**Table 3.3** - Adsorption rates calculated for the first 12 h of kinetic study.

Pollutant	Adsorption rate (mmol h <sup>-1</sup> )			
	GAC	BCA	BCVD600-2TT	BCVD600-1pTT
Pentane	0.0066	0.0012	0.0053	0.0052
Hexane	0.0023	0.0014	0.0032	0.0022
Benzene	0.0007	0.0015	0.0036	0.0034
Toluene	0.0005	0.0012	0.0013	0.0014



Regarding the magnitude of the pentane adsorption capacity, it is important to point out that its higher vapor pressure and small kinetic diameter have more influence in the intraparticle diffusion [101]. This last one promoted a higher pentane concentration, conferring driving force to diffuse into the narrow porosity of activated carbon. In this sense, the small pores and thus the entire surface area of all materials are accessible for pentane molecules, resulting in a greater adsorption capacity. On the other hand, biochar/carbon nanostructures composites showed similar adsorption rate for benzene and hexane at the first 12 h, since the unblocked interspaces generated by the arrangement of the carbon nanostructures did not show important diffusional restrictions by either molecule. However, the higher kinetic diameter of benzene also limited the mass transfer in narrow micropores of activated carbon.

The kinetic results were fitted by nonlinear convergence to pseudo-first and pseudo-second equation to obtain the kinetic parameters. According to the correlation coefficients ( $R^2$ ), the experimental data were well fitted to both models, although the pseudo-first model slightly better described the adsorption process. Even though this result suggest that physical adsorption could be the rate limiting step, the well fit to both models also suggest that the adsorption of different VOCs onto carbon-based materials was also affected by chemical interaction adsorbate-adsorbent [37]. By comparing the pseudo-second order rate constants ( $k_2$ ) of all samples, it is observed that pentane molecules diffuse faster, which agrees with what was discussed above. Additionally, it is observed that biochar/carbon nanostructures composite showed similar adsorption rates constant for hexane, benzene, and toluene, which indicates a faster mass transfer in comparison to that in activated carbon [91].

**Table 3.4** - Kinetic constants for adsorption of evaporative emissions onto adsorbent materials.

	Parameters	Pollutant			
		Pentane	Hexane	Benzene	Toluene
<b>GAC</b>					
Pseudo first-order	$k_1$ ( $\text{min}^{-1}$ )	71.4	0.042	0.050	0.006
	$q_e$ ( $\text{mg g}^{-1}$ )	87.14	77.79	26.43	81.23
	$R^2$	0.993	0.983	0.958	0.945
Pseudo second-order	$k_2$ ( $\text{g (mg min)}^{-1}$ )	0.0002	0.0004	0.001	0.0002
	$q_e$ ( $\text{mg g}^{-1}$ )	208.74	102.95	36.45	58.533
	$R^2$	0.963	0.984	0.963	0.941
<b>BCA</b>					
Pseudo first-order	$k_1$ ( $\text{min}^{-1}$ )	1.113	0.041	0.062	0.056
	$q_e$ ( $\text{mg g}^{-1}$ )	48.61	55.08	45.66	29.36
	$R^2$	0.878	0.981	0.963	0.979
Pseudo second-order	$k_2$ ( $\text{g (mg min)}^{-1}$ )	0.029	0.0004	0.001	0.001
	$q_e$ ( $\text{mg g}^{-1}$ )	51.88	76.51	58.74	38.88
	$R^2$	0.931	0.981	0.965	0.985
<b>BCVD600-2TT</b>					
Pseudo first-order	$k_1$ ( $\text{min}^{-1}$ )	0.225	0.051	0.076	0.024
	$q_e$ ( $\text{mg g}^{-1}$ )	94.88	66.51	77.85	51.73
	$R^2$	0.946	0.984	0.983	0.986
Pseudo second-order	$k_2$ ( $\text{g (mg min)}^{-1}$ )	0.003	0.0004	0.001	0.0002
	$q_e$ ( $\text{mg g}^{-1}$ )	106.86	76.51	99.28	73.33
	$R^2$	0.979	0.981	0.986	0.987
<b>BCVD600-1pTT</b>					
Pseudo first-order	$k_1$ ( $\text{min}^{-1}$ )	0.177	0.049	0.057	0.061
	$q_e$ ( $\text{mg g}^{-1}$ )	82.73	69.36	73.94	40.56
	$R^2$	0.970	0.975	0.995	0.972
Pseudo second-order	$k_2$ ( $\text{g (mg min)}^{-1}$ )	0.002	0.001	0.001	0.001
	$q_e$ ( $\text{mg g}^{-1}$ )	95.70	89.43	99.78	52.47
	$R^2$	0.992	0.982	0.995	0.979

$k_1$  = pseudo-first order rate constant.

$k_2$  = pseudo-second order rate constant.

$q_e$  = adsorption capacities at equilibrium.

$R^2$  = Determination coefficient.



### 3.3.3.2. Correlation adsorbate-adsorbent in VOCs adsorption

To analyze the effect of adsorbate and adsorbent properties on adsorption capacity, a correlation assessment of surface area, pore volume,  $\text{pH}_{\text{PZC}}$ , contact angle, molecular cross-sectional area and vapor pressure with adsorption capacities was performed (Fig. 3.13). The correlation coefficients ( $R^2$ ) of the relationship between VOCs adsorption capacities and adsorbent physical properties were lower than 0.77, while the correlation with adsorbent chemical properties and adsorbate features showed values smaller than 0.62 and 0.94, respectively.

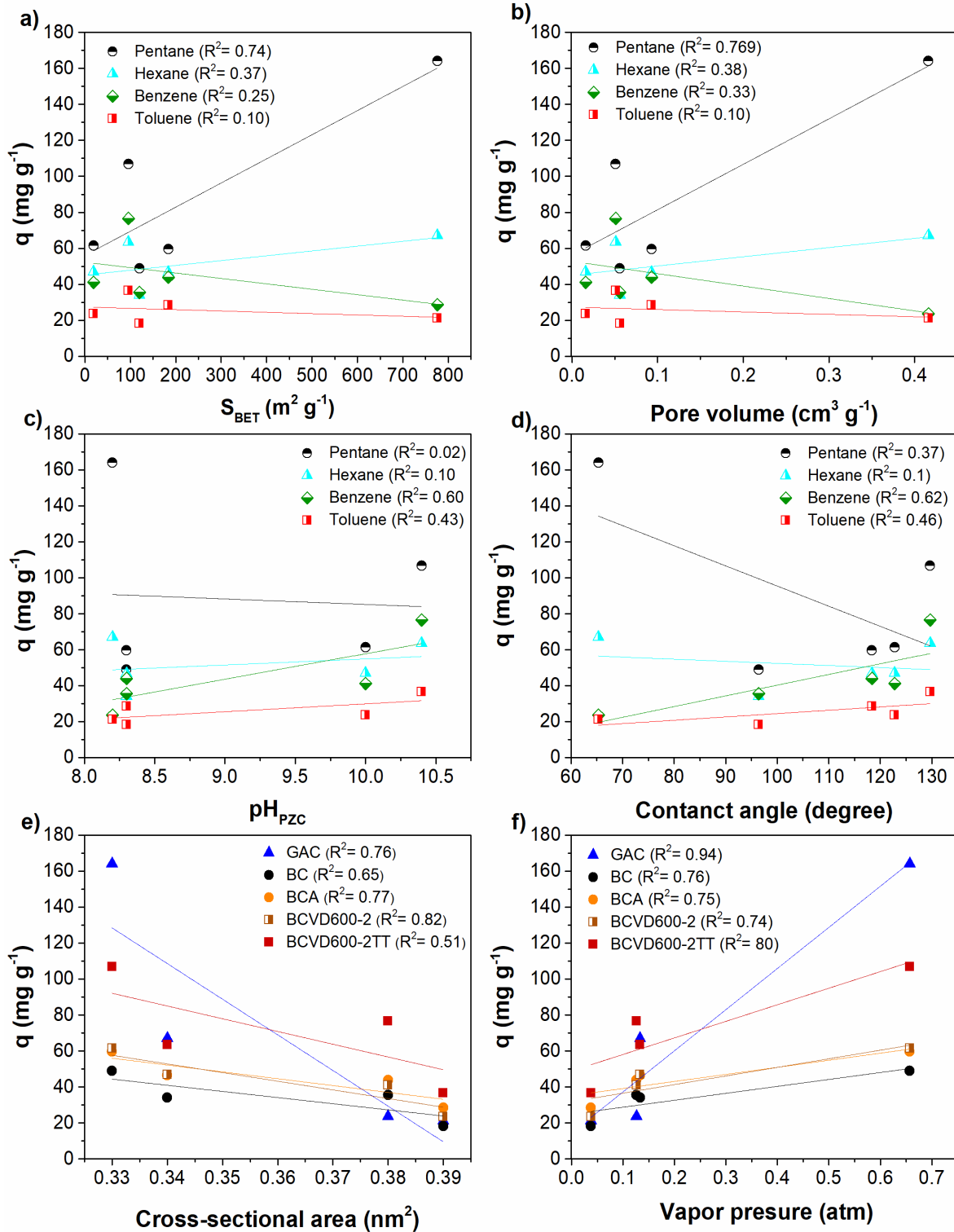
As it is known, the adsorption behaviors of various porous adsorbents are usually studied by the assessment of the adsorbent physical properties. Therefore, the linear relationship between surface area and adsorption capacity of VOCs was first explored. As it is shown in Fig. 3.13a, a slight negative correlation was observed on benzene ( $R^2=0.25$ ) and toluene ( $R^2=0.10$ ). Oppositely, aliphatic molecules displayed positive correlations, being more significant on pentane ( $R^2=0.74$ ). Similarly, there is a high linearity between pentane adsorption capacity and pore volume ( $R^2=0.77$ ) (Fig. 3.13b). These relationships indicate that the smaller the molecule, the higher adsorption capacity will be. Moreover, it suggested that VOCs adsorption is mainly physical and exothermic. A similar result has been previously reported [55]. The adsorbent chemical properties such as the  $\text{pH}_{\text{PZC}}$  and hydrophobicity are another important factor to evaluate VOC adsorption onto carbonaceous adsorbent (Fig. 3.13c, d). The correlations between both parameters and VOCs adsorption capacity were poor, with  $R^2$  values of 0.02–0.62. The negative correlation between pentane adsorption capacity and contact angle confirmed that the adsorption capacity of nonpolar VOC is closely associated with the adsorbent textural properties, and no obvious trend was found with the adsorbent chemical features. However, it is worth noting that the positive linear relationship between benzene adsorption capacity,  $\text{pH}_{\text{PZC}}$  and contact angle pointed out that



the more basic the carbon adsorbent, the greater the ability to adsorb aromatic molecules. The latter is explained by the fact that the increase of  $sp^2$  delocalized electrons on carbon nanostructures promotes a major affinity for benzene aromatic rings, since these are mainly attached face-to-face by  $\pi$ - $\pi$  interactions [118].

The shape of the molecule also influences VOC adsorption onto carbon materials (Fig. 3.13e). According to the size exclusion theory, only when the pore diameter is larger than the molecular diameter, the VOCs molecules can enter the pores of the adsorbent material. For nonpolar VOCs, the larger their molecular diameter, the lower their diffusion capacity in the adsorbent micropore [36]. Based on the above, the negative linear relationship between the adsorption capacity of the VOCs and the molecular cross-section area made evident the diffusional restrictions of larger molecules. Indeed, the higher correlation coefficient value for activated carbon (0.76) confirmed the effect of the adsorbent microporosity on the adsorption of larger VOCs. In contrast, the poor microporosity and the most exposed surfaced of carbon nanostructures on biochar promoted the mass transfer of all VOCs to the active sites, which agree with their similar capacity to uptake all four VOC. Finally, the positive lineal relationship between VOCs vapor pressure and adsorption capacity confirmed that the more volatile the molecule, the greater the VOC mass transfer in the adsorbent.





**Fig. 3.13** - Correlation between VOCs adsorption capacity and adsorbate (a-d) and adsorbent properties (e, f).



### 3.3.3.3. Adsorption mechanism

In general, the adsorption of polar and nonpolar VOCs onto carbonaceous adsorbents are mainly controlled by five potential interactions related to van de Waals forces,  $\pi$ - $\pi$  bond, hydrophobic effect, hydrogen bond, and covalent and electrostatic interactions [11]. On the other hand, it has been pointed out that the VOC adsorption performance onto carbonaceous materials is not only related to the features of the adsorbate molecules, but also to the properties of the adsorbent. Thus, it is necessary to illustrate the effect of the physical and chemical properties of the adsorbent, as well as influence of VOCs features on adsorption behavior to clarify their contribution in the overall adsorption process.

Physical adsorption can be attributed to the intermolecular gravitation, namely van de Waals forces. Because of the weak interactions, no chemical bonds and low adsorption heat are involved [163], the solid adsorbent can be regenerated easily and keep its original structure unchanged [164]. In porous (GAC) and nonporous (BCVD600-1pTT) adsorbents, the mass transfer occurs from the gas phase to the surface of the adsorbent via axial dispersion, and the adsorption rate is determined by micropore volume. In the case of activate carbon, it is worth noting that its narrow microporous structure increased the diffusion resistance leading to low diffusion rates [7], whereas the poor microporosity of BCVD600-1pTT significantly increased the intraparticle diffusion, resulting in a fast VOCs removal. This last interpretation is in concordance with the results of kinetic studies. Moreover, it was observed that the physical adsorption rate was controlled by the VOCs concentration, related to its vapor pressure.

By analyzing the interactions that govern the adsorption of VOC onto carbonaceous adsorbents, the contribution of different VOCs to the adsorption process has been earlier reported by Liu et al., [60]. Indeed, dispersive interactions (induced dipoles) have been



described as the mainly contribution to the adsorption of all VOCs onto carbon-based materials. Particularly, the dispersive interactions are the only mechanism to cause the adsorption of pentane and hexane. Furthermore, dispersive interactions increase with the increase of carbon atoms in the adsorbate.

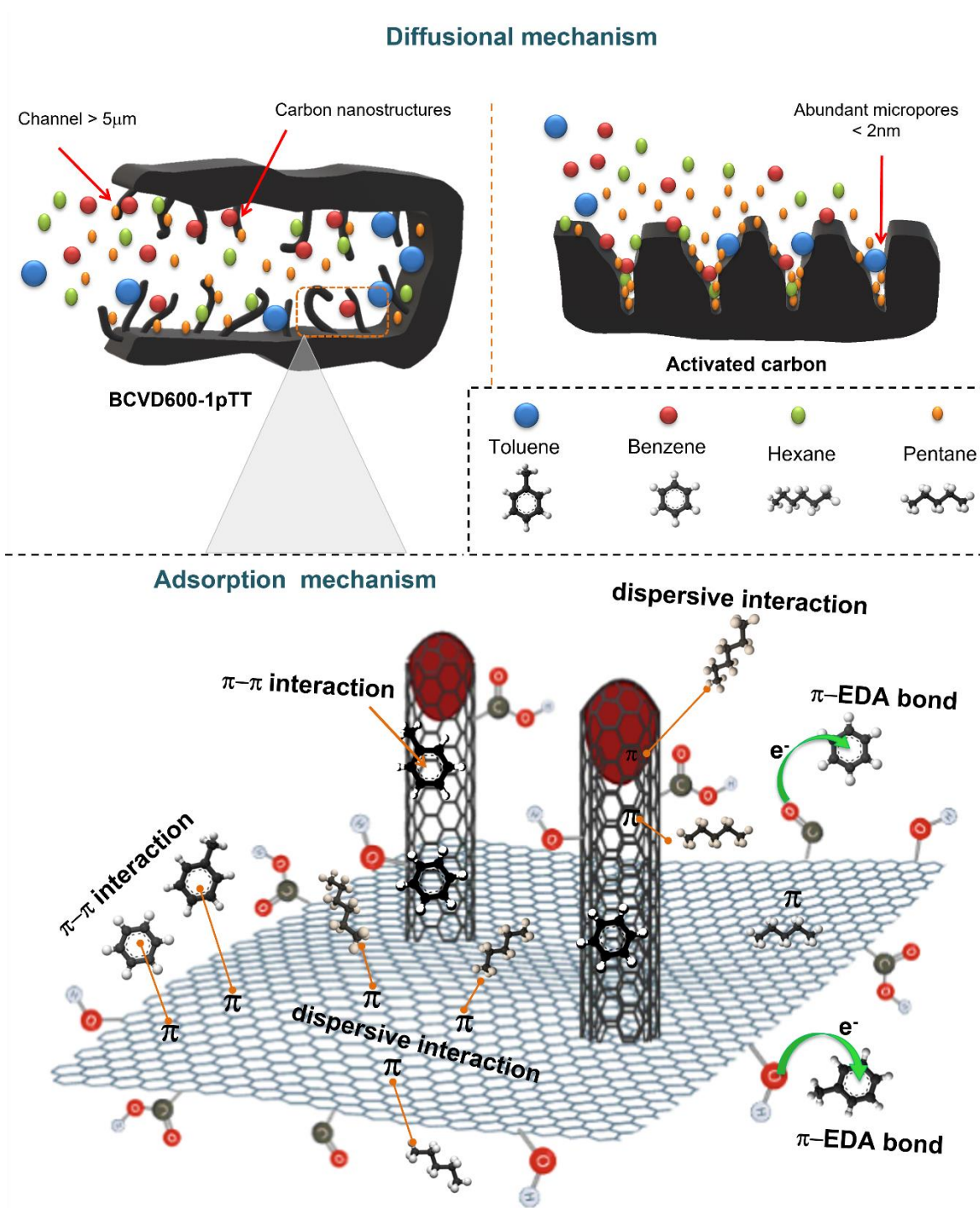
In addition to the van de Waals forces,  $\pi$ - $\pi$  dispersive interaction is another important mechanism of VOCs adsorption. Most of the carbon atoms in carbonaceous materials have the  $\pi$  electron orbit, which can be bound with benzene and toluene molecules with  $\pi$  electrons to form  $\pi$ - $\pi$  dispersive interaction with face to face or offset face-to-face orientations [87]. However, all the carbon atoms of pentane and hexane are  $sp^3$  hybridized, and there are no extra orbitals available to form the  $\pi$  bond.

Since the aliphatic VOCs were adsorbed on the carbonaceous materials only by dispersive forces, a combined adsorption mechanism of specific and dispersive interactions should be considered when the aromatic VOCs were adsorbed. Regarding the adsorption controlled by chemical process, there was a stable electron donor-acceptor complex formed owing to the delocalized  $\pi$  electron density of benzene and toluene as electron acceptor to combine with ion pair electrons of oxygen atoms from functionalities on carbon adsorbent as electron donor [97]. Clearly, since the presence of the methyl group in toluene increases the  $\pi$  electron density of the aromatic ring, its adsorption energy is larger than that of benzene. Herein, the specific interaction could be mainly attributed to the hydroxyl groups on the surface of BCVD600-1pTT sample.

Considering the molecular shape, the aromatic molecules are more strongly adsorbed than linear molecules because the various possibilities of interaction and by the multilayer arrangement possibilities, which are very suitable. Moreover, dispersive interactions of toluene were stronger than those of benzene. Toluene has a stronger specific interaction



than benzene because toluene presents a slight dipole moment (0.36 D) compared to the zero-dipole moment of benzene. It was understandable that toluene was mainly trapped through  $\pi$ - $\pi$  dispersive interactions with the aromatic ring moving to the carbon surface. It has been reported that the plane adsorption geometry of toluene was highly stable [73]. Regardless of the highest affinity of carbon-based materials for heavier VOCs described here, experimental results showed the highest adsorption capacities for pentane because the wide concentration difference with the other VOCs, as occurs in a real automotive system. Nevertheless, by using the same concentration of these VOC, it would be possible to observe a higher adsorption capacity for toluene and benzene in an experimental system.



**Fig. 3.14** - Diffusional and adsorption mechanisms of toluene, benzene, hexane, and pentane on carbonaceous adsorbents by chemical and physical adsorption.



### 3.4. Conclusions

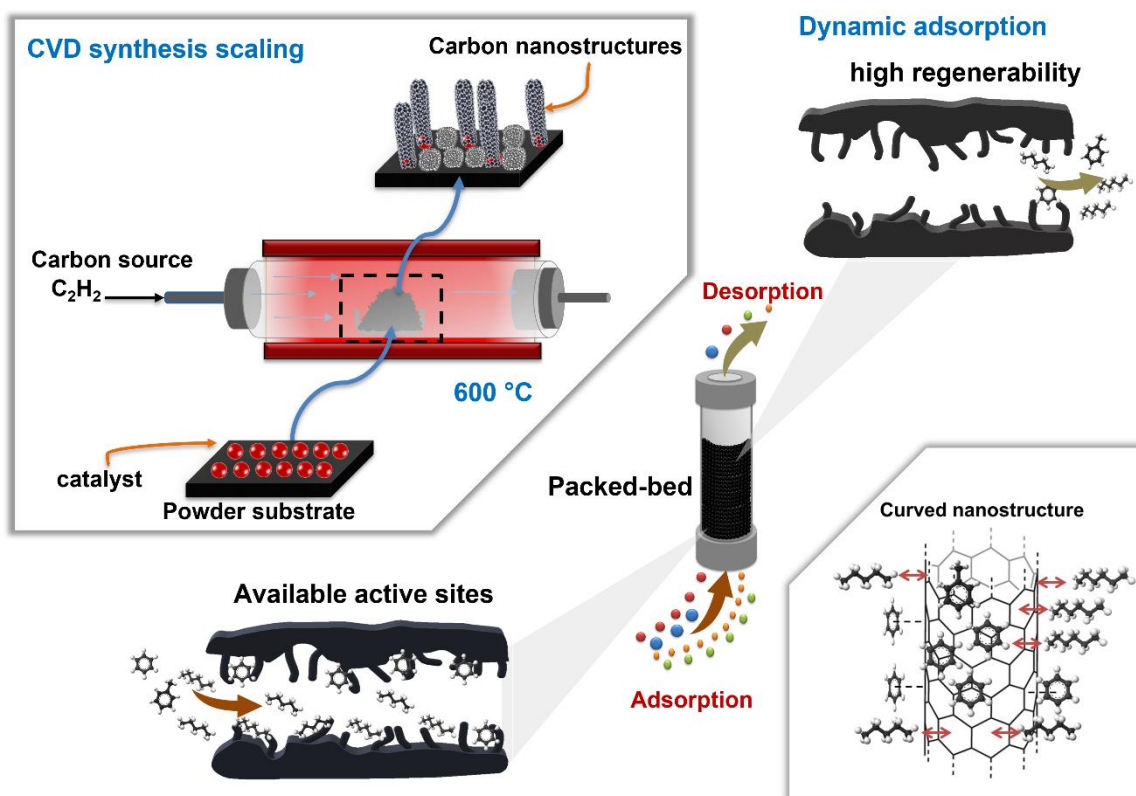
The purpose of this work was to synthesize low-cost adsorbents with high exposed surface area and excellent adsorption capacity for evaporative emissions. In brief, the efficacy of growing carbon nanostructures on biochar by CVD pulsed-injection process was investigated to increase the adsorption kinetics of pentane, hexane, benzene, and toluene as VOCs representative of evaporative emissions in static mode. Electronic microscopy makes evident the effect of injecting two carbon sources pulsed of one minute at 600 °C (CVD pulsed-injection). The use of two pulses of carbon of only 1 min promoted a higher growth of CNTs and CNFs than when a continuous CVD process was used. In addition, by CVD pulsed-injection the biochar surface area increased from 184 to 240 m<sup>2</sup> g<sup>-1</sup>, which depicted the effect of exposed carbon nanostructures. Therefore, adsorption studies demonstrated that BCVD600-1pTT had a high pentane (169 mg g<sup>-1</sup>), hexane (63 mg g<sup>-1</sup>), benzene (73 mg g<sup>-1</sup>), and toluene (38 mg g<sup>-1</sup>) adsorption capacity, and faster kinetic adsorption than activated carbon. Particularly, pentene was adsorbed faster on activated carbon because its smaller size enhances mostly the mass transfer through narrow micropores. The adsorption capacity of toluene and benzene was bigger in biochar/carbon nanostructures composites than on commercial activated carbon, due to more exposed delocalized  $\pi$  electrons on carbon nanostructures, which strongly interact with nonpolar VOCs. According to the correlation assessment, the textural properties of the adsorbents have positive linear relationship with the adsorption capacity of smaller VOCs, while aromatic VOCs showed a negative correlation between pore volume and adsorption capacity. Furthermore, the more basic the adsorbent surface, the greater the adsorption capacity of nonpolar aromatic VOCs, which is conducted via dispersive interaction between aliphatic molecules and delocalized  $\pi$ -electrons, and by  $\pi$ - $\pi$  interactions between the  $\pi$ -electrons in the benzene ring and those in the carbon graphitic layers. Considering these



results, it can be suggested that this novel biochar/carbon nanostructures composite could be used in automotive canister instead of activated carbon.

# CHAPTER 4

## Adsorption/desorption of aromatic and aliphatic VOCs by carbon nanostructures modified biochar in dynamic regime







### Abstract

In this study, the dynamic adsorption/desorption behavior of different volatile organic compounds onto a biochar tailored with carbon nanostructures was investigated and compared with the efficiency of a commercial activated carbon. Biochar/carbon nanostructures composite (BCVD600-1pTT) was synthesized by chemical vapor deposition at 600 °C in a rotary furnace. Carbonaceous adsorbents were characterized by XRD, Raman spectroscopy, SEM, TEM and N<sub>2</sub> physisorption. The resultant composite had an increment in surface area from 1 to 300 m<sup>2</sup> g<sup>-1</sup> after CVD process due to the synthesis of carbon nanostructures like carbon nanofibers and onion-like carbons. BCVD600-1pTT exhibited similar adsorption capacities for pentane, hexane and benzene than activated carbon. Furthermore, the regeneration process only affected the adsorption performance of BCVD600-1pTT by about 10%, while the commercial activated carbon reduced its capacity by up to 50%. The excellent adsorption/desorption performance of BCVD600-1pTT in dynamic mode was mainly related to the basic character and exposed surface area of carbon nanostructures, and to the least mass transfer resistance compared with that of activated carbon. In addition, BCVD600-1pTT showed similar breakthrough curves after four cycles of adsorption/desorption of benzene, with only a decrease of breakthrough time of 16 min, while that of activated carbon decreased up to 20 min in the second cycle. These results indicated that BCVD600-1pTT would become a promising candidate for VOC recovery in automotive canisters.



#### 4.1. Introduction

According to the vehicular emission inventory, evaporative emissions have been a growing concern in recent years [9], [23]. Evaporative emissions result from gasoline vapor leakage from the automotive's fuel tank [19]. In fact, evaporative emissions currently represent the sixth highest sources of anthropogenic volatile organic compounds (VOCs) in the world [18]. Regulations on the reduction of VOCs emissions have been strengthened. For instance, the Goteborg protocol stipulated that the amount of VOCs emissions in 2020 should have been half the amount released in 2000 [166]. In addition, the European Union obligated member states to cut the emissions of VOCs by 40% by 2030 [167]. Therefore, due to their high toxicity and carcinogenic character, combined with their contribution to the formation of tropospheric ozone and photochemical smog [23], [29], the recovery and reuse of evaporative emissions from gasoline are of significant importance from both economic and environmental point of view.

Until now, the automotive industry has considered adsorption process as the most efficient and energy-saving candidate for capturing and recovering VOCs from evaporative emissions [107]. Modern vehicles are equipped with an evaporative loss control device, also known as canister, which is packed with activated carbon to prevent VOCs leakage into the atmosphere when the vehicle is not running. Subsequently when the vehicle is running, some of the air that is sucked into the intake air system is circulated through the canister to desorb the VOCs and draw them into the engine; thus, a closed system must be formed [27]. However, the narrow microporosity in activated carbon implies serious diffusional restrictions to completely desorb the VOCs, which over time leads to a lack of regenerative ability [13]. Thus, it is required a new adsorbent with the capability of adsorb and desorb the VOCs from evaporative emissions faster enough to exceed the regenerative ability of a commercial activated carbon under diurnal conditions.



The choice of an adsorbent for VOC removal must consider a wide variety of factors, including surface area, pore structure, and chemical functional groups. Examples of adsorbents that have been proposed to replace activated carbon in automotive canisters are zeolites, silica gel, metal-organic frameworks and polymers [97]. To date, most research is focused on investigating the influence of physicochemical properties of different adsorbents on VOCs adsorption capacity. However, few works have addressed the impact of the porous structure of different materials in dynamic adsorption/desorption process. For instance, the pore structure and morphology of mesoporous silica has been correlated with VOCs adsorption/desorption [168]. Additionally, the effect of different pore sizes of zeolites has been further studied on the dynamic adsorption/desorption of VOCs [169]. On the other hand, it has been reported that the breakthrough adsorption capacity of a regenerated activated carbon decreased three times more than that of a macroporous hyper-crosslinked polymer [30]. Nevertheless, the expensive cost of these adsorbents is one of the major challenges for its commercial application. Over the past few decades, biochar has emerged as a potential alternative to activated carbon due to its null presence of micropores, stable physicochemical properties, and regeneration ability [41]. Many agro-industrial and forestry waste materials have been given special emphasis as raw materials for the preparation of biochar because they are renewable, highly available, reduce the cost of production and their reuse reduces potential environmental pollution [170]. Recently, our research group synthesized macroporous biochar from waste agave bagasse, a typical byproduct from the tequila production industry, increasing the adsorption kinetics of benzene in comparison with those of activated carbon [42]. However, one of the potential problems associated with biochar is that its low surface area does not allow to obtain high adsorption capacity for VOCs. Thus, there have been some efforts to modify the biochar surface to improve evaporative emissions recovery.



In regard to improve the exposed surface area of carbon-based materials, the growth of carbon nanostructures on biochar have attracted increasing attention because this modification has enhanced the VOCs adsorption capacity of biochar. The growth of carbon nanostructures offers excellent features such as high exposed surface area, high affinity for VOCs and reliable desorption performance [121]. According to previous studies, by growing carbon nanostructures by chemical vapor deposition synthesis, it was possible to double the biochar's surface area from 120 to 240 m<sup>2</sup> g<sup>-1</sup>, enhancing the benzene and toluene adsorption capacity of activated carbon 260% and 98%, respectively [17]. In contrast with the porous carbon-based materials obtained by chemical and physical activation processes, the modified biochar with carbon nanostructures exhibits more suitable physical and chemical properties to improve the adsorption performance of evaporative emissions [171]. These previous results encourage us set up a fixed-bed system to measure the adsorption/desorption performance of VOCs from a model gas stream by carbon materials in dynamic configuration. For this assessment, first the available surface area of a macroporous biochar was increased by chemical vapor deposition (CVD). In addition, the adsorbents physicochemical properties were characterized by N<sub>2</sub> physisorption, Raman spectroscopy, X-Ray diffraction, scanning and transmission electron microscopies, and potentiometric titrations. Finally, breakthrough curves of representative VOCs were measured evaluating dynamic adsorption and desorption performance of raw and CVD-processed biochar, and also a commercial activated carbon was considered for comparison. In this study, pentane, hexane, benzene, and toluene were chosen as the representative pollutants from evaporative emissions.



## 4.2. Methods

### 4.2.1. Materials

All chemicals used in this research (HCl 0.1 N, NaOH 0.1 N, NaCl, NaBH<sub>4</sub>, FeSO<sub>4</sub>·7H<sub>2</sub>O, C<sub>2</sub>H<sub>2</sub>, C<sub>5</sub>H<sub>12</sub>, C<sub>6</sub>H<sub>14</sub>, C<sub>6</sub>H<sub>6</sub>, C<sub>7</sub>H<sub>9</sub> and sodium carboxymethylcellulose (CMC)) were reagent grade obtained from commercial vendors. Biochar was obtained by the pyrolysis of waste agave bagasse at 600 °C in nitrogen atmosphere, and washed with HCl 4M to remove the inorganic content. In addition, the selected commercial granular activate carbon (AC) was a bituminous based (Filtrasob 400) supplied by Calgon Carbon Company. In order to obtain a suitable particle size for packing the columns, carbon adsorbents were crushed and sieved with a mesh number of 170-270. After the particles were sieved, the biochar was rinsed with deionized water and then dried at 80 °C for 24 h.

### 4.2.2. Chemical vapor deposition process

Prior to CVD process, the catalyst was impregnated on biochar by the following procedure. Under inert atmosphere, 100 mL of CMC 4.96x10<sup>-5</sup> M were mixed with 50 mL of FeSO<sub>4</sub>·7H<sub>2</sub>O 0.11 M, followed by the dropwise addition of 10 mL of NaBH<sub>4</sub> 0.22 M [126]. Then, 0.2 g of biochar were contacted with 20 mL of the Fe<sup>0</sup>/CMC suspension previously prepared. The container was sealed and stirred at 125 m<sup>-1</sup> for 48 h at 25 °C to introduce zero-valent iron nanoparticles on the biochar surface [42]. After impregnation, the material was rinsed with double deionized water to eliminate residual chemicals and dried at 90°C for 24 h.

The CVD system consisted of a horizontal tubular furnace with one-zone heating and a quartz tube with an internal diameter of 7 cm. The sample was first placed in the middle zone of the tubular reactor while it was purged with 90 mL min<sup>-1</sup> of N<sub>2</sub> gas. Then, the sample was heated up at a rate of 25 °C min<sup>-1</sup> until 600 °C. Once the CVD temperature was reached,



it was held for 2 min before the carbon source ( $C_2H_2$ ) was injected at  $20 \text{ mL}\cdot\text{min}^{-1}$  for 1 min, followed by 5 min without  $C_2H_2$  supply, then  $C_2H_2$  was injected for another 1 min, followed by another 7 min without  $C_2H_2$  supply. Once the CVD process ended, samples were cooled down to room temperature. To increase the surface area and reduce oxygen functionalities of biochar/carbon nanostructures composite, the sample was thermally treated at  $650 \text{ }^\circ\text{C}$  using a heating rate of  $10^\circ\text{C min}^{-1}$  during 10 min under  $N_2$  atmosphere.

### 4.2.3. Analytical methods

Chemical and textural features of an adsorbent are the decisive factors that determine its adsorption performance. Therefore, the properties of the different carbonaceous adsorbents studied in this research were comprehensively studied. In this sense, the external and internal morphologies of carbon nanostructures onto biochar were analyzed by scanning electron microscopy (SEM, FEI - FIB Dual Beam Helios Nanolab 600) and transmission electron microscopy (TEM, Tecni FEI 300 operated at 300 kV with  $CuK_\alpha$  radiation), respectively. The surface area, porosity and crystal structure of carbonaceous adsorbents were investigated by nitrogen adsorption-desorption measurements (Micromeritics ASAP-2020 at 77 K) and X-ray powder diffraction (XRD, SmartLab Rigaku diffractometer), respectively. Furthermore, the structural carbon differences between carbonaceous adsorbents were studied by Raman spectroscopy (inVia MICRORAMAN: RENISHAW using a 514 nm laser). The surface chemical changes were determined by the surface charge distribution and points of zero charge ( $pH_{PZC}$ ) obtained by potentiometric titrations (Titrator Metler Toledo, PL 70).

### 4.2.4. Dynamic adsorption measurements

In order to determine the dynamic adsorption behavior, breakthrough measurements were performed as shown schematically in Fig. 4.1. Prior to adsorption measurements, samples were degassed overnight at  $90 \text{ }^\circ\text{C}$ . Then,  $\sim 0.5 \text{ g}$  of adsorbent (170-270 mesh)



were loaded into the adsorption column ( $D = 0.5$  cm,  $L = 10$  cm) made of glass. A glass filter plate was located at the bottom of the column as support of the adsorbent bed. Dry nitrogen, at a flow rate of  $25 \text{ mL min}^{-1}$ , was used as carrier gas. During the experiment, the inlet concentration ( $C_0$ ) of each VOC was constant by maintaining the same nitrogen flow rate. To saturate the carrier gas with a desired VOC, this was passed through a glassy stripping reactor containing the liquid VOC sample. As a result, the VOCs vapor thoroughly mixed with the nitrogen stream was led from the stripping reactor toward packed bed. The breakthrough curves were obtained by analyzing the inlet and outlet concentrations of each VOC as a function of time in a gas chromatography instrument equipped with a flame ionization detector (GC-FID). Herein, the equilibrium dynamic adsorption capacity ( $q$ , mg VOCs  $\text{g}^{-1}$ ) was calculated by the numerical integration of the breakthrough curves, according to the following equation [172].

$$q_{calc} = \frac{Q}{m \cdot 10^{-6}} \int_0^{t_s} (C_0 - C) dt \quad (\text{Eq. 4.1})$$

where  $Q$  is the flow rate of gas stream,  $\text{mL min}^{-1}$ ;  $m$  is the mass of the adsorbent, g;  $C_0$  and  $C$  are the inlet and outlet concentration in  $\text{mg L}^{-1}$  of each component, respectively;  $t_s$  is the saturation breakthrough time, min; and  $q_{calc}$  is the calculated adsorption capacity,  $\text{mg g}^{-1}$ . To obtain  $q_{calc}$  and additional important parameter used to estimate dynamic adsorption performance the following calculations were needed:

a) *Fractional capacity*:

$$\phi = \frac{\int_{V_{0.1}}^{V_{0.9}} (C_{0.85} - C_{0.1}) dV}{(V_{0.9} - V_{0.1}) C_0} \quad (\text{Eq. 4.2})$$



where  $V_{0.1}$  is the volume treated to the 0.1 breakthrough points [L], and  $V_{0.9}$  is the volume treated at 0.9 breakthrough points [L].  $C_0$  is the initial concentration of the effluent [ $\text{mg L}^{-1}$ ].  $C_{0.1}$  and  $C_{0.85}$  are the concentration at 10 and 85 % of exhaustion.

b) *Height of the mass transfer zone [cm]:*

$$H_{MTZ} = H \left[ \frac{V_{0.85} - V_{0.1}}{V_{0.1} + \phi(V_{0.85} - V_{0.1})} \right] \quad (\text{Eq. 4.3})$$

where  $H$  is the height of the adsorber [cm].

c) *Rate of the mass transfer zone [cm]:*

$$R_{MTZ} = \frac{H_{MTZ} \times Q}{V_{0.85} - V_{0.1}} \quad (\text{Eq. 4.4})$$

where  $Q$  is the influent flux [ $\text{mL min}^{-1}$ ]

d) *Area under the breakthrough curve:*

$$A = \int_{t=0}^{t_s} C_{ads} dt \quad (\text{Eq. 4.5})$$

$$C_{ads} = C_0 - C$$

where  $C_{ads}$  is the adsorbed concentration in the solid [ $\text{mg L}^{-1}$ ].  $C_0$  and  $C$  are the initial and registered concentration at certain time.  $C$  is the breakthrough point ( $C/C_0 = 0.85$ ).  $t_s$  is the saturation breakthrough time, min

e) *Total mass adsorbed [mg]:*

$$q_{total} = \frac{Q \times A}{1000} \quad (\text{Eq. 4.6})$$

f) *Total mass [mg]:*

$$m_{total} = \frac{C_0 \times Q \times t_s}{1000} \quad (\text{Eq. 4.7})$$

g) *% total removal [%]:*





$$\% \text{ total removal} = \frac{q_{total}}{m_{total}} \times 100 \quad (\text{Eq. 4.8})$$

h) *Removal capacity* [ $\text{mg g}^{-1}$ ]:

$$q_e = \frac{q_{total}}{m} \quad (\text{Eq. 4.9})$$

In this study, the breakthrough point was considered as the point where the effluent concentration reached 10% of the influent concentration ( $C/C_0 = 0.1$ ). The time corresponding to this point is known as breakthrough time ( $t_b$ ). When the effluent concentration reaches 85% of the influent concentration, it is considered the saturated point (referring to saturating time ( $t_s$ )).

The empty-bed contact time (EBCT) was constant in all experiments, which refers to the time required for a fluid to pass through the volume equivalent of the packed bed, and it is expressed by:

$$EBCT = \frac{V_A}{Q} \quad (\text{Eq. 4.10})$$

where  $V_A$  is the volume occupied of the packed-bed, mL; and  $Q$  is the flow rate of gas stream,  $\text{mL min}^{-1}$ . Furthermore, detailed computations of the main operational condition in packed-bed were obtained as follows:

$$\text{Step 1) Adsorber area } [\text{cm}^2]: \quad A_R = \pi r^2 \quad (\text{Eq. 4.11})$$

where  $r$  is the radio of the adsorber column [cm].

$$\text{Step 2) Adsorber volume } [\text{cm}^3]: \quad V_R = A_R h \quad (\text{Eq. 4.12})$$



where  $h$  is the height of the adsorber [cm].

$$\text{Step 3) Particle density [g cm}^{-3}\text{]} \quad \rho_P = \frac{m_{total}}{V_R} \quad (\text{Eq. 4.13})$$

where  $m_A$  is the mass of the adsorbent [g].

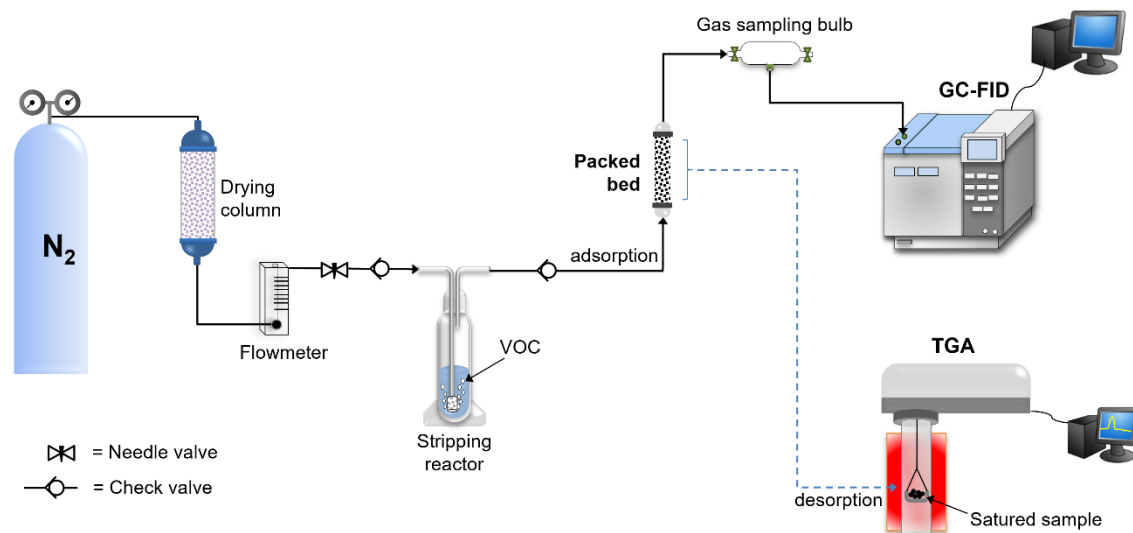
$$\text{Step 4) Bed density [g cm}^{-3}\text{]:} \quad \rho_B = \frac{m_{total}}{V_A} \quad (\text{Eq. 4.14})$$

where  $V_A$  is the adsorbent volume [cm<sup>3</sup>].

$$\text{Step 5) Bed Porosity} \quad \epsilon_B = 1 - \frac{\rho_B}{\rho_P} \quad (\text{Eq. 4.15})$$

#### 4.2.5. Regeneration experiments

After adsorption experiments, the desorption of VOCs was carried out in a thermogravimetric analyzer (Versa Therm) (see Fig. 4.1). After the adsorption procedure, the column was disassembled, and the saturated adsorbent sample from the packed bed was placed in TGA capsule. Then, the sample was heated up to 150 °C under air atmosphere at a heating rate of 10 °C min<sup>-1</sup>. This temperature was maintained by 30 min by using air at a flow of 30 mL min<sup>-1</sup>.



**Fig. 4.1** - Schematic diagram of dynamic VOCs adsorption/desorption experiments set-up.

Note: the materials tested herein are label as follows: AC, activated carbon; BCA, biochar; and BCVD600-1pTT, biochar processed by CVD synthesis.

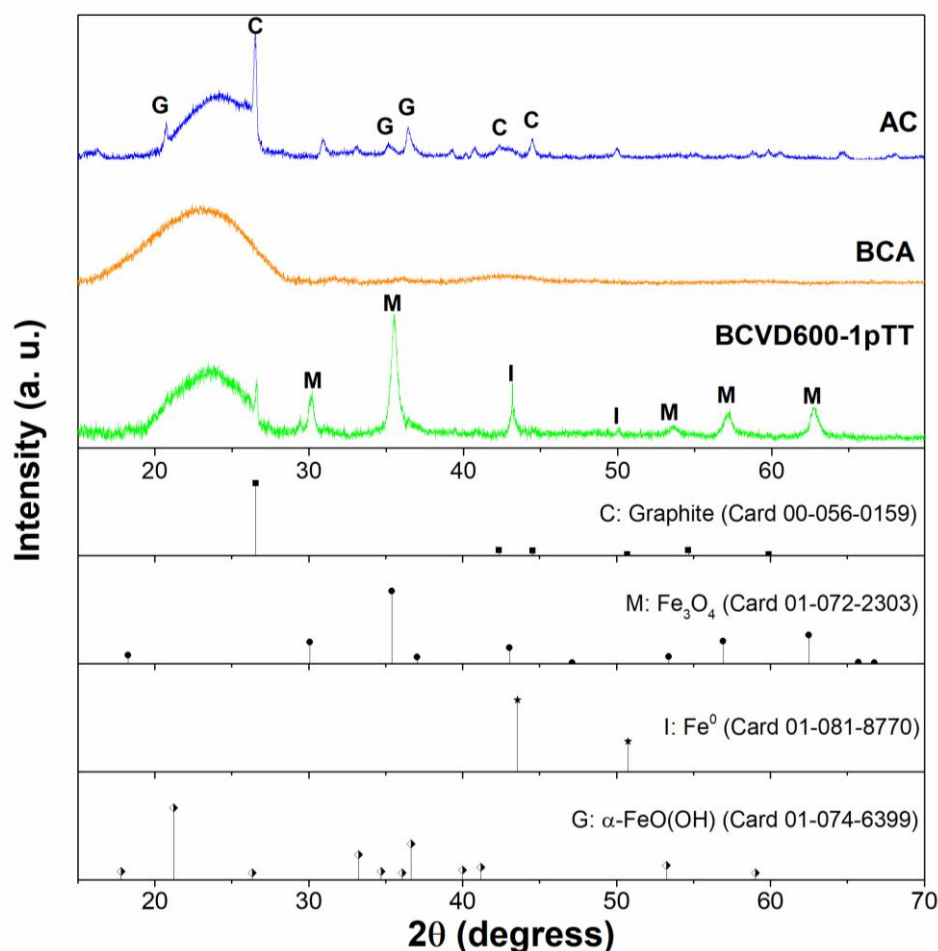
### 4.3. Results and Discussions

#### 4.3.1. Structural *properties of the adsorbent*

Since the presence of minerals on carbon-based materials and their crystalline structure are related with hydrophilicity, which could affect in the adsorption performance of nonpolar VOCs, carbonaceous adsorbents were analyzed by XRD spectroscopy (Fig. 4.2a). The XRD patterns of biochar and BCVD600-1pTT agree with the previous analysis reported in Chapter 3 (Fig. 3.7), confirming the similarity of crystalline structure between these materials. The broad Bragg reflection of XRD patterns of all the materials at  $2\theta$  interval of  $22\text{-}30^\circ$  were related to the small particle size effects [62] After the CVD process on the biochar, the peaks at  $2\theta$  values of  $26$  and  $44^\circ$  were observed (ICDD-PDF Card 00-56-0159), indicating the presence of (0 0 2) and (1 0 0) planes well defined for crystalline graphitic structures. Additional diffraction peaks related to the catalyst presence were observed at  $2\theta$



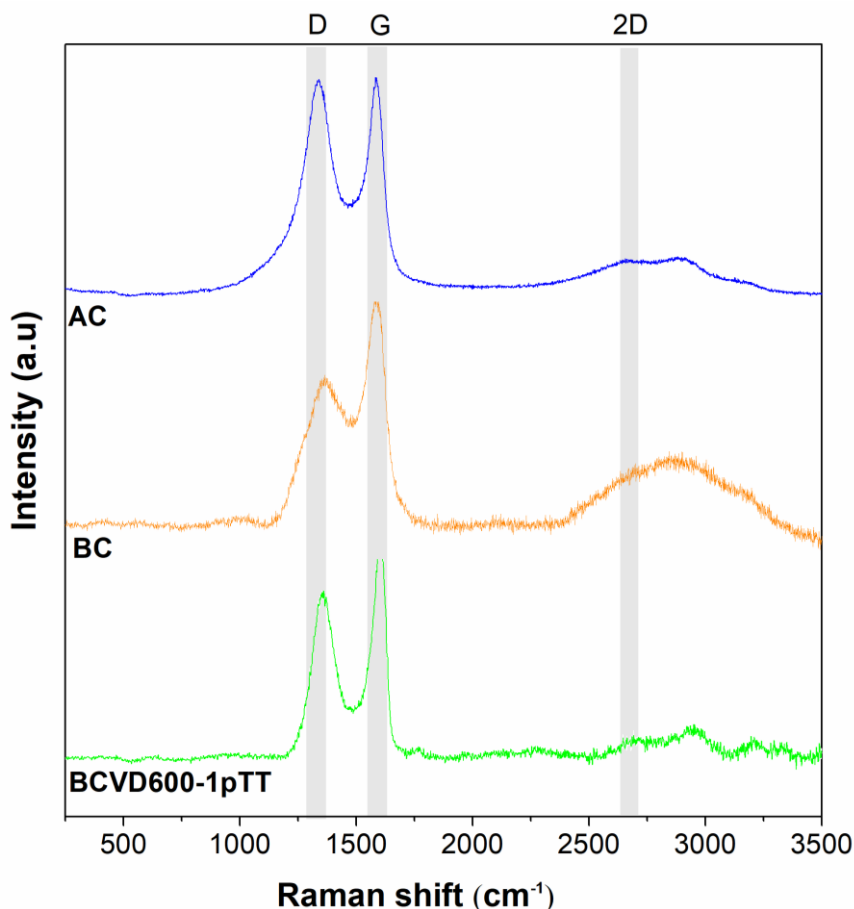
of 43 and 50° for iron (ICDD-PDF Card 01-081-8770); and 30, 35, 54, 57 and 63° for magnetite (ICDD-PDF Card 01-072-2303). It has been broadly reported that the presence of iron ( $\text{Fe}^0$ ) and magnetite ( $\text{Fe}_3\text{O}_4$ ) stimulate the  $\text{C}_2\text{H}_2$  and CMC decomposition during CVD synthesis, which promote the growth of different carbon nanostructures at 600 °C [80]. On the other hand, activated carbon also exhibits the characteristics peaks related to crystalline graphitic structures. Furthermore, extra sharp peaks at  $2\theta$  of 21, 34, 36° were observed on activated carbon and were assigned to goethite (ICDD-PDF Card 00-029-0713), which is a common mineral found in bituminous coal-based activated carbon.



**Fig. 4.2** - XRD patterns of carbon adsorbent by using a step size of  $0.01^\circ 2\theta$  at 10 sec per step.



Raman spectroscopy was another technique used to characterize the carbonaceous adsorbents. From Fig. 4.2b, two noticeable peaks appear at  $1350\text{ cm}^{-1}$  (D-band) and  $1590\text{ cm}^{-1}$  (G-band), similar to the spectra of all  $\text{sp}^2$ -carbons. Indeed, the Raman spectra of activated carbon exhibit a typical D-band representing the disordered carbon or defective graphitic structure, and an evident G-band related to the crystalized and graphitic layers. It can be noticed that the relative height of the D- and G-bands showed similar intensity because of the notorious presence of both, domains forming  $\text{sp}^2$  hybridized carbon on basal planes, and  $\text{sp}^3$  hybridized bonds mainly present in functionalities, edge sites, and vacancy defects [32]. The spectra of the biochar showed broad peaks at the first-order spectra, indicating a rather low degree of ordering of the graphitic structures very similar to that of carbon black. The increase in the intensity and sharpness of D- and G-band after CVD process suggest the growth of carbon nanostructures dominated by graphitic fraction ( $\text{sp}^2$  hybridization) on biochar [141]. On the other hand, the low profile of two peaks on the second-order region of activated carbon between  $2600 - 2700\text{ cm}^{-1}$  (2D-band) are characteristic of stacked few graphene layers. In this sense, the reduction of these second-order peaks on biochar after CVD also implies the loss of the turbostratic carbon and the increase of three-dimensional graphitic ordering [143]. The latter could be due to the growth of carbon nanostructures or to the condensation of graphitic carbon which is in concordance with the crystalline graphitic structure reported by XRD analysis.



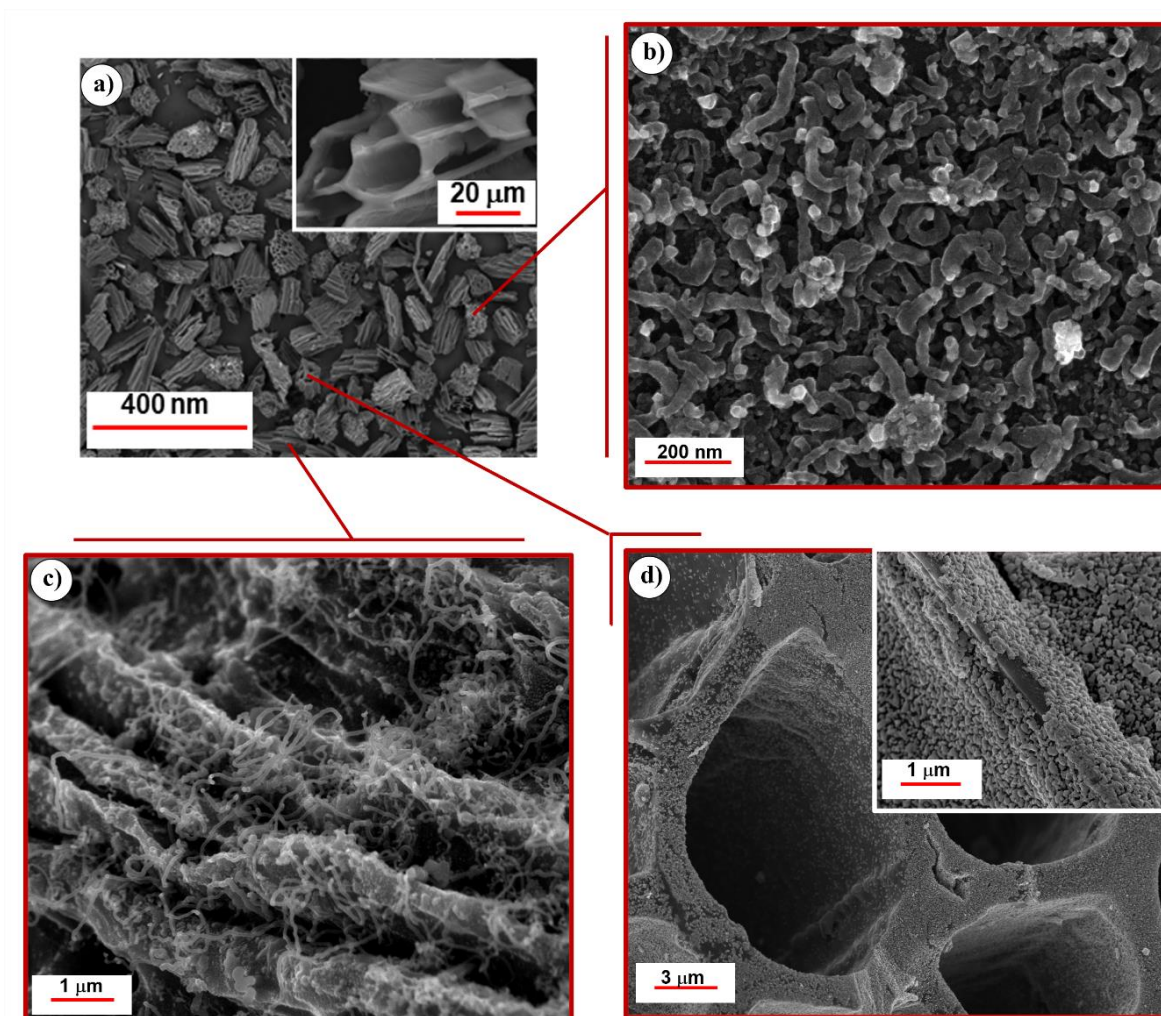
**Fig. 4.3** - Raman spectra of the different carbonaceous adsorbents.

The biochar/carbon nanostructures composite was analyzed by scanning electron microscopy (SEM) (Fig. 4.3). It was observed a very homogeneous particle size of composite with an average value of 60  $\mu\text{m}$ . The particle size is important with respect to the dynamic adsorption performance in packed-bed systems since very heterogeneous particle sizes can cause channeling, as will be described below. Sample BCVD600-1pTT was analyzed to corroborate the effect of CVD synthesis on particulate biochar by using a rotary furnace. It should be noted that in this study the scaling of the CVD process was carried out by using the same synthesis conditions implemented in the TGA equipment, as it was previously reported in Chapter 2. Even though the used CVD conditions were the same, the morphology of carbon nanostructures formed on particulate biochar was significantly different. The SEM analysis revealed a broad covered surface with different shapes and



sizes of carbon nanostructures distributed on the entire biochar surface. Herein, CVD synthesis induced mainly the formation of carbon nanostructures with morphological similarities to CNTs and CNFs (Fig. 4.3b, c). Particularly, the largest nanostructures detected in Fig. 4.3c had an average diameter of 100 nm, while the shortest ones had an average diameter of 26 nm with a more irregular surface as it is revealed in Fig. 4.3b. This morphology of carbon nanostructures has also been described when CVD temperature was lower than 700 °C [62], [80], [83], [157]. According to the carbon deposition process in a rotary furnace, it has been previously reported that in regions of the reactor where the temperature is lower the growth of carbon nanostructures is difficult, observing a null longitudinal growth as in the case of CNTs. The aforementioned findings are in good agreement with the SEM observations reported in Fig 4.3d, where the extensive shell of carbon deposited on biochar had a textural roughness without defined morphology. This could be related to the carbon sources from CMC decomposition that condensed on catalyst at the initial steps of the CVD process, therefore, a further growth of nanostructures was not promoted under these conditions.





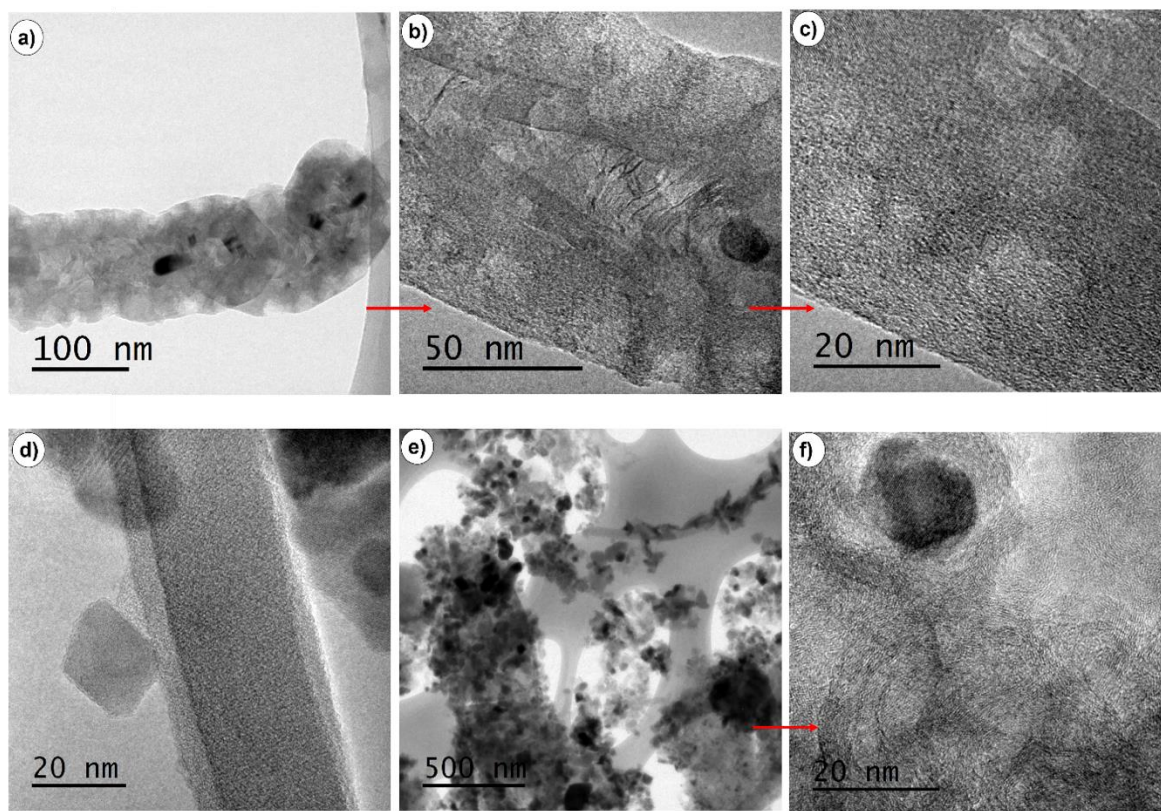
**Fig.4.3** - SEM secondary electrons images of powder biochar/carbon nanostructures composite with homogeneous particle size (a), and the morphological differences onto biochar after processed by CVD at 600 °C (b-c). A comparison was made between distinct morphologies observed in different zones.

Based on the latest, more detailed morphological information is provided by transmission electron microscopy (TEM). Even though the CVD process in the rotatory furnace used the same synthesis conditions than those in the TGA, various morphological differences were evident in the TEM analysis. It is worth mentioning that the formation of morphologies similar than CNFs was mainly induced on biochar (Fig. 4.4a, b, c). In fact, the inner structure of CNFs displayed the alignment of graphite planes that tends to form a cup-shaped morphology, where graphene planes are stanced forming the 1D fibrous morphology [55].





CNFs are characterized by the absence of tubular nanostructure. In addition, along the CNFs a nonhomogeneous morphology was observed, being previously reported as a physical abnormality that could be related to lattice defects, impurities, local charge sites, or a combination thereof [53]. Instead, certain synthesis methodologies can also produce carbon nanofibers with a quasi-amorphous structure, marked by the absence of graphitic  $sp^2$  carbon [55], as it is observed in Fig. 4.4d.



**Fig. 4.4** - TEM images of carbon nanostructures formed by CVD synthesis at 600°C showing formation of CNFs (a-c), amorphous CNFs (d), and onion-like carbon (e-f).

As it is well known, the structural features of carbon nanostructures grown by CVD strongly depend on the experimental conditions which include the preparation and pre-treatment of the catalyst and the synthesis conditions [80]. Indeed, it has been reported that by decreasing the CVD temperature the carbon nanostructure length decreases, which agrees with the formation of onion-like carbon observed in Fig. 4.4e, f. Herein, TEM images



revealed that onion-like carbon present quasi-spherical shape and have a core-shell structure. The onion-like carbon diameters varied in the range of 20-40 nm. The TEM analysis also showed that carbon layers are surrounding nanoparticles. In addition to the low CVD temperature, the formation of onion-like carbon could be attributed to the CMC decomposition which induce the formation of turbostratic carbon on catalyst particles, as it was well described in [Chapter 2](#).

Considering the ability of carbonaceous adsorbents to rapidly adsorb organic compounds, the most available surface area could be an advantageous factor. In order to determine the effect of growing carbon nanostructures on biochar on the dynamic adsorption/desorption performance of VOCs, the pore volume and surface area of raw and CVD processed biochar were analyzed and compared with a highly microporous activated carbon, currently used in automotive canisters ([Table 4.2](#)). The surface area of biochar remarkably dropped from 184 to 1 m<sup>2</sup> g<sup>-1</sup> after the grinding process. Regardless of whether the open channels remained, the lower surface area of biochar could be consequence of porosity loss. The low micropore volume of granular biochar (0.075 cm<sup>3</sup> g<sup>-1</sup>) could be formed by the removal of organic and inorganic fractions throughout the carbonization of raw agave bagasse and acid-washed of biochar, respectively. However, the zero microporosity of powder biochar suggest that granular biochar micropores could be directly connected to the outer surface in such a way that they were destroyed during the grinded process. On the other hand, the specific surface area and pore volume of biochar notably increased from 1 to 330 m<sup>2</sup> g<sup>-1</sup> after the CVD process. The roughness of the external nanostructures surface could contribute to the increase of surface area of the modified biochar. It is worth noting that the scaling of the CVD process in a tubular furnace was beneficial in increasing biochar surface area by 300 %, while TGA allowed to increase only 30 %. Regarding the porous structure, micropores correspond to 75 % of the total of pore volume. This increment of pore



volume, after CVD process, suggests that the arrangement of carbon nanostructures generated porosity by the interspaces formed between them [53]. Oppositely, the narrow microporosity of activated carbon implies a limited mass transfer of VOCs during dynamic adsorption and even more during the regeneration process. Thus, the textural properties of BCVD600-1pTT make it a promising material for a fast regeneration in automotive canister.

**Table 4.1** - Textural properties of powder adsorbent materials tested in dynamic adsorption experiments.

ID samples	$S_{\text{BET}}$ ( $\text{m}^2 \text{g}^{-1}$ )	$V_{\text{total}}$ ( $\text{cm}^3 \text{g}^{-1}$ )	$V_{\text{micro}}$ ( $\text{cm}^3 \text{g}^{-1}$ )	$V_{\text{meso}}$ ( $\text{cm}^3 \text{g}^{-1}$ )	$V_{\text{macro}}$ ( $\text{cm}^3 \text{g}^{-1}$ )
AC	729	0.460	0.263	0.181	0.016
BCA*	1	0.007	0.000	0.002	0.005
BCVD600-1pTT	331	0.160	0.123	0.033	0.003

\* Powdered biochar

#### 4.3.2. Dynamic adsorption/desorption study

In this study, consecutive column runs were carried out to understand the dynamic adsorption behavior of representative evaporative emissions in a fixed-bed, in addition to the simultaneous adsorbent regeneration. In order to analyze the fixed-bed performance, a number of operational parameters have to be known previous each dynamic experiment (Table 4.2). The main operational parameters are the volumetric flow, volume and height of packed bed, empty bed contact time, and ratio column:particle diameter. To prevent wall effects, the ratio column:particle diameter should be higher than 25, which also ensure uniform streaming and avoids channeling [86]. Maintaining operational parameters constant during the dynamic adsorption experiments allow comparing the adsorbent performance for each VOC.



**Table 4.2** - Operating parameters on dynamic adsorption of VOCs in the fixed-bed column.

Parameter	Symbol	Units	value
Bed height	$h$	cm	8.1 - 11.4
Cross sectional area	$A_R$	cm <sup>2</sup>	0.2
Volumetric flow	$Q$	cm <sup>3</sup> min <sup>-1</sup>	20-30
Empty bed contact time	$EBCT$	min	0.05-0.10
Particle diameter	$d_R$	cm	0.008
Ratio column:particle diameter	$d_R:d_p$	--	64
Bed volume	$V_A$	cm <sup>3</sup>	1.95
Column volume	$V_R$	cm <sup>3</sup>	2.32
Bed porosity	$\varepsilon_B$	%	0.16

The breakthrough curves of different VOCs representative of evaporative emissions are presented in Fig 4.4. To maintain the most realistic behavior of gasoline stored in vehicles, each VOC inlet concentration was ruled for its own physical properties. Accordingly, toluene showed the lowest average concentration (28 mg L<sup>-1</sup>) due to its lower vapor pressure (less volatile), whereas the highest average concentration was for pentane (274 mg L<sup>-1</sup>), as a consequence of its high vapor pressure value (more volatile). Similarly, benzene and hexane have average concentrations of 74 and 113 mg L<sup>-1</sup>, respectively. All the breakthrough curves followed the typical S-shape when plotting  $C/C_0^{-1}$  versus time. The most efficient adsorption performance could be obtained when the shape of the breakthrough curve is as sharp as possible [173]. Overall, at the first stage of the dynamic adsorption process, the VOCs are rapidly adsorbed due to high availability surface of the adsorbents. When the feed stream is introduced through the inlet of the column, VOCs are adsorbed most rapidly and effectively by the fresh adsorbent during the initial stage of the experiment. Once the VOCs concentration in the outlet reached 10 % of the inlet concentration the breakthrough time ( $t_b$ )



was reached [111]. After the breakthrough time, the concentration in the effluent increases because the adsorbent becomes saturated with the incoming VOCs that continue to flow into the packed bed and become less effective to the additional gas stream. The process continues until the saturation point was reached at 85 % of the inlet concentration value.

Results show that the breakthrough time decreased when increasing the VOC vapor pressure and also when decreasing the adsorbent surface area. As it can be seen for pentane and hexane, the higher the vapor pressure, the higher the concentration and the faster the breakthrough time. Conversely, toluene and benzene showed the larger breakthrough time as they had the lowest vapor pressure. Regarding pentane adsorption, its higher inlet concentration could saturate the carbonaceous adsorbent more quickly because the increase in concentration reduced the treated volume before the bed gets saturated, decreasing the operation time [174]. In order to increase the volume of feed gas that can be treated, it is necessary that the inlet concentration be lower, which agrees with the longer breakthrough times shown for toluene. The effect of the adsorbate inlet concentration on the breakthrough curves behavior has been previously reported [173]–[175]. These results demonstrated that the diffusion process during VOCs removal is highly concentration dependent. It is worth noting that the performance of carbonaceous adsorbents packed in an automotive canister will depend on the evaporative emissions features, where a large number of the most volatile molecules reach the adsorbent surface faster, but it also saturates quickly.

When comparing the adsorbents, the effect of surface area is obvious. For the case of activated carbon ( $729 \text{ m}^2 \text{ g}^{-1}$ ), the breakthrough time was determined at 20, 19, 40 and 80 min for pentane, hexane, benzene, and toluene, respectively. When BCVD600-1pTT was evaluated, the curves of aliphatic VOCs showed similar breakthrough times to those of activated carbon, while benzene and toluene breakthrough took place 5 and 40 min earlier,



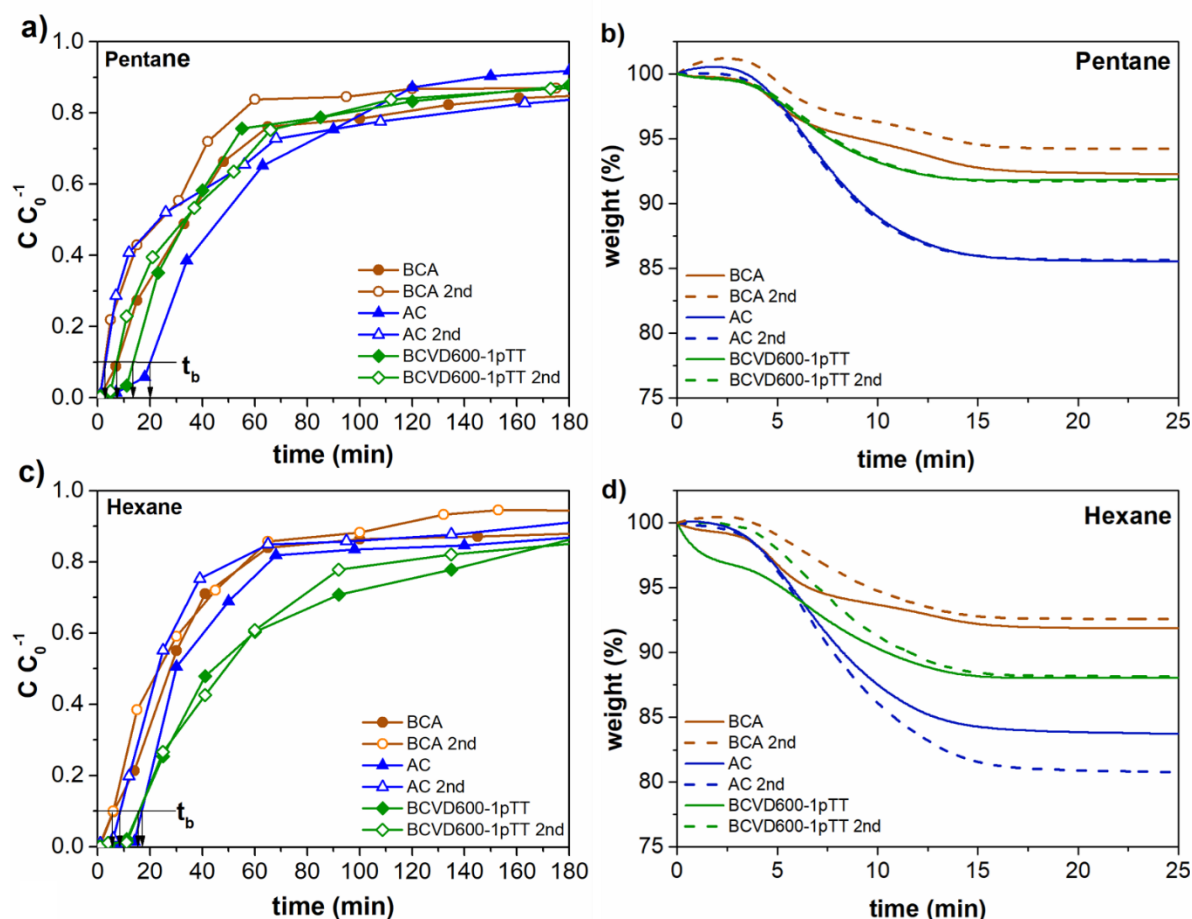
respectively. All this confirms that in addition to the effect of both the surface area and the surface chemistry of adsorbents on adsorption performance, the VOC features can also strongly influence the breakthrough curves behavior. The latter becomes more evident when analyzing the data of the breakthrough curves of the second adsorption cycle. Herein, the adsorbent BCVD600-1pTT was shown to have a higher regeneration efficiency than a commercial activated carbon, as it is notably observed in breakthrough curves of Fig. 4.4a, c, e, g. In this sense, breakthrough curves of regenerated BCVD600-1pTT decreased only by 4, 0.5, 6 and 5 min, for pentane, hexane, benzene, and toluene, respectively, while regenerated activated carbon gave an earlier breakthrough time, from 20 to 5, 18 to 9, 40 to 22, and 81 to 42 min, respectively.

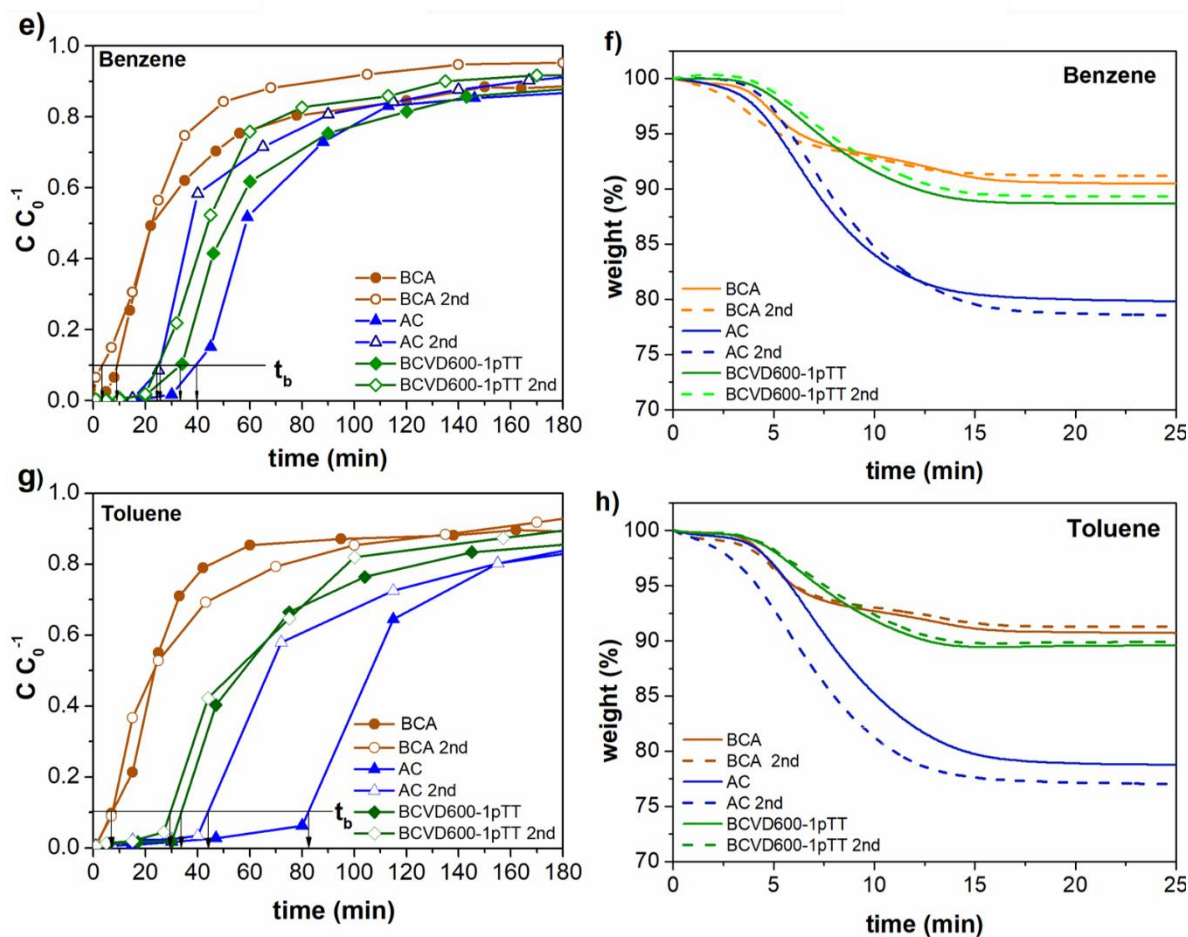
Due to the driving forces for VOC mass transfer, adsorption occurs even in the narrowest micropores, however, the highest adsorption energy in micropores compared to meso and macropores makes regeneration challenging [30]. In this sense, the narrowest pore size measured by physisorption analysis (0.9 nm) corresponded to almost 50% of the micropore volume and 31% of total pore volume of activated carbon, whereas the pore volume in smaller pores than 0.9 nm on BCVD600-1pTT corresponded to 40% and 32% of micropore and total pore volume, respectively. Even though the percentage of the narrowest pores were not very different in both adsorbents, it is important to highlight that the higher pores volume of activated carbon, where their volumes of total pores, micropores and pores smaller than 0.9 nm were 2.88, 2.14, and 2.36 times higher than BCVD600-1pTT, respectively. Considering the effect of textural properties on the dynamic adsorption/desorption performance, it was evident that the greater volume of the narrowest micropore in activated carbon allowed to adsorb a higher number of molecules than BCVD600-1pTT, which agree with the longest breakthrough times on the first adsorption cycle. Nevertheless, the breakthrough time decreased during the second adsorption cycle





suggesting that the activated carbon regeneration was limited by its higher tortuosity, pore shape, and by the presence of acidic functionalities and reactive sites (border sites and vacancies) than decreased the affinity of nonpolar VOCs. In fact, the above has a greater influence on intraparticle diffusion of VOCs in both adsorption and desorption process. On the other hand, the difference of mesopore volume in both adsorbents should also be considered in the above discussion. The larger contribution of mesopores to the total pore volume observed in activated carbon (39.4%) suggests a longer intraparticle diffusion of VOCs in comparison to BCVD600-1pTT. The latter is supported by the low mesopore contribution in the total pore volume of BCVD600-1pTT (20%), indicating that micropores could be connected to the outer surface and not necessary connected with the mesopores, as occurs in activated carbons.





**Fig. 4.4** - Adsorption breakthrough and desorption curves of representative VOCs from gasoline at 25 °C on activated carbon (AC), biochar (BC) and biochar processed with CVD (BCVD600-1pTT).  $t_b$  is the breakthrough time at which the outlet concentration reached 10% of the inlet concentration. Open symbols and dotted lines represent the second adsorption and desorption cycles, respectively. Vapor pressures: toluene (0.038 atm), benzene (0.126 atm), hexane (0.133 atm), pentane (0.657 atm).

To simulate desorption conditions in an automotive canister, the adsorbent regeneration was carried out in a TG analyzer at 150 °C, using air stream. In fact, the saturated porous adsorbents have been commonly regenerated by thermal methods [176]. As it is seen in Fig. 4.4b, d, f, h; the highest weight loss of activated carbon indicated a higher concentration of VOCs desorbed, while the increase of weight loss after the second cycles could be related to the desorption of VOCs no released during the first desorption cycles. It is interesting to note that the greater weight loss of activated carbon after the second cycle demonstrated





the diffusional restrictions for VOCs desorption from narrow micropores, which is consistent with the left shift of its breakthrough curves. In addition, chemical surface of activate carbon also affected their VOCs desorption. In this sense, it is most restricted the desorption of VOCs adsorbed by the electron donor-acceptor (EDA) complex formed between the delocalized  $\pi$  electron density of benzene and toluene and the pair electrons of oxygen atoms from functionalities [7]. Regarding the smaller size and higher concentration of pentane and hexane, it is highly probable that diffuse further into the activated carbon porosity than aromatic VOCs. In addition, VOCs desorption could be affected by both the type of pore morphology and by the effect of steric hindrance caused by the acid functionalities present in the pore. In contrast, desorption curves of BCVD600-1pTT behave similarly after two desorption cycles, being an adsorbent with less tortuosity and a more graphitized surface, indicating a higher regenerative ability than activated carbon.

By analyzing the desorption rates shown in [Table 4.3](#), it was observed that VOCs desorbed more slowly from BCVD600-1pTT than from activated carbon. This effect was attributed to the adsorbent chemical properties. The extensive coverage of the  $sp^2$  hybridized carbon on the carbon nanostructures and the low presence of acidic functionalities (shown below) makes that nonpolar VOCs adsorb slightly stronger than on the more defective surface of activated carbon. The latter is related to the high number of functional groups of activated carbon ( $0.291 \text{ mmol g}^{-1}$ ) compared with those of BCVD600-1pTT ( $0.139 \text{ mmol g}^{-1}$ ), whereas after desorption functionalities density increased as will be described below. The curvature of the carbon nanostructures provides a greater surface reactivity, implying a greater exposure of surface electronic cloud which favors the dipole induction on the VOC. This last one is based on the dispersive interaction between nonpolar VOCs and basal plane of adsorbent. Finally, it is worth noting that despite the faster



desorption rate of activated carbon between the min 4 and 9, the diffusional restrictions in narrow micropores avoid the complete desorption of VOCs.

**Table 4.3** - VOC desorption rates calculated at the highest weight loss, between minutes 4 and 12.

VOCs	Desorption rates (mmol min <sup>-1</sup> )					
	AC	AC 2 <sup>nd</sup> cycle	BCA	BCA 2 <sup>nd</sup> cycle	BCVD600- 1pTT	BCVD600-1pTT 2 <sup>nd</sup> cycle
Pentane	0.0048	0.0047	0.0016	0.0017	0.0031	0.0032
Hexane	0.0062	0.0071	0.0046	0.0021	0.0028	0.0033
Benzene	0.0070	0.0074	0.0023	0.0035	0.0045	0.0043
Toluene	0.0064	0.0062	0.0026	0.0031	0.0033	0.0031

To further explain the dynamic adsorption curves, the area to the left of the breakthrough curves, and other important column parameters reported in [Table 4.4](#), were used to estimate the total quantity of gas adsorbed during dynamic experiments. Other important parameters are showed in supplementary information ([Table SI4](#)). The mass transfer zone (MTZ) is the most important parameter highly related with the steepness of the breakthrough curve. In fact, it is well-known that the breakthrough curve is a mirror of the MTZ, being affected by flow rate, adsorption affinity, adsorbent porosity and, as mentioned previously, on the adsorbate properties [86]. From dynamic experiments, it was observed that, in most cases, the height of the mass transfer zone ( $H_{MTZ}$ ) exceeded the average bed height. Even though 20 mL min<sup>-1</sup> is known as a low flow rate in gas phase based on dynamic adsorption reported in literature,  $d_R:d_p$  ratio was much higher than 25, and non-polar VOCs have high affinity for carbonaceous adsorbent, the adsorbate diffusion through the column in gas phase is much faster. [Fig. 4.4](#) suggest that there are little to no mass transfer limitations in the breakthrough system. The inability of these carbonaceous adsorbents to achieve a maximum of breakthrough saturation higher than 0.95 in the short time evaluated is explained by having a  $H_{MTZ}$  greater than the bed height. In this sense, the mass transfer zone is so large that



when 85% of the packed bed has been spent or covered with VOCs, there are still unused zones at the beginning of the column, without implying a channeling effect. In contrast, the low rates of the mass transfer zone ( $R_{MTZ}$ ) indicated the high affinity of VOCs for all the carbonaceous adsorbents. The slightly lower  $R_{MTZ}$  of activated carbon was more related to its higher surface area ( $729 \text{ m}^2 \text{ g}^{-1}$ ) than its chemical surface, where the more hydrophobic and basic surface of BCVD600-1pTT suggested a high affinity for VOCs showing  $R_{MTZ}$  values close to activated carbon despite having a surface area 2.2 times smaller.

Activated carbon showed a  $H_{MTZ}$  increase from 2 to 10.9 cm after the adsorbent regeneration, while BCVD600-1pTT regeneration did not affect the  $H_{MTZ}$ . This behavior was also observed in the fractional capacities ( $\phi$ ) and the rate of removal at maximum adsorption capacity (%R) for BCVD600-1pTT, which indicated that the amount of solute adsorbed and the rate at which it is absorbed were similar in both adsorption cycles because the total capacity of the MTZ also was comparable. Regardless of the high reproducibility of the breakthrough curves of BCVD600-1pTT, its lower fractional capacity, compared to activated carbon, suggest an increase in the bed height necessary to increase the service time.

Concerning the total amount of VOCs passed through the packed bed, it can be seen that the higher vapor pressure of lighter VOCs reduced both the breakthrough and saturation times, whereas the adsorption capacity increased. These findings are associate to the increase of the concentration gradient between the nitrogen stream and VOCs molecules. For instance, the high concentration of pentane provided greater driving force to rapidly saturate the sorption sites, while the low concentration of toluene complicated the transfer process duo to the lower dispersion rates from the influent to the adsorbent particles. Similar outcomes were previously recorded in packed bed system [174], [175], [177]. By comparing the dynamic adsorption capacities of BCVD600-1pTT in both cycles with those obtained in



activated carbon, it is important to point out the viability of using BCVD600-1pTT for the recovery of evaporative emissions.

**Table 4.4** - Experimental parameters obtained from breakthrough curves for different adsorbents and adsorbates.

Adsorbent	VOC	Cycles	$t_b$	$t_{exh}$	$H_{MTZ}$	$R_{MTZ}$	$\phi$	% R	$q_e$
AC	Pentane	1	22	114	10.6	0.12	0.71	12.8	273.3
		2	4	192	22.5	0.12	0.47	17.3	287.2
	Hexane	1	18	150	14.3	0.11	0.44	16.5	170.5
		2	10	70	17.1	0.28	0.35	14.2	125.8
	Benzene	1	41	145	8.5	0.08	0.69	16.9	107.8
		2	26	121	10.5	0.11	0.61	12.3	85.5
	Toluene	1	84	218	7.8	0.06	0.60	19.8	34.5
		2	43	190	12.3	0.09	0.56	11.4	25.7
BC	Pentane	1	6	130	30.7	0.25	0.39	17.7	200.9
		2	5	104	29.7	0.30	0.32	13.2	221.9
	Hexane	1	8	80	22.3	0.31	0.23	12.8	85.7
		2	7	62	19.9	0.36	0.43	6.7	43.8
	Benzene	1	10	81	24.3	0.34	0.29	11.6	60.5
		2	4	51	17.1	0.36	0.54	8	34.1
	Toluene	1	8	70	19.3	0.31	0.24	12.8	19.3
		2	8	90	16.9	0.21	0.48	14.6	18.9
BCVD600-1pTT	Pentane	1	14	95	18.3	0.23	0.36	12.2	269.6
		2	9	120	22.7	0.20	0.35	13.2	259.5
	Hexane	1	17	170	15.9	0.17	0.52	11.9	123.5
		2	17	170	16.3	0.17	0.50	14.3	114.9
	Benzene	1	34	142	11.4	0.11	0.51	14.3	81.2
		2	26	109	10.7	0.14	0.57	8.3	64.4
	Toluene	1	34	166	12.2	0.09	0.48	16.6	36.9
		2	30	120	12.7	0.14	0.40	12.6	29.2

$t_b$  = breakthrough time (min)

$t_{exh}$  = saturation time (min)

$H_{MTZ}$  = height of the mass transfer zone (cm)

$R_{MTZ}$  = rate of the mass transfer zone (cm min<sup>-1</sup>)

$\phi$  = fractional capacity

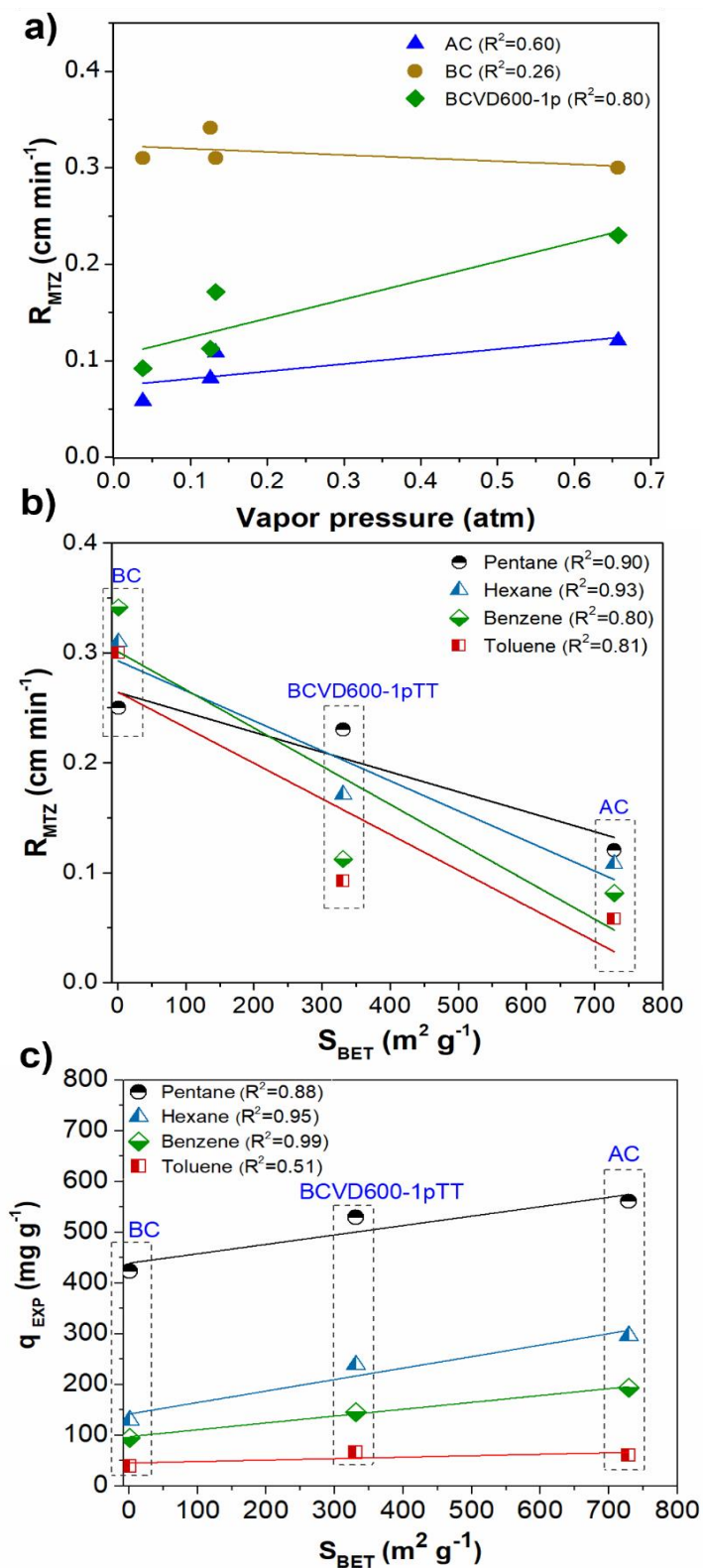
% R = rate of removal at maximum adsorption capacity

$q_e$  = calculated adsorption capacity from breakthrough data (mg g<sup>-1</sup>)



Dynamic adsorption performance was more evident by analyzing the relationship of the adsorbent surface area with mass transfer zone rates and adsorption capacities, the effect of Vapor pressure in with mass transfer zone rates (Fig. 4.5). The positive linear relation between VOCs vapor pressure and mass transfer zone rates of AC and BCVD600-1pTT showed that the mobility of adsorbate through the column was consistent with the aforementioned premise that adsorbate volatility governs the inlet concentration and provides a greater driving force for the diffusional process. Conversely, it was found that the mass transfer zone rate is negatively correlated with the adsorbent surface area. In this case, as the adsorbent surface area increases, the mass transfer zone decreases and moves slowly because the adsorption process is mostly controlled by intraparticle diffusion [177].

The influence of surface area on the adsorption capacity after two cycles was positively correlated ( $R^2$  ranging 0.51- 0.99). The least steep positive slopes observed in Fig. 4.5c may be related to the less proportion of basal planes domains on activated carbon. If the slopes were more pronounced as the surface area values increased, the effect basal planes would be more evident because physical interactions are favored [11]. To consider chemisorption as the most important mechanism, it should be oxidized adsorbent surface and observed a high correlation between adsorption capacity and surface acidification. The importance of surface area for the VOCs removal by carbonaceous adsorbents has been recognized in the literature [7], [28], [36], [37], [165], [168].



**Fig. 4.5** - Linear relationship between VOCs vapor pressure and mass transfer zone rate (a), adsorbent BET surface area and mass transfer zone rate (b), and adsorbent BET surface area and adsorption capacity (c).

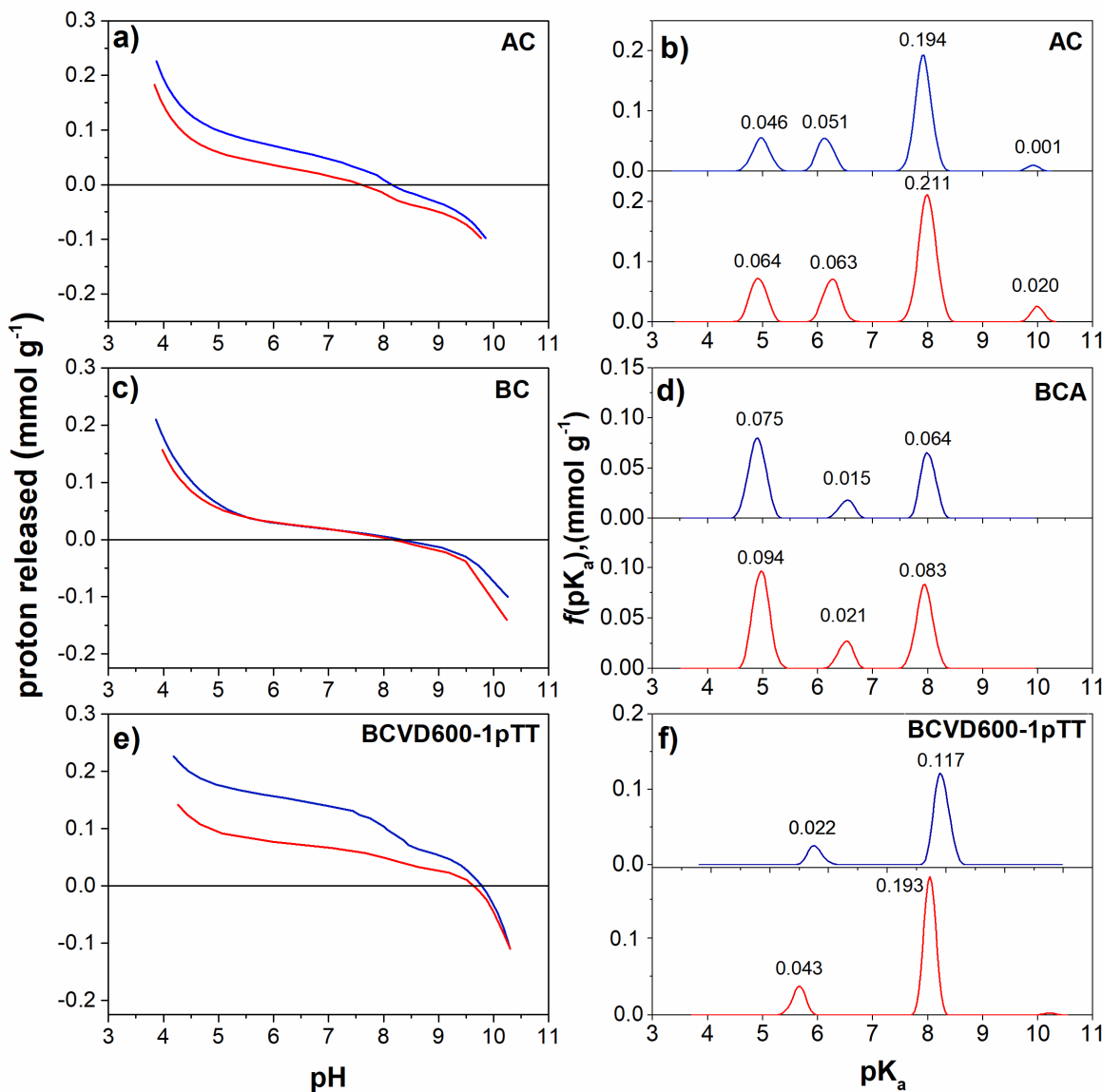


Based on the operational regeneration of automotive canisters, it could be said that the high engine temperatures and air current used to desorb VOCs molecules could oxidize the most exposed adsorbent surface. For this reason, the changes in surface chemistry after two cycles of adsorption/desorption of VOCs was analyzed by potentiometric titrations (Fig.4.6). It was observed a slightly basic surface on biochar and activated carbon with  $\text{pH}_{\text{PZC}}$  values of 8 and 7.7, respectively, whereas the growth of carbon nanostructures increased the surface basicity to a  $\text{pH}_{\text{PZC}}$  of 9.7. This result agrees with Raman analysis since the increase in  $\text{pH}_{\text{PZC}}$  values has often been attributed to a high density of  $\text{sp}^2$  graphitic domains of the carbon nanostructures. Considering that moisture was previously removed by using a drying column, the chemical equilibrium by dissociation of the functionalities could be negligible during dynamic adsorption process. However, the analysis of surface chemistry by determining the  $\text{pH}_{\text{PZC}}$  values and  $\text{pK}_a$  distribution is of interest for VOC adsorption since the basic character of BCVD600-1pTT may be relate to a weak polar and more graphitized surface, while more acidic surface of activated carbon implies a larger polar and more amorphous surface [36]. Thus, it should be noticed that the adsorbent basicity favors the adsorption of nonpolar VOCs by dispersive forces.

After the regeneration process, the adsorbent surface was acidified, which was reflected in a decrease of the  $\text{pH}_{\text{PZC}}$  of 0.01, 0.15 and 0.5 for BC, BCVD600-1pTT and AC, respectively. To better illustrate the effect of regeneration on the surface chemical functionalities, characteristics  $\text{pK}_a$  of acidic functionalities were reported in Fig 4.6b, d, f. The increase in the  $\text{pK}_a$  peaks confirmed the slight surface oxidation after regeneration. The facility to oxidize activated carbon may be a consequence of the high occurrence of edge sites and vacancy defects characteristics of carbon materials induced to activation process. These results denote that in addition to the adsorbent textural properties effect on dynamic



adsorption/desorption performance, the increase in acidic functionalities could imply a decrease in the adsorption efficiency of VOCs.

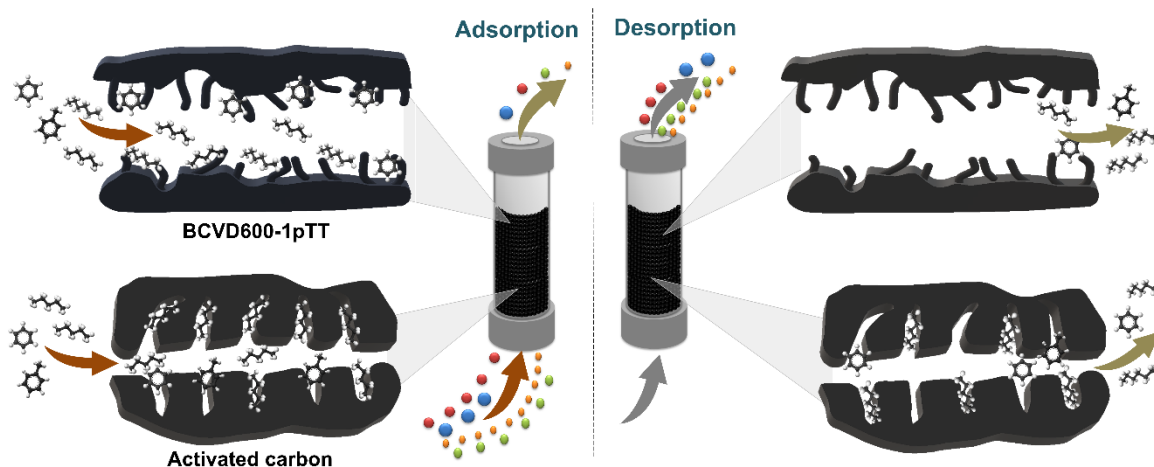


**Fig. 4.6** - Regeneration effect on surface charge distribution and  $pK_a$  distribution of carbonous adsorbents as a function of pH at 25 °C. The blue and red lines correspond to the pristine and after being used in adsorption of VOCs, respectively.





To clarify the overall adsorption-desorption process in carbonaceous adsorbents with different textural features, the following diffusional illustration is proposed (Fig. 4.7).



**Fig. 4.7** - Overall illustration depicted the favorable mass transfer on exposed surface area of BCVD600-1pTT versus the diffusional difficulties of microporous activated carbon during dynamic adsorption in packed-bed columns.

The highest concentration of pentane promoted the molecular diffusion from the bulk to the pores or the external surfaces, while the decremental concentrations of hexane, benzene, and toluene, respectively, slowed the mass transfer. In this sense, pentane was adsorbed faster compared to other VOCs. Hexane and Benzene were adsorbed a few minutes later and toluene should have taken longer to be adsorbed. Based on the kinetic diameter of the adsorbed VOCs ( $< 0.6$  nm), all molecules can readily gain access to the micropores of activated carbon and BCVD600-1pTT, however, the narrow microporosity of activated carbon implies a gradual interparticle diffusion. The shorter breakthrough times shown by BCVD600-1pTT agree with this assumption. Once VOCs molecules reached the carbonaceous surface, the adsorption is mainly controlled through van de Waals interactions and  $\pi$ - $\pi$  bond. As it was previously described in Chapter 3, pentane and hexane adsorption was controlled by dispersive forces, while the uniform electron clouds of benzene and



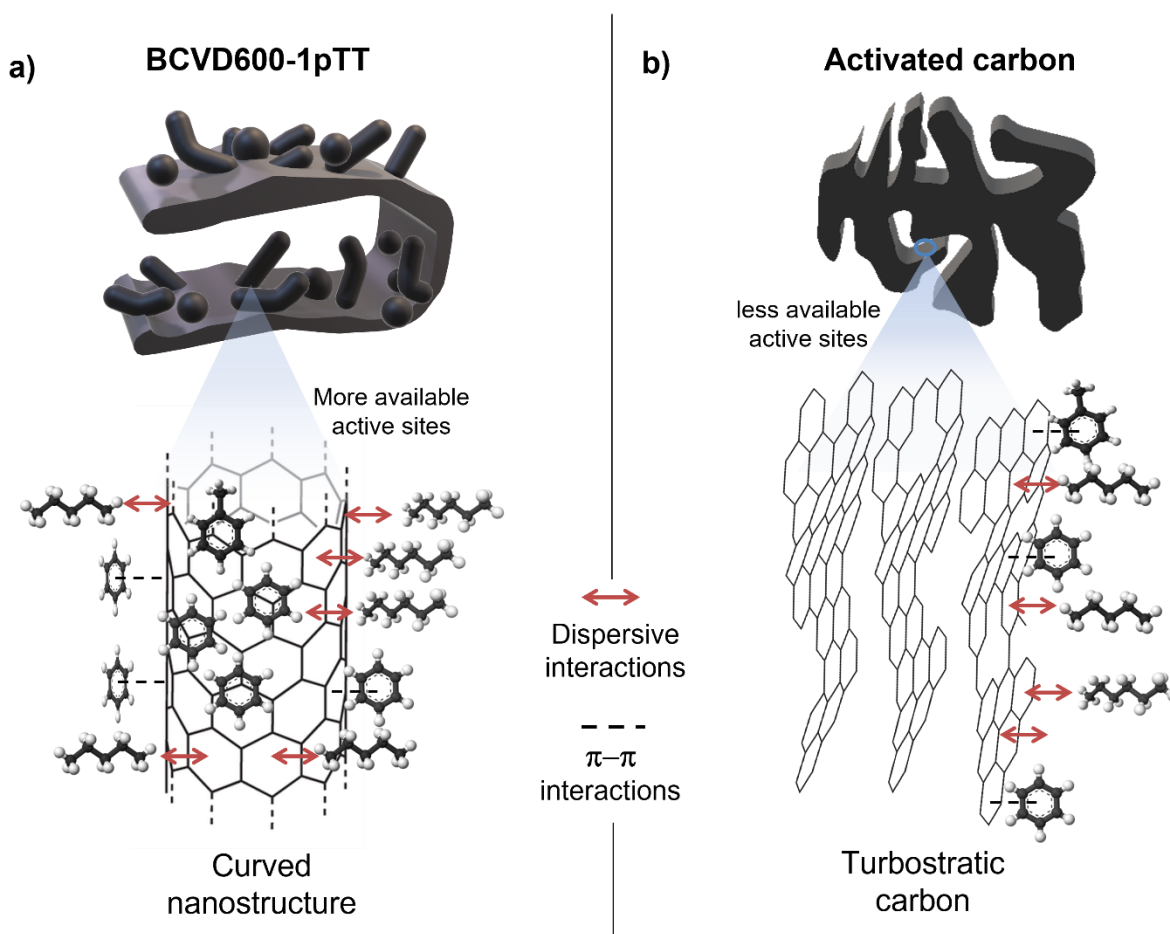
toluene allowed them to form an electron donor-acceptor (EDA) complex with the adsorbent functionalities in addition to the  $\pi$ - $\pi$  interaction [37]. However, it has been mentioned that VOCs adsorption is mainly controlled by dispersive forces during dynamic adsorption experiment [7], [11], [36], [103].

Regarding the basic surface properties of carbonaceous adsorbents, the high extension of delocalized  $\pi$  electrons on graphitic structures promote the dispersive interaction with nonpolar VOCs. This interaction is also known as induced dipole-induced dipole or London forces. These forces take place when adjacent nonpolar VOCs come close enough that the electron density of these neighboring molecules vibrates leading to fluctuating or varying dipoles, which are not oriented but are held together by the induction of polarity in each other [51].

The characteristic graphitic structure of both adsorbents BCVD600-1pTT and activated carbon allows them to possess similar chemical properties such as high hydrophobicity and a delocalized  $\pi$  electron rich surface [118], while the pores structure of activated carbon differed from that of BCVD600-1pTT. It has been reiterated that the high surface area of activated carbon mainly located in a network of micro and mesopores has promoted a greater adsorption capacity than BCVD600-1pTT, however, it was evident that the adsorption capacities differences were not proportional to the surface area magnitudes. Thus, the differences in adsorption behavior could also be related to the spatial arrangement or morphological shape of the graphitic-like structure that forms most of the surface of the carbonaceous adsorbents. For activated carbon, the cross-linked microcrystalline layers randomly oriented show a disordered orientation caused by the presence of heteroatoms, and by the defects such as vacant lattice sites [32]. Even though activated carbon has a higher surface area, these structural features play a role in the adsorption mechanism since the broad heterogeneous surface prevent adsorbing further nonpolar VOCs. In contrast, the



less defective, most graphitized surface of BCVD600-1pTT allows it to take better advantage of active sites for VOCs uptake. In addition, the adsorption capacity was enhanced by the curvature of the carbon nanostructures grown on biochar. The curvature provides unusual features causing a significant orbital perturbation where the electronic cloud is more exposed than on graphene-like layers [178], [179]. Considering the adsorption of nonpolar VOCs, the curved carbon nanostructures suggest a greater feasibility for promoting the induced dipoles between adsorbate and adsorbent (Fig.4.8).



**Fig. 4.8** - Adsorption mechanism on BCVD600-1pTT(a) and activated carbon (b). The effect of both curvature on carbon nanostructure and a more defective carbon structure on adsorption of aliphatic and aromatic VOC were illustrated.



On the other hand, adsorbent regeneration was also mainly ruled by activated carbon microporosity and by carbon nanostructures curvature. Accordingly, activated carbon microporosity limited the desorption of VOCs due the high pore tortuosity and the different pore shapes. In addition, as the molecule was larger, the diffusional restriction was higher, limiting the desorption performance. Conversely, desorption of aliphatic and aromatic VOCs from curved carbon nanostructures could imply a higher energy compared to the lineal surface, although desorption temperature (150 °C) promoted the breakdown of dispersive forces.

### **4.3.3. Reusability of biochar/carbon nanostructures composite**

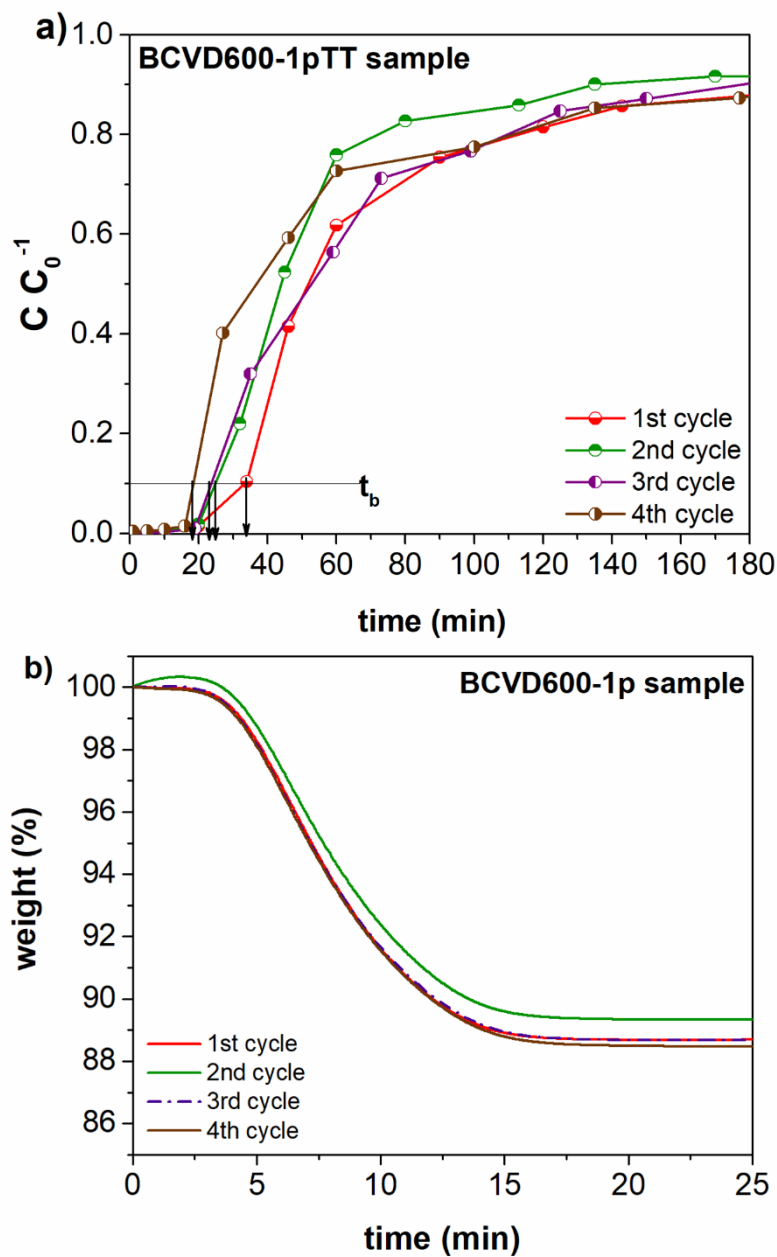
The efficiency of regeneration of an adsorbent in a cyclic adsorption-desorption process plays an important role in the practical application of automotive canisters. In order to determine the reusability of biochar/carbon nanostructures composite on evaporative emissions adsorption, the recovery of benzene was evaluated over four consecutive adsorption-desorption processes. On the basis of dynamic adsorption and desorption results, BCVD600-1pTT seems to be the best adsorbent to remove different representative VOCs from gasoline. Desorption temperature of 150 °C was chosen to overcome the boiling point of benzene (80°C).

According to the [Fig. 4.9a](#), the BCVD600-1pTT still maintains a good adsorption capacity after four adsorption-desorption cycles. The regeneration efficiency at 150 °C is good enough to only reduce the breakthrough times from 34 to 19 min after four regenerative cycles. The main loss of regeneration efficiency occurred from the first to the second cycle and from the third to the fourth cycle, reducing the breakthrough time by 9 and 4 min, respectively. The total breakthrough time reduction of 13 min after four cycles indicated a better regenerative efficiency than activated carbon as the latter showed a decrease in



service time of up to 40 min after two cycles. The post-breakthrough curves sharpness on the posterior cycles is more rapid, implying less diffusion resistance in the adsorbent during the adsorption process. Considering that physical adsorption of organic molecules is mainly ruled by an exothermic process, using a high regeneration temperature could contribute to more efficient desorption of VOCs.

Based on the purge region from [Fig. 4.9b](#), the amount of benzene adsorbed on the external surface adsorbent can be desorbed at 150 °C during thermal treatment with air. The desorption curve for the second cycle decreases more slowly than the other cycles, which may be related to the interspaces of carbon nanostructures or an experimental effect during desorption in the TGA. Adsorbed benzene molecules on the external surface of carbon nanostructures can be desorbed by purged gases. However, benzene adsorbed in the interspaces of carbon nanostructures could be accumulated between cycles, although in the following desorption cycles it was possible to regenerate as much as possible the adsorbent. Thereby, BCVD600-1pTT could be potential adsorbent for long term operations in automotive canisters, owing to the presence of scarce irreversible bounds between this adsorbent and the molecules of evaporative emissions.



**Fig. 4.9** - Reusability of BCVD600-1pTT after four adsorption (a) and desorption (b) cycles of benzene under air stream at 150 °C.



#### 4.4. Conclusions

In this work, BCVD600-1pTT adsorbent is successfully synthesized in a rotary furnace at 600 °C by scaling the CVD conditions used in a TGA equipment for the growth of carbon nanostructures. By characterizing with Raman spectra and X-ray diffraction, it is confirmed that after the CVD process the composition of biochar is tailored via the growth of carbon nanostructures with a prominent  $sp^2$  hybridized carbon domain and a crystalline graphitic structure. SEM analysis shows the extensive coverage of carbon nanostructures on biochar; however, TEM images evidence the morphological differences by using a rotary furnace in comparison with a TGA. The growth of carbon nanofibers and onion-like carbons is promoted. Moreover, the specific surface area of biochar increases after CVD process from 1 to 300  $m^2 g^{-1}$ , and the micropore volume increases from 0.007 to 0.160  $cm^3 g^{-1}$ . In this study the particle size of the adsorbent is reduced to avoid channeling of VOCs through the packed-bed.

The dynamic adsorption/desorption behavior of different VOCs representative of evaporative emissions (toluene, benzene, hexane, and pentane) is measured in a packed bed column by using similar experimental conditions. By comparing adsorption performance of VOCs, earlier breakthrough times are found for adsorbates with lower boiling temperature, and a longer breakthrough time for the less volatile molecules. Accordingly, the lower boiling temperature of pentane (36 °C) is related to its highest inlet concentration (356  $mg L^{-1}$ ), while higher boiling temperature of toluene (111 °C) implies the lowest inlet concentration (22  $mg L^{-1}$ ). As indicated by dynamic adsorption-desorption results, BCVD600-1pTT has good affinity toward aliphatic and aromatic VOCs. Breakthrough curves of BCVD600-1pTT display adsorption capacities of 269.6, 123.5, 81.2, and 36.9  $mg g^{-1}$  for pentane, hexane, benzene, and toluene, respectively. Furthermore, the specific area of activated carbon is 2.2 times higher than that of BCVD600-1pTT, while its adsorption capacity is no more than 7%. The

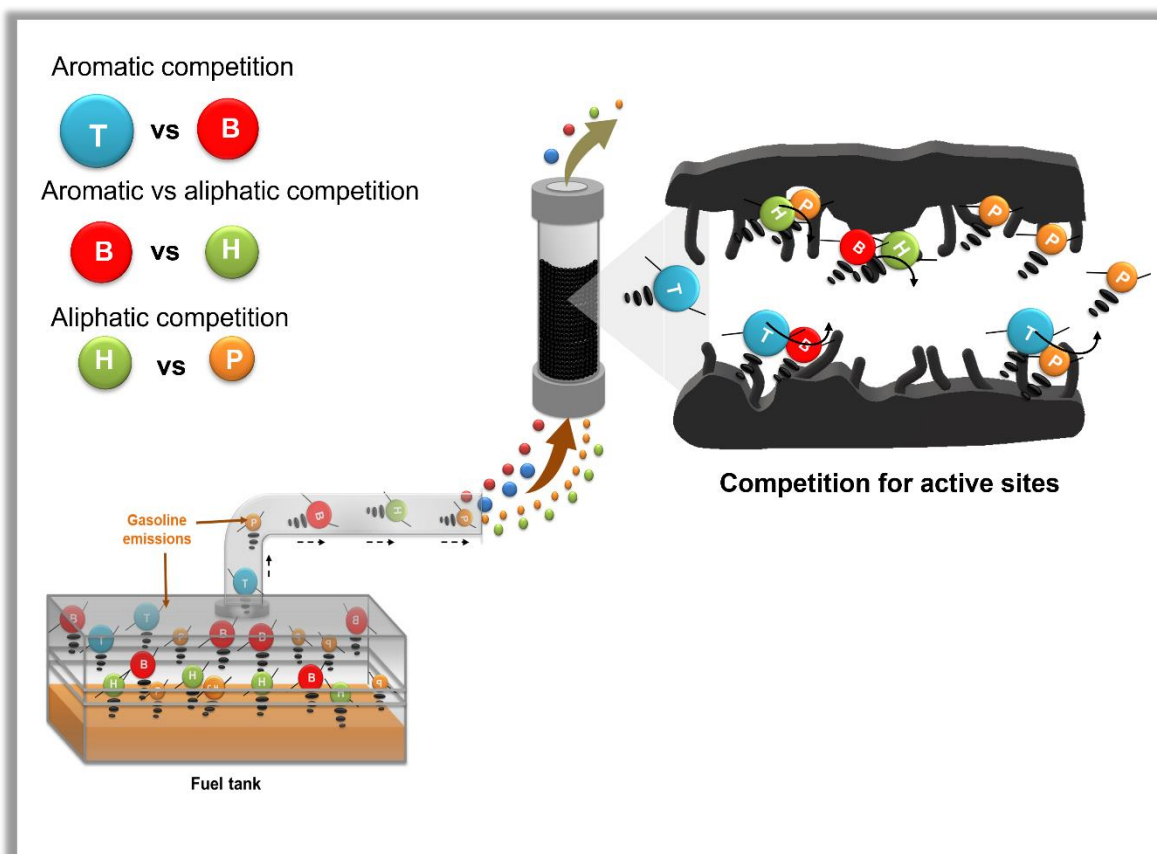


competitive adsorption performance of BCVD600-1pTT is associated with its higher graphitized and basic surface of carbon nanostructures, in addition to its highly reactive curvature which facility nonpolar VOCs uptake. It is suggested that the predominant adsorption mechanisms are dispersive forces, for aliphatic VOCs, and  $\pi$ - $\pi$  interaction for aromatic VOCs, although the EDA complex could occur on acidic functionalities. The most notably difference is observed after the adsorbent regeneration, herein activated carbon showed a decrease in service time of up to 40 min, while BCVD600-1pTT shows a better regenerative efficiency by only decreasing 13 min the service time after four regenerative cycles. As a consequence, the most exposed surface of carbon nanostructures provides a less mass transfer resistance than narrow micropores of activated carbon. At the same time, the regeneration process acidifies the adsorbent surface by decreasing 0.05, 0.1, and 0.5 the  $\text{pH}_{\text{PZC}}$  value of biochar, BCVD600-1pTT, and activated carbon, respectively. Surface acidifications is associated to a decrease in the adsorption capacity of nonpolar VOCs. Finally, BCVD600-1pTT shows a good reusability after four cycles, suggesting that it can be used as an effective adsorbent for evaporative emissions recovery in an automotive canister.



# CHAPTER 5

Adsorption of model and real gasoline emissions by carbon nanostructures modified biochar in packed-bed columns.





### Abstract

This work aimed to investigate the dynamic adsorption performance of a biochar/carbon nanostructures composite (BCVD600-1pTT) for the removal of different gaseous mixtures of volatile organic compounds from gasoline on packed-bed columns. The effect of co-adsorption in binary systems was also investigated in terms of the aliphatic and aromatic molecules interaction: pentane-hexane, benzene-toluene, and hexane-benzene systems. Multicomponent systems were also studied for all adsorbates, and the results were compared with those reported for activated carbon. Data showed that the breakthrough time patterns of binary and multicomponent systems behave similarly to those of single systems. Accordingly, the lightest VOCs in each mixture showed the shortest breakthrough time and the highest adsorption capacity. In the case of binary systems, BCVD600-1pTT adsorbed 44 and 35% more pentane and hexane, respectively, than activated carbon, as well as more than 37% of the total adsorption of hexane-benzene mixture. Nevertheless, toluene had an average adsorption capacity of  $35 \text{ mg g}^{-1}$  regardless of the adsorbate mixture and the adsorbent used. It was observed a change in the slope on the breakthrough curves of activated carbon, associated with the displacement of VOCs for competitive adsorption of active sites, while the S-shape curves of BCVD600-1pTT suggested a more homogeneous adsorption and mass transfer process. The breakthrough curves profiles of the competitive adsorption on binary and multicomponent mixtures were fitted by the Yoon-Nelson model, which is the most well-accepted model in dynamic adsorption of volatile organic compounds. In the case of the real gasoline emission adsorption, BCVD600-1pTT and activated carbon obtained similar service time (12 and 15 min, respectively) and adsorption capacities (153 and  $187 \text{ mg g}^{-1}$ , respectively). Hence, BCVD600-1pTT adsorbent proved to be adequate for the dynamic co-adsorption of gasoline emissions.



### 5.1. Introduction

The growing trend of industrialization and urbanization have triggered an increase in air pollution and hazardous materials emission, becoming an unprecedented threat to human health and environment [1]. The emission of gasoline vapors is currently a matter of scientific and legislative concern because they have been one of the main sources of air pollution. The vast emissions from gasoline contain volatile hydrocarbons with chains of 4-7 carbons [30]. It was estimated that the emission of gasoline vapor in develop countries reached more than 600 thousand tons per year [146]. For this reason, modern vehicles are equipped with an activated carbon canister to adsorb gasoline emissions. However, the diffusional restrictions of microporous activated carbons cause their poor recovery and regeneration [180]. Therefore, numerous works have focused on developing non-microporous adsorbents to overcome this disadvantage, such a macroporous resins [2], mesoporous zeolites [166], mesoporous graphene [108], carbon nanofibers [56], and biochar from agro-industrial residues [29].

Biochar from waste sources has emerged as a potential alternative to activated carbon due to its poor microporosity, stable physical and chemical properties and easy regenerability in site [40]. Although recent works have notably improved the VOCs adsorption capacity of biochar through activation and tailoring strategies, there are still some mass transfer disadvantages in dynamic experimental conditions [10]. Accordingly, a novel adsorbent by the growth of carbon nanostructures onto biochar (BCVD600-pTT) has been previously developed and studied as a substitute for microporous activated carbon. Biochar/carbon nanostructures composite, which was produced by CVD process, represents a class of materials with high exposed surface areas and basic surface character. In comparison to commercial activated carbon, BCVD600-pTT possessed similar adsorption capacities for benzene, toluene, hexane, and pentane by using the same operational



parameter in dynamic experiments. Our previous study has shown that the effect of the exposed surface area of carbon nanostructures promotes faster VOCs adsorption/desorption considering the canister operating times [42]. There is a great number of researchers dealing with representative volatile organic compounds (VOCs) of gasoline (lineal aliphatic and aromatic hydrocarbons) by non-microporous carbon adsorbents [7], [11], [36], [114], [168], [181]. Nevertheless, most studies are focused on the adsorption behavior of single VOCs on carbonaceous adsorbents, and limited information is available concerning the adsorption behavior of multicomponent VOCs and gasoline on non-microporous carbon adsorbents. In addition, the interactions among the VOC molecules during dynamic adsorption of multicomponent mixtures are unclear. Thus, further research is needed for better understand the real dynamic adsorption behavior of gasoline on carbon canisters.

In the present study, a commercial microporous activated carbon and biochar/carbon nanostructures composite were employed in the adsorption removal of different gasses mixtures of benzene, toluene, hexane, and pentane, which are common VOCs in gasoline emissions. The adsorption capacity and selectivity behaviors were fully investigated in dynamic adsorption experiments. Moreover, the removal of actual VOCs from gasoline in a nitrogen stream was also investigated. This work also aimed to understand the competitive adsorption process of multicomponent VOCs by breakthrough profiles of carbonaceous adsorbents. Finally, to evaluate the mass transfer process in packed-bed columns, the experimental data were fitted by the Yoon-Nelson model.

## 5.2. Experimental section

### 5.2.1. Materials

All the analytical grade reagents involved in this study (Sigma-Aldrich Ltd) were used as received. The biochar/carbon nanostructures composite was first prepared via pyrolysis of



waste agave bagasse, followed by a CVD process in a rotatory furnace, the synthesis process had been described in detail in [Chapter 4](#). The commercial activated carbon used was Filtrasorb 400 from Calgon Carbon Company.

### 5.2.2. Dynamic adsorption experiments

Measurement of the adsorption capacities of carbonaceous adsorbents in a packed bed experimental set up was explored for binary mixtures of benzene-toluene, hexane-pentane, and hexane-benzene; multicomponent mixture of pentane-hexane-benzene-toluene; and commercial gasoline. The experimental set up was previously illustrated in [Chapter 4](#) (see [Fig. 4.1](#)). Prior to the adsorption measurement, samples were degassing at 90 °C overnight. Then, ~ 0.5 g of adsorbent (170-270 mesh) was loaded into a glass adsorption column (D = 0.5 cm, L = 8-10.2 cm). A glass filter plate was located at the bottom of the column as support of the adsorbent bed. The experiments were performed in the same packed-bed column configuration. The same nitrogen flow (~25 mL min<sup>-1</sup>) was used to the stripping reactor containing 100 mL of equal VOC volumetric proportions, or commercial gasoline. During the adsorption experiment, the inlet concentration ( $C_0$ ) of the VOCs was maintained constant, and the VOCs vapor flowed through the packed-bed from the bottom of the adsorbent column. For the multicomponent mixtures, bed saturation was achieved when the outlet concentration (C) for all VOCs matched the inlet concentrations. The breakthrough curves were obtained by analyzing the inlet and outlet concentration of each VOC as a function of the time by a gas chromatography instrument equipped with a flame ionization detector (GC-FID). The dynamic adsorption capacity was determined by the difference between the inlet and outlet concentration until the adsorption bed reached the saturated state, and the adsorption amount ( $q$ , mg VOCs g<sup>-1</sup>) was calculated according to the following equation [29] ([Eq. 5.2](#)).



$$q_e = \frac{Q}{m \cdot 10^{-6}} \int_0^{t_s} (C_0 - C) dt \quad (\text{Eq. 5.1})$$

where  $Q$  is the flow rate of gas stream,  $\text{mL min}^{-1}$ ;  $m$  is the mass of the adsorbent,  $\text{g}$ ;  $C_0$  and  $C$  are the inlet and outlet concentration of each component, respectively,  $\text{mg L}^{-1}$ ;  $t_s$  is the saturation breakthrough time,  $\text{min}$ ; and  $q_e$  is the calculated adsorption capacity,  $\text{mg g}^{-1}$ .

To quantitatively elucidate the adsorption kinetics, the breakthrough curves were fitted using the Yoon Nelson model (Y-N model) [182], expressed as the following equation (Eq. 5.2):

$$\frac{C}{C_0} = \frac{e^{(k_{YN}t - k_{YN}t_{50\%})}}{1 + e^{(k_{YN}t - k_{YN}t_{50\%})}} \quad (\text{Eq. 5.2})$$

where  $k_{YN}$  is the Yoon-Nelson adsorption kinetic constant ( $\text{min}^{-1}$ ) and  $t_{50\%}$  ( $\text{min}$ ) is the time necessary to reach the 50% amount of adsorbate loss of the initial hydrocarbon content ( $C/C_0 = 0.5$ ). Nonlinear regression curve fitting was carried out by using STATISTICA software with a Rosenbrock and quasi-Newton estimation methodology.

### 5.3. Results and discussion

#### 5.3.1. Adsorption study of multicomponent mixtures of VOCs

Based on the high single VOCs capacity and good regeneration potential of biochar/carbon nanostructures composite (BCVD600-1pTT) reported in Chapter 4, it seems to be a potential adsorbent to replace the activated carbon used in automotive canisters. It is well-known that under real conditions, numerous VOCs always coexist between them in gasoline emissions, in which VOCs species compete with each other for limited adsorption sites [166]. Therefore, the competitive adsorption of VOCs representatives of gasoline emissions was investigated herein. The effect of the competitive adsorption of VOCs, were first examined by binary adsorption, as it was shown Fig 5.1. Compared with the single



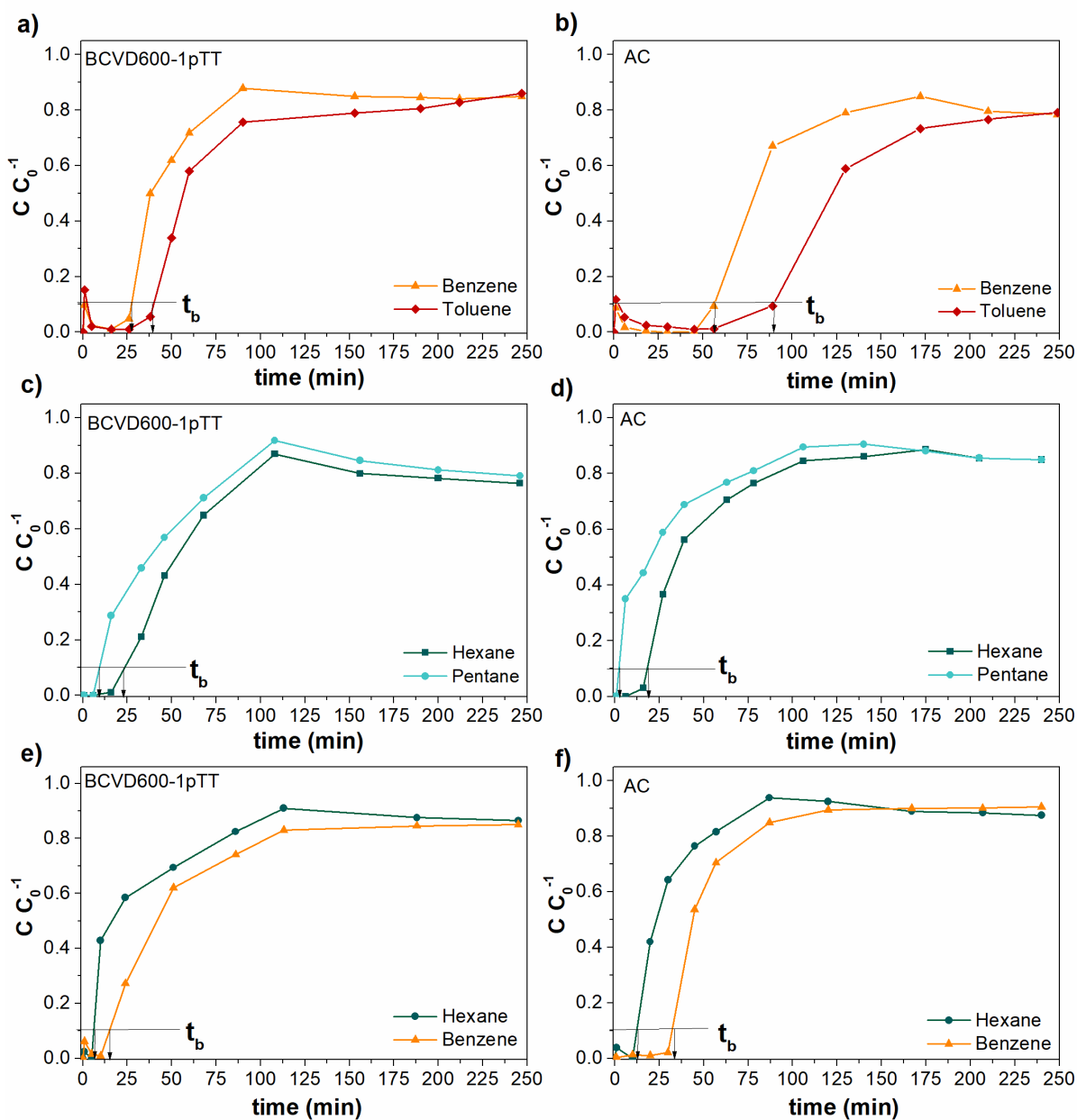
component adsorption shown in [Chapter 4](#), the binary mixture clearly showed competitive adsorption due to the different breakthrough curves. For instance, competitive adsorption of aromatic molecules slightly decreased the breakthrough times of toluene and benzene on BCVD600-1pTT from 37 to 36 min, and 36 to 24 min, respectively. Similarly, binary adsorption of aliphatic VOCs was also affected in both adsorbents, reducing up to 19 min the breakthrough time of pentane compared to single adsorption. The mixture of hexane-benzene also revealed a left shift of the breakthrough curves for activated carbon and BCVD600-1pTT adsorbents. It is worth noting that the longest breakthrough times in competitive adsorption experiments are promoted by less volatile VOCs, but when comparing binary and single adsorption only aromatic VOCs increase the service time. The latter is clearly observed by the increase in the breakthrough time of toluene and benzene on activated carbon from 81 to 96 min, and 40 to 57 min, respectively. This effect could be assigned to the competition of adsorbates to adsorptive zones such as  $sp^2$  hybridized carbon and functionalities active sites. In this sense, the spatial orientation of aromatic VOCs allows them to have three possible attractive interaction: stacked, T-shape, and displaced stacking geometry [183].

Regarding to this binary adsorption system, individuals mass transfer zones (MTZ) take place for each VOC of the mixture, which travel with different velocities through the packed bed. The displacement between VOCs could lead to quite different breakthrough behavior compared to single VOC adsorption [86]. In this sense, the shape of the breakthrough curves observed in [Fig. 5.1](#) did not follow the typical S-shape curve observed in single adsorption. Conversely, it was observed a change in slope of the breakthrough curve of mixtures once the outlet concentration reached between 80-90% of the inlet concentration. This change in the slopes was more pronounced on activated carbon. Several works related to dynamic adsorption of adsorbate mixtures assign the change in slope of breakthrough curves to the



displacement of adsorbates due to the competitiveness for active sites onto the adsorbent [28], [29], [86]. However, this behavior is frequently observed as an overshoot of concentration since at this point the outlet concentration is higher than the inlet concentration ( $C/C_0 > 1$ ). Even though this overshoot of concentration was not observed in Fig. 5.1, the change in the slopes of the curves for most volatile VOCs of each mixture suggest a competition of less volatile VOCs for non-polar zones and for active sites in the case of aromatic VOCs. The traveling velocity of the MTZ depends on the adsorption affinity of adsorbent for the adsorbate, causing that MTZ of the most volatile VOCs travels faster through the packed bed. This last one agrees with the longer breakthrough time of heaviest VOCs (aromatics). Accordingly, the most volatile VOC of each mixture reaches faster the adsorbent surface to be adsorbed as single component. However, when a heavier VOC reaches the adsorbent surface, a partial displacement of the previously adsorbed VOC occurs, establishing a new equilibrium with the two VOCs. This is consistent with the statement in numerous reports that the adsorbed molecules were replaced by other molecules and re-adsorbed in the unsaturated zone of the packed-bed, increasing ultimately the outlet concentration when the bed was completely saturated [166], [184], [185]. Despite of the larger molecular size favored the displacement of smaller molecules, the higher concentration of smaller molecules promoted that their high incidence also competed for absorption sites throughout the entire column. The latter may explain why an overshoot was not observed. Therefore, a plateau zone was produced when  $C/C_0 > 0.85$  and then the curve decreased until form another plateau together with less volatile VOCs.





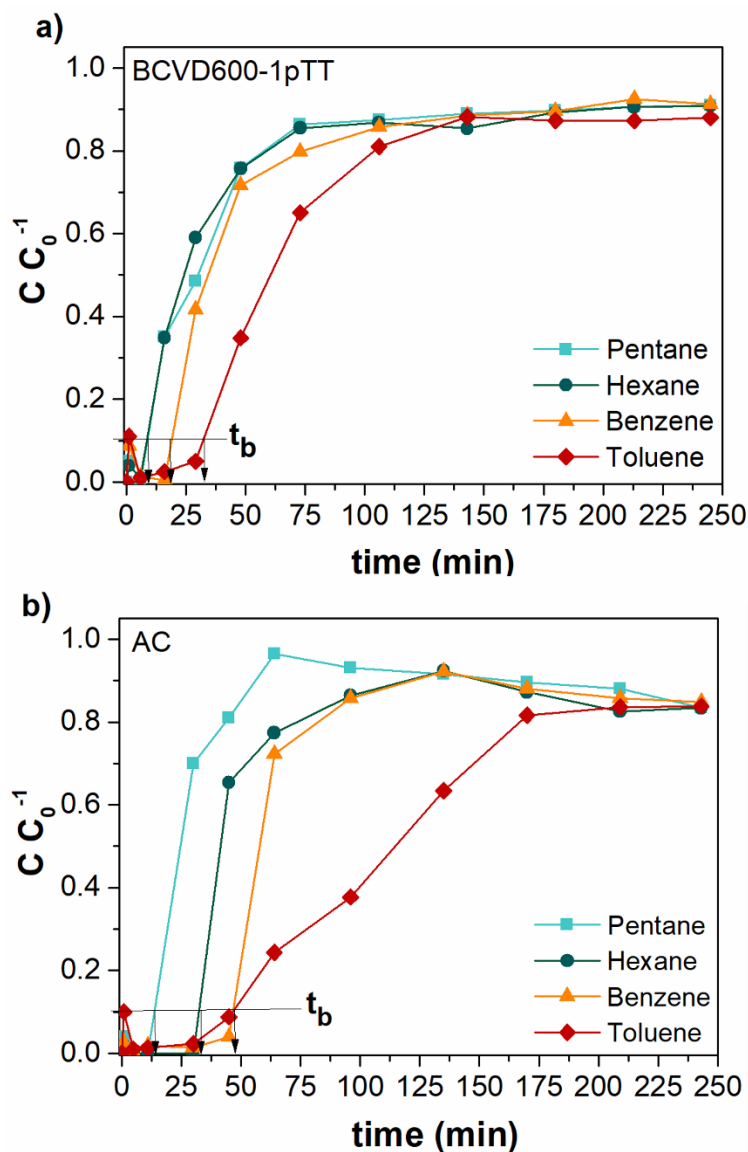
**Fig. 5.1** - Breakthrough curves of binary VOCs mixtures evaluating the interaction between a) aromatics VOCs, b) aliphatic VOCs, and c) aliphatic-aromatics in dynamic adsorption at 25 °C.  $t_b$  is the breakthrough time ( $C/C_0^{-1}$ ).

To further study the affinity between VOCs molecules and the carbonaceous surface of the adsorbents, simultaneous adsorption of pentane, hexane, benzene, and toluene on activated carbon and biochar/carbon nanostructures composite were investigated. The breakthrough curves of the multicomponent system were shown in Fig. 5.2. Overall, the



breakthrough time for toluene on activated carbon and BCVD600-1pTT was evidently longer than that for benzene, hexane, and pentane. The less volatile the VOCs, the longer the breakthrough time, following the same pattern as binary and single VOCs adsorption systems. Furthermore, the typical displacement for competitive adsorption was evident on activated carbon, while all four breakthrough curves of the VOCs mixture on BCVD600-1pTT did not follow competitive behaviors, suggesting a most homogeneous adsorption and mass transfer process during dynamic experiment. This behavior could be associated to the exposed adsorptive area of carbon nanostructures, where equilibrium could take place faster than in activated carbon micropores.

Regardless of the competitive VOCs adsorption, BCVD600-1pTT did not display highest plateau zones since breakthrough curves of pentane, hexane, and benzene have similar breakthrough (3-5 min) and saturations times (75-90 min). By carefully analyzing the breakthrough curves on activated carbon, a broad plateau zone was observed from 50 to 220 min for pentane, located above the other VOC curves. The most pronounced change in slope for pentane could be associated with the displacement by competition, first of hexane, followed by benzene and then for toluene. In contrast, the less pronounced change in slope of benzene curve observed between 90 and 160 min suggested competition mainly with toluene. Nevertheless, the displacement of benzene and toluene for hexane and pentane should not be discarded, as already described above. The latter indicated that in microporous materials, adsorption of a considered VOC in a multicomponent system can hardly be influenced by other VOCs as a result of competition for the existing adsorption sites and the interaction during the transport to the adsorption sites [186]. These results encourage the use of biochar/carbon nanostructures composite instead of activated carbon for the removal of multicomponent VOCs from gasoline emissions.



**Fig. 5.2** - Multicomponent adsorption breakthrough curves for BCVD600-1pTT and activated carbon at 25 °C.

As shown in Table 5.1, in binary systems the adsorption capacities of pentane and hexane on activated carbon were about 44 and 35% lower than those of BCVD600-1pTT, respectively. Considering hexane-benzene mixture, BCVD600-1pTT also showed an adsorption capacity up to 37% higher than activated carbon. Meanwhile, the adsorption capacities of aromatic mixtures were similar in both adsorbents. It is important to highlight that toluene was adsorbed in an average of 35 mg g<sup>-1</sup> in both single and competitive



adsorption. This similarity is due to the fact that the low vapor pressure of toluene (0.038 atm) did not promote driving forces, being the last VOC to reach the adsorbent surface partially covered with lighter VOCs, thus the larger molecular size of toluene implies greater affinity for active sites.

The total adsorption amount of binary and multicomponent mixtures of VOCs in both adsorbents was lower than those of single VOCs, indicating that the competitive adsorption of two or more VOCs may limit the use of adsorptive zones on the carbonaceous surface for each VOC. The much lower adsorption capacities of pentane, hexane, and benzene in a multicomponent mixture than in binary systems make competition for adsorption active sites more evident. The adsorption capacity of BCVD600-1pTT for pentane, hexane, and benzene in a multicomponent mixture only account 12, 25, and 31% of that in the simple system, respectively. Additionally, the adsorption amount of pentane in BCVD600-1pTT from multicomponent was only 1.01, 1.43 and 4.1 times greater than that of hexane, benzene, and toluene, respectively. These results indicate that the basic character of BCVD600-1pTT surface ( $\text{pH}_{\text{PZC}} = 9.7$ ) promotes a physical and non-selective adsorption of the nonpolar VOCs, and the slightly higher adsorption capacity of pentane than that of the other VOCs was due to its highest concentration, which implied a greater number of molecules to be adsorbed. The higher adsorption capacity as a consequence of the concentration and not of a higher selectivity has already been reported [28]. The dynamic adsorption comparison of single and mixtures of VOCs is broadly reported by using the same inlet concentration of each VOC [29], [93], [166]. In these studies, it was notorious that the heavier VOCs shows the longest breakthrough and thus the higher adsorption capacities. Additionally, it was even reported that the increase in inlet concentration also improve both breakthrough time and adsorption capacity. However, the VOCs concentration in real multicomponent mixtures such as gasoline varies based on their own features, where



the low vapor pressure of the heavier VOCs results in a low concentration in the gas mixture. Accordingly, the lowest vapor pressure of toluene was in concordance with its low concentration, which caused the lowest mass transfer in the mixture, and thus, by increasing the concentration (higher vapor pressure), the diffusion of VOCs in the adsorbent can be accelerated. Even though the largest kinetic diameter of toluene (0.6 nm) and benzene (0.58 nm) may imply a higher adsorption energy than aliphatic VOCs, the smallest adsorption capacities for aromatic VOCs in single and multicomponent mixtures were a consequence of its lowest concentration.

Taking in consideration the MTZ parameter, it is observed that this travels through the packed bed with a velocity ( $0.009\text{--}0.081\text{ mL min}^{-1}$ ) that is much slower than the gas velocity ( $20\text{--}23\text{ mL min}^{-1}$ ). After analyzing the height of mass transfer zone ( $H_{\text{MTZ}}$ ) and the rate of mass transfer zone ( $R_{\text{MTZ}}$ ) between mixtures in activated carbon, a direct correspondence with the molecular weight was found. The lightest VOCs showed the largest  $H_{\text{MTZ}}$  and  $R_{\text{MTZ}}$ , while the heaviest VOCs presented the shortest values, respectively. For instance, toluene did not diffuse faster through the packed bed in binary mixtures because its largest size promotes a high adsorption energy with surface adsorbent and thus its low concentration did not promote a faster mass transfer. These results agree with those reported in the literature where the dynamic adsorption capacities of aromatic VOCs are greater by using higher concentrations in multicomponent mixtures [28], [29], [181], [184]. In the case of BCVD600-1pTT, the highest  $H_{\text{MTZ}}$  of toluene and benzene in toluene-benzene and benzene-hexane mixtures agree with the breakthrough curves behavior since no change in slope by adsorption competition was observed. Other worthy aspect to note is that even though the percentage occupied by the MTZ ( $H_{\text{MTZ}}/H$ ) within the packed-bed of BCVD600-1pTT ( $>100\%$ ) was higher than that in activated carbon, the total adsorption capacities of multicomponent mixtures were similar.



**Table 5.1** - Dynamic adsorption parameters and capacities of activated carbon and BCVD600-1pTT.

Adsorbent	Parameter	Component mixtures				$q_{\text{total}}$ ( $\text{mg g}^{-1}$ )
		Pentane	Hexane	Benzene	Toluene	
AC	$q_e$ ( $\text{mg g}^{-1}$ )	72.54	42.94	--	--	115.48
	$H_{\text{Bed}}$ (cm)	8.00		--	--	
	$H_{\text{MTZ}}$ (cm)	15.59	12.16	--	--	
	$R_{\text{MTZ}}$ ( $\text{cm min}^{-1}$ )	0.179	0.133	--	--	
	$q_e$ ( $\text{mg g}^{-1}$ )	--	--	43.61	37.33	80.95
	$H_{\text{Bed}}$ (cm)	--	--	9.20		
	$H_{\text{MTZ}}$ (cm)	--	--	7.71	7.69	
	$R_{\text{MTZ}}$ ( $\text{cm min}^{-1}$ )	--	--	0.067	0.048	
	$q_e$ ( $\text{mg g}^{-1}$ )	--	55.52	41.82	--	97.35
	$H_{\text{Bed}}$ (cm)	--	8.20		--	
	$H_{\text{MTZ}}$ (cm)	--	9.75	7.44	--	
	$R_{\text{MTZ}}$ ( $\text{cm min}^{-1}$ )	--	0.195	0.138	--	
	$q_e$ ( $\text{mg g}^{-1}$ )	30.39	29.13	25.34	19.94	104.81
	$H_{\text{Bed}}$ (cm)	8.00				
	$H_{\text{MTZ}}$ (cm)	7.88	7.71	5.33	8.78	
	$R_{\text{MTZ}}$ ( $\text{cm min}^{-1}$ )	0.225	0.138	0.124	0.049	
BCVD600-1pTT	$q_e$ ( $\text{mg g}^{-1}$ )	129.32	67.03	--	--	196.35
	$H_{\text{Bed}}$ (cm)	10.20		--	--	
	$H_{\text{MTZ}}$ (cm)	13.68	9.81	--	--	
	$R_{\text{MTZ}}$ ( $\text{cm min}^{-1}$ )	0.171	0.137	--	--	
	$q_e$ ( $\text{mg g}^{-1}$ )	--	--	42.43	34.78	77.21
	$H_{\text{Bed}}$ (cm)	--	--	9.60		
	$H_{\text{MTZ}}$ (cm)	--	--	8.22	11.13	
	$R_{\text{MTZ}}$ ( $\text{cm min}^{-1}$ )	--	--	0.161	0.060	
	$q_e$ ( $\text{mg g}^{-1}$ )	--	62.00	61.24	--	123.24
	$H_{\text{Bed}}$ (cm)	--	9.90		--	
	$H_{\text{MTZ}}$ (cm)	--	14.28	15.68	--	
	$R_{\text{MTZ}}$ ( $\text{cm min}^{-1}$ )	--	0.172	0.126	--	
	$q_e$ ( $\text{mg g}^{-1}$ )	33.84	31.26	24.61	8.86	98.58
	$H_{\text{Bed}}$ (cm)	10.20				
	$H_{\text{MTZ}}$ (cm)	23.86	23.88	16.38	10.66	
	$R_{\text{MTZ}}$ ( $\text{cm min}^{-1}$ )	0.411	0.405	0.205	0.122	

$H_{\text{Bed}}$ : packed bed height;  $H_{\text{MTZ}}$ : mass transfer zone height;  $R_{\text{MTZ}}$ : mass transfer zone rate.



The Yoon Nelson (YN) adsorption model was fitted to the experimental data to obtain a valid prediction of the breakthrough parameters. YN model is successfully applied in S-shaped curves from continuous systems because it is assumed that the probability of adsorbed molecules during the process is proportional to the probability of the breakthrough and saturation on the adsorbent [187]. An acceptable fit quality was achieved by observing the  $R^2$  ( $> 0.83$ ) and the SSE values ( $< 0.204$ ) for all the evaluated systems (Table 5.2). Furthermore, the predicted  $t_{50\%}$  values were corroborated to be near the linear interpolation values from the breakthrough curves.

In general, the relationship of the calculated adsorption rate constant ( $K_Y$ , [ $\text{min}^{-1}$ ]) for the binary systems can be divided in three groups (Table 5.2, and Fig. 5.3a and b) in terms of the adsorbents: (a) pentane and hexane systems (P-H) registered similar  $K_Y$  values with a slightly increase in the case of hexane, probably due to its higher hydrophobicity; (b) benzene and hexane (B-H) systems achieved higher values for the activated carbon adsorbent. The aromatic nature of benzene probably promotes major gas adsorption interactions with the well-developed textural features of activated carbon. In the case of the BCVD600-1pTT adsorbent, closer differences were observed between both pollutants, but with lower predicted values in comparison with activated carbon; (c) benzene and toluene (B-T) systems registered rate values between 0.026 to 0.083  $\text{min}^{-1}$ . For benzene, similar values were recorded for both adsorbents. On the other hand, the toluene capacity was lower onto activated carbon. It is suggested that benzene occupied the majority of the available micropores, lowering the surface-active interactions with toluene. In the case of the BCVD6000-11TT adsorbent, its most exposed surface granted by nanostructures may hinder the benzene-toluene competence for available sites, resulting in closer rate values.



**Table 5.2** - Breakthrough curve parameters of Yoon-Nelson model for binary and multicomponent pollutants onto activated carbon and BCVD6000-11TT.

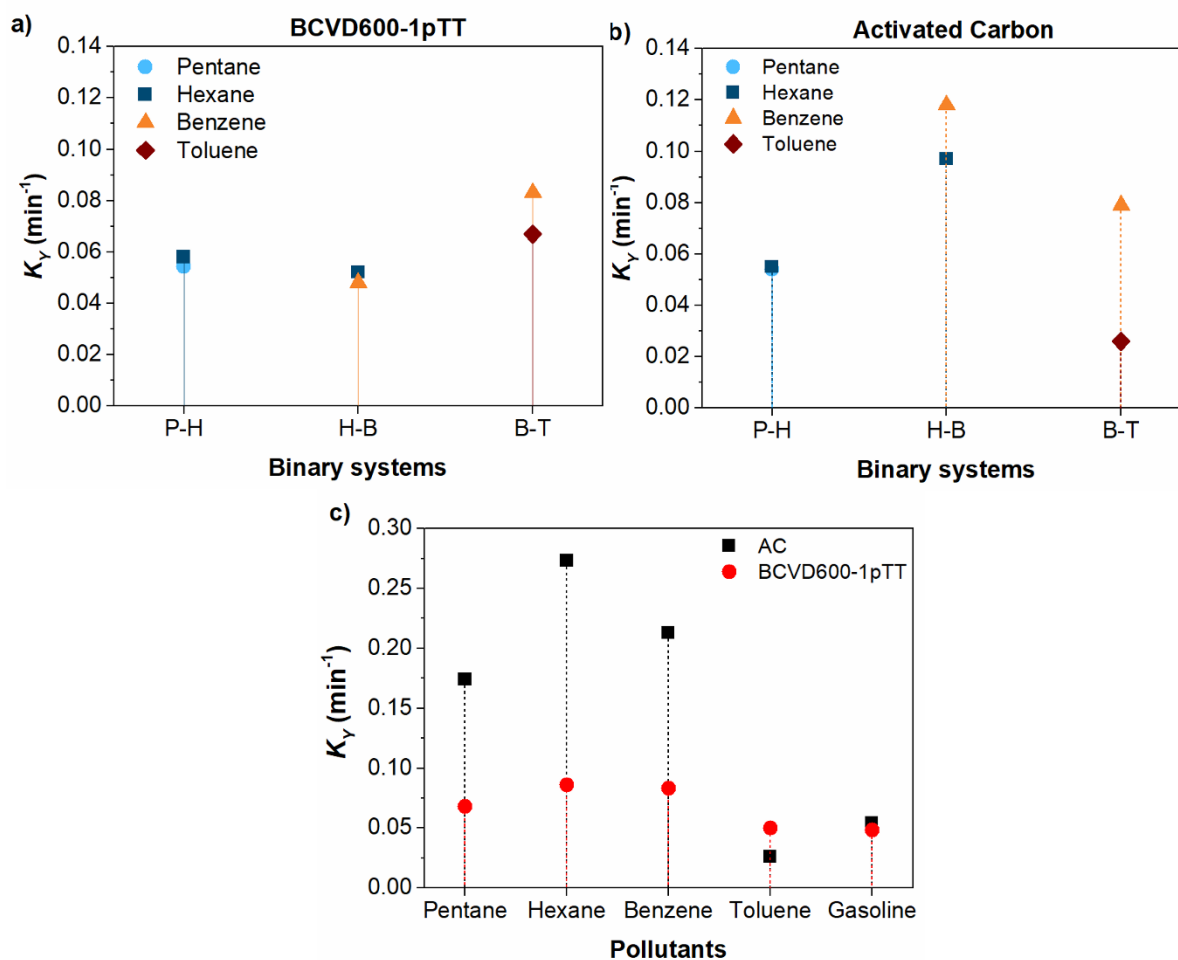
	Pollutant				
	Pentane	Hexane	Benzene	Toluene	Gasoline
<b>Activated carbon</b>					
$K_Y$ [min <sup>-1</sup> ]	0.0540	0.055	---	---	---
$t_{50\%}$ [min]	27.84	45.66	---	---	---
$R^2$	0.839	0.902	---	---	---
SSE	0.204	0.171	---	---	---
$K_Y$ [min <sup>-1</sup> ]	---	---	0.079	0.026	---
$t_{50\%}$ [min]	---	---	82.17	141.0	---
$R^2$	---	---	0.905	0.926	---
SSE	---	---	0.158	0.094	---
$K_Y$ [min <sup>-1</sup> ]	---	0.097	0.118	---	---
$t_{50\%}$ [min]	---	27.64	47.00	---	---
$R^2$	---	0.927	0.960	---	---
SSE	---	0.118	0.082	---	---
$K_Y$ [min <sup>-1</sup> ]	0.174	0.273	0.213	0.026	---
$t_{50\%}$ [min]	26.30	42.77	59.52	119.1	---
$R^2$	0.952	0.925	0.960	0.971	---
SSE	0.096	0.145	0.085	0.040	---
$K_Y$ [min <sup>-1</sup> ]	---	---	---	---	0.054
$t_{50\%}$ [min]	---	---	---	---	51.24
$R^2$	---	---	---	---	0.880
SSE	---	---	---	---	0.171
<b>BCVD600-1pTT</b>					
$K_Y$ [min <sup>-1</sup> ]	0.0544	0.058	---	---	---
$t_{50\%}$ [min]	42.93	56.33	---	---	---
$R^2$	0.878	0.880	---	---	---
SSE	0.161	0.167	---	---	---
$K_Y$ [min <sup>-1</sup> ]	---	---	0.083	0.067	---
$t_{50\%}$ [min]	---	---	44.84	61.97	---
$R^2$	---	---	0.913	0.883	---
SSE	---	---	0.154	0.194	---
$K_Y$ [min <sup>-1</sup> ]	---	0.052	0.048	---	---
$t_{50\%}$ [min]	---	29.43	52.14	---	---
$R^2$	---	0.837	0.914	---	---
SSE	---	0.167	0.115	---	---
$K_Y$ [min <sup>-1</sup> ]	0.068	0.086	0.083	0.050	---
$t_{50\%}$ [min]	31.04	28.38	38.21	65.53	---
$R^2$	0.937	0.920	0.940	0.952	---
SSE	0.084	0.127	0.113	0.085	---
$K_Y$ [min <sup>-1</sup> ]	---	---	---	---	0.048
$t_{50\%}$ [min]	---	---	---	---	46.60
$R^2$	---	---	---	---	0.883
SSE	---	---	---	---	0.148

$K_Y$  = Yoon-Nelson adsorption kinetic constant;  $R^2$  = determination coefficient; SSE = sum square error.





Regarding multicomponent systems (Fig. 5.3c), a high rate of adsorption was reported for the pollutants under study onto activated carbon with the exception of toluene. It is suggested that the microporosity of activated carbon, in addition to its tortuosity, decrease the intraparticle diffusion of large molecules. Moreover, toluene registered a cooperative adsorption process (at  $C/C_0$  values over 0.1), possibly forming multilayers of adsorbate with the other nonpolar molecules, which limit the interaction probability with available sites.

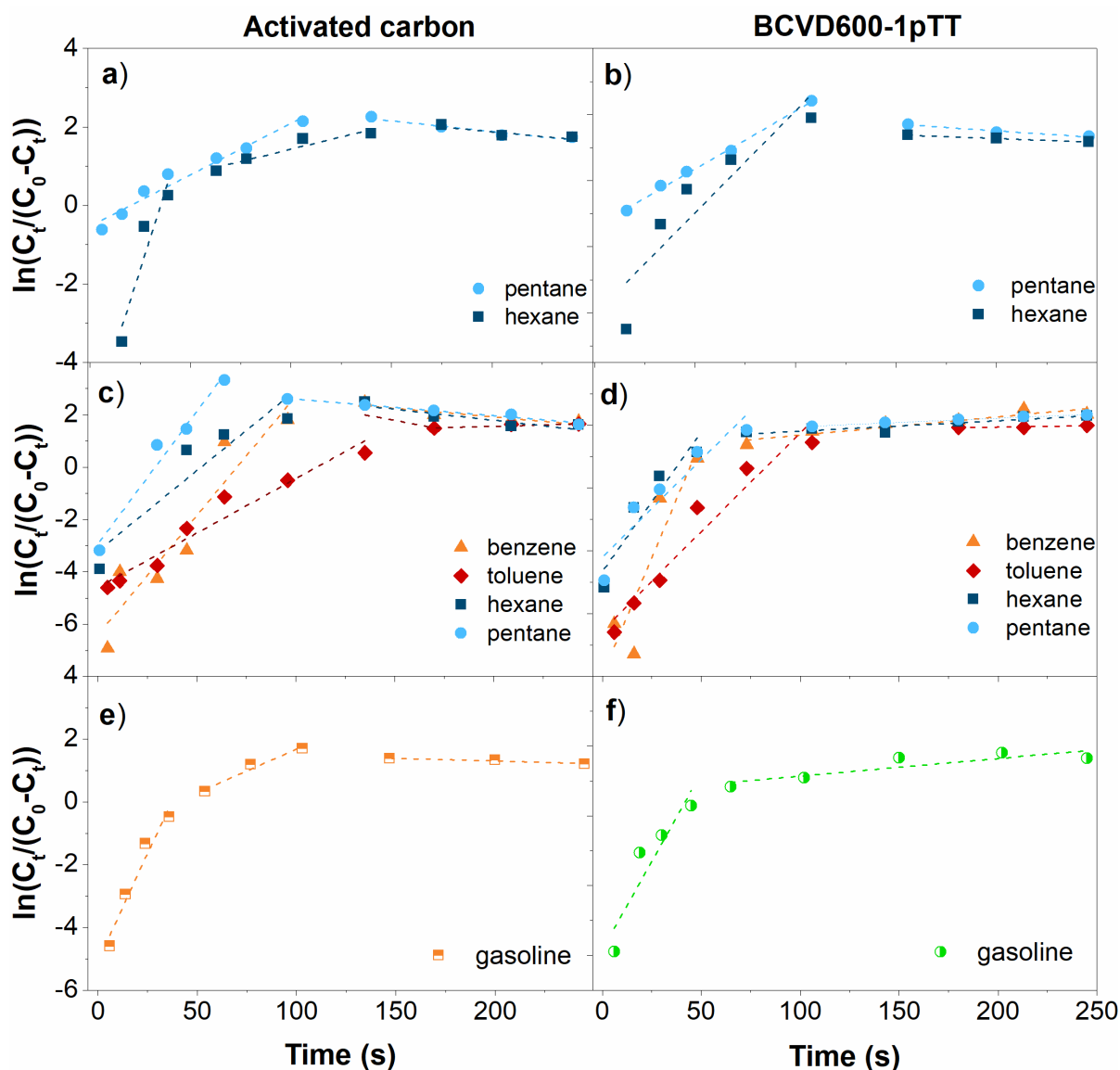


**Fig. 5.3** - Adsorption rate values ( $K_Y$ , [ $\text{min}^{-1}$ ]) for the evaluated systems. a) Binary systems with activated carbon and, b) Binary systems with BCVD6000-1pTT. c) Multicomponent evaluations for both adsorbents with the pollutants under study. P-H: pentane-hexane; H-B: hexane-benzene; and B-T: benzene-toluene mixture.



Additionally, the linearized Yoon-Nelson model was employed to identify an overall change in the mass transfer rate  $K_Y$  [ $\text{min}^{-1}$ ] by identifying the different slopes in the regression fitting procedure (Fig. 5.4a-d). In general, two steps were identified in three binary systems with the similar pattern observed for pentane-hexane mixture. The first slopes prior to the initial breakthrough points of each system are related to a fast diffusion into macro and mesopores. At longer periods of time up to the material saturation, a diminish in the intraparticle rate is noticeable.

Finally, the adsorption rate value for gasoline onto BCVD600-1pTT ( $0.048 \text{ min}^{-1}$ ) was comparable to pentane, hexane, and benzene rate values (Table 5.2, Fig. 5.3c). This feature probably suggests a high exposure of active site onto carbon nanostructures since these model VOCs and the multicomponents of real gasoline were adsorbed with similar rate regardless the concentrations and features of each VOC, which is consistent with the mentioned above. It is necessary to conduct more experiments to support this observation. The linearized model also described a two-step adsorption process for the adsorbents (Fig. 5.4e-f).



**Fig. 5.4** - Linearized Yoon-Nelson equations for pentane-hexane (a,b), multicomponent (c,d) and gasoline (e,f) systems with activated carbon and BCVD600-1pTT adsorbents.

### 5.3.2. Gasoline breakthrough curves

To prove the capability of BCVD600-1pTT to adsorb gasoline emissions under dynamic conditions, the breakthrough curves were obtained and are presented in Fig. 5.5. Herein, it was found that the whole gasoline emission was similarly adsorbed on activated carbon and on BCVD600-1pTT. For the first 12 min, gasoline emissions were completely adsorbed in



both adsorbents, and the outlet concentration tend to zero. Over the time, the surface of the adsorbent was covered by a greater quantity and diversity of VOCs of increasing molecular weight, which belong to gasoline emissions. The increase in gasoline emission concentration at the outlet was attributed to the decrease in the sticking probability of the several VOCs as more active sites were occupied [28]. The breakthrough time of activated carbon (19 min) and BCVD600-1pTT (12 min) indicated a similar affinity for gasoline, also reflected in the breakthrough adsorption capacities of 187 and 153 mg g<sup>-1</sup>, respectively.

It was worth noting that the breakthrough curves shapes shown in Fig. 5.5a did not follow the typical S-shape. Even though BCVD600-1pTT showed a curve similar to a sigmoid, the breakthrough curve of activated carbon presented an overlap typical of competitive dynamic adsorption. It has been reported that during adsorption of VOCs gas mixture, the complexity of the adsorption process increases with the number of components in the multicomponent mixture [29]. In this sense, it is well-known that gasoline emission is a mixture of over 100 VOCs [30], therefore, to evaluate the effect of each VOC in the total breakthrough curve is a real challenge. Considering that gas chromatography separates the more than 30 components detected in the analysis based on their molecular weight, it was considered to separate the total spectra into four groups. The first group of VOCs detected between 2.2-2.5 min were associated to those with molecular weights lower than 78 g mol<sup>-1</sup>, the second group detected between 2.5-2.8 min were associate with VOC molecular weights between 78 and 86 g mol<sup>-1</sup>, the times between 2.8-3.2 min were related to molecular weights between 86 and 92 g mol<sup>-1</sup>, and finally VOCs heavier than 92 g mol<sup>-1</sup> was analyzed after 3.2 min. The relationship of these times with their molecular weight was considered based on the time of detection of the model VOCs (pentane, hexane, benzene, and toluene) and the complete range of components of a real gasoline, from 58 to 106 g mol<sup>-1</sup>.

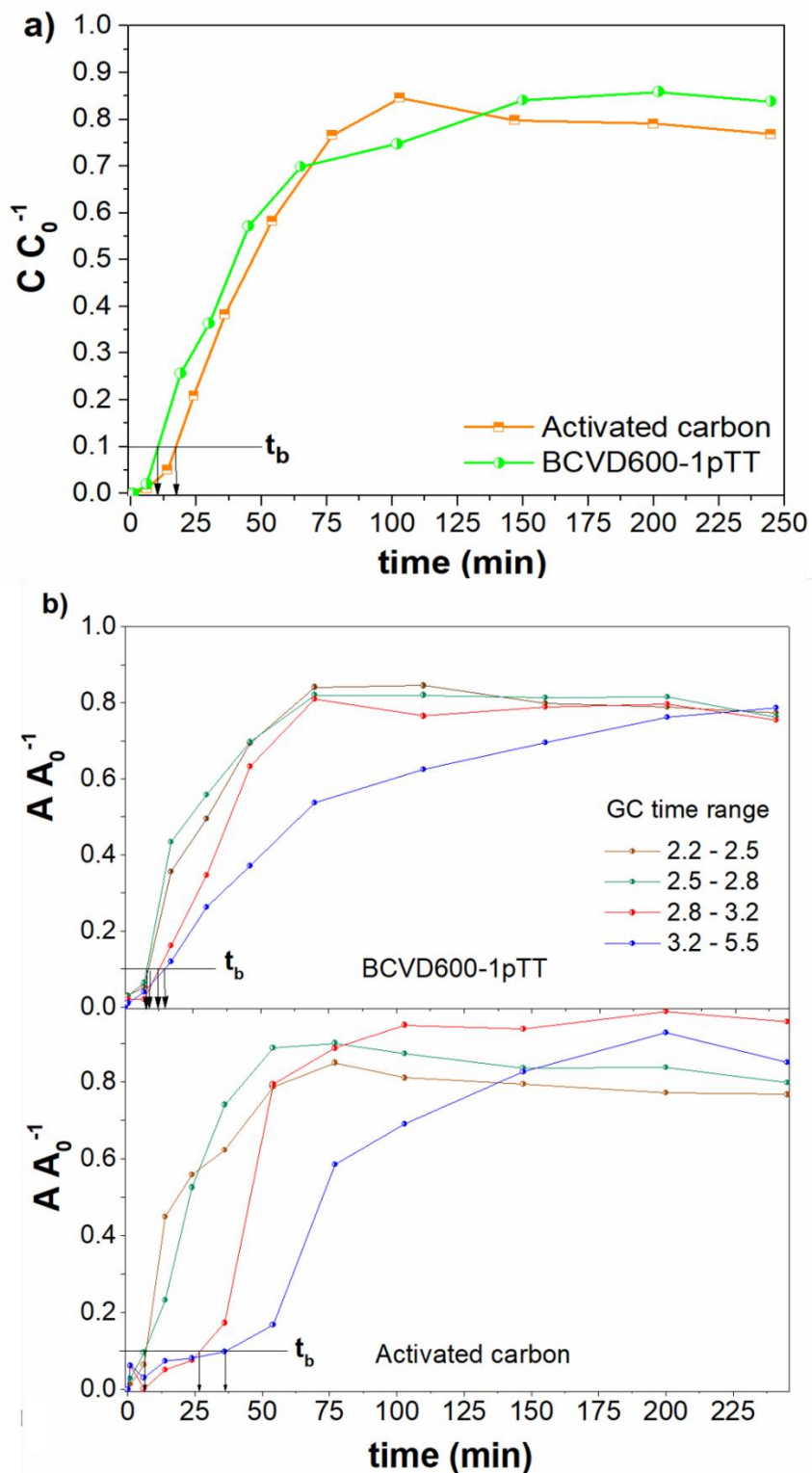


The breakthrough curves of multicomponent groups were reported in Fig 5.5b. All four curves on activated carbon showed changes in slope without a typical S-shape. Similar to the co-adsorption effect observed in the model multicomponent mixtures (see Fig. 5.2), it is suggested that the VOCs from real gasoline emissions with smaller molecular weights (detected from 2.2 to 2.5 min), reaching faster the surface active sites than the heaviest detected after 3.5 min. Accordingly, the two changes in slope observed at 32 and 75 min suggest a competition for active sites with heavier VOCs. The breakthrough curves of the following two detection ranges (2.5 to 2.8 min and 2.8 to 3.2 min) did not show an important change in slopes. This behavior could be associated to the similarity in the molecular weight of the VOCs detected in these ranges, which also implies others similar features such as common diffusional rates (attributed to their vapor pressure) and adsorption energies. Furthermore, the change in the slope observed at 200 min of the breakthrough curve associated to the heaviest VOC (3.2 to 5.5) suggests that the components of the complex gasoline mixture continued to compete for active sites even near the end of the experiment. As it was expected, the very low concentration of aromatic molecules reported in commercial gasolines agrees with this breakthrough curve since this behavior was similar to the breakthrough curve of toluene in multicomponent mixture.

Finally, the use of BCVD600-1pTT registered a noticeable effect on the removal of gasoline components. The absence of a clear change in slopes indicated that diffusion of most VOCs behaves very similar throughout the packed-bed column. All this demonstrated that the biochar/carbon nanostructures composite is suitable for the removal of the complex composition of gasoline emissions due to its comparable adsorption capacity to that of commercial activated carbon. On the other hand, it is worth noting that dynamic experiments were carried out for four hours to evaluate similar operation conditions to those use in an automotive canister, which mainly involves the adsorption of several VOCs from evaporative



emissions during the first hours after the vehicle is turned off. In this sense, the analysis of the packed bed performance for the adsorption of VOCs for many more hours would allow observing more changes in the slopes until reaching a total saturation of the column ( $C/C_0 = 1$ ). However, when an automatic system is used, the canister regeneration occurs before the adsorbent is saturated.



**Fig. 5.5** - a) Breakthrough curves of gasoline emission for activated carbon and BCVD600-1pTT. b) Adsorption behavior of gasoline multicomponent emission by separating gas-chromatography detection times. The areas under the curve of GC analysis at the inlet and outlet of the column were used to develop the plotted curves vs. time.



Based on what has been discussed above, it can be inferred that the co-adsorption of multicomponent mixtures of VOCs is a complicated process, controlled by many factors such as the diffusion in the porous structure and the interaction between VOCs and the carbonaceous surface. In addition, the adsorption process in multicomponent systems may be interpreted in several stages, mainly based on the number of adsorbates in the mixture (Fig. 5.6). For instance, the co-adsorption process of pentane, hexane, benzene, and toluene on a microporous adsorbent such as activated carbon can be divided into five stages. At the beginning, the external surface adsorption takes place as the first stage, which involves the molecular diffusion of the VOCs from the bulk phase to the external surface area of the adsorbent. In this stage, the inlet concentration of VOCs and the textural features of the adsorbent are the ones that most influence the external surface adsorption. Considering the breakthrough curves performance, pentane showed the fastest mass transfers to be first adsorbed. As it was previously noted, the highest concentration of pentane further promoted the molecular diffusion from the external surface area into the pores. Then, hexane and pentane are adsorbed on the external surface and in pores, while toluene adsorption occurs slowly. The ability of carbonaceous materials to adsorb VOC mixtures allowed that the outlet concentration was equal to zero in stage 1. Particle diffusion is generally a function of pore volume and pore size distribution of the adsorbents used [186]. Consecutively, as heavier VOCs arrive to the adsorptive surface, some pre-adsorbed pentane molecules can be displaced by hexane or benzene molecules. For this reason, a certain concentration of pentane was first detected at the outlet of the column (stage 2). In stage 3, pre-adsorbed pentane is constantly replaced by heavier VOCs, which is reflected in a change in slope of the curve at  $C/C_0 > 0.85$ . Once the adsorption surface was almost covered, the available surface to adsorb more pentane was very limited and, therefore, its outlet concentration stabilized upon reaching saturation concentration in an asymptotic manner as it was observed at the stage 4. It is also suggested that hexane was replaced by



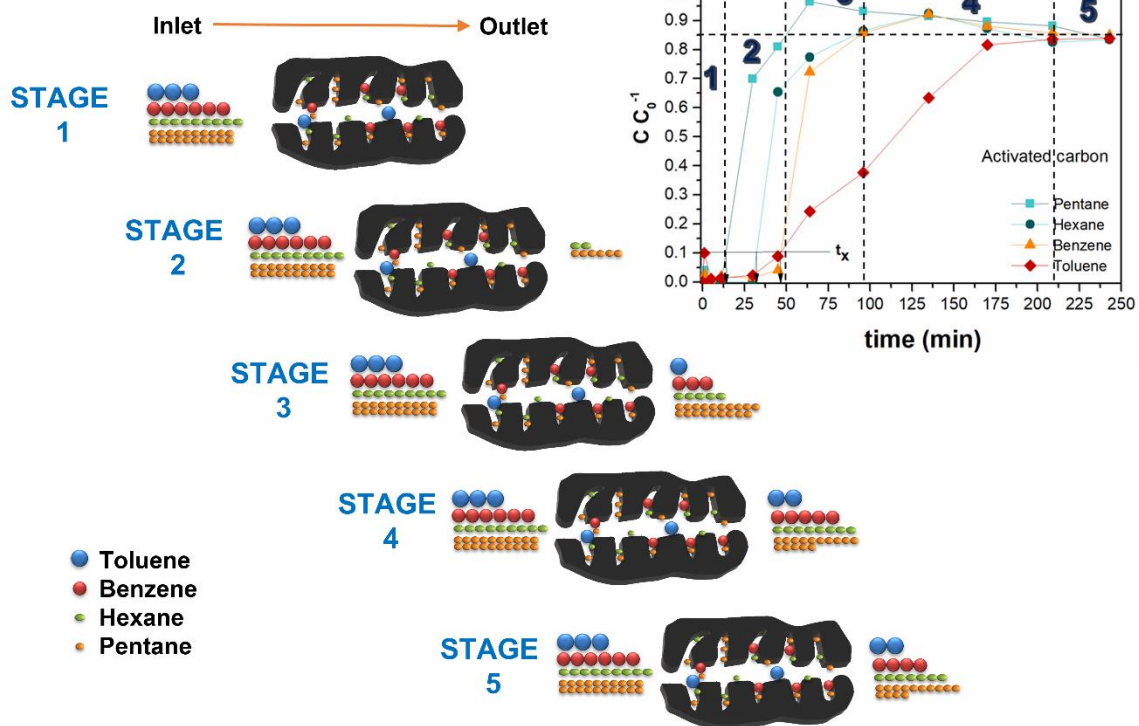


benzene, and benzene was also replaced by toluene, as it was observed by the change in slopes. At this stage, toluene diffused through the column to reach the outlet. The equilibrium was considered once the outlet concentration of all the VOCs was maintained stable at 85% of the inlet concentration (stage 5).

Considering the behavior of the breakthrough curves of BCVD600-1pTT, it is possible to interpretate its co-adsorption of multicomponents only in three stages, as it was observed in [Fig. 5.6b](#). These stages agree with the interpretation of the stage 1, 4 and 5 from activated carbon, while the change in the slope observed in the stage 2 and 3 was not observed in the BCVD600-1pTT curves. In contrast, the lower tortuosity and microporosity of BCVD600-1pTT suggests a most homogeneous mass transfer of multicomponents from the gas mixture to the active sites. The latter was evident by the absence of a change in the slopes. In this sense, although the displacement of molecules by competition for active sites take place, the typical adsorption-desorption equilibrium process occurs relatively quickly compared to activated carbon.



a) Co-adsorption on activated carbon



b) Co-adsorption on BCVD600-1pTT

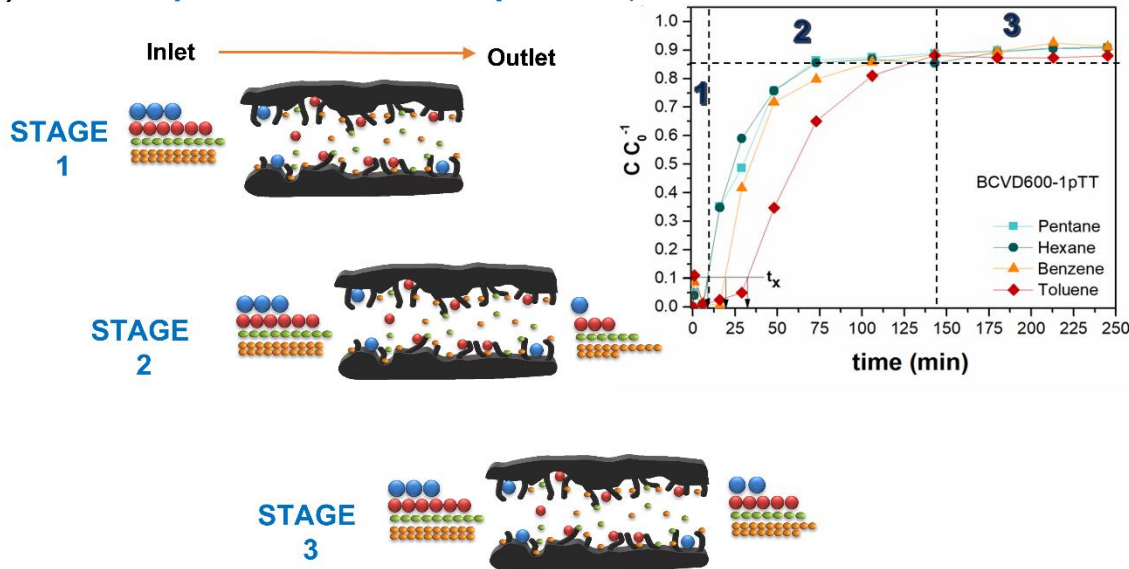


Fig. 5.6 - Schematic mechanism of multicomponent adsorption system on activated carbon and BCVD600-1pTT adsorbents.



#### 5.4. Conclusions

In this work, dynamic adsorptions of multicomponent mixtures of gasoline emissions onto biochar/carbon nanostructures composite are evaluated and compared with a commercial activated carbon. The breakthrough curves of binary and multicomponent mixtures follow the same pattern than single adsorption since the heavier VOCs have a higher service time, up to 80 min. However, the adsorption capacities of activated carbon and BCVD600-1pTT are similar in binary and multicomponent systems, although their total adsorption for each mixture is still less than that of the single adsorption. Here, pentane is the most efficiently adsorbed VOC, followed by hexane and benzene, while toluene adsorption is less favored. The adsorption performance mainly depends on the VOCs physical properties, where the lower molecular weight (boiling point) of pentane and, thus, its higher concentration promotes a faster mass transfer to surface active sites. The adsorption capacity of pentane in BCVD600-1pTT from multicomponent VOCs is 1.01, 1.43 and 4.1 times greater than that of hexane, benzene, and toluene. Furthermore, the adsorption capacity for pentane, hexane, and benzene in multicomponent mixture only account 12, 25, and 31% of that in the single system, respectively, while toluene behaves similar in single and multicomponent systems ( $q = 35 \text{ mg g}^{-1}$ ). During the multicomponent study, it was observed a change in the slopes of the breakthrough curves of activated carbon once  $C/C_0 > 0.85$ , which is related with competition and displacement of VOCs. The breakthrough curves of BCVD600-1pTT did not follow this change in the slopes, suggesting a more homogeneous adsorption and mass transfer process during dynamic experiments. The adsorption breakthrough experiment of real gasoline emissions confirm how competitive BCVD600-1pTT can be in automotive canisters compared to activated carbon: similar breakthrough time of 12 and 15 min, respectively, and adsorption capacities of 153 and 187  $\text{mg g}^{-1}$ , respectively, were obtained. The multicomponent co-adsorption on activated carbon is represented by 5-stages,



involving the effect of competitive adsorption while the more homogeneous adsorption on BCVD600-1pTT reduces the adsorption stage to 3. Overall, it is confirmed the exceptional ability of BCVD600-1pTT to simultaneously adsorb several VOCs from gasoline emissions. More knowledge is necessary in order to assess gasoline vapor recovery in modern vehicles.

# CHAPTER 6

---

## General discussion

---

---

The economic and social growth of recent decades has led to an exponential deterioration of air quality since urbanization increase has been related to the increase in vehicle emissions. Of these, evaporative emissions represent one of the main sources of atmospheric VOCs, impacting air quality. Nowadays, modern vehicles use activated carbon for the recovery of gasoline emissions due to its versatility to remove several pollutants from the gas phase. Despite of the well-known effectiveness of activated carbon for VOCs removal, its diffusional restriction in narrow micropores through adsorption and desorption means that fast in situ regenerations remain a challenge today. This has opened new approaches to design efficient carbonaceous adsorbents with high recovery of VOCs from gasoline and reuse capacity. One option that has attracted considerable attention to overcome this disadvantage has been the development of non-polar carbonaceous adsorbents that combine a considerable exposed surface area with a wide pore arrangement.

Because of the latest, the first approach in this thesis was to develop a macroporous biochar from the pyrolysis of agave bagasse, a raw lignocellulosic waste material from a local mezcal industry. The valorization of this renewable carbon source has received increasing attention due to the potential reduction of the environmental pollution that causes its confinement. As it was exposed in [Chapter 2](#), the thermal instability at 600 °C of cellulose



and hemicellulose from agave bagasse led to the formation of a carbon skeleton with an arrangement of wide parallel channels along the particle with diameters between 2 to 15  $\mu\text{m}$ . Further analytical characterization showed the presence of calcium carbonate with rod-like morphology at biochar periphery. Biochar production for application in the automotive industry can benefit from its low energy consumption and high production rate, however, its small surface area ( $120 \text{ m}^2 \text{ g}^{-1}$ ) limits its applications as an effective adsorbent. Therefore, it was necessary to improve the biochar surface area by the growth of carbon nanostructures in order to be competitive with the adsorption capacity of a commercial activated carbon. One of the greatest challenges of grown carbon nanostructures by CVD synthesis on heterogeneous substrates like biochar has been to control its dispersibility and particle size. Such drawbacks were overcome using CMC during the iron catalyst impregnation. SEM backscattered electrons images revealed a homogeneous distribution and a smaller particle size of the catalyst on biochar. Furthermore, it was proposed that the role of CMC during its thermal decomposition throughout the CVD process had additional effects in the formation of carbon nanostructures. First, the decomposition and dehydration of this oligosaccharide at elevated temperatures could form free radicals, including CHO, which promoted the formation of spherical amorphous carbon. Second, CMC could develop diverse aromatic molecules such as 1,2,4-benzenetriol, and furfural-like compounds that promote mainly the growth of curved CNT. Third, it provided a carbon coating that strengthened the biochar surface and improved its thermal stability.

SEM secondary electrons images of modified biochar revealed consistent and uniform growth of carbon nanostructures, being observable even at low magnification, while detailed TEM analyses displayed the typical so-called morphologies of bamboo-like CNT, onion-like carbon, and carbon black. Considering the occurrence of heteroatoms during CVD process, it was found that nitrogen (9%) from raw agave bagasse played a role in the formation of the



typical bamboo-like compartments in CNTs, whereas the presence of oxygen (32.1%) mainly from turbostratic carbon could promote the formation of the closed quasi-spheres shape similar to onion-like carbon. In addition to that it bended the CNTs structure. Regardless of the iron concentration and CVD time, the samples exhibited similar morphologies, although it was observed that the longer the CVD time and the lower the iron concentration, the more carbon black formation was possible. Indeed, it was required a post-thermal treatment at 800 °C to increase the surface area of the biochar modified with 300 s of CVD which allowed to remove this amorphous carbon and promoted an improvement in the degree of graphitization of carbon nanostructures. Conversely, by reducing the CVD time to 60 s, the premise of increasing the biochar surface area was managed, reaching a value of 243 m<sup>2</sup> g<sup>-1</sup>. Accordingly, the first adsorption approach using benzene vapor as a model VOC from gasoline emission proved that CVD treated biochar exceeded 1.5 times the benzene uptake and 5 times the adsorption rates of a commercial activated carbon under diurnal conditions. This result demonstrated that the high exposed surface area and low tortuosity of the novel biochar/carbon nanostructures composite enhanced the benzene mass transport in short periods of time, which is demanded in automotive canisters.

In order to take full advantage of the iron catalyst for the growth of carbon nanostructures, the biochar was washed with non-oxidizing acid to remove calcium rods which presented a strong affinity for iron oxides (Fig. 2.3b), preventing its optimal dispersion. According to the results included in Chapter 3, it was possible to reduce the inorganic content of biochar from 8.6 to 4.5 % w/w without suffering any structural carbon transformation or surface acidification. In fact, the removal of inorganics allowed to increase the biochar surface area, the hydrophobicity and thus its adsorption uptake of benzene and pentane in 20 and 22 %, respectively.



To largely prevent the formation of amorphous carbon during CVD synthesis, it was explored the possibility of controlling the uniform occurrence of carbon source on the catalyst by using the CVD pulsed-injection strategy. When making a comparison between continuous CVD and CVD pulsed-injection, the last one produced a better dispersion and longer carbon nanostructures (Fig. 3.3). The intermittent supply of acetylene as a carbon source, in addition to the decomposition of CMC, avoided saturating the CVD chamber with excess carbon to such an extent that carbon black was not observed in TEM analysis, as reported in Chapter 1. Even though the CVD process was carried out at 600 °C, it was feasible the growth of different well graphitized nanostructures such as CNTs, CNFs, carbon nanoribbons and onion-like carbon since the decomposition of acetylene was thermodynamically viable at this temperature. The effect of the CVD pulsed-injection was more evident due to the longer CNTs, where the catalyst allowed the longitudinal growth of the CNTs in two different zones of the particle (see Fig. 3.4a). The latter suggested that the catalyst activity of iron did not cease between first and second pulsed carbon supply, allowing the further growth during the second pulse. Regarding the applicability of these novel composites for adsorption of nonpolar VOCs purposes, the dispersibility of these nanostructures and their morphological composition were of significant advantage.

As it is known, the static adsorption behaviors in the gas phase of various porous adsorbents have been usually studied by the assessment of the maximum adsorption capacity, while most of the kinetic studies have been carried out under dynamic conditions. Thus, to our best knowledge, no research has investigated the static adsorption kinetics of different aromatic and aliphatic VOCs representatives of gasoline emissions. For this reason, the static adsorption performance was always compared with those of a commercial activated carbon. Herein, the overall mass transfer of each VOC from liquid bulk, through its natural evaporation, to adsorption sites, occurred in a similar way to the process that takes





place in automotive canisters. Considering that the most demanded adsorption performance of an automotive canister is evaluated in the first 12 h of operation, biochar/carbon nanostructures composite exhibited the fastest adsorption kinetics for aromatic VOCs, while aliphatic molecules can be removed at similar rates on an adsorbent with different magnitudes of tortuosity and micropore volume. In this sense, the most exposed surface area of biochar/carbon nanostructures composite counteracted the mass transfer limitations presented by the microporous of activated carbon. This behavior was commonly attributed here and in several works to the textural and chemical properties of the adsorbent; however, the physical properties of the VOCs also played a major role in the adsorption kinetics as occur in stored gasoline. In this sense, the highest concentration of pentane was related to its highest vapor pressure that, in addition to its smallest kinetic diameter, conferred a greater driving force to diffuse faster to the adsorption sites on the carbon nanostructures or on the narrow porosity of activated carbon. In contrast, the lower adsorption performances of toluene, regardless of the adsorbent properties, were a consequence of its largest kinetic diameter and lower vapor pressure.

It was also proposed that the adsorption mechanism of nonpolar VOCs on carbonaceous adsorbents was mainly dominated by dispersive interactions. Considering the increase of  $sp^2$  delocalized electrons on the most basic and hydrophobic surface of biochar/carbon nanostructures composite, the affinity for nonpolar molecules increased. Nevertheless, electron donor-acceptor complexes formed between the delocalized  $\pi$  electron of aromatic molecules with the ion pair electrons from the adsorbent functionalities should not be discarded.

As a second part of this work, the escalation process was proposed to grow carbon nanostructures on biochar in a rotary furnace ([Chapter 4](#)). This scale-up was intended to increase the mass production of biochar/carbon nanostructure composites up to 10 g per



synthesis, as the TGA was only able to produce an average of 30 mg per synthesis. The interest in obtaining a greater amount of adsorbent per synthesis was also with a view to scaling up its application in the dynamic adsorption of different VOCs in packed-bed columns. The implemented conditions for CVD synthesis in a rotary furnace were those used in the TGA and based on the CVD pulsed-injection strategy. These conditions were mainly taken into consideration by the greater increase in biochar surface area, as well as the increment in its surface basicity and hydrophobicity after the CVD process.

When making a comparison between the CVD process by TGA and rotatory furnace, there were morphological differences. As it was revealed by SEM and TEM analysis, the presence of long carbon nanostructures was characterized by the absence of a tubular structure and, instead, the inner structure morphology with cup-shaped or amorphous carbon-filled morphology was observed. In addition, a broad covered surface of carbon condensed on the entire biochar could be related to the presence of amorphous carbon and onion-like carbon clusters. These morphological differences compared to those reported in [Chapter 3](#) were related with zones of low-temperature of the reaction tube reported in previous work, where its reproducibility was impeded compared to the synthesis by TGA. Concerning the aim of its applicability in adsorption processes, the CVD process in rotary furnace also allowed to considerably increase the biochar surface area from 1 to 300 m<sup>2</sup> g<sup>-1</sup>. It should be mentioned that the grinding of biochar, to ensure a particle diameter at least 25 times smaller than the column diameter, could destroy the most external pores of biochar, resulting in a poor surface area.

To acquire more insight about the applicability of this novel adsorbent for automotive canisters, scaled up in packed-bed columns also allowed to compare the uptake of VOCs representative of gasoline from a gas stream. Even though experiments were carried out in dynamic mode using a carrier gas to stimulate the evaporation of each VOC, the inlet



concentration was related to the physical properties of each VOC as in the static experiments. Analyzing the breakthrough curves, it was found that the higher the VOC vapor pressure and the smaller the adsorbent surface area, the earlier the breakthrough. Additionally, the high concentration dependence on breakthrough time agrees with literature. Indeed, the highest pentane inlet concentration ( $274 \text{ mg L}^{-1}$ ) promoted a fast intra and interparticle diffusion to quickly saturate the adsorbent in such a way that it is detected in the first 20 min at the outlet of the columns. According to the regenerative performance of the adsorbents, it was found that biochar/carbon nanostructures composite showed a higher regeneration efficiency and presented a decrease in the breakthrough time of no more than 6 min in the second cycle, whereas activated carbon displayed an important decrease in service time up to 40 min for toluene after the regeneration. The latter was more evident after four adsorption/desorption cycles of benzene, where biochar/carbon nanostructures composite displayed similar breakthrough curves with only a decrease of 16 min, while the breakthrough time of benzene on activated carbon decreased up to 20 min just in the second regenerative cycle.

Regarding the continuous regeneration of the carbon adsorbent in a real canister, the desorption process occurs by air stream injection to the canister once the vehicle is running. However, the acidification of activated carbon after its regeneration was proved in this work since its  $\text{pH}_{\text{PZC}}$  decreased 0.5 unit. This chemical instability was associated with its high occurrence of edge sites and vacancy defects. In contrast, biochar/carbon nanostructures composite showed higher stability by negligible surface acidification after four regeneration cycles. The latter indicated the effectiveness of the novel composite for the recovery of evaporative emission.



Finally, Chapter 5 explored the co-adsorption behavior of biochar/carbon nanostructures in multicomponent systems and in gasoline. Even though several works reported the effect of competitive adsorption of mixtures with equimolar inlet concentration of VOCs, here, the mixture of a model gasoline where the VOCs concentration depends on its physical properties was explored. In a first approach, the co-adsorption in binary VOCs mixtures in function of the interaction between aliphatic and aromatic molecules was evaluated, followed by a multicomponent VOC mixture as a model gasoline. Overall, the breakthrough curves of the VOCs in binary and multicomponent mixtures displayed similar pattern to that of single adsorption. In this sense, it was determined that the heaviest VOCs of each mixture promoted longer breakthrough times. Nevertheless, the interaction between the molecules promoted earlier breakthrough times and lower adsorption capacities for each VOC in mixtures than in single adsorption, indicating that when co-adsorption occurred not all adsorption sites were occupied on the adsorbent surface. In the literature, a common behavior of competitiveness has been reported in the breakthrough curves, which was observed as a change in the slopes of the breakthrough curve of lighter VOCs once outlet concentration exceeded 85 % of the inlet concentration. The use of multicomponent dynamic experiments provided information about the interaction of molecules between them and with the adsorbent. This effect seemed to be more pronounced in activated carbon, where the dynamic adsorption process of multicomponent was illustrated in 5 stages. The stages implied the diffusion of molecules from the bulk phase to the external surface area and finally to the active sites mainly in micropores, however, once heavier VOCs reached the active sites, they replace the lightest VOC. This displacement of the previously adsorbed VOC allows its re-adsorbed in the unsaturated zone of the packed-bed or to be carried in the stream, increasing the outlet concentration when the packed-bed is completely saturated. In contrast, the breakthrough curves for BCVD600-1pTT did not follow a typical co-adsorption behavior, suggesting a most homogeneous adsorption and mass transfer process during



dynamic experiments summarized in 3 stages. This behavior was associated to the highest exposure of active sites on carbon nanostructures surface, where equilibrium could take place faster than in microporous activated carbon.

The final approach demonstrated the feasibility to replace activated carbon for our novel CVD processed biochar in automotive canisters. For the sake of comparison, gasoline emissions were adsorbed in both carbonaceous adsorbents in packed-bed column experiments. Interestingly, biochar/carbon nanostructures composite presented similar breakthrough times (12 min) and adsorption capacity ( $153 \text{ mg g}^{-1}$ ) than activated carbon (15 min,  $187 \text{ mg g}^{-1}$ ). The main difference was presented in the overlapping of activated carbon curve which indicated the typical competitive adsorption. The latter became more evident when analyzing the gasoline components in four groups, where, as in mixture of model gasoline the biochar/carbon nanostructures composite registered absence of change in slope on breakthrough curves, indicating a similar diffusion of more than 30 VOCs from gasoline through the packed-bed, which did not happen in activated carbon. These results demonstrated that biochar/carbon nanostructures composite was effective and practical in removing real gasoline emissions from automobiles.

The results presented in this doctoral thesis demonstrated the potential of the biochar/carbon nanostructures composite for the uptake of several VOCs from gasoline emissions in gas phase. It is a fact that the deep characterization not only allowed to understand the physical and chemical properties of the adsorbent, but also allowed to understand the effect of its features on the adsorption performance throughout various regenerative cycles. In addition, the applicability of our novel composite adsorbent was corroborated by the direct comparison with a commercial activated carbon. Thus, this work represents a significant advance in the development of an adsorbent from an agro-industrial



waste enhanced with carbon nanostructures appropriated to remove key pollutants in gas phase.

# CHAPTER 7

---

## Final Conclusions

---

---

### 7.1. Conclusions

To the best of our knowledge, no study prior to this work had attempted the growth of carbon nanostructures onto biochar for the recovery and reuse of VOCs from evaporative emissions. According to results, it is possible to produce a macroporous adsorbent with low tortuosity by the pyrolysis of a lignocellulosic waste from the mescal industry. Furthermore, the CVD process in a thermogravimetric analyzer successfully grows carbon nanostructures, specifically CNTs, CNFs, onions-like carbon, and carbon black onto biochar, which in turn allows to increase the biochar surface area and, thus, to adsorb various VOCs from gas phase.

The carboxymethylcellulose allows to control the size and dispersibility of iron catalyst onto the biochar, which promotes to obtain a high yield of homogeneously distributed carbon nanostructures. The highest distribution of catalyst on biochar is achieved with an iron concentration of  $1 \text{ g L}^{-1}$ . By using CVD during 60 s and  $700 \text{ }^{\circ}\text{C}$ , it is possible to increase the biochar surface area from 120 to  $243 \text{ m}^2 \text{ g}^{-1}$ . However, when using CVD for more than 60 s the surface area of the biochar decreases to  $5 \text{ m}^2 \text{ g}^{-1}$ , but after thermal post-treatment at  $800 \text{ }^{\circ}\text{C}$  this increases to  $241 \text{ m}^2 \text{ g}^{-1}$ . On the other hand, when using CVD injection-pulses at  $600 \text{ }^{\circ}\text{C}$  the growth of similar carbon nanostructures is also promoted, resulting in a better dispersion and similar surface area ( $241 \text{ m}^2 \text{ g}^{-1}$ ) than when continuous CVD is implemented.



Notoriously, the scaled-up of the CVD process at 600 °C in a rotatory furnace also allows to increase 300 times the biochar surface area with the extensive coverage of biochar with carbon nanostructures. TEM analysis evidence the morphological differences between using a rotatory furnace and a TGA. By characterizing with Raman spectra and X-ray diffraction, it is confirmed that after the CVD process the composition of biochar is tailored via growth of carbon nanostructures with a prominent  $sp^2$  hybridized carbon domain and crystalline graphitic structures. The thermal instability of CMC at temperatures higher than 500 °C allows it to produce turbostratic carbon with oxygen functionalities that promote the formation of onions-like carbon and carbon black, while the nitrogen content from raw biochar could induces the formation of bamboo-like CNTs and CNFs.

As it is indicated by static adsorption studies, biochar/carbon nanostructures composite shows a higher pentane ( $169 \text{ mg g}^{-1}$ ), hexane ( $63 \text{ mg g}^{-1}$ ), benzene ( $73 \text{ mg g}^{-1}$ ), and toluene ( $38 \text{ mg g}^{-1}$ ) adsorption capacity at 25 °C, and faster adsorption kinetics than activated carbon under diurnal conditions. Particularly, large surface areas play a positive effect on adsorption capacity of different VOCs but a negative correlation between pore volume and adsorption capacity of larger VOCs like toluene is observed. Furthermore, the more basic the adsorbent surface, the greater the adsorption capacity of nonpolar VOCs, which is conducted via dispersive interactions between aliphatic molecules and delocalized  $\pi$ -electrons, and by  $\pi$ - $\pi$  interactions between the  $\pi$ -electrons in the benzene ring and those in the carbon graphitic layers. Based on this mechanism, the curvature of the basal planes of carbon nanostructures has a greater reactivity that increases the VOCs uptake in comparison to the disordered stacked graphitic layers of activated carbon, which allows to increase up to 3.8 times the static adsorption capacity of activated carbon. The adsorbate properties such as vapor pressure have a positive relationship with the adsorption capacity of BCVD600-1pTT ( $R^2 = 0.8$ ), whereas the molecular size shows a negative lineal relationship ( $R^2 = 0.82$ ).





The particle size of the adsorbent is reduced to an average of 60  $\mu\text{m}$  to avoid channeling during dynamic experiments in the packed bed. In brief, earlier breakthrough times are found for adsorbates with lower boiling temperature (pentane and hexane), and a longer breakthrough time for the less volatile molecules (benzene and toluene). Accordingly, the breakthrough curves of biochar/carbon nanostructures display adsorption capacities of 269.6, 123.5, 81.2, and 36.9  $\text{mg g}^{-1}$  for pentane, hexane, benzene, and toluene, respectively. The biochar/carbon nanostructures composite has a higher regeneration efficiency by presenting a decrease in the breakthrough time of no more than 6 min, whereas activated carbon reveals an important decrease in service time up to 40 min for toluene. Indeed, the breakthrough time of this novel adsorbent decreases only 16 min after four adsorption/desorption cycles of benzene and that of activated carbon decreases up 20 min just in the second regenerative cycle. Additionally, the higher chemical stability of carbon nanostructures after the regenerative process with air at 150  $^{\circ}\text{C}$  is also associated to the reproducible adsorption behavior of these nonpolar VOCs.

Lastly, the dynamic adsorption of multicomponent mixtures of model and real gasoline emissions onto biochar/carbon nanostructures composite was accomplished. As in single adsorption, heavier VOCs from each mixture show a longer service time, being up to 80 min for toluene in the binary aromatic mixture. However, the total adsorption capacity of the mixture is less than the single adsorption capacity of each component. The latter is due to the competition of VOCs for the adsorbent active sites during dynamic co-adsorption experiments. In this sense, a competitive adsorption process is detected in activated carbon by the change in the slopes on the breakthrough curve of the lighter VOCs at  $C/C_0$  values higher than 0.85. In contrast, the co-adsorption on the adsorbent with low tortuosity and low microporous volume, such as biochar/carbon nanostructures composite, the typical S-shape breakthrough curves are observed. This last one suggests a more homogeneous adsorption



and mass transfer process during dynamic experiments. Finally, this work demonstrated the potential of biochar/carbon nanostructures composite to be used in the simultaneous removal of several VOCs from real gasoline emissions, which could replace commercial activated carbons currently used in automotive canisters.

## 7.2. Perspectives and challenges

In the present research, great progress has been made in the study of static and dynamic adsorption of real VOCs from gasoline emissions onto a macroporous adsorbent modified with carbon nanostructures, in addition to the factors that most influence the adsorption behavior. However, the following knowledge gaps still need to be further investigated:

- Considering the acid-washed pretreatment to remove biochar inorganic content and the size reduction by grinding for its proper application in packed-bed columns, would be interesting to explore both pretreatment to the bagasse agave fibers, prior to being carbonized. This could prevent damage to the biochar strength, as well as avoid considerable loss in biochar mass during grinding and sieving.
- There is a need to further optimize the growth of carbon nanostructures on biochar by developing a design of experiments using either factorial or response surface analysis in order to assess the influence of the most important CVD parameters such as temperature, the time, the catalyst type, and the carbon source, obtaining as a response an increase in biochar surface area and VOCs adsorption capacity.
- Based on the effect of CMC on the growth of different carbon morphologies, evaluation of different catalyst impregnation strategies is needed to ensure homogeneous size and dispersion of nanoparticles in biochar. In this sense, the use of techniques such as microwave impregnation or thermal hydrolysis would be explored. In addition to exploring the synergistic effect of the use of catalyst mixtures in the CVD process to increase the yield in the growth of carbon nanostructures.



- Another approach of interest regarding biochar damage prevention and process scaling, it would be interesting to carry out CVD processes based on the oxidative dehydrogenation reaction between  $C_2H_2$  and  $CO_2$ . This synthesis variant allows to grow CNTs on carbon substrates at 500 °C without any deterioration of the carbon skeleton.
- In order to better understand the differences on the growth of carbon nanostructures or by using different CVD temperature and catalyst, it is suggested to explore the analysis of the activation energy of CVD synthesis from the Arrhenius plots by also comparing the growth rate under various synthesis conditions. Therefore, the activation energy can be calculated directly from the slope of the linear fit to the TGA data by plotting CNTs grown rate ( $nm \cdot s^{-1}$ ) versus  $T^{-1}$  ( $K^{-1}$ ), assuming a first order reaction.
- Regarding static adsorption assessment, it would be necessary to explore kinetic experiment at different temperatures, for instance, 15, 25, 35, and 45 ° C in regard to exploring the adsorption behavior based on the actual diurnal conditions in the automotive system.
- Once the dynamic adsorption of single and multicomponent mixtures is known, it is important to evaluate the additional effect of moisture during VOCs uptake. To do this, it will be necessary to perform the experiments with a set-up in which the passage of a stream of air or nitrogen through a column of water will allow the generation of water vapor that will be mix with the current of VOCs and, thus, the humidity percentage will be controlled.
- According to the experimental set up showed in Chapter 4, it was possible to obtain the breakthrough curves by analyzing the inlet and outlets concentration in a GC-FID analyzer, while desorption was determined in a TGA equipment. However, in several studies the adsorption/desorption processes take place in situ where the desorption process can be carried out by inducing an increase in the temperature of the column and passing a tangential flow of air or by a vacuum desorption. Therefore, it would be



recommended to evaluate the regenerative performance of the adsorbent by using these strategies.

- Based on the high precision in the control of parameters during the dynamic adsorption of pollutants in gas phase, it is suggested the use of precision accessories such mass flow controllers and high precision needle valves.
- Finally, to evaluate the feasibility of implementing the synthesized material on an industrial scale, the environmental evaluation of the VOC adsorption process through life cycle analysis could be interesting.



# References

- [1] J.-H. Park *et al.*, "Active Atmosphere-Ecosystem," no. August, pp. 643–648, 2013.
- [2] A. Berenjian, N. Chan, and H. Jafarizadeh Malmiri, "VOLATILE ORGANIC COMPOUNDS REMOVAL METHODS : A REVIEW," *Biochemistry and biotechnology*, vol. 8, no. x, pp. 220–229, 2012, doi: 10.3844/ajbbbsp.2012.220.229.
- [3] A. Mirzaei, S. G. Leonardi, and G. Neri, "Detection of hazardous volatile organic compounds (VOCs) by metal oxide nanostructures-based gas sensors: A review," *Ceramics International*, vol. 42, no. 14, pp. 15119–15141, 2016, doi: 10.1016/j.ceramint.2016.06.145.
- [4] A. Luengas, A. Barona, C. Hort, G. Gallastegui, V. Platel, and A. Elias, "A review of indoor air treatment technologies," *Reviews in Environmental Science and Bio/Technology*, vol. 14, no. 3, pp. 499–522, 2015, doi: 10.1007/s11157-015-9363-9.
- [5] I. Covarrubias-García, A. Aizpuru, and S. Arriaga, "Effect of the continuous addition of ozone on biomass clogging control in a biofilter treating ethyl acetate vapors," *Science of The Total Environment*, vol. 584–585, pp. 469–475, Apr. 2017, doi: 10.1016/j.scitotenv.2017.01.031.
- [6] W.-K. Jo and K.-B. Song, "Exposure to volatile organic compounds for individuals with occupations associated with potential exposure to motor vehicle exhaust and/or gasoline vapor emissions," 2001.
- [7] L. Zhu, D. Shen, and K. H. Luo, "A critical review on VOCs adsorption by different porous materials: Species, mechanisms and modification methods," *Journal of Hazardous Materials*, vol. 389, no. January, p. 122102, May 2020, doi: 10.1016/j.jhazmat.2020.122102.
- [8] H. Rajabi, M. Hadi Mosleh, P. Mandal, A. Lea-Langton, and M. Sedighi, "Emissions of volatile organic compounds from crude oil processing – Global emission inventory and environmental release," *Science of The Total Environment*, vol. 727, p. 138654, Jul. 2020, doi: 10.1016/j.scitotenv.2020.138654.
- [9] B. Li, S. Sai, H. Ho, Y. Xue, Y. Huang, and L. Wang, "Characterizations of volatile organic compounds ( VOCs ) from vehicular emissions at roadside environment : The first comprehensive study in Northwestern China," *Atmospheric Environment*, vol. 161, pp. 1–12, 2017, doi: 10.1016/j.atmosenv.2017.04.029.
- [10] V. J. Feron, H. P. Til, F. de Vrijer, and P. J. van Bladeren, "Toxicology of Volatile Organic Compounds in Indoor Air and Strategy for Further Research," 2015.
- [11] X. Zhang, B. Gao, A. Elise, C. Cao, and Y. Li, "Adsorption of VOCs onto engineered carbon materials : A review," *Journal of Hazardous Materials*, vol. 338, pp. 102–123, 2017, doi: 10.1016/j.jhazmat.2017.05.013.



- [12] I. Covarrubias-García, A. Aizpuru, and S. Arriaga, "Effect of the continuous addition of ozone on biomass clogging control in a biofilter treating ethyl acetate vapors," *Science of the Total Environment*, vol. 584–585, pp. 469–475, Apr. 2017, doi: 10.1016/j.scitotenv.2017.01.031.
- [13] X. Li *et al.*, "Hydrophobic modified activated carbon using PDMS for the adsorption of VOCs in humid condition," *Separation and Purification Technology*, vol. 239, p. 116517, 2020, doi: 10.1016/j.seppur.2020.116517.
- [14] M. M. Khin, A. S. Nair, V. J. Babu, R. Murugan, and S. Ramakrishna, "A review on nanomaterials for environmental remediation," *Energy & Environmental Science*, vol. 5, no. 8, p. 8075, 2012, doi: 10.1039/c2ee21818f.
- [15] Y. Liu, X. Feng, and D. Lawless, "Separation of gasoline vapor from nitrogen by hollow fiber composite membranes for VOC emission control," vol. 271, pp. 114–124, 2006, doi: 10.1016/j.memsci.2005.07.012.
- [16] K. Yang, L. Zhu, and B. Xing, "Adsorption of polycyclic aromatic hydrocarbons by carbon nanomaterials," *Environmental Science and Technology*, vol. 40, no. 6, pp. 1855–1861, 2006, doi: 10.1021/es052208w.
- [17] T. Yue *et al.*, "Characteristics of volatile organic compounds (VOCs) from the evaporative emissions of modern passenger cars," *Atmospheric Environment*, vol. 151, pp. 62–69, Feb. 2017, doi: 10.1016/j.atmosenv.2016.12.008.
- [18] H. Yamada, "Contribution of evaporative emissions from gasoline vehicles toward total VOC emissions in Japan," *Science of The Total Environment*, vol. 449, pp. 143–149, Apr. 2013, doi: 10.1016/j.scitotenv.2013.01.045.
- [19] H. Hata, S. Tanaka, G. Noumura, H. Yamada, and K. Tonokura, "Evaluation of Gasoline Evaporative Emissions from Fuel-Cap Removal after a Real-World Driving Event," *Atmosphere (Basel)*, vol. 11, no. 10, p. 1110, Oct. 2020, doi: 10.3390/atmos11101110.
- [20] J.-Y. Chin and S. A. Batterman, "VOC composition of current motor vehicle fuels and vapors, and collinearity analyses for receptor modeling," *Chemosphere*, vol. 86, no. 9, pp. 951–958, 2012, doi: 10.1016/j.chemosphere.2011.11.017.
- [21] B. I. Bertelsen, "Future US motor vehicle emission standards and the role of advanced emission control technology in meeting those standards," no. x, pp. 15–22, 2009.
- [22] G. Mellios and Z. Samaras, "An empirical model for estimating evaporative hydrocarbon emissions from canister-equipped vehicles," vol. 86, pp. 2254–2261, 2007, doi: 10.1016/j.fuel.2007.01.031.
- [23] I. Schifter, L. Díaz, R. Rodríguez, and C. González-Macías, "The contribution of evaporative emissions from gasoline vehicles to the volatile organic compound inventory in Mexico City," *Environmental Monitoring and Assessment*, vol. 186, no. 6, pp. 3969–3983, Jun. 2014, doi: 10.1007/s10661-014-3672-2.



- [24] L. Romagnuolo, R. Yang, E. Frosina, G. Rizzoni, and A. Andreozzi, "Physical modeling of evaporative emission control system in gasoline fueled automobiles : A review," vol. 116, no. May, 2019.
- [25] H. Hata, H. Yamada, K. Yanai, M. Kugata, G. Noumura, and K. Tonokura, "Modeling evaporative emissions from parked gasoline cars based on vehicle carbon canister experiments," *Science of The Total Environment*, vol. 675, pp. 679–685, Jul. 2019, doi: 10.1016/j.scitotenv.2019.04.112.
- [26] L. Hiltzik, J. Z. Jagiello, E. D. Tolles, and R. S. Williams, "METHOD FOR REDUCING EMISSIONS FROM EVAPORATIVE EMISSIONS CONTROL SYSTEM," *United States Patent*, vol. 1, no. 12, 2003.
- [27] K. Sato and N. Kobayashi, "Adsorption and Desorption Simulation of Carbon Canister Using n-Butane as Model Compound of Gasoline," vol. 54, no. 3, pp. 136–145, 2011.
- [28] M. Ouzzine, A. J. Romero-Anaya, M. A. Lillo-Ródenas, and A. Linares-Solano, "Spherical activated carbons for the adsorption of a real multicomponent VOC mixture," *Carbon*, vol. 148, pp. 214–223, 2019. doi: 10.1016/j.carbon.2019.03.075.
- [29] X. Yao *et al.*, "Adsorption behavior of multicomponent volatile organic compounds on a citric acid residue waste-based activated carbon: Experiment and molecular simulation," *Journal of Hazardous Materials*, vol. 392, 2020. doi: 10.1016/j.jhazmat.2020.122323.
- [30] L. Jia, W. Yu, C. Long, and A. Li, "Adsorption equilibrium and dynamics of gasoline vapors onto polymeric adsorbents," no. 163, pp. 3756–3763, 2014, doi: 10.1007/s11356-013-2328-z.
- [31] D. O. Conney, *Adsorption design for wastewater treatment*. Lewis, 1998.
- [32] M. G. R.C. Bansal, *Activated carbon adsorption*. 2005.
- [33] S. M. Abegunde, K. S. Idowu, O. M. Adejuwon, and T. Adeyemi-Adejolu, "A review on the influence of chemical modification on the performance of adsorbents," *Resources, Environment and Sustainability*, vol. 1, p. 100001, Sep. 2020, doi: 10.1016/j.resenv.2020.100001.
- [34] Fransisco. Rodríguez-Reinoso and Harry. Marsh, *Activated Carbon (Activation Processes)*. 1992.
- [35] M. J. Lashaki, M. Fayaz, S. Niknaddaf, and Z. Hashisho, "Effect of the adsorbate kinetic diameter on the accuracy of the Dubinin-Radushkevich equation for modeling adsorption of organic vapors on activated carbon," *Proceedings of the Air and Waste Management Association's Annual Conference and Exhibition, AWMA*, vol. 3, pp. 2133–2151, 2012.
- [36] X. Li, L. Zhang, Z. Yang, P. Wang, Y. Yan, and J. Ran, "Adsorption materials for volatile organic compounds (VOCs) and the key factors for VOCs adsorption process: A review," *Separation and Purification Technology*, vol. 235, 2020. doi: 10.1016/j.seppur.2019.116213.
- [37] X. Zhang *et al.*, "Adsorption of acetone and cyclohexane onto CO<sub>2</sub> activated hydrochars," *Chemosphere*, vol. 245, p. 125664, Apr. 2020, doi: 10.1016/j.chemosphere.2019.125664.



- [38] X. Hu, Z. Ding, A. R. Zimmerman, S. Wang, and B. Gao, "Batch and column sorption of arsenic onto iron-impregnated biochar synthesized through hydrolysis," vol. 8, 2014.
- [39] W. Xiang *et al.*, "Enhanced adsorption performance and governing mechanisms of ball-milled biochar for the removal of volatile organic compounds (VOCs)," *Chemical Engineering Journal*, p. 123842, 2019, [Online]. Available: <https://doi.org/10.1016/j.cej.2019.123842>
- [40] J. S. Cha *et al.*, "Production and utilization of biochar: A review," *Journal of Industrial and Engineering Chemistry*, vol. 40. Korean Society of Industrial Engineering Chemistry, pp. 1–15, Aug. 25, 2016. doi: 10.1016/j.jiec.2016.06.002.
- [41] A. Kumar, E. Singh, A. Khapre, N. Bordoloi, and S. Kumar, "Sorption of volatile organic compounds on non-activated biochar," *Bioresource Technology*, 2020.
- [42] J. Gutiérrez-Martínez, C. Nieto-Delgado, M. Avalos-Borja, E. Basiuk, and J. R. Rangel-Mendez, "Fast benzene vapor capture by natural macroporous carbonized fibers improved with carbon nanostructures," *Separation and Purification Technology*, vol. 257, 2021, doi: 10.1016/j.seppur.2020.117956.
- [43] K. Montiel-Centeno, D. Barrera, J. Villarroel-Rocha, M. S. Moreno, and K. Sapag, "Hierarchical nanostructured carbons as CO<sub>2</sub> adsorbents," *Adsorption*, vol. 25, no. 7, pp. 1287–1297, Oct. 2019, doi: 10.1007/s10450-019-00089-3.
- [44] J. Zhang *et al.*, "Carbon science in 2016 : Status , challenges and perspectives," *Carbon N Y*, vol. 98, pp. 708–732, 2016, doi: 10.1016/j.carbon.2015.11.060.
- [45] Y. Ando, X. Zhao, T. Sugai, and M. Kumar, "carbon nanotubes," no. October, pp. 22–29, 2004.
- [46] S. Kabiri, D. N. H. Tran, T. Altalhi, and D. Losic, "Outstanding adsorption performance of graphene – carbon nanotube aerogels for continuous oil removal," vol. 0, 2014.
- [47] S. Gotovac, C. Yang, Y. Hattori, K. Takahashi, and H. Kanoh, "Adsorption of polyaromatic hydrocarbons on single wall carbon nanotubes of different functionalities and diameters," vol. 314, pp. 18–24, 2007, doi: 10.1016/j.jcis.2007.04.080.
- [48] A. A. MUATAZ, F. AHMADUN, C. GUAN, E. MAHDI, and A. RINALDI, "EFFECT OF REACTION TEMPERATURE ON THE PRODUCTION OF CARBON NANOTUBES," *Nano*, vol. 01, no. 03, pp. 251–257, Nov. 2006, doi: 10.1142/S1793292006000288.
- [49] R. H. Baughman, A. A. Zakhidov, and W. A. de Heer, "Carbon Nanotubes — the Route Toward Applications," vol. 297, no. August, pp. 787–793, 2002.
- [50] J. Zhao, A. Buldum, J. Han, and J. P. Lu, "Gas molecule adsorption in carbon nanotubes and nanotube bundles," 2002.
- [51] B. Pan, B. Xing, B. O. Pan, and B. Xing, "Critical Review Adsorption Mechanisms of Organic Chemicals on Carbon Nanotubes," vol. 42, no. November, pp. 9005–9013, 2008, doi: 10.1021/es801777n.
- [52] S. Tulaphol, S. Bunsan, E. Kanchanatip, H. Y. Miao, N. Grisdanurak, and W. Den, "Influence of chlorine substitution on adsorption of gaseous chlorinated phenolics on multi-walled carbon





- nanotubes embedded in SiO<sub>2</sub>,” *International Journal of Environmental Science and Technology*, vol. 13, no. 6, pp. 1465–1474, Jun. 2016, doi: 10.1007/s13762-016-0984-5.
- [53] Quoc Ngo *et al.*, “Structural and Electrical Characterization of Carbon Nanofibers for Interconnect Via Applications,” *IEEE Transactions on Nanotechnology*, vol. 6, no. 6, pp. 688–695, Nov. 2007, doi: 10.1109/TNANO.2007.907400.
- [54] Y. K. Kim, S. il Cha, S. H. Hong, and Y. J. Jeong, “A new hybrid architecture consisting of highly mesoporous CNT/carbon nanofibers from starch,” *Journal of Materials Chemistry*, vol. 22, no. 38, p. 20554, Oct. 2012, doi: 10.1039/c2jm32631k.
- [55] J. Restivo, O. S. Gonçalves Pinto Soares, and M. F. Ribeiro Pereira, “Processing Methods Used in the Fabrication of Macrostructures Containing 1D Carbon Nanomaterials for Catalysis,” *Processes*, vol. 8, no. 11, p. 1329, Oct. 2020, doi: 10.3390/pr8111329.
- [56] E. Díaz, S. Ordóñez, and A. Vega, “Adsorption of volatile organic compounds onto carbon nanotubes, carbon nanofibers, and high-surface-area graphites,” *Journal of Colloid and Interface Science*, vol. 305, no. 1, pp. 7–16, Jan. 2007, doi: 10.1016/j.jcis.2006.09.036.
- [57] Y. Kojima *et al.*, “Hydrogen adsorption and desorption by carbon materials,” *Journal of Alloys and Compounds*, vol. 421, no. 1–2, pp. 204–208, Sep. 2006, doi: 10.1016/j.jallcom.2005.09.077.
- [58] H. Kristianto, C. D. Putra, A. A. Arie, M. Halim, and J. K. Lee, “Synthesis and Characterization of Carbon Nanospheres Using Cooking Palm Oil as Natural Precursors onto Activated Carbon Support,” *Procedia Chemistry*, vol. 16, pp. 328–333, 2015, doi: 10.1016/j.proche.2015.12.060.
- [59] S.-W. Cao and Y.-J. Zhu, “Iron oxide hollow spheres: Microwave–hydrothermal ionic liquid preparation, formation mechanism, crystal phase and morphology control and properties,” *Acta Materialia*, vol. 57, no. 7, pp. 2154–2165, Apr. 2009, doi: 10.1016/j.actamat.2009.01.009.
- [60] G. Moussa, C. Matei Ghimbeu, P. L. Taberna, P. Simon, and C. Vix-Guterl, “Relationship between the carbon nano-onions (CNOs) surface chemistry/defects and their capacitance in aqueous and organic electrolytes,” *Carbon N Y*, vol. 105, pp. 628–637, 2016, doi: 10.1016/j.carbon.2016.05.010.
- [61] M. Zeiger, N. Jäckel, V. N. Mochalin, and V. Presser, “Review: Carbon onions for electrochemical energy storage,” *Journal of Materials Chemistry A*, vol. 4, no. 9, pp. 3172–3196, 2016, doi: 10.1039/c5ta08295a.
- [62] E. Tovar-Martinez, J. A. Moreno-Torres, J. v. Cabrera-Salazar, M. Reyes-Reyes, L. F. Chazaro-Ruiz, and R. López-Sandoval, “Synthesis of carbon nano-onions doped with nitrogen using spray pyrolysis,” *Carbon N Y*, vol. 140, pp. 171–181, Dec. 2018, doi: 10.1016/j.carbon.2018.08.056.



- [63] Y. Z. Jin *et al.*, "Large-scale synthesis and characterization of carbon spheres prepared by direct pyrolysis of hydrocarbons," *Carbon N Y*, vol. 43, no. 9, pp. 1944–1953, 2005, doi: 10.1016/j.carbon.2005.03.002.
- [64] A. F. Hassan, "Synthesis of carbon nano-onion embedded metal–organic frameworks as an efficient adsorbent for cadmium ions: kinetic and thermodynamic studies," *Environmental Science and Pollution Research*, vol. 26, no. 23, pp. 24099–24111, 2019, doi: 10.1007/s11356-019-05581-5.
- [65] C. Sakulthaew, C. Chokejaroenrat, A. Poapolathep, T. Satapanajaru, and S. Poapolathep, "Hexavalent chromium adsorption from aqueous solution using carbon nano-onions (CNOs)," *Chemosphere*, vol. 184, pp. 1168–1174, Oct. 2017, doi: 10.1016/j.chemosphere.2017.06.094.
- [66] Y. J. Ko *et al.*, "Chromate adsorption mechanism on nanodiamond-derived onion-like carbon," *Journal of Hazardous Materials*, vol. 320, pp. 368–375, 2016, doi: 10.1016/j.jhazmat.2016.08.041.
- [67] L. K. de Assis, B. S. Damasceno, M. N. Carvalho, E. H. C. Oliveira, and M. G. Ghislandi, "Adsorption capacity comparison between graphene oxide and graphene nanoplatelets for the removal of coloured textile dyes from wastewater," *Environmental Technology (United Kingdom)*, vol. 41, no. 18, pp. 2360–2371, 2020, doi: 10.1080/09593330.2019.1567603.
- [68] J. Rivera-Utrilla, M. Sánchez-Polo, V. Gómez-Serrano, P. M. Álvarez, M. C. M. Alvim-Ferraz, and J. M. Dias, "Activated carbon modifications to enhance its water treatment applications. An overview," *Journal of Hazardous Materials*, vol. 187, no. 1–3, pp. 1–23, 2011, doi: 10.1016/j.jhazmat.2011.01.033.
- [69] J. L. Figueiredo, M. F. R. Pereira, M. M. a Freitas, and J. J. M. Órfão, "Modification of the surface chemistry of activated carbons," *Carbon N Y*, vol. 37, pp. 1379–1389, 1999, doi: 10.1016/S0008-6223(98)00333-9.
- [70] C. Y. Yin, M. K. Aroua, and W. M. A. W. Daud, "Review of modifications of activated carbon for enhancing contaminant uptakes from aqueous solutions," *Separation and Purification Technology*, vol. 52, no. 3, pp. 403–415, 2007, doi: 10.1016/j.seppur.2006.06.009.
- [71] J. A. Menéndez, J. Phillips, B. Xia, and L. R. Radovic, "On the modification and characterization of chemical surface properties of activated carbon: In the search of carbons with stable basic properties," *Langmuir*, vol. 12, no. 18, pp. 4404–4410, 1996, doi: 10.1021/la9602022.
- [72] Y. Nakagawa, M. Molina-Sabio, and F. Rodríguez-Reinoso, "Modification of the porous structure along the preparation of activated carbon monoliths with H<sub>3</sub>PO<sub>4</sub> and ZnCl<sub>2</sub>," *Microporous and Mesoporous Materials*, vol. 103, no. 1–3, pp. 29–34, 2007, doi: 10.1016/j.micromeso.2007.01.029.
- [73] C. Su, Y. Guo, H. Chen, J. Zou, Z. Zeng, and L. Li, "VOCs adsorption of resin-based activated carbon and bamboo char: Porous characterization and nitrogen-doped effect," *Colloids and Surfaces A: Physicochemical and Engineering Aspects*, vol. 601, 2020. doi: 10.1016/j.colsurfa.2020.124983.



- [74] K. A. Shah and B. A. Tali, "Synthesis of carbon nanotubes by catalytic chemical vapour deposition: A review on carbon sources, catalysts and substrates," *Materials Science in Semiconductor Processing*, vol. 41, pp. 67–82, Jan. 2016, doi: 10.1016/j.mssp.2015.08.013.
- [75] R. Purohit, K. Purohit, S. Rana, R. S. Rana, and V. Patel, "Carbon Nanotubes and Their Growth Methods," *Procedia Materials Science*, vol. 6, pp. 716–728, 2014, doi: 10.1016/j.mspro.2014.07.088.
- [76] P. M. Ajayan, "Nanotubes from Carbon," 1999.
- [77] N. M. Mubarak, E. C. Abdullah, N. S. Jayakumar, and J. N. Sahu, "An overview on methods for the production of carbon nanotubes," *Journal of Industrial and Engineering Chemistry*, vol. 20, no. 4, pp. 1186–1197, Jul. 2014, doi: 10.1016/j.jiec.2013.09.001.
- [78] N. Latorre *et al.*, "Carbon Nanotube Growth by Catalytic Chemical Vapor Deposition : A Phenomenological Kinetic Model," no. iii, pp. 4773–4782, 2010.
- [79] S. Yellampalli, *CARBON NANOTUBES - SYNTHESIS*, Edited by Siva Yellampalli. 2011.
- [80] V. Jourdain and C. Bichara, "Current understanding of the growth of carbon nanotubes in catalytic chemical vapour deposition," *Carbon N Y*, vol. 58, pp. 2–39, 2013, doi: 10.1016/j.carbon.2013.02.046.
- [81] G. Hong, Y. Chen, P. Li, and J. Zhang, "Controlling the growth of single-walled carbon nanotubes on surfaces using metal and non-metal catalysts," *Carbon N Y*, vol. 50, no. 6, pp. 2067–2082, 2012, doi: 10.1016/j.carbon.2012.01.035.
- [82] D. He, K. Cheng, T. Peng, M. Pan, and S. Mu, "Graphene/carbon nanospheres sandwich supported PEM fuel cell metal nanocatalysts with remarkably high activity and stability," *Journal of Materials Chemistry A*, vol. 1, no. 6, pp. 2126–2132, 2013, doi: 10.1039/c2ta00606e.
- [83] N. de Greef *et al.*, "Direct growth of carbon nanotubes on carbon fibers: Effect of the CVD parameters on the degradation of mechanical properties of carbon fibers," *Diamond and Related Materials*, vol. 51, pp. 39–48, Jan. 2015, doi: 10.1016/j.diamond.2014.11.002.
- [84] W. Chen, L. Duan, D. Zhu, W. E. I. Chen, and L. I. N. Duan, "Adsorption of Polar and Nonpolar Organic Chemicals to Carbon Nanotubes Adsorption of Polar and Nonpolar Organic Chemicals to Carbon Nanotubes," *Environmental Science and Technology*, vol. 41, no. 24, pp. 8295–8300, 2007, doi: 10.1021/es071230h.
- [85] L. Hu, Y. Peng, F. Wu, S. Peng, J. Li, and Z. Liu, "Tubular activated carbons made from cotton stalk for dynamic adsorption of airborne toluene," *J Taiwan Inst Chem Eng*, vol. 80, pp. 399–405, 2017, doi: 10.1016/j.jtice.2017.07.029.
- [86] E. Worch, *Adsorption Technology in Water Treatment*. 2012.
- [87] H.-B. Liu, B. Yang, and N.-D. Xue, "Enhanced adsorption of benzene vapor on granular activated carbon under humid conditions due to shifts in hydrophobicity and total micropore



- volume,” *Journal of Hazardous Materials*, vol. 318, pp. 425–432, Nov. 2016, doi: 10.1016/j.jhazmat.2016.07.026.
- [88] X. Yu *et al.*, “Insight into the significant roles of microstructures and functional groups on carbonaceous surfaces for acetone adsorption,” *RSC Advances*, vol. 8, no. 38, pp. 21541–21550, 2018, doi: 10.1039/C8RA03099E.
- [89] F. Chu, Y. Zheng, B. Wen, L. Zhou, J. Yan, and Y. Chen, “Adsorption of toluene with water on zeolitic imidazolate framework-8/graphene oxide hybrid nanocomposites in a humid atmosphere,” *RSC Advances*, vol. 8, no. 5, pp. 2426–2432, 2018, doi: 10.1039/C7RA12931A.
- [90] X. Ma, L. Li, R. Chen, C. Wang, K. Zhou, and H. Li, “Porous carbon materials based on biomass for acetone adsorption: Effect of surface chemistry and porous structure,” *Applied Surface Science*, vol. 459, pp. 657–664, Nov. 2018, doi: 10.1016/j.apsusc.2018.07.170.
- [91] J. Qi *et al.*, “Nitrogen doped porous hollow carbon spheres for enhanced benzene removal,” *Separation and Purification Technology*, vol. 188, pp. 112–118, 2017, doi: 10.1016/j.seppur.2017.07.021.
- [92] K. Xiao, H. Liu, Y. Li, G. Yang, Y. Wang, and H. Yao, “Excellent performance of porous carbon from urea-assisted hydrochar of orange peel for toluene and iodine adsorption,” *Chemical Engineering Journal*, vol. 382, p. 122997, Feb. 2020, doi: 10.1016/j.cej.2019.122997.
- [93] B. Dou, J. Li, Y. Wang, H. Wang, C. Ma, and Z. Hao, “Adsorption and desorption performance of benzene over hierarchically structured carbon – silica aerogel composites,” vol. 196, pp. 194–200, 2011, doi: 10.1016/j.jhazmat.2011.09.019.
- [94] S. Agnihotri and M. J. Rood, “Adsorption equilibrium of organic vapors on single-walled carbon nanotubes,” vol. 43, no. 2, pp. 2379–2388, 2005, doi: 10.1016/j.carbon.2005.04.020.
- [95] J. Carratala, “Regeneration of activated carbons saturated with benzene or toluene using an oxygen-containing atmosphere,” vol. 65, pp. 2190–2198, 2010, doi: 10.1016/j.ces.2009.12.017.
- [96] Z. Cheng *et al.*, “Novel biosorbents synthesized from fungal and bacterial biomass and their applications in the adsorption of volatile organic compounds,” *Bioresource Technology*, vol. 300, Mar. 2020, doi: 10.1016/j.biortech.2019.122705.
- [97] N. H. M. Hossein Tehrani *et al.*, “Preparation and characterization of a new waste-derived mesoporous carbon structure for ultrahigh adsorption of benzene and toluene at ambient conditions,” *Journal of Hazardous Materials*, vol. 384, 2020. doi: 10.1016/j.jhazmat.2019.121317.
- [98] I. K. Shah, P. Pre, and B. J. Alappat, “Effect of thermal regeneration of spent activated carbon on volatile organic compound adsorption performances,” *J Taiwan Inst Chem Eng*, vol. 45, no. 4, pp. 1733–1738, Jul. 2014, doi: 10.1016/j.jtice.2014.01.006.
- [99] K.-J. Kim and H.-G. Ahn, “The adsorption and desorption characteristics of a binary component system of toluene and methylethylketone on activated carbon modified with



- phosphoric acid," *Carbon N Y*, vol. 48, no. 8, pp. 2198–2202, Jul. 2010, doi: 10.1016/j.carbon.2010.02.021.
- [100] A. S. Subrenat and P. A. le Cloirec, "VOLATILE ORGANIC COMPOUND (VOC) REMOVAL BY ADSORPTION ONTO ACTIVATED CARBON FIBER CLOTH AND ELECTROTHERMAL DESORPTION: AN INDUSTRIAL APPLICATION," *Chemical Engineering Communications*, vol. 193, no. 4, pp. 478–486, Apr. 2006, doi: 10.1080/00986440500191768.
- [101] M. Jahandar Lashaki, J. D. Atkinson, Z. Hashisho, J. H. Phillips, J. E. Anderson, and M. Nichols, "The role of beaded activated carbon's surface oxygen groups on irreversible adsorption of organic vapors," *Journal of Hazardous Materials*, vol. 317, pp. 284–294, Nov. 2016, doi: 10.1016/j.jhazmat.2016.05.087.
- [102] X. Zhou *et al.*, "A novel MOF/graphene oxide composite GrO@MIL-101 with high adsorption capacity for acetone," *J. Mater. Chem. A*, vol. 2, no. 13, pp. 4722–4730, 2014, doi: 10.1039/C3TA15086K.
- [103] M. Popescu, J. P. Joly, J. Carré, and C. Danatoiu, "Dynamical adsorption and temperature-programmed desorption of VOCs (toluene, butyl acetate and butanol) on activated carbons," *Carbon N Y*, vol. 41, no. 4, pp. 739–748, 2003, doi: 10.1016/S0008-6223(02)00391-3.
- [104] G.-Y. Oh, Y.-W. Ju, M.-Y. Kim, H.-R. Jung, H. J. Kim, and W.-J. Lee, "Adsorption of toluene on carbon nanofibers prepared by electrospinning," *Science of The Total Environment*, vol. 393, no. 2–3, pp. 341–347, Apr. 2008, doi: 10.1016/j.scitotenv.2008.01.005.
- [105] R. R. Bansode, J. N. Losso, W. E. Marshall, R. M. Rao, and R. J. Portier, "Adsorption of volatile organic compounds by pecan shell- and almond shell-based granular activated carbons," *Bioresource Technology*, vol. 90, no. 2, pp. 175–184, Nov. 2003, doi: 10.1016/S0960-8524(03)00117-2.
- [106] M. Molina-Sabio and F. Rodríguez-Reinoso, "Role of chemical activation in the development of carbon porosity," *Colloids and Surfaces A: Physicochemical and Engineering Aspects*, vol. 241, no. 1–3, pp. 15–25, 2004, doi: 10.1016/j.colsurfa.2004.04.007.
- [107] J. Qi *et al.*, "Synthesis of porous carbon beads with controllable pore structure for volatile organic compounds removal," *Chemical Engineering Journal*, vol. 307, pp. 989–998, 2017, doi: 10.1016/j.cej.2016.09.022.
- [108] S. T. Lim *et al.*, "Mesoporous graphene adsorbents for the removal of toluene and xylene at various concentrations and its reusability," *Scientific Reports*, vol. 9, no. 1, p. 10922, Dec. 2019, doi: 10.1038/s41598-019-47100-z.
- [109] H. Benaddi *et al.*, "Surface functionality and porosity of activated carbons obtained from chemical activation of wood," *Carbon N Y*, vol. 38, no. 5, pp. 669–674, 2000, doi: 10.1016/S0008-6223(99)00134-7.
- [110] I. I. Salame and T. J. Bandoz, "Surface Chemistry of Activated Carbons: Combining the Results of Temperature-Programmed Desorption, Boehm, and Potentiometric Titrations.," *J Colloid Interface Sci*, vol. 240, no. 1, pp. 252–258, 2001, doi: 10.1006/jcis.2001.7596.



- [111] H. Liu, B. Yang, and N. Xue, "Enhanced adsorption of benzene vapor on granular activated carbon under humid conditions due to shifts in hydrophobicity and total micropore volume," vol. 318, pp. 425–432, 2016.
- [112] F. Meng, M. Song, Y. Wei, and Y. Wang, "The contribution of oxygen-containing functional groups to the gas-phase adsorption of volatile organic compounds with different polarities onto lignin-derived activated carbon fibers," *Environmental Science and Pollution Research*, vol. 26, no. 7, pp. 7195–7204, Mar. 2019, doi: 10.1007/s11356-019-04190-6.
- [113] A. J. Fletcher, Y. Yüzak, and K. M. Thomas, "Adsorption and desorption kinetics for hydrophilic and hydrophobic vapors on activated carbon," *Carbon N Y*, vol. 44, no. 5, pp. 989–1004, 2006, doi: 10.1016/j.carbon.2005.10.020.
- [114] S. Wu, W.-Q. Huang, R. Xu, R.-Y. Qi, Q. Zhang, and J. Zhong, "Adsorption of gasoline vapor/water vapor mixtures on TMCS-functionalized MIL-101(Cr)," *Gao Xiao Hua Xue Gong Cheng Xue Bao/Journal of Chemical Engineering of Chinese Universities*, vol. 30, no. 4, 2016, doi: 10.3969/j.issn.1003-9015.2016.04.011.
- [115] H. Wang *et al.*, "Elaborate control over the morphology and pore structure of porous silicas for VOCs removal with high efficiency and stability," *Adsorption*, vol. 23, no. 1, pp. 37–50, Jan. 2017, doi: 10.1007/s10450-016-9815-8.
- [116] C. Nieto-Delgado, M. Terrones, and J. R. Rangel-Mendez, "Development of highly microporous activated carbon from the alcoholic beverage industry organic by-products," *Biomass and Bioenergy*, vol. 35, no. 1, pp. 103–112, Jan. 2011, doi: 10.1016/j.biombioe.2010.08.025.
- [117] L. H. Velazquez-Jimenez, A. Pavlick, and J. R. Rangel-Mendez, "Chemical characterization of raw and treated agave bagasse and its potential as adsorbent of metal cations from water," *Industrial Crops and Products*, vol. 43, no. 1, pp. 200–206, 2013, doi: 10.1016/j.indcrop.2012.06.049.
- [118] O. G. Apul and T. Karanfil, "Adsorption of synthetic organic contaminants by carbon nanotubes : A critical review," *Water Research*, vol. 8, pp. 34–55, 2014.
- [119] R. B. Mathur, S. Chatterjee, and B. P. Singh, "Growth of carbon nanotubes on carbon fibre substrates to produce hybrid/phenolic composites with improved mechanical properties," *Composites Science and Technology*, vol. 68, no. 7–8, pp. 1608–1615, Jun. 2008, doi: 10.1016/j.compscitech.2008.02.020.
- [120] L. Escobar-Alarcón *et al.*, "Two-dimensional carbon nanostructures obtained by laser ablation in liquid: effect of an ultrasonic field," *Applied Physics A: Materials Science and Processing*, vol. 124, no. 2, pp. 1–7, 2018, doi: 10.1007/s00339-018-1559-8.
- [121] S. Agnihotri, M. J. Rood, and M. Rostam-Abadi, "Adsorption equilibrium of organic vapors on single-walled carbon nanotubes," *Carbon N Y*, vol. 43, no. 11, pp. 2379–2388, 2005, doi: 10.1016/j.carbon.2005.04.020.





- [122] S. Agnihotri, M. J. Rood, and M. Rostam-Abadi, "Adsorption equilibrium of organic vapors on single-walled carbon nanotubes," *Carbon N Y*, vol. 43, no. 11, pp. 2379–2388, Sep. 2005, doi: 10.1016/j.carbon.2005.04.020.
- [123] N. M. Gibson, T. J. M. Luo, O. Shenderova, Y. J. Choi, Z. Fitzgerald, and D. W. Brenner, "Fluorescent dye adsorption on nanocarbon substrates through electrostatic interactions," *Diamond and Related Materials*, vol. 19, no. 2–3, pp. 234–237, 2010, doi: 10.1016/j.diamond.2009.10.005.
- [124] J. M. Rosolen *et al.*, "Electron field emission from composite electrodes of carbon nanotubes-boron-doped diamond and carbon felts," *Applied Physics Letters*, vol. 88, no. 8, p. 083116, Feb. 2006, doi: 10.1063/1.2178247.
- [125] M. F. De Riccardis, D. Carbone, Th. D. Makris, R. Giorgi, N. Lisi, and E. Salernitano, "Anchorage of carbon nanotubes grown on carbon fibres," *Carbon N Y*, vol. 44, no. 4, pp. 671–674, Apr. 2006, doi: 10.1016/J.CARBON.2005.09.024.
- [126] F. He and D. Zhao, "Manipulating the size and dispersibility of zerovalent iron nanoparticles by use of carboxymethyl cellulose stabilizers," *Environmental Science and Technology*, vol. 41, no. 17, pp. 6216–6221, 2007, doi: 10.1021/es0705543.
- [127] S. Brunauer, P. H. Emmett, and E. Teller, "Adsorption of Gases in Multimolecular Layers," *J Am Chem Soc*, vol. 60, no. 1, pp. 309–319, 1938, doi: citeulike-article-id:4074706\rdoi: 10.1021/ja01269a023.
- [128] H. Qiu, L. Lv, B. Pan, Q. Q. Zhang, W. Zhang, and Q. Q. Zhang, "Critical review in adsorption kinetic models," *Journal of Zhejiang University SCIENCE A*, vol. 10, no. 5, pp. 716–724, 2009, doi: 10.1631/jzus.A0820524.
- [129] R. Palomo-Briones *et al.*, "Agave bagasse biorefinery: processing and perspectives," *Clean Technologies and Environmental Policy*, vol. 20, no. 7, pp. 1423–1441, Sep. 2018, doi: 10.1007/s10098-017-1421-2.
- [130] J. A. Perez-Pimienta *et al.*, "Characterization of agave bagasse as a function of ionic liquid pretreatment," *Biomass and Bioenergy*, vol. 75, pp. 180–188, 2015, doi: 10.1016/j.biombioe.2015.02.026.
- [131] M. Sevilla and A. B. Fuertes, "Sustainable porous carbons with a superior performance for CO<sub>2</sub> capture," *Energy and Environmental Science*, vol. 4, no. 5, pp. 1765–1771, 2011, doi: 10.1039/c0ee00784f.
- [132] M. Sevilla and A. B. Fuertes, "The production of carbon materials by hydrothermal carbonization of cellulose," *Carbon N Y*, vol. 47, no. 9, pp. 2281–2289, 2009, doi: 10.1016/j.carbon.2009.04.026.
- [133] S. Liu, J. Sun, and Z. Huang, "Carbon spheres activated carbon composite materials with high Cr adsorption capacity prepared by a hydrothermal method," *Journal of Hazardous Materials*, vol. 173, pp. 377–383, 2010.



- [134] S. Kestur G., T. H. S. Flores-Sahagun, L. P. Dos Santos, J. Dos Santos, I. Mazzaro, and A. Mikowski, "Characterization of blue agave bagasse fibers of Mexico," *Composites Part A: Applied Science and Manufacturing*, vol. 45, pp. 153–161, 2013, doi: 10.1016/j.compositesa.2012.09.001.
- [135] C. Tang, Y. Bando, D. Golberg, and F. Xu, "Structure and nitrogen incorporation of carbon nanotubes synthesized by catalytic pyrolysis of dimethylformamide," *Carbon N Y*, vol. 42, no. 12–13, pp. 2625–2633, 2004, doi: 10.1016/j.carbon.2004.05.047.
- [136] H. Liu *et al.*, "Structural and morphological control of aligned nitrogen-doped carbon nanotubes," *Carbon N Y*, vol. 8, no. 5, pp. 1–10, 2009, doi: 10.1016/j.carbon.2009.12.045.
- [137] L. Chen, K. Xia, L. Huang, L. Li, L. Pei, and S. Fei, "Facile synthesis and hydrogen storage application of nitrogen-doped carbon nanotubes with bamboo-like structure," *International Journal of Hydrogen Energy*, vol. 38, no. 8, pp. 3297–3303, 2013, doi: 10.1016/j.ijhydene.2013.01.055.
- [138] K. Bogdanov *et al.*, "Annealing-induced structural changes of carbon onions: High-resolution transmission electron microscopy and Raman studies," *Carbon N Y*, vol. 73, pp. 78–86, 2014, doi: 10.1016/j.carbon.2014.02.041.
- [139] M. S. Dresselhaus, G. Dresselhaus, R. Saito, and A. Jorio, "Raman spectroscopy of carbon nanotubes," *Physics Reports*, vol. 409, no. 2, pp. 47–99, 2005, doi: 10.1016/j.physrep.2004.10.006.
- [140] N. Larouche and B. L. Stansfield, "Classifying nanostructured carbons using graphitic indices derived from Raman spectra," *Carbon N Y*, vol. 48, no. 3, pp. 620–629, 2010, doi: 10.1016/j.carbon.2009.10.002.
- [141] M. S. Dresselhaus, A. Jorio, M. Hofmann, G. Dresselhaus, and R. Saito, "Perspectives on carbon nanotubes and graphene Raman spectroscopy," *Nano Letters*, vol. 10, no. 3, pp. 751–758, 2010, doi: 10.1021/nl904286r.
- [142] H. J. Seong and A. L. Boehman, "Evaluation of Raman Parameters Using Visible Raman Microscopy for Soot Oxidative Reactivity," *Energy and Fuels*, vol. 27, pp. 1643–1624, 2013.
- [143] S. L. H. Rebelo, A. Guedes, M. E. Szeftczyk, A. M. Pereira, J. P. Araújo, and C. Freire, "Progress in the Raman spectra analysis of covalently functionalized multiwalled carbon nanotubes: Unraveling disorder in graphitic materials," *Physical Chemistry Chemical Physics*, vol. 18, no. 18, pp. 12784–12796, 2016, doi: 10.1039/c5cp06519d.
- [144] C. Nieto-Delgado and J. R. Rangel-Mendez, "Production of activated carbon from organic by-products from the alcoholic beverage industry: Surface area and hardness optimization by using the response surface methodology," *Industrial Crops and Products*, vol. 34, no. 3, pp. 1528–1537, Nov. 2011, doi: 10.1016/j.indcrop.2011.05.014.
- [145] A. Aqel, K. M. M. A. El-Nour, R. A. A. Ammar, and A. Al-Warthan, "Carbon nanotubes, science and technology part (I) structure, synthesis and characterisation," *Arabian Journal of Chemistry*, vol. 5, no. 1, pp. 1–23, Jan. 2012, doi: 10.1016/j.arabjc.2010.08.022.





- [146] J. Wu, L. Zhang, C. Long, and Q. Zhang, "Adsorption Characteristics of Pentane , Hexane , and Heptane : Comparison of Hydrophobic Hypercrosslinked Polymeric Adsorbent with Activated Carbon," 2012, doi: 10.1021/je300550x.
- [147] F. I. Khan and A. K. Ghoshal, "Removal of Volatile Organic Compounds from polluted air," vol. 13, no. x, pp. 527–545, 2000.
- [148] L. M. Apátiga and V. M. Castaño, "Magnetic behavior of cobalt oxide films prepared by pulsed liquid injection chemical vapor deposition from a metal-organic precursor," *Thin Solid Films*, vol. 496, no. 2, pp. 576–579, Feb. 2006, doi: 10.1016/j.tsf.2005.08.344.
- [149] A. K. Roy and W. A. Goedel, "Control of thickness and morphology of thin alumina films deposited via Pulsed Chemical Vapor Deposition (Pulsed CVD) through variation of purge times," *Surface and Coatings Technology*, vol. 205, no. 17–18, pp. 4177–4182, May 2011, doi: 10.1016/j.surfcoat.2011.03.009.
- [150] T. Ichikawa, N. Shimizu, K. Ishikawa, M. Hiramatsu, and M. Hori, "Synthesis of isolated carbon nanowalls via high-voltage nanosecond pulses in conjunction with CH<sub>4</sub>/H<sub>2</sub> plasma enhanced chemical vapor deposition," *Carbon N Y*, vol. 161, pp. 403–412, May 2020, doi: 10.1016/j.carbon.2020.01.064.
- [151] J. A. Arcibar-Orozco, D.-B. Josue, J. C. Rios-Hurtado, and J. R. Rangel-Mendez, "Influence of iron content, surface area and charge distribution in the arsenic removal by activated carbons," *Chemical Engineering Journal*, vol. 249, pp. 201–209, 2014, doi: 10.1016/j.cej.2014.03.096.
- [152] T. J. Bandoz, J. Jagiello, C. Contescu, and J. A. Schwarz, "Characterization of the surfaces of activated carbons in terms of their acidity constant distributions," *Carbon N Y*, vol. 31, no. 7, pp. 1193–1202, 1993, doi: 10.1016/0008-6223(93)90072-l.
- [153] J. Jagiello, T. J. Bandoz, K. Putyera, and J. A. Schwarz, "Determination of Proton Affinity Distributions for Chemical Systems in Aqueous Environments Using a Stable Numerical Solution of the Adsorption Integral Equation," *Journal of Colloid and Interface Science*, vol. 172, no. 2, pp. 341–346, 1995. doi: 10.1006/jcis.1995.1262.
- [154] W. Z. Li, D. Z. Wang, S. X. Yang, J. G. Wen, and Z. F. Ren, "Controlled growth of carbon nanotubes on graphite foil by chemical vapor deposition," vol. 335, no. February, pp. 141–149, 2001.
- [155] E. Tovar-Martinez, J. A. Moreno-Torres, J. v. Cabrera-Salazar, M. Reyes-Reyes, L. F. Chazaro-Ruiz, and R. López-Sandoval, "Synthesis of carbon nano-onions doped with nitrogen using spray pyrolysis," *Carbon N Y*, vol. 140, pp. 171–181, Dec. 2018, doi: 10.1016/j.carbon.2018.08.056.
- [156] L. S. Lobo, "Nucleation and growth of carbon nanotubes and nano fi bers : Mechanism and catalytic geometry control," *Carbon N Y*, vol. 114, pp. 411–417, 2017, doi: 10.1016/j.carbon.2016.12.005.



- [157] T. R. Pozegic, I. Hamerton, J. v Anguita, W. Tang, P. Jenkins, and S. R. P. Silva, "Low temperature growth of carbon nanotubes on carbon fibre to create a highly networked fuzzy fibre reinforced composite with superior electrical conductivity," vol. 4, 2014.
- [158] H. J. Seong and A. L. Boehman, "Evaluation of Raman Parameters Using Visible Raman Microscopy for Soot Oxidative Reactivity," *Energy & Fuels*, vol. 27, no. 3, pp. 1613–1624, Mar. 2013, doi: 10.1021/ef301520y.
- [159] J. A. Quezada-Renteria, C. O. Ania, L. F. Chazaro-Ruiz, and J. R. Rangel-Mendez, "Influence of protons on reduction degree and defect formation in electrochemically reduced graphene oxide," *Carbon N Y*, vol. 149, pp. 722–732, Aug. 2019, doi: 10.1016/j.carbon.2019.04.109.
- [160] T. J. Bandoz, J. Jagiello, and J. a Schwarz, "Effect of Surface Chemical Groups on Energetic Heterogeneity of Activated Carbons," *Langmuir*, vol. 9, no. 9, pp. 2518–2522, 1993, doi: 10.1021/la00034a008.
- [161] C. Nieto-Delgado, J. Gutiérrez-Martínez, and J. R. Rangel-Méndez, "Modified activated carbon with interconnected fibrils of iron-oxyhydroxides using  $Mn^{2+}$  as morphology regulator, for a superior arsenic removal from water," *Journal of Environmental Sciences (China)*, vol. 76, 2019, doi: 10.1016/j.jes.2018.06.002.
- [162] W. Stumm and J. J. Morgan, *Aquatic Chemistry: Chemical Equilibria and Rates in Natural Waters*, Third Edit. New York: Environmental Science and Technology, 1996.
- [163] X. Zhang *et al.*, "Chemically activated hydrochar as an effective adsorbent for volatile organic compounds (VOCs)," *Chemosphere*, vol. 218, pp. 680–686, Mar. 2019, doi: 10.1016/j.chemosphere.2018.11.144.
- [164] M. Badruzzaman, P. Westerhoff, and D. R. U. Knappe, "Intraparticle diffusion and adsorption of arsenate onto granular ferric hydroxide (GFH)," *Water Research*, vol. 38, no. 18, pp. 4002–4012, 2004, doi: 10.1016/j.watres.2004.07.007.
- [165] H. Liu, Y. Yu, Q. Shao, and C. Long, "Porous polymeric resin for adsorbing low concentration of VOCs: Unveiling adsorption mechanism and effect of VOCs' molecular properties," *Separation and Purification Technology*, vol. 228, p. 115755, Dec. 2019, doi: 10.1016/j.seppur.2019.115755.
- [166] H. Deng *et al.*, "Adsorptive removal of toluene and dichloromethane from humid exhaust on MFI, BEA and FAU zeolites: An experimental and theoretical study," *Chemical Engineering Journal*, vol. 394, no. April, p. 124986, Aug. 2020, doi: 10.1016/j.cej.2020.124986.
- [167] M. Plata-Gryl, M. Momotko, S. Makowiec, and G. Boczkaj, "Highly effective asphaltene-derived adsorbents for gas phase removal of volatile organic compounds.pdf," pp. 315–312, 2019.
- [168] K. Kosuge, S. Kubo, N. Kikukawa, and M. Takemori, "Effect of Pore Structure in Mesoporous Silicas on VOC Dynamic Adsorption / Desorption Performance," no. 23, pp. 3095–3102, 2007, doi: 10.1021/la062616t.



- [169] W. Zhang, Z. Qu, X. Li, Y. Wang, D. Ma, and J. Wu, "Comparison of dynamic adsorption / desorption characteristics of toluene on different porous materials," 2012.
- [170] Z. Wang *et al.*, "Structural evolution of hydrothermal carbon spheres induced by high temperatures and their electrical properties under compression," *Carbon N Y*, vol. 121, pp. 426–433, 2017, doi: 10.1016/j.carbon.2017.06.003.
- [171] S. Agnihotri, J. P. B. Mota, M. Rostam-Abadi, and M. J. Rood, "Structural Characterization of Single-Walled Carbon Nanotube Bundles by Experiment and Molecular Simulation," *Langmuir*, vol. 21, no. 3, pp. 896–904, 2005, doi: 10.1021/la047662c.
- [172] Q. Hu, J. J. Li, Z. P. Hao, L. D. Li, and S. Z. Qiao, "Dynamic adsorption of volatile organic compounds on organofunctionalized SBA-15 materials," *Chemical Engineering Journal*, vol. 149, no. 1–3, pp. 281–288, 2009, doi: 10.1016/j.cej.2008.11.003.
- [173] A. Abdolali *et al.*, "Application of a breakthrough biosorbent for removing heavy metals from synthetic and real wastewaters in a lab-scale continuous fixed-bed column," *Bioresource Technology*, vol. 229, pp. 78–87, Apr. 2017, doi: 10.1016/j.biortech.2017.01.016.
- [174] M. A. Acheampong, K. Pakshirajan, A. P. Annachatre, and P. N. L. Lens, "Removal of Cu(II) by biosorption onto coconut shell in fixed-bed column systems," *Journal of Industrial and Engineering Chemistry*, vol. 19, no. 3, pp. 841–848, May 2013, doi: 10.1016/j.jiec.2012.10.029.
- [175] A. A. Azzaz, S. Jellali, R. Souissi, K. Ergaieg, and L. Bousselmi, "Alkaline-treated sawdust as an effective material for cationic dye removal from textile effluents under dynamic conditions: breakthrough curve prediction and mechanism exploration.," *Environ Sci Pollut Res Int*, vol. 24, no. 22, pp. 18240–18256, Aug. 2017, doi: 10.1007/s11356-017-9388-4.
- [176] Y. Shen and N. Zhang, "A facile synthesis of nitrogen-doped porous carbons from lignocellulose and protein wastes for VOCs sorption," *Environmental Research*, vol. 189, p. 109956, Oct. 2020, doi: 10.1016/j.envres.2020.109956.
- [177] C. I. A. Ferreira, V. Calisto, M. Otero, H. Nadais, and V. I. Esteves, "Fixed-bed adsorption of Tricaine Methanesulfonate onto pyrolysed paper mill sludge," *Aquacultural Engineering*, vol. 77, pp. 53–60, May 2017, doi: 10.1016/j.aquaeng.2017.02.006.
- [178] T. Georgiou *et al.*, "Graphene bubbles with controllable curvature," *Applied Physics Letters*, vol. 99, no. 9, Aug. 2011, doi: 10.1063/1.3631632.
- [179] P. Tian *et al.*, "Curvature-induced electronic tuning of molecular catalysts for CO<sub>2</sub> reduction," *Catalysis Science and Technology*, vol. 11, no. 7, pp. 2491–2496, Apr. 2021, doi: 10.1039/d0cy01589j.
- [180] Sam. R. Reddy, "EVAP Canister purge prediction for engine and air control," *United States Patent*, vol. 2, no. 12, 2007.
- [181] Y. Ryu, J. Chang, S. Jung, and C. Lee, "Adsorption Isotherms of Toluene and Gasoline Vapors on DAY Zeolite," pp. 363–366, 2002.



- [182] C. E. Flores-Chaparro, M. C. Rodriguez-Hernandez, L. F. Chazaro-Ruiz, Ma. C. Alfaro-De la Torre, M. A. Huerta-Diaz, and J. R. Rangel-Mendez, "Experimental and modeling of competitive biosorption of benzene, toluene, ethylbenzene, xylenes, and naphthalene (BTEXN) in a packed-bed column with a macroalgae-based composite: Effect of dissolved organic matter and flow rate on breakthrough curves," *Journal of Water Process Engineering*, vol. 40, p. 101874, Apr. 2021, doi: 10.1016/j.jwpe.2020.101874.
- [183] Marcus Knappert, "Supramolecular Chemistry of Poly(ester imide)s," Reading, Reino Unido, 2019.
- [184] M. Kraus, U. Trommler, F. Holzer, F.-D. Kopinke, and U. Roland, "Competing adsorption of toluene and water on various zeolites," *Chemical Engineering Journal*, vol. 351, pp. 356–363, Nov. 2018, doi: 10.1016/j.cej.2018.06.128.
- [185] M. S. Hussein and M. J. Ahmed, "Fixed bed and batch adsorption of benzene and toluene from aromatic hydrocarbons on 5A molecular sieve zeolite," *Materials Chemistry and Physics*, vol. 181, pp. 512–517, Sep. 2016, doi: 10.1016/j.matchemphys.2016.06.088.
- [186] M. Shafiei, M. S. Alivand, A. Rashidi, A. Samimi, and D. Mohebbi-Kalhari, "Synthesis and adsorption performance of a modified micro-mesoporous MIL-101(Cr) for VOCs removal at ambient conditions," *Chemical Engineering Journal*, vol. 341, pp. 164–174, Jun. 2018, doi: 10.1016/j.cej.2018.02.027.
- [187] Y. H. YOON and J. H. NELSON, "Application of Gas Adsorption Kinetics I. A Theoretical Model for Respirator Cartridge Service Life," *American Industrial Hygiene Association Journal*, vol. 45, no. 8, pp. 509–516, Aug. 1984, doi: 10.1080/15298668491400197.

# Supplementary information

**Table SI4.** Overall variables and parameters obtained at the evaluated experimental conditions of dynamic adsorption.

Parameter	Units	Activated carbon (AC)							
		Pentane		Hexane		Benzene		Toluene	
		first	second	first	second	first	second	first	second
Q	mL min <sup>-1</sup>	25.00	20.00	33.00	35.00	32.00	33.00	30.00	30.00
C <sub>0.85</sub>	mg L <sup>-1</sup>	302.66	236.96	140.11	125.01	86.00	74.07	19.00	19.16
C <sub>0.1</sub>	mg L <sup>-1</sup>	35.61	27.88	16.48	14.71	10.12	8.71	2.24	2.25
C <sub>0</sub>	mg L <sup>-1</sup>	356.07	278.78	164.83	147.08	101.18	87.14	22.36	22.55
t <sub>exh</sub>	min	114	192	150.00	70.00	145.00	121.00	218.00	190.00
t <sub>b</sub>	min	22	4	18.00	10.00	41.00	26.00	84.00	43.00
V <sub>0.85</sub>	L	2.85	3.84	4.95	2.45	4.64	3.87	6.54	5.32
V <sub>0.1</sub>	L	0.55	0.08	0.59	0.35	1.31	0.83	2.52	1.20

**Table S14.** (Continued).

$V_{0.9}$	L	2.99	6.14	7.98	4.85	4.93	4.60	7.52	6.76
$\phi$		0.71	0.47	0.44	0.35	0.69	0.61	0.60	0.56
H	cm	10.01	10.95	8.26	8.83	9.18	9.26	9.54	10.45
$H_{MTZ}$	cm	10.58	22.49	14.27	17.09	8.47	10.54	7.75	12.32
$R_{MTZ}$	cm min <sup>-1</sup>	0.12	0.12	0.11	0.28	0.08	0.11	0.06	0.09
m	g	0.50	0.55	0.52	0.55	0.57	0.58	0.60	0.65
C	mg L <sup>-1</sup>	310.50	230.55	137.63	126.19	84.08	76.42	17.93	19.98
$C_{ads}$	mg L <sup>-1</sup>	45.58	48.23	27.20	20.88	17.10	10.72	4.43	2.57
$t_{total}$	min	120.00	163.00	98.00	95.00	113.00	140.00	155.00	218.00
A	cm <sup>2</sup>	5469.28	7861.32	2665.30	1984.04	1932.14	1500.59	686.14	560.34
$q_{total}$	mg	136.73	157.23	87.95	69.44	61.83	49.52	20.58	16.81
$m_{total}$	mg	1068.22	908.82	533.06	489.02	365.85	402.60	103.96	147.46
% Removal		12.80	17.30	16.50	14.20	16.90	12.30	19.80	11.40
$q_{calc}$	mg g <sup>-1</sup>	273.33	287.19	170.48	125.81	107.75	85.53	34.54	25.73

**Table S14.** (Continued).

		Biochar (BC)							
parameter	units	Pentane		Hexane		Benzene		Toluene	
		first	second	first	second	first	second	first	second
Q	mL min <sup>-1</sup>	20.00	25.00	20.00	24.00	25.00	32.00	20.00	20.00
C <sub>0.85</sub>	mg L <sup>-1</sup>	200.98	257.09	93.81	98.24	62.04	57.35	29.94	26.73
C <sub>0.1</sub>	mg L <sup>-1</sup>	23.64	30.25	11.04	11.56	7.30	6.75	3.52	3.14
C <sub>0</sub>	mg L <sup>-1</sup>	236.45	302.46	110.37	115.58	72.99	67.47	35.22	31.44
t <sub>exh</sub>	min	130	104	80	62.00	81.00	51.00	70	90
t <sub>b</sub>	min	6	5	8	7.00	10.00	4.00	8	8
V <sub>0.85</sub>	L	2.60	2.60	1.60	1.49	2.03	1.63	1.40	1.80
V <sub>0.1</sub>	L	0.12	0.13	0.16	0.17	0.25	0.13	0.16	0.16
V <sub>0.9</sub>	L	4.90	6.00	4.82	2.45	4.80	2.22	4.05	2.75
φ		0.39	0.32	0.23	0.43	0.29	0.54	0.24	0.48
H	cm	11.40	10.80	8.65	11.21	10.50	10.65	8.11	9.71
H <sub>MTZ</sub>	cm	30.65	29.46	22.31	19.96	24.25	17.06	19.32	16.96
R <sub>MTZ</sub>	cm min <sup>-1</sup>	0.25	0.30	0.31	0.36	0.34	0.36	0.31	0.21

**Table S14.** (Continued).

m	g	0.56	0.54	0.48	0.56	0.53	0.53	0.44	0.49
C <sub>out</sub>	mg L <sup>-1</sup>	194.60	262.54	96.24	107.84	64.52	62.07	30.71	26.85
C <sub>ads</sub>	mg L <sup>-1</sup>	41.85	39.92	14.13	7.74	8.47	5.40	4.51	4.59
t <sub>total</sub>	min	134.00	120.00	145.00	132.00	150.00	105.00	95.00	100.00
A	cm <sup>-2</sup>	5608.07	4790.97	2048.47	1022.19	1270.03	566.75	428.28	459.07
q <sub>total</sub>	mg	112.16	119.77	40.97	24.53	31.75	18.14	8.57	9.18
m <sub>total</sub>	mg	633.68	907.38	320.07	366.16	273.71	226.70	66.92	62.89
% Removal		17.70	13.20	12.80	6.70	11.60	8.00	12.80	14.60
q <sub>cal</sub>	mg g <sup>-1</sup>	200.90	221.87	85.71	43.76	60.45	34.07	19.29	18.91



**Table S14.** (Continued).

BCVD600-1p sample											
Parameter	Units	Pentane		Hexane		Benzene				Toluene	
		first	second	first	second	first	second	third	fourth	first	second
Q	mL min <sup>-1</sup>	24.00	20.00	33.00	35.00	34.00	34.00	34.00	34.00	23.00	25.00
C <sub>0.85</sub>	mg L <sup>-1</sup>	210.44	189.58	70.06	51.36	47.05	54.03	48.04	45.03	25.33	23.35
C <sub>0.1</sub>	mg L <sup>-1</sup>	24.76	22.30	8.24	6.04	5.54	6.36	5.65	5.30	2.98	2.75
C <sub>0</sub>	mg L <sup>-1</sup>	247.58	223.03	82.43	60.42	55.36	63.57	56.52	52.98	29.80	27.47
t <sub>exh</sub>	min	95	120	170.00	170.00	142.00	109.00	126.00	131.00	166.00	120.00
t <sub>b</sub>	min	14	9	17.00	17.00	34.00	26.00	22.00	19.00	34.00	30.00
V <sub>0.85</sub>	L	2.28	3.00	3.40	3.74	4.54	3.49	4.03	4.19	3.82	3.00
V <sub>0.1</sub>	L	0.34	0.23	0.34	0.37	1.09	0.83	0.70	0.61	0.78	0.75
V <sub>0.9</sub>	L	4.43	6.15	4.78	5.41	6.13	4.32	5.99	6.65	5.57	4.95
φ		0.36	0.35	0.52	0.50	0.51	0.57	0.47	0.45	0.48	0.40
H	cm	9.68	9.81	9.96	10.00	9.48	9.47	9.56	9.10	8.93	9.31
H <sub>MTZ</sub>	cm	18.30	22.70	15.88	16.32	11.43	10.70	13.99	14.80	12.17	12.66
R <sub>MTZ</sub>	cm min <sup>-1</sup>	0.23	0.20	0.17	0.17	0.11	0.14	0.14	0.14	0.09	0.14

**Table S14.** (Continued).

m	g	0.48	0.49	0.50	0.50	0.47	0.47	0.48	0.45	0.45	0.47
C <sub>out</sub>	mg L <sup>-1</sup>	217.37	193.59	72.62	51.78	47.44	58.29	51.60	48.21	24.85	24.01
C <sub>ads</sub>	mg L <sup>-1</sup>	30.20	29.44	9.81	8.64	7.92	5.28	4.92	4.77	4.95	3.46
t <sub>total</sub>	min	180.00	173.00	190.00	190.00	143.00	170.00	190.00	210.00	145.00	157.00
A	cm <sup>2</sup>	5436.79	5093.16	1863.70	1641.56	1131.95	896.93	934.26	1001.30	717.19	543.33
Q <sub>total</sub>	mg	130.48	127.33	61.50	57.45	38.49	30.50	31.76	34.04	16.50	13.58
m <sub>total</sub>	mg	1069.53	964.61	516.82	401.78	269.14	367.42	365.11	378.27	99.37	107.80
% Removal		12.20	13.20	11.90	14.30	14.30	8.30	8.70	9.00	16.60	12.60
q <sub>calc</sub>	mg g <sup>-1</sup>	269.57	259.54	123.45	114.92	81.23	64.43	66.47	74.84	36.95	29.19